

**Study on Relationship between Molecular Structures and Exchange Couplings
in Magnetic Materials Having 4f–3d, 3d–3d, and 3d–2p Spins**

Atsushi Okazawa

The University of Electro-Communications

March 2009

STUDY ON RELATIONSHIP BETWEEN MOLECULAR
STRUCTURES AND EXCHANGE COUPLINGS IN
MAGNETIC MATERIALS HAVING
4F–3D, 3D–3D, AND 3D–2P SPINS

ATSUSHI OKAZAWA

*THESIS SUBMITTED TO GRADUATE SCHOOL OF
ELECTRO-COMMUNICATIONS,
THE UNIVERSITY OF ELECTRO-COMMUNICATIONS
IN FULFILLMENT OF THE REQUIREMENT FOR THE
DEGREE OF PHILOSOPHY*

MARCH 2009

STUDY ON RELATIONSHIP BETWEEN MOLECULAR
STRUCTURES AND EXCHANGE COUPLINGS IN
MAGNETIC MATERIALS HAVING
4F–3D, 3D–3D, AND 3D–2P SPINS

APPROVED BY SUPERVISORY COMMITTEE:

CHAIRPERSON: Prof. Takayuki Ishida

MEMBER: Prof. Shigeo Hayashi

MEMBER: Prof. Kichizo Asai

MEMBER: Prof. Katsuyasu Kawano

MEMBER: Prof. Hiroyuki Nojiri (Tohoku University)

Copyright © 2009 by Atsushi Okazawa

4f-3d, 3d-3d および 3d-2p スピンを有する磁性材料における 分子構造と交換相互作用の相関についての研究

岡澤 厚

概要

本論文は、分子性磁性材料における化合物を開発し、それらを特徴づける交換相互作用に着目して分子構造との相関性を調べた研究について述べたものである。

以下に記す、三つの主題について研究を行った。

- (1) ランタノイドイオン(4f スピン)-遷移金属イオン(3d スピン)間の交換相互作用
- (2) 遷移金属イオン(3d スピン)-有機ラジカル(2p スピン)間の交換相互作用
- (3) 同種遷移金属イオン(3d スピン)間の交換相互作用

本論文は全部で十章から構成されており、第一章では研究分野となる分子性磁性物質開発の歴史について簡単に紹介し、後に続く章で議論する研究の意義について述べてある。第二章では、磁気測定実験に対する物理的な背景・理論について、要点を絞ってまとめている。これら導入の後に続いて、まず主題(1)の研究から議論している。

主題(1)の研究意義は次の通りである。低温下で遅い磁化の緩和を持つために分子一つに由来する磁気ヒステリシスを持ち、量子トンネリングなど興味深い物性を示す単分子磁石は特に注目を集めている研究であるといえる。その中でも、4f-3d ヘテロスピンを利用した材料開発は特に盛んである。物性向上のための的確な指針を得るためにも、エネルギー構造の詳細などを調べることは重要である。

第三章では、4f-3d ヘテロスピ系単分子磁石である $[\text{Dy}_2\text{Ni}]$ および $[\text{Dy}_2\text{Cu}]$ に、パルス磁場下磁化測定と高磁場・高周波数電子常磁性共鳴(HF-EPR)測定を行った実験について述べている。これら測定結果により、各化合物のエネルギー構造を明らかにし、交換相互作用 J_{4f-3d} を詳細に決定したことについて議論している。本研究は、HF-EPR を用いて 4f-3d スピン間の交換相互作用を正確に決めた最初の例である。

第四章は、より複雑なスピン構造を持つ系に対して、この新規手法が特に有効であることを示している。本章ではまず、鎖状構造を持つ $[\text{Dy}_2\text{Cu}_2]_n$ の新規合成と、単分子磁石性について記述している。続いて、HF-EPR 測定を用いた交換相互作用の決定法について議論している。第三章で述べた化合物は単一の交換相互作用のみを持つ系であるのに対して、 $[\text{Dy}_2\text{Cu}_2]_n$ では二つの異なる交換相互作用が存在する。

さらに、 $[\text{Dy}_2\text{Cu}_2]_n$ の各種ランタノイド誘導体 $[\text{Ln}_2\text{Cu}_2]_n$ ($\text{Ln} = \text{Tb}, \text{Ho}, \text{Er}$)を合成し、同様に HF-EPR 測定を用いることで重希土類内の原子番号の違いが交換相互作用の値にどのように影響するかを調べた。第五章では、これら実験について述べている。本研究結果から、 J_{4f-3d} の絶対値が原子番号の増加

に伴い単調的に減少することを見出した。これら研究が、今後の 4f-3d スピン系単分子磁石開発に対する大きな指針となることが言える。

続いて第六章から第八章までは、主題(2)について議論している。本主題の研究意義は以下の通りである。分子性磁性体の開発を目指した合成戦略として、有機ラジカル配位子と遷移金属イオンによるヘテロスピンを利用した研究も盛んである。磁性源を遷移金属イオンのみに頼らず、配位子にもスピンを持たせることでスピン密度を高めるのみならず三次元的にスピンを揃えやすくできる。そこで、室温級に相互作用の大きなニトロキシドラジカルと遷移金属イオンとの錯体を新規に合成し、磁性と構造の相関性について調べていった。具体的には、*tert*-ブチルニトロキシド置換 2-ピリジン誘導体を新規合成し、これらラジカル配位子を用いて銅(II)およびニッケル(II)の 2:1 錯体を得ている。八種類の類似骨格を持つ錯体について、それぞれ X 線結晶構造解析から分子構造を明らかにし、SQUID 装置を使用した磁気測定により交換相互作用の値を求めていった。

第六章では、これまで安定単離できないと考えられていた *tert*-ブチル 2-ピリジルニトロキシドを、錯形成を利用して単離に成功したことについて述べている。

第七章では、安定なニトロキシド誘導体の錯化合物の合成・物性と、これまでの類似分子も合わせた構造と磁性の相関性について議論している。キレート面の平面性のずれを表す変数として $M-O-N-C_{2py}$ のねじれ角 ϕ を定義し、 $|\phi|$ の値に強く相関して交換相互作用が変化することを見出した。

さらに、第八章は別のラジカル配位子を用いた錯体についても議論している。

第九章では、主題(3)について述べている。スピロ骨格を有するニッケル(II)およびマンガン二核錯体(II)を合成し、同種イオン間の磁氣的相互作用の制御を試みた。当初の分子設計指針通り、それぞれ分子内強磁性相互作用と反強磁性相互作用を示すことを明らかにした。

各種スピン間の交換相互作用の決定を主眼に置き、分子性磁性物質の物理的性質について分子構造との関連性から明らかにしてきた。以上研究結果を第十章に総括として記している。本論文で示された研究結果が、今後の分子性磁性物質の開発・物性向上の指針の一部になるであろうと期待される。

Study on Relationship between Molecular Structures and
Exchange Couplings in Magnetic Materials
Having 4f–3d, 3d–3d, and 3d–2p Spins

Atsushi Okazawa

ABSTRACT

This thesis describes relationship between the molecular structure and the exchange interaction, which characterizes nature of molecular magnetic materials. Determination of magnetic exchange coupling is one of the most important issues in the study of magnetic clusters.

The contents are mainly divided into the three following subjects.

- (i) Exchange couplings between lanthanoid ion (4f spin) and transition-metal ion (3d spin)
- (ii) Exchange couplings between transition-metal ion and organic free radical (2p spin)
- (iii) Exchange couplings between homo transition-metal ions

The purpose of Subject (i) is as follows. The exchange couplings between a lanthanide ion and a transition-metal ion have been only roughly determined by means of pulsed-field magnetization measurements. We applied a high-frequency (HF)-EPR technique to the 4f–3d heterometallic SMMs, which has never been utilized for such purpose before our work.

The determination of exchange couplings between 4f- and 3d-spins in $[\text{Dy}_2\text{Cu}]$ and $[\text{Dy}_2\text{Ni}]$ SMMs is demonstrated. The one-dimensional compound $[\text{Dy}_2\text{Cu}_2]_n$ showed SMM behavior and two Dy–Cu exchange parameters were precisely evaluated. The study on isomorphous $[\text{Ln}_2\text{Cu}_2]_n$ (Ln = Gd, Tb, Dy, Ho, and Er) revealed that the J_{4f-3d} value monotonically decreased in the order of increasing the number of the 4f-electrons.

The purpose of Subject (ii) is to establish strongly ferromagnetic couplings in the metal–radical hybrid systems. 3d- and 2p-spins seem to be promising for development of strongly correlated magnetic materials, in comparison with 4f-spins.

A simple magneto-structure relationship in copper(II) and nickel(II) complexes chelated with *tert*-butyl 2-pyridyl nitroxide radicals was proposed. *tert*-Butyl 2-pyridyl nitroxide, known to be unisolable under ambient conditions, was successfully utilized in this work. Furthermore, synthesis, crystal structures, and magnetic properties of the two novel stable nitroxide and its coordination compounds are presented.

The purpose of Subject (iii) is to construct homometallic spin systems showing ferromagnetic couplings. Heterometallic approaches have a disadvantage of potential difficulty in preparation, because of possible metal-scrambling and low positional selectivity. Facile preparation is desired. Magnetic interactions between 3d–3d spins connected with a spiro-bridge were investigated. Intramolecular 3d–3d couplings are ferro- and antiferromagnetic for the dinuclear nickel(II) and manganese(II) complexes, respectively. This finding can be explained in terms of the orthogonal arrangement of SOMO–SOMO orbitals.

Acknowledgements

This doctorate thesis is a summary of author's study from April 2003 to March 2009 at Department of Applied Physics and Chemistry, The University of Electro-Communications.

The present work has been completed under the guidance and supervision of Professor Takayuki Ishida (Department of Applied Physics and Chemistry, The University of Electro-Communications). The author would like to express sincere gratitude for his support, valuable suggestions and encouragement. Sincerely acknowledgement is also made to Professor Takashi Nogami (Department of Applied Physics and Chemistry, The University of Electro-Communications) for his valuable and helpful advice.

The Chapters 3–5 resulted from the collaboration with Professor Hiroyuki Nojiri (Institute for Materials Research, Tohoku University). He kindly allowed the author to utilize his home-made apparatus. The author gratefully acknowledges for his helpful discussion and kind assistance in pulsed-field magnetization and HF-EPR measurements.

Thanks are given to all members of Nogami & Ishida Lab. (Department of Applied Physics and Chemistry, The University of Electro-Communications) for their various discussions, especially to Mr. Ryo Watanabe and Yasunori Nagaichi for the preparations of some samples.

The present work was supported by Research Fellowships of the Japan Society for the Promotion of Science for Young Scientist from April 2008 to March 2009.

Finally the author wishes to express grateful acknowledgement to his family and his friends for many years of encouragements.

Contents

Abstract (Japanese)	i
Abstract (English)	iii
Acknowledgements.....	v
Abbreviations	xiii

CHAPTER 1 1

GENERAL INTRODUCTION

1.1 History of Molecular Magnetic Materials	1
1.2 Advantages of Molecular Magnetic Materials.....	2
1.3 Scope of This Thesis.....	2
References	5

CHAPTER 2 6

THEORETICAL SECTION

2.1 Definitions and Units	6
2.2 Diamagnetic and Paramagnetic Susceptibilities	6
2.3 van Vleck Formula	7
2.4 Temperature-Independent Paramagnetism	8
2.5 The Curie Law	9
2.6 Spin Hamiltonian	10
2.7 Intermolecular Interaction; Molecular Field.....	11
2.8 Singlet–Triplet Model as an Example for Clusterized Spin Systems.....	12
2.9 Zero-Field Splitting	14
2.10 Ac Susceptibility.....	15
2.11 Single-Molecule Magnets	18
2.12 Lanthanoid Ions	20
2.13 Oximate Ligands.....	21
References	22

CHAPTER 323**MAGNETIC PROPERTIES AND EXCHANGE COUPLINGS IN SINGLE-MOLECULE MAGNETS [Dy₂Ni] AND [Dy₂Cu]**

	Graphical Abstract	
3.1	Introduction.....	23
3.2	Results.....	24
3.3	Discussion.....	27
3.4	Conclusion.....	32
3.5	Experimental Section.....	32
	3.5.1 Preparation	
	3.5.2 Physical Measurements	
	References.....	34

CHAPTER 436**A 4F–3D HETEROMETALLIC CHAIN [Dy₂Cu₂]_n COMPOUND SHOWING SINGLE-MOLECULE MAGNET BEHAVIOR**

	Graphical Abstract	
4.1	Introduction.....	37
4.2	Results.....	38
	4.2.1 Crystal Structure	
	4.2.2 Magnetic Properties	
	4.2.3 HF-EPR Spectra	
4.3	Discussion.....	46
	4.3.1 Magnetic Anisotropy	
	4.3.2 Ferrimagnetic Ground State and Exchange Coupling	
	4.3.3 Effective Ising Model	
	4.3.4 Evaluation of Exchange Parameters	
	4.3.5 Estimation of Inter-macrocycle Interaction	
	4.3.6 Fine Structure in the Magnetization	
4.4	Conclusion.....	54
4.5	Experimental Section.....	55
	4.5.1 Preparation	
	4.5.2 X-ray Crystallographic Study	
	4.5.3 Physical Measurements	
	References.....	57

CHAPTER 5 60**EXCHANGE COUPLINGS OF 4F-3D HETEROMETALLIC CHAIN $[\text{Ln}_2\text{Cu}_2]_n$ COMPOUNDS EVALUATED BY HIGH-FREQUENCY ELECTRON PARAMAGNETIC RESONANCE**

Graphical Abstract

5.1	Introduction.....	60
5.2	Results.....	61
5.3	Discussion.....	67
5.4	Conclusion.....	70
5.5	Experimental Section.....	70
	5.5.1 Preparations	
	5.5.2 X-ray Crystallographic Studies	
	5.5.3 Physical Measurements	
	References.....	72

CHAPTER 6 73***TERT*-BUTYL 2-PYRIDYL NITROXIDE AVAILABLE AS PARAMAGNETIC CHELATE LIGANDS FOR STRONGLY EXCHANGE-COUPLED METAL-RADICAL COMPOUNDS**

Graphical Abstract

6.1	Introduction.....	73
6.2	Results and Discussion.....	74
6.3	Conclusion.....	80
6.4	Experimental Section.....	80
	6.4.1 Preparations	
	6.4.2 X-ray Crystallographic Studies	
	6.4.3 Physical Measurements	
	6.4.4 Molecular Orbital Calculations	
	References.....	83

CHAPTER 7 85**MAGNETO-STRUCTURE RELATIONSHIP IN COPPER(II) AND NICKEL(II) COMPLEXES CHELATED WITH STABLE *TERT*-BUTYL 5-PHENYL-2-PYRIDYL NITROXIDE AND RELATED RADICALS**

Graphical Abstract

7.1	Introduction.....	86
-----	-------------------	----

7.2	Results.....	87
	7.2.1 Characterization of phpyNO	
	7.2.2 Crystal Structure Analysis of the Copper(II) and Nickel(II) Complexes	
	7.2.3 Intermolecular Magnetic Coupling	
7.3	Discussion.....	95
	7.3.1 Magneto-Structure Relationship	
7.4	Conclusion.....	102
7.5	Experimental Section.....	102
	7.5.1 Preparation	
	7.5.2 X-ray Crystallographic Studies	
	7.5.3 Physical Measurements	
	7.5.4 Molecular Orbital Calculation	
	References.....	106

CHAPTER 8 108

STRONG INTRAMOLECULAR FERROMAGNETIC COUPLING IN NICKEL(II) AND COPPER(II) COMPLEXES CHELATED WITH *TERT*-BUTYL 5-METHOXY-2-PYRIDYL NITROXIDE

Graphical Abstract

8.1	Introduction.....	108
8.2	Results.....	109
	8.2.1 Characterization of meopyNO	
	8.2.2 Crystal Structure Analysis of the Nickel(II) and Copper(II) Complexes	
	8.2.3 Intramolecular Magnetic Coupling in the Nickel(II) and Copper(II) Complexes	
8.3	Discussion.....	113
8.4	Conclusion.....	114
8.5	Experimental Section.....	114
	8.5.1 Preparations	
	8.5.2 X-ray Crystallographic Studies	
	8.5.3 Magnetic Measurements	
	References.....	116

CHAPTER 9 117

FERROMAGNETIC AND ANTIFERROMAGNETIC EXCHANGE COUPLINGS IN SPIRO-FUSED DINUCLEAR NICKEL(II) AND MANGANESE(II) COMPLEXES WITH AN APPROXIMATE D_{2D} SYMMETRY

Graphical Abstract

9.1	Introduction.....	117
9.2	Results.....	118
	9.2.1 Syntheses	
	9.2.2 Crystal Structures	
	9.2.3 Magnetic Properties	
9.3	Discussion.....	122
	9.3.1 Intramolecular Ferromagnetic Interaction in 1	
	9.3.2 Intramolecular Antiferromagnetic Interaction in 2	
	9.3.3 DFT calculation for 1	
9.4	Conclusion	124
9.5	Experimental Section.....	126
	9.5.1 Preparations	
	9.5.2 X-ray Crystallographic Studies	
	9.5.3 Magnetic Susceptibility and Magnetization Measurements	
	9.5.4 Molecular Orbital Calculations	
	References	128
	CHAPTER 10	130
	CONCLUDING REMARKS	
	List of Publications Related to The Thesis.....	133

Abbreviations

(General)

HF-EPR	high-frequency electron paramagnetic resonance
SQUID	superconducting quantum interference device
SMM	single-molecule magnet
SCM	single-chain magnet
QTM	quantum tunneling of the magnetization
dc	direct current
ac	alternate current
SAPR	square antiprism
ZFS	zero-field splitting
DFT	density functional theory
SOMO	singly-occupied molecular orbital
NHOMO	next-highest-occupied molecular orbital

(Compounds)

NO	<i>tert</i> -butyl nitroxide
NN	nitronyl nitroxide (= 4,4,5,5-tetramethyl-4,5-dihydro-1 <i>H</i> -imidazolyl-1-oxyl 3-oxide)
Hhfac	1,1,1,5,5,5-hexafluoropentane-2,4-dione
Hdpk	di-2-pyridyl ketoxime
H ₂ dmg	dimethylglyoxime
H ₂ emg	ethylmethylglyoxime
2pyNO	<i>tert</i> -butyl 2-pyridyl nitroxide
phpyNO	<i>tert</i> -butyl 5-phenyl-2-pyridyl nitroxide
meopyNO	<i>tert</i> -butyl 5-methoxy-2-pyridyl nitroxide

Chapter 1

General Introduction

1.1 History of Molecular Magnetic Materials¹

Molecular magnetic materials have been added to the library of magnetism only at the end of the twentieth century through the concerted action of chemists and physicists. Much research has been prompted in the field of the molecule-based materials, because the materials containing organic components can take advantage of low cost and the possibility of tuning the properties using chemical techniques. Kinoshita and co-workers² reported the first evidence of a genuine organic ferromagnet, based on the paramagnetic NN group. NPNN shown in Figure 1.1a is ferromagnetically ordered only below 0.6 K,² nevertheless it was important because it showed that it is indeed possible to have a permanent magnet in which the magnetic orbitals are s and p in nature.

Before NPNN, some other examples of the molecular ferro- and ferrimagnets had been reported, based on molecular lattices comprising various transition metal ions and also transition metal ion–organic radicals pairs.^{3–5} In this way, a high-temperature ferrimagnet was obtained, using vanadium ions attached to the radical anions of tetracyanoethylene, TCNE^{•-} sketched in Figure 1.1b.⁶ The structure is not known because V(TCNE)₂ is highly insoluble and no single crystals suitable for crystallographic analysis were obtained. However, the material orders above room temperature. The ferromagnetic order arises from the antiferromagnetic coupling between the $S = 3/2$ of vanadium(II) and the $S = 1/2$ of the TCNE^{•-}. Another room-temperature ferrimagnet is a Prussian blue type compound comprising chromium(III), vanadium(II), and vanadium(III) ions, of formula [V^{II}_{0.42}V^{III}_{0.58}(Cr^{III}(CN)₆)_{0.86}] \cdot 2H₂O.⁷

Beyond providing some new magnetically ordered systems, molecular magnetism provided several new types of low-dimensional magnetic materials, which attracted the interest of a growing number of physicists, looking for new types of magnetic materials. Magnetochemistry is essentially the use of the magnetic techniques for obtaining structural information on simple paramagnetic systems, and it is a branch of chemistry which uses physical measurements.

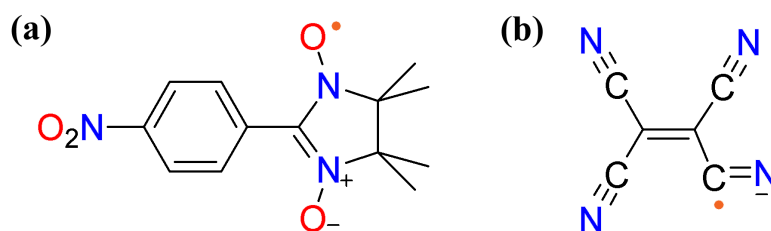


Figure 1.1. Sketches of the molecular structures of (a) the *p*-nitrophenyl nitronyl nitroxide, NPNN and (b) the TCNE^{•-} anion radical. All the CN groups in the TCNE^{•-} are equivalent.

As mentioned above, molecular magnetic compounds have been recently developed to a large extent,⁸⁻¹¹ and suitable strategies have been worked out to obtain new materials with expected properties, like molecular ferro- and ferrimagnets, organic magnets, SMM, high-spin molecules, etc. An advantage of molecular compounds, compared to those based on continuous lattices, is that it is relatively easy to obtain systems containing isolated pairs of magnetic centers, with different relative orientations of the so-called magnetic orbitals, in such a way that the structural features responsible for the magnetic coupling clearly emerge. Binuclear and oligonuclear spin clusters are important for the study of magneto-structural correlations.

1.2 Advantages of Molecular Magnetic Materials

One of the important characteristics of molecule-based magnetic materials is that it is composed of molecules or molecular building blocks. In other words, various functions could be added to the magnetic materials by designing the characteristics of composing molecules or molecular building blocks. Molecular magnetic materials have many advantages over metal and inorganic materials.

There are a number of different strategies to assemble spins in molecule-based magnetic materials, including inorganic, organic, and hybrid spin systems, in which both metal ions and radical groups are paramagnetic. From the viewpoint of synthetic chemistry, rational synthetic methodology is highly demanded in preparation of spin-clusters with high nuclearity. The $[\text{Mn}_{12}]$ cluster is one of the most intensively studied SMMs, but it has been prepared by a typical serendipitous way for this decade.¹² Synthetic procedure should be designed to arrange desired number of magnetic centers to desired positions and sequences in the development of further functional SMMs. At the same time, mutual geometry among the magnetic orbitals should also be arranged on-demand, so that magnetic exchange couplings would be ferromagnetic or antiferromagnetic under control.

The design and synthesis of simple molecules containing paramagnetic metal centers that are able to self-assemble through metal–ligand interactions rendering supramolecular assemblies of increasing structural and magnetic complexity is a major challenge in modern molecular coordination chemistry and molecular magnetism. These include discrete zero-dimensional coordination clusters as well as infinite one-, two-, or three-dimensional coordination polymers.

1.3 Scope of This Thesis

This article will mainly describe relationship between the molecular structure and the exchange interaction of several zero- and one-dimensional spin-systems, which characterizes nature of molecular magnetic materials.

Determination of magnetic exchange coupling is one of the most important issues in the study of magnetic clusters. Large three-dimensional exchange interaction among spins will lead to a molecule-based magnet with a higher critical temperature. Large spin multiplicity is a requirement

for SMM behavior, in which ferromagnetic or ferrimagnetic ground states would be characterized. Magnetic anisotropy and ZFS are also essential in characterizing magnetic materials and in applying them to technology. The structural and physicochemical diversity in these classes of compounds requires a great deal of fundamental effort to better understand new generations of molecule-based magnets.

The contents will be divided into the three following subjects.

- (i) Study on exchange couplings between lanthanide ion (4f spin) and transition-metal ion (3d spin)
- (ii) Study on exchange couplings between transition-metal ion and organic radical (2p spin)
- (iii) Study on exchange couplings between homo transition-metal ions

This article consists of ten chapters. In Chapter 2, the background theories about molecule-based magnetism will be introduced in order to comprehend the following studies.

The purpose of the studies in the subject (i) is as follows: SMMs have a hysteresis with the steps due to the slow relaxation of the magnetization at low temperatures on the single molecular level, and show interesting physical properties such as quantum tunneling of the magnetization. One of the novel approaches for the developments of SMMs is to assemble 4f- and 3d-spins in magnetic materials. The exchange couplings between lanthanoid and transition-metal ions have been roughly determined by means of pulsed-field magnetization measurements. We applied a HF-EPR technique for the 4f–3d heterometallic SMMs, which has never been applied for such purpose before our work.

In Chapter 3, $[\text{Dy}_2\text{Ni}]$ and $[\text{Dy}_2\text{Cu}]$ SMMs will be presented. This is the first report of determination of exchange coupling between 4f- and 3d-spins on a SMM by means of HF-EPR and pulsed-field magnetization.

In Chapter 4, 4f–3d heterometallic one-dimensional compounds $[\text{Dy}_2\text{Cu}_2]_n$ will be reported. The exchange coupling constants in $[\text{Dy}_2\text{Cu}_2]_n$ cannot be determined solely by magnetization steps in pulsed-field magnetization measurements because there are two types of exchange paths in the quasi-diamond-arrayed motif. To breakthrough this difficulty, we applied a HF-EPR technique for this compound.

In Chapter 5, a few isomorphous $[\text{Ln}_2\text{Cu}_2]_n$ ($\text{Ln} = \text{Tb}, \text{Ho}, \text{and Er}$) complexes will be described. The exchange couplings in the compounds were precisely evaluated by HF-EPR and pulsed-field magnetization studies. This study revealed that the J_{4f-3d} value monotonically decreased in the order of the atomic number (from ${}_{64}\text{Gd}$ to ${}_{68}\text{Er}$).

The purpose of the subject (ii) is to establish strongly ferromagnetic couplings in the metal–radical approach.¹³ Room-temperature magnets would require magnetic couplings as large as ≥ 300 K. We can expect only small exchange couplings when 4f-spins are utilized because 4f-spins are shielded and buried by the electrons of outer shells. In this context, 3d- and 2p-spins are promising for development of strongly correlated magnetic materials. Actually transition-metal coordination compounds bound directly with organic free radicals show very large magnetic couplings; sometimes

ferromagnetic and mostly antiferromagnetic. The study on magneto-structure relationship for copper(II) and nickel(II) complexes with *tert*-butyl 2-pyridyl nitroxide radical and its derivatives will be reported in Chapters 6–8. Three novel radicals with chelating ability are synthesized. Furthermore, the molecular structures and magnetic properties of coordinated compounds with these paramagnetic ligands are described there. It will be demonstrated that a strong π -d interaction has a simple relationship with the planarity of the chelate ring involving a metal ion.

In Chapter 6, *tert*-butyl 2-pyridyl nitroxide, which is known to be unisolable under ambient conditions, will be described.

In Chapter 7, synthesis, crystal structures, and magnetic properties of the novel stable nitroxide and its coordination compounds will be discussed. This study revealed that magneto-structure relationship on the π -d spin system was regulated by a unique geometrical parameter.

In Chapter 8, two complexes containing copper(II) or nickel(II) ion with another novel stable nitroxide will be shown.

The purpose of the subject (iii) is construction of homometallic spin systems showing ferromagnetic couplings. It is well known that $d\sigma$ (e_g) orbitals are orthogonal to $d\pi$ (t_{2g}) orbitals, and several 3d–3d heterometallic systems show ferromagnetic couplings; $\text{Cu}^{\text{II}}-\text{V}^{\text{IV}}=\text{O}$ systems have been exploited by Kahn.^{14,15} However, heterometallic approaches have a disadvantage in preparation because of possible metal-scrambling and low positional selectivity. Therefore, ferromagnetic homometallic systems are desired for facile preparation procedures.

In Chapter 9, magnetic interactions between 3d–3d spins will be discussed. Homometallic dinuclear complexes containing a spiro-bridge, which are rare, were synthesized, and magnetic interactions between the two nickel(II) or manganese(II) ions were investigated.

Finally, the results and discussion will be overviewed in Chapter 10.

References

- (1) Gatteschi, D.; Sessoli, R.; Villain, J. *Molecular Nanomagnets*; Oxford University Press: New York, USA, 2006.
- (2) Tamura, M.; Nakazawa, Y.; Shiomi, D.; Nozawa, Y.; Hosokoshi, M.; Ishikawa, M. Takahashi, M.; Kinoshita, M. *Chem. Phys. Lett.* **1991**, *186*, 401.
- (3) Miller, J. S.; Calabrese, J. C.; Rommelmann, H.; Chittapeddi, S. R.; Zhang, J. H.; Reiff, W. M.; Epstein, A. J. *J. Am. Chem. Soc.* **1987**, *109*, 769.
- (4) Kahn, O.; Pei, Y.; Verdaguer, M.; Renard, J.-P.; Sletten, J. *J. Am. Chem. Soc.* **1988**, *110*, 782.
- (5) Caneschi, A.; Gatteschi, D.; Renard, J. P.; Rey, P.; Sessoli, R. *Inorg. Chem.* **1989**, *28*, 1976.
- (6) Manriquez, J. M.; Yee, G. T.; McLean, R. S.; Epstein, A. J.; Miller, J. S. *Science* **1991**, *252*, 273.
- (7) Ferlay, S.; Mallah, T.; Ouahs, R.; Veillet, P.; Verdaguer, M. *Nature* **1995**, *378*, 701.
- (8) Miller, J. S.; Drillon, M. *Magnetism: Molecules to Materials I*; Wiley-VCH: Weinheim, Germany, 2001.
- (9) Miller, J. S.; Drillon, M. *Magnetism: Molecules to Materials II*; Wiley-VCH: Weinheim, Germany, 2001.
- (10) Miller, J. S.; Drillon, M. *Magnetism: Molecules to Materials III*; Wiley-VCH: Weinheim, Germany, 2002.
- (11) Christou, G.; Gatteschi, D.; Hendrickson, D. N.; Sessoli, R. *MRS Bull.* **2000**, *25*, 66.
- (12) Sessoli, R.; Gatteschi, D.; Caneschi, A.; Novak, M.A. *Nature* **1993**, *365*, 141.
- (13) Chaneschi, A.; Gatteschi, D.; Sessoli, R. *Acc Chem. Res.* **1989**, *22*, 392.
- (14) Kahn, O. Galy, J.; Journaux, Y.; Jaud, J.; Morgenstern-Badarau, I. *J. Am. Chem. Soc.* **1982**, *104*, 2165.
- (15) Kahn, O. *Structure and Bonding* **1987**, *68*, 89.

Chapter 2

Theoretical Section

2.1 Definitions and Units¹

To begin with, we consider a sample containing 1 mol of a molecular compound within a homogenous magnetic field H . The sample acquires a molar magnetization M related to H through

$$\frac{\partial M}{\partial H} = \chi_{\text{mol}} \quad (2.1)$$

where χ_{mol} is the molar magnetic susceptibility. It is always possible to choose the reference axes in order for χ_{mol} to be diagonal with the χ_u ($u = x, y, z$) principal values. If the sample is magnetically isotropic, then χ_{mol} becomes a scalar.

When the magnetic field is weak enough, χ_{mol} is independent of H , such that one can write

$$M = \chi_{\text{mol}} H. \quad (2.2)$$

Most of the researchers involved in the field of molecular magnetism prefer to use the cgsemu system rather than the SI. The unit of magnetic field is the Oersted. In the vacuum B is related to H through $B = \mu_0 H$, and the permeability μ_0 in the cgsemu system is equal to 1. The molar magnetic susceptibility is expressed in $\text{cm}^3 \text{mol}^{-1}$. The product of the molar magnetic susceptibility by the temperature, $\chi_{\text{mol}} T$, is expressed in $\text{cm}^3 \text{K mol}^{-1}$. As for the molar magnetization M , it is expressed in $\text{cm}^3 \text{G mol}^{-1}$. Alternatively, M may be expressed in $N_A \mu_B$ units, N_A being Avogadro's number and μ_B the electronic Bohr magneton. The correspondence between the two units is

$$1 N_A \mu_B = 5585 \text{ cm}^3 \text{G mol}^{-1}. \quad (2.3)$$

2.2 Diamagnetic and Paramagnetic Susceptibilities¹

In principle χ_{obs} is the algebraic sum of two contributions associated with different phenomena:

$$\chi_{\text{obs}} = \chi^{\text{D}} + \chi^{\text{P}} \quad (2.4)$$

where χ^{D} and χ^{P} represent the diamagnetic and paramagnetic susceptibility, respectively. The former is negative and the latter positive. When χ^{D} dominates, the sample is said to be diamagnetic; it is repelled from the magnetic field. When χ^{P} is the leading contribution, the sample is said to be paramagnetic; it is attracted by the applied field. Diamagnetism is an underlying property of matter.

The diamagnetism is due to the interaction of the magnetic field with the motion of the electrons in their orbits. It is sufficient to specify that χ^D is independent of the temperature and the strength of the applied field. Since we are interested in χ^P , the observed susceptibility χ_{obs} must be corrected for the diamagnetic contribution. χ^D can be estimated from Pascal's law. Some of these data are gathered in Table 2.1.

Table 2.1. Diamagnetic Susceptibilities and Constitutive Corrections (in $10^{-6} \text{ cm}^3 \text{ mol}^{-1}$)^{1,2}

atoms		transition metal cations		cations and anions	
H	-2.9	V ⁴⁺	-7	Li ⁺	-1.0
B	-7.2	Cr ²⁺	-15	Na ⁺	-6.8
C	-6.0	Mn ²⁺	-14	K ⁺	-14.9
N (ring)	-4.6	Mn ³⁺	-13	Mg ²⁺	-5.0
N (open chain)	-5.6	Mn ⁴⁺	-8	Ca ²⁺	-10.4
N (imide)	-2.1	Fe ²⁺	-13	O ²⁻	-12.0
O (ether or alcohol)	-4.6	Fe ³⁺	-10	F ⁻	-9.1
O (carbonyl)	-1.7	Co ²⁺	-12	Cl ⁻	-23.4
P	-26.3	Ni ²⁺	-10	Br ⁻	-34.6
F	-6.3	Cu ⁺	-12	I ⁻	-50.6
Cl	-20.1	Cu ²⁺	-11	CN ⁻	-13.0
Br	-30.6	Zn ²⁺	-15.0	NO ₃ ⁻	-10.0
I	-44.6	Cd ²⁺	-20	NCS ⁻	-31.0
S	-15.0	Rare earth ³⁺	-20	ClO ₄ ⁻	-32.0
constitutive corrections					
C=C	5.5	C≡C	0.8	C (aromatic ring)	-0.25
C=N	8.1	N=N	1.8	N=O	1.7

2.3 van Vleck Formula¹

In 1932 van Vleck proposed a simplification based on a few approximations for the macroscopic molar paramagnetic susceptibility.³ The first of them is that it is legitimate to expand the energies E_n according to the increasing powers of H :

$$E_n = E_n^{(0)} + E_n^{(1)}H + E_n^{(2)}H^2 + \dots \quad (2.5)$$

where $E_n^{(0)}$ is the energy of level n in zero field. $E_n^{(1)}$ and $E_n^{(2)}$ are called first- and second-order Zeeman coefficients, respectively. We can define a microscopic magnetization as $\mu_n = -\partial E_n / \partial H$. From eq 2.5, μ_n becomes

$$\mu_n = -E_n^{(1)} - 2E_n^{(2)}H + \dots \quad (2.6)$$

The second approximation is that $H/k_B T$ is small with respect to unity. In other words, it is assumed that H is not too large and T not too small. From these approximations, we obtain

$$M = \frac{N_A \sum_n \mu_n \exp(-E_n/k_B T)}{\sum_n \exp(-E_n/k_B T)} = \frac{N_A \sum_n (-E_n^{(1)} - 2E_n^{(2)}H) (1 - E_n^{(1)}H/k_B T) \exp(-E_n^{(0)}/k_B T)}{\sum_n (1 - E_n^{(1)}H/k_B T) \exp(-E_n^{(0)}/k_B T)} \quad (2.7)$$

In zero field, the magnetization vanishes, such that $\sum_n E_n^{(1)} \exp(-E_n^{(0)}/k_B T) = 0$. Substituting this equation into eq 2.7 and retaining only term linear in H results in

$$M = \frac{N_A H \sum_n (E_n^{(1)2}/k_B T - 2E_n^{(2)}) \exp(-E_n^{(0)}/k_B T)}{\sum_n \exp(-E_n^{(0)}/k_B T)} \quad (2.8)$$

and finally

$$\chi_{\text{mol}} = \frac{N_A \sum_n (E_n^{(1)2}/k_B T - 2E_n^{(2)}) \exp(-E_n^{(0)}/k_B T)}{\sum_n \exp(-E_n^{(0)}/k_B T)} \quad (2.9)$$

which is the van Vleck formula. The van Vleck equation gives the magnetic susceptibility only in the magnetic field range where the M versus H plot is linear. When all energies E_n are linear in H , the second-order Zeeman coefficients $E_n^{(2)}$ vanish and eq 2.9 becomes

$$\chi_{\text{mol}} = \frac{N_A \sum_n E_n^{(1)2} \exp(-E_n^{(0)}/k_B T)}{k_B T \sum_n \exp(-E_n^{(0)}/k_B T)} \quad (2.10)$$

2.4 Temperature-Independent Paramagnetism¹

eq 2.9 can be rewritten as

$$\chi_{\text{mol}} = \frac{N_A \sum_n E_n^{(1)2} \exp(-E_n^{(0)}/k_B T)}{k_B T \sum_n \exp(-E_n^{(0)}/k_B T)} - \frac{2N_A \sum_n E_n^{(2)} \exp(-E_n^{(0)}/k_B T)}{\sum_n \exp(-E_n^{(0)}/k_B T)} \quad (2.11)$$

Let energy $E_0^{(0)}$ of the ground state be the energy origin. If $E_n^{(0)} \gg k_B T$ ($n = 1, 2, \dots$), the second term of eq 2.11 becomes

$$-2N_A E_0^{(2)} = -2N_A \sum_{m \neq 0} \frac{\langle 0 | H_{ZE} | m \rangle^2}{E_0^{(0)} - E_m^{(0)}}. \quad (2.12)$$

H_{ZE} is the Zeeman operator. The diamagnetic ground state may couple with excited states through the Zeeman perturbation provided that the energy gaps are not too large. eq 2.12 is positive since all denominators are negative, and temperature independent. This contribution is often called temperature-independent paramagnetism (TIP). The TIP is sometimes observed in a compound in which transition metal ions exhibiting a large spin-orbit interaction are included. For example it is estimated to be about $60 \times 10^{-6} \text{ cm}^3 \text{ mol}^{-1}$ for copper(II) mononuclear species, $100 \times 10^{-6} \text{ cm}^3 \text{ mol}^{-1}$ for nickel(II) mononuclear species. Since spin-orbit coupling is not sufficiently large in the light elements to induce mixing, TIP is rarely observed in purely organic materials.

2.5 The Curie Law¹

The simplest situation in molecular magnetism is that of molecules in which the $^{2S+1}\Gamma$ ground state has a large separation in energy from the first excited states and the orbital angular momentum is quenched. In the absence of external magnetic field the $2S+1$ spin degeneracy is then retained. When the field is applied, the energies of each sublevel with the magnetic spin quantum number m_s are given by

$$E_n = m_s g \mu_B H \quad (2.13)$$

with varying by an integer value or a half integer from $-S$ to $+S$. The molar magnetization M is deduced by employing eq 2.10 as

$$M = N_A g \mu_B S B_s(x) \quad (2.14)$$

where $x = g \mu_B S H / k_B T$. $B_s(x)$ is the Brillouin function defined by

$$B_s(x) = \frac{2S+1}{2S} \coth \frac{2S+1}{2S} x - \frac{1}{2S} \coth \frac{1}{2S} x. \quad (2.15)$$

A plot of $B_s(x)$ for several values of S is illustrated in Figure 2.1. When x becomes very large, that is, at high field and low temperature, $B_s(x)$ tends to unity and M tends to the saturation magnetization M_s :

$$M_s = N_A g \mu_B S = 5585 \times g S \text{ cm}^3 \text{ G mol}^{-1}. \quad (2.16)$$

For $x \ll 1$, χ_{mol} ($= \partial M / \partial H$) can be written as

$$\chi_{\text{mol}} = \frac{N_{\text{A}} g^2 \mu_{\text{B}}^2 S(S+1)}{k_{\text{B}} T}. \quad (2.17)$$

The molar magnetic susceptibility varies as

$$\chi_{\text{mol}} = \frac{C}{T} \left(C = \frac{N_{\text{A}} g^2 \mu_{\text{B}}^2 S(S+1)}{3k_{\text{B}}} \right). \quad (2.18)$$

The constant C depends on the spin multiplicity $2S+1$ of the ground state. This relation is called the Curie's law where C is the Curie constant.

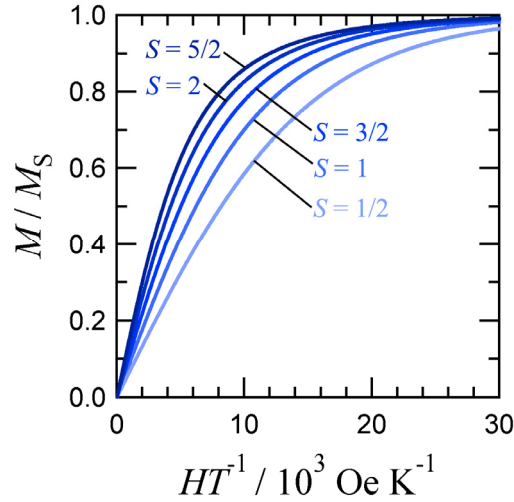


Figure 2.1. The Brillouin function shown as M/M_s vs. H/T plot.

2.6 Spin Hamiltonian⁴

In general, a vector coupling scheme may be used to model the quantitative behavior of system with exchange-coupled spins with the Heisenberg–Dirac–van Vleck (HDvV) spin Hamiltonian^{5,6}

$$\mathcal{H} = -2 \sum_{i,j} J_{ij} \hat{S}_i \cdot \hat{S}_j \quad (2.19)$$

where the subscripts i and j correspond to the two different spins between nearest-neighbor sites and J_{ij} is the exchange coupling constant. When J is positive, the exchange interaction is ferromagnetic, and negative J designates antiferromagnetic exchange interactions.

The exchange coupling parameter is defined usually as $\mathcal{H} = -2J\hat{S}_i\hat{S}_j$, but sometimes as $\mathcal{H} = -J\hat{S}_i\hat{S}_j$ or $\mathcal{H} = +J\hat{S}_i\hat{S}_j$. Readers should pay attention to the definition.

2.7 Intermolecular Interaction; Molecular Field^{1,2}

Most magnetic measurements are carried out in the solid state and the molecular magnetic species are rarely perfectly isolated from a magnetic viewpoint. In the molecular field approximation where a perturbation is added to the Zeeman term, the perturbation takes the form $-zJ\langle S_z \rangle \hat{S}_z$ where $\langle S_z \rangle$ is the mean value of the \hat{S}_z component of the spin operator. J is the exchange coupling constant between two nearest-neighbor spin centers and z is the number of nearest neighbors around the given magnetic molecule in a crystal lattice. According to whether J is positive or negative, the intermolecular interaction is said to be ferromagnetic or antiferromagnetic, respectively. The total spin Hamiltonian is

$$\mathcal{H} = g\mu_B \hat{S}_z \cdot H - zJ\langle S_z \rangle \hat{S}_z \quad (2.20)$$

where the magnetic field is assumed to be along the z direction and the g tensor to be isotropic. $\langle S_z \rangle$ is given through the Boltzmann distribution law as

$$\langle S_z \rangle = -\frac{S(S+1)g\mu_B H}{3k_B T - zJS(S+1)}. \quad (2.21)$$

$\langle S_z \rangle$ is negative because the Zeeman components with negative m_s are more populated than those with positive m_s . The molar magnetization may be expressed as

$$M = -N_A g\mu_B \langle S_z \rangle. \quad (2.22)$$

The minus sign comes from the negative charge of the electron. The molar magnetic susceptibility defined as $\partial M/\partial H$ is

$$\chi_{\text{mol}} = \frac{N_A g^2 \mu_B^2 S(S+1)}{3k_B T - zJS(S+1)}. \quad (2.23)$$

χ_{mol} may be rewritten as:

$$\chi_{\text{mol}} = \frac{C}{T - \theta} \quad (2.24)$$

which is known as the Curie–Weiss law where θ is the Weiss temperature defined by

$$\theta = \frac{zJS(S+1)}{3k_B}. \quad (2.25)$$

If the magnetic data follow the Curie-Weiss law, $1/\chi_{\text{mol}}$ versus T plot shows a straight line. The intercept with the T -axis yields both the sign and the value of θ . In the framework of this model positive θ indicates ferromagnetic intermolecular interactions and negative θ indicates antiferromagnetic intermolecular interactions. If the magnetic data are represented in the form of a $\chi_{\text{mol}}T$ versus T plot, positive θ leads to an increase and negative θ to a decrease of $\chi_{\text{mol}}T$ on cooling, as shown in Figure 2.2. This effect is more pronounced when the temperature is lowered. It is important to point out that a deviation with respect to the Curie law may have other origins than intermolecular interactions. The ZFS has quite similar effects on the average magnetic susceptibility.

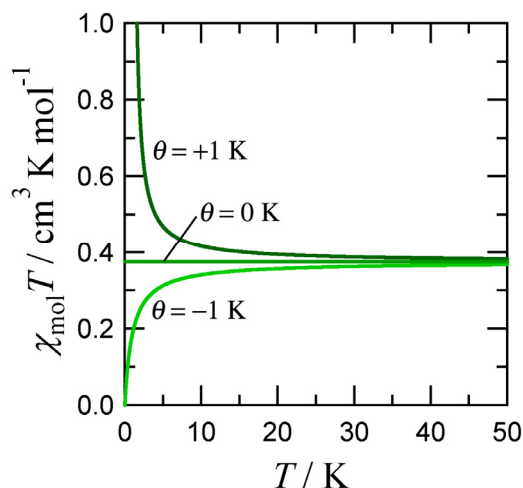


Figure 2.2. $\chi_{\text{mol}}T$ versus T plot for an assembly of molecules obeying the Curie–Weiss law with a Curie constant $C = 0.375 \text{ cm}^3 \text{ K mol}^{-1}$ and the Weiss temperature $\theta = +1 \text{ K}$, 0 K , and -1 K .

2.8 Singlet–Triplet Model as an Example for Clusterized Spin Systems¹

If the two metal ions interact through the bridge, then the local spins $S_A = S_B = 1/2$ are not good quantum numbers. The good spin quantum numbers are $S = 0$ and 1 . However, it is often formally described by a coupling between the local spin operators \hat{S}_A and \hat{S}_B . The HDvV spin Hamiltonian is written as

$$\mathcal{H} = -2J\hat{S}_A \cdot \hat{S}_B. \quad (2.26)$$

Since $\hat{S}_T = \hat{S}_A + \hat{S}_B$, hence $\hat{S}_T^2 = \hat{S}_A^2 + \hat{S}_B^2 + 2\hat{S}_A \cdot \hat{S}_B$. The spin Hamiltonian is rewritten as

$$\mathcal{H} = -J(\hat{S}_T^2 - \hat{S}_A^2 - \hat{S}_B^2) \quad (2.27)$$

the eigenvalues of which are

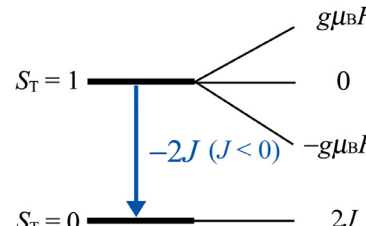
$$E(S_T, S_A, S_B) = -J[S_T(S_T + 1) - S_A(S_A + 1) - S_B(S_B + 1)] \quad (2.28)$$

which, after a change of origin, can be rewritten as

$$E(S_T) = -JS_T(S_T + 1). \quad (2.29)$$

If the energy of the triplet state is taken as the origin, the $E_n^{(0)}$ and $E_n^{(1)}$ coefficients intervening in eq 2.10 are

n	$E_n^{(0)}$	$E_n^{(1)}$
1	0	$-g\mu_B$
2	0	0
3	0	$+g\mu_B$
4	$2J$	0



and the molar magnetic susceptibility is given by

$$\chi_{\text{mol}} = \frac{2N_A g^2 \mu_B^2}{k_B T} \frac{1}{3 + \exp(-2J/k_B T)}. \quad (2.30)$$

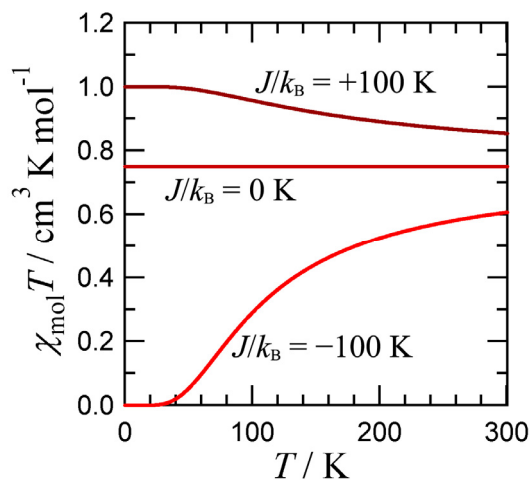


Figure 2.3. $\chi_{\text{mol}}T$ versus T curves for a singlet-triplet model (eq 2.30) with $g = 2.00$ and $J/k_B = +100, 0,$ and -100 K.

It is important to stress that the HDvV spin Hamiltonian is easy to handle. However, it is purely phenomenological, and does not provide any information on the real mechanism of the isotropic interaction. The $\chi_{\text{mol}}T$ versus T plots are shown in Figure 2.3, for $J/k_{\text{B}} = 0$ and ± 100 K. For $J/k_{\text{B}} = 0$, $\chi_{\text{mol}}T$ is constant and equal to $N_{\text{A}}g^2\mu_{\text{B}}^2/2k_{\text{B}}$ (= ca. $0.75 \text{ cm}^3 \text{ K mol}^{-1}$). For $J > 0$, $\chi_{\text{mol}}T$ is close to $N_{\text{A}}g^2\mu_{\text{B}}^2/2k_{\text{B}}$ when $k_{\text{B}}T \gg J$. On cooling, $\chi_{\text{mol}}T$ increases, due to the depopulation of the diamagnetic excited state in favor of the triplet ground state, and tends to a plateau with $\chi_{\text{mol}}T = 2N_{\text{A}}g^2\mu_{\text{B}}^2/3k_{\text{B}}$ (= ca. $1.0 \text{ cm}^3 \text{ K mol}^{-1}$) corresponding to the temperature range where the excited singlet state is fully depopulated.

2.9 Zero-Field Splitting^{1,2}

The ZFS within a $^{2S+1}\Gamma$ state without first-order angular momentum is expressed by the total spin Hamiltonian take into account the Zeeman perturbation as

$$\mathcal{H} = g\mu_{\text{B}}\hat{S}H + D\left[\hat{S}_z^2 - \frac{S(S+1)}{3}\right] + E(\hat{S}_x^2 - \hat{S}_y^2) \quad (2.31)$$

where D and E are the axial and rhombic ZFS parameters, respectively. If $D < 0$ and $D > 0$, the single-ion magnetic anisotropy is uniaxial (easy-axis type) and rhombic (easy-plane type) anisotropy, respectively. In case of $D < 0$ and small E , the uniaxial-type magnetic anisotropy is called as ‘‘Ising-type’’ anisotropy. This means that the spin forced to be either up or down. For $D > 0$ and $E = 0$, it is called as ‘‘XY-type’’ anisotropy.

In the sample with $S = 1$ (i.e. a nickel(II) ion in trigonally distorted octahedral surroundings), the energies are as follows when the field H_z is parallel to the unique axis:

$$E_0 = 0, \quad E_{1,2} = \pm g_{\parallel}\mu_{\text{B}}H_z + D. \quad (2.32)$$

When those energies are introduced in the van Vleck formula, the parallel magnetic susceptibility χ_{\parallel} is found as

$$\chi_{\parallel} = \frac{2N_{\text{A}}g_{\parallel}^2\mu_{\text{B}}^2}{k_{\text{B}}T} \frac{\exp(-D/k_{\text{B}}T)}{1 + 2\exp(-D/k_{\text{B}}T)}. \quad (2.33)$$

When the field H_x (or H_y) is perpendicular to the unique axis, the eigenvalues are

$$E_1 = D, \quad E_{2,3} = (\pm\sqrt{4g_{\perp}^2\mu_{\text{B}}^2H_x^2 + D^2} + D)/2. \quad (2.34)$$

We can note that the energies E_n ($n = 1, 2, 3$) have no term in H_x . The three $E_n^{(1)}$ coefficients are zero. The $E_n^{(0)}$ and $E_n^{(2)}$ coefficients may be introduced in the van Vleck formula, which leads to the perpendicular magnetic susceptibility χ_{\perp} :

$$\chi_{\perp} = \frac{2N_A g_{\perp}^2 \mu_B^2}{D} \frac{1 - \exp(-D/k_B T)}{1 + 2 \exp(-D/k_B T)}. \quad (2.35)$$

The χ_{\parallel} and χ_{\perp} versus T plots for $D = \pm 10 \text{ cm}^{-1}$ and $g_{\parallel} = g_{\perp} = 2$ are shown in Figure 2.4.

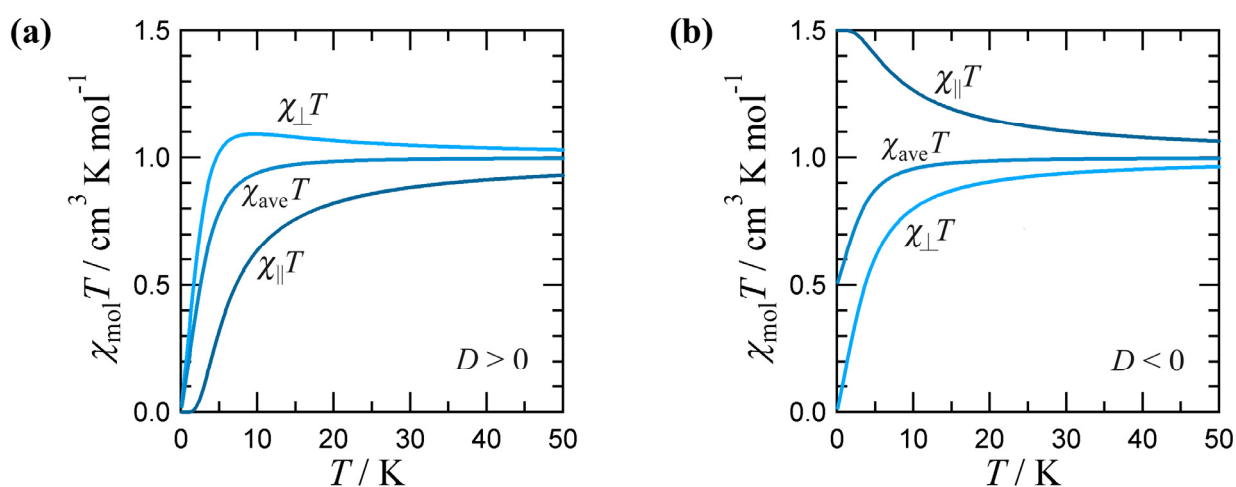


Figure 2.4. $\chi_{\text{mol}}T$ versus T plots for a spin triplet molecule with an axial anisotropy; (a) the axial ZFS D is positive; (b) $D < 0$. Both g_{\parallel} and g_{\perp} are taken equal to 2.00.

2.10 Ac Susceptibility^{7,8}

Slow relaxation of magnetization is one of the exciting features of the magnetic behavior of a molecular cluster. This was first discovered in $[\text{Mn}_{12}]$ by performing ac susceptibility measurements.⁹ The inductive response of a specimen might be measured in the presence of an oscillating magnetic field, and in this case it depends on the frequency ω of the field. It can, in general, be expressed as the sum of an in-phase component, χ' , and an out-of-phase component, χ'' , of the susceptibility. If the change of the external field is slow compared with the relaxation time of the magnetization, (i.e. $\omega \ll \tau^{-1}$) τ , then the magnetization is always in equilibrium over the time-scale of the experiment. The measured susceptibility is the same as the static susceptibility and is called the isothermal susceptibility, χ_T . If the frequency is much faster than the reorientation of the magnetization (i.e. $\omega \gg \tau^{-1}$), then the magnetic system is effectively isolated from the surroundings

and an adiabatic susceptibility, χ_s , is measured, which is smaller than χ_T . The dynamic susceptibility can be expressed as:

$$\chi(\omega) = \chi_s + \frac{\chi_T - \chi_s}{1 + (i\omega\tau)^{1-\alpha}} \quad (2.36)$$

and

$$\chi'(\omega) = \chi_s + (\chi_T - \chi_s) \frac{1 + (\omega\tau)^{1-\alpha} \sin(\pi\alpha/2)}{1 + 2(\omega\tau)^{1-\alpha} \sin(\pi\alpha/2) + (\omega\tau)^{2(1-\alpha)}} \quad (2.37)$$

$$\chi''(\omega) = (\chi_T - \chi_s) \frac{(\omega\tau)^{1-\alpha} \cos(\pi\alpha/2)}{1 + 2(\omega\tau)^{1-\alpha} \sin(\pi\alpha/2) + (\omega\tau)^{2(1-\alpha)}}.$$

As the distribution in relaxation times is wide, α is larger. When $\alpha = 0$ eq 2.36 represents Debye-type relaxation,¹⁰ which is the response of an ideal with one relaxation time. The real part of susceptibility is in dispersion, and the imaginary is in absorption, as shown in Figure 2.5. When $\chi''(\omega)$ is plotted against $\chi'(\omega)$, the so-called Argand or Cole–Cole plot,^{11,12} a semicircle is obtained. We can easily derived α by the experimental ac data in the Cole–Cole plot because the semicircle becomes an arc of circle with its center translated in the fourth quadrant. The angle that subtends the arc is given by $\pi(1 - \alpha)$, as shown in Figure 2.6. The two parameters χ_s and χ_T can be extracted as the two intercepts of the semicircle with the χ' axis, being obviously constrained such that $\chi_T > \chi_s$, by fitting the experimental curve with the following expression:

$$\chi''(\omega) = \frac{1}{2}(\chi_s - \chi_T) \tan(\pi\alpha/2) + \frac{1}{2} \sqrt{[(\chi_T - \chi_s) \tan(\pi\alpha/2)]^2 - 4[A]} \quad (2.38)$$

where

$$A = \chi'^2 - \chi'(\chi_T + \chi_s) + \frac{1}{4}(\chi_T + \chi_s)^2 - \frac{(\chi_T - \chi_s)^2}{4[\sin(\pi(\alpha - 1)/2)]^2} + \frac{1}{4}(\chi_T + \chi_s)^2 [\tan(\pi\alpha/2)]^2.$$

A non-zero χ'' is observed in some cases, for instance at the magnetic phase transition when the magnetic order produces an internal field. As the dynamics follow a critical behavior at T_c , no significant frequency dependence of $\chi(T)$ around T_c is observed. In some cases, as in spin-glasses, frequency dependence is more evident and it can become tricky to distinguish between the SMM behavior and the freezing of a spin-glass. Analysing the frequency-dependent shift of the temperature of the maxima of $\chi(\omega, T)$ has been suggested, i.e. the freezing temperature T_f , by evaluating:

$$F = \frac{\Delta T_f(\omega) / T_f(\omega)}{\Delta \ln(\omega)} \quad (2.39)$$

where $\Delta T_f(\omega)$ is the difference between the highest and lowest blocking temperatures corresponding to the extremes of the investigated frequency range that appears, on a logarithmic scale, in the denominator.

While for spin-glasses F ranges from 0.001 to 0.08, in the case of paramagnetic relaxation F has the value of 0.28. This can only be observed when no distribution of τ is observed. For instance, $[\text{Fe}_8]$, probably the SMM that best approaches the ideal behavior, has $F = 0.24$.¹³

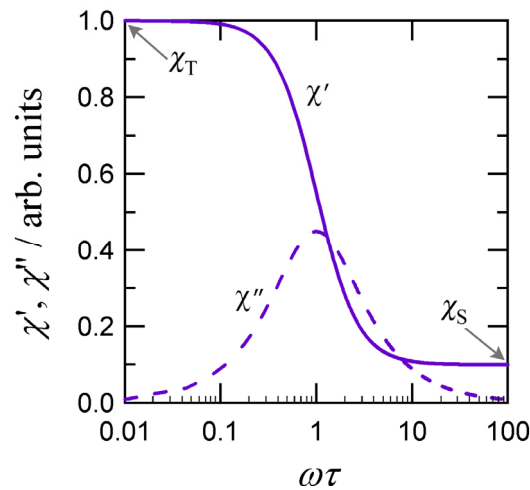


Figure 2.5. Theoretical frequency dependence of the real and imaginary components of the magnetic susceptibility in a semi-log scale. χ_T and χ_S are the isothermal and adiabatic limits of the susceptibility, respectively.

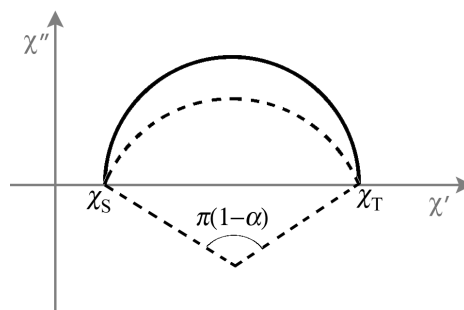


Figure 2.6. Cole-Cole plot where at a given temperature χ'' is plotted versus χ' , for each frequency. Solid line: no distribution in relaxation time; broken line: a distribution in τ according to eq 2.36.

2.11 Single-Molecule Magnets

In 1980 Lis¹⁴ reported the structure of a dodecanuclear manganese cluster of formula $[\text{Mn}_{12}\text{O}_{12}(\text{CH}_3\text{COO})_{16}(\text{H}_2\text{O})_4] \cdot 4\text{H}_2\text{O} \cdot 2\text{CH}_3\text{COOH}$, abbreviated as $[\text{Mn}_{12}]$ here after. The structure of the cluster is shown in Figure 2.7. In the original paper the magnetic properties were reported as a temperature dependence of the effective magnetic moment, but no interpretation was stated. The nature of the ground state was later shown to be $S_{\text{total}} = 10$.

The major breakthrough occurred in 1993 when Sessoli et al.⁹ reported that the relaxation time of the magnetization of $[\text{Mn}_{12}]$ at low temperature follows the Arrhenius law:

$$\tau = \tau_0 \exp\left(\frac{\Delta}{k_{\text{B}}T}\right) \quad (2.40)$$

where Δ is the difference in energy between the lowest $m_S = \pm S$ states and the highest $S = 0$ one(s), that is $|D|S^2$ for integer spin and $|D|(S^2 - 1/4)$ for half-integer spin values, with $\tau_0 = 2 \times 10^{-6}$ s and $\Delta/k_{\text{B}} = 62$ K.⁹ This means that at 2 K the relaxation time becomes of the order of a few months. Polycrystalline powder spectra of $[\text{Mn}_{12}]$ were shown to give rise to magnetic hysteresis of molecular origin. It was suggested that it would be possible to store information in a single molecule, opening the possibility of absolutely fantastic information densities.

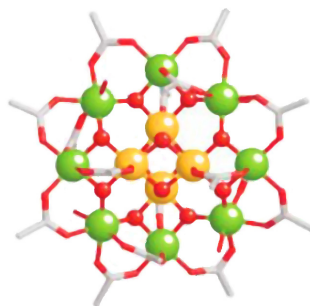


Figure 2.7. Sketch of the structure of $[\text{Mn}_{12}]$. The large green and orange spheres correspond to manganese(III) and manganese(IV) ions, respectively.

The flat regions of the curve monitor fields at which the relaxation is very slow, while the steps correspond to fields at which comparatively faster relaxation occurs. The fields of the steps are to a good approximation equally spaced, and are given by

$$H_n = -nD / g\mu_{\text{B}} \quad (2.41)$$

where $n = 0, 1, 2, \dots$. D is the ZFS parameter of the ground multiplet.

The physical origin of the steps is associated to the presence of two relaxation mechanisms. The first is the thermally activated process described above, while the second is quantum tunneling. Resonant quantum tunneling can occur when pairs of levels are degenerate. The presence of an applied magnetic field parallel to the unique axis z lowers the energies of the states in the negative m_S well and increase the energies of the levels in the positive m_S well. At zero field the $+m_S$ and $-m_S$ levels are to a certain approximation degenerate. Under these conditions comparatively fast relaxation occurs. A non-zero field mismatches the energies of the $+m_S$ and $-m_S$ level, destroying the conditions for tunnel relaxation, thus increasing the relaxation time. The conditions for degenerate levels occur again when the $m_S = +S$ level for instance crosses the $m_S = -S + n$ (figure 2.8a shows on the condition that $n = 1$).

The requirements for observing the SMM behavior was early understood to be: (i) a large spin in the ground state; (ii) a large magnetic anisotropy of the Ising type, i.e. of the easy axis type ($D < 0$).

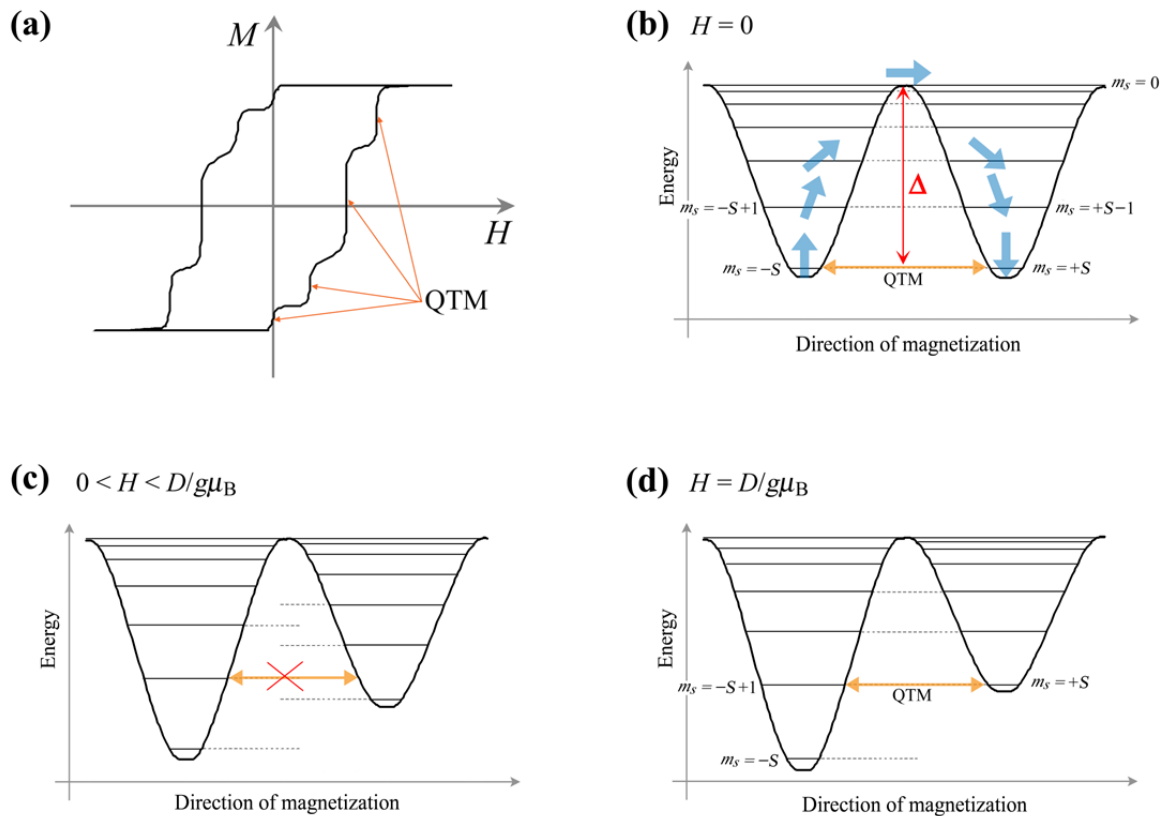


Figure 2.8. Magnetic hysteresis curve for a SMM (a) and energy levels for a spin state S with easy axis magnetic anisotropy (b) – (c). The $+m_S$ levels are localized in the left well and the $-m_S$ levels in the right well. The QTM occurs when the energy levels come to the same level between the two wells.

2.12 Lanthanoid Ions¹⁵

Lanthanoid ions are characterized by large unquenched orbital angular momentum associated with the internal nature of the valence f orbitals. In fact, with the exception of gadolinium(III) and europium(II), which have an f^7 electron configuration and an orbitally nondegenerate ground state, all the rare earth ions have orbitally degenerate ground states, which are split by spin-orbit coupling and crystal field effects. Since crystal-field effects are smaller and spin-orbit coupling larger for f electrons compared to the d electrons of transition-metal ions, the orbital component of the magnetic moment is much more important for the lanthanoid ions compared to the transition-metal ions. The magnetic properties of lanthanoid ions are strongly influenced by this, in particular the magneto-crystalline anisotropy, which is in general large. This is one of the reasons why rare earths are widely used in magnet technology. Some examples of this are provided by the SmCo_5 and $\text{Nd}_2\text{Fe}_{14}\text{B}$ permanent magnets, which have found large market use in the past few years.

Table 2.2. Electron Configurations, Ground States, Landé's g_J Values, and Room Temperature $\chi_{\text{mol}}T$ Values for Trivalent Lanthanoid Ions¹⁵

element	Ln	Ln^{3+}			
		configuration	ground state	g_J	$\chi_{\text{mol}}T / \text{emu mol}^{-1} \text{K}$
lanthanum	La	f^0	$^1\text{S}_0$		
cerium	Ce	f^1	$^2\text{F}_{5/2}$	6/7	0.80
praseodymium	Pr	f^2	$^3\text{H}_4$	4/5	1.60
neodymium	Nd	f^3	$^4\text{I}_{9/2}$	8/11	1.64
promethium	Pm	f^4	$^5\text{I}_4$	3/5	0.90
samarium	Sm	f^5	$^6\text{H}_{5/2}$	2/7	0.09
europium	Eu	f^6	$^7\text{F}_0$		
gadolinium	Gd	f^7	$^8\text{S}_{7/2}$	2	7.88
terbium	Tb	f^8	$^7\text{F}_6$	3/2	11.82
dysprosium	Dy	f^9	$^6\text{H}_{15/2}$	4/3	14.17
holmium	Ho	f^{10}	$^5\text{I}_8$	5/4	14.07
erbium	Er	f^{11}	$^4\text{H}_{15/2}$	6/5	11.48
thulium	Tm	f^{12}	$^3\text{H}_6$	7/6	7.15
ytterbium	Yb	f^{13}	$^2\text{F}_{7/2}$	8/7	2.57
lutetium	Lu	f^{14}	$^1\text{S}_0$		

The magnetic properties of lanthanoid ions are well-known and dominated by the internal nature of the f orbitals, which give rise to strong unquenched orbital angular momentum, and by spin-orbit coupling. The trivalent ions are characterized by f^n configurations, which give rise to ^{2S+1}L multiplets, split by spin-orbital coupling to give J . J is defined by the angular momentum summation rules:

$$|L - S| \leq J \leq L + S. \quad (2.42)$$

For heavier ($n > 7$) and lighter ($n < 7$) lanthanoid ions, $J = L + S$ and $J = |L - S|$, respectively. The ground states for the different lanthanoid ions are listed in Table 2.2. For f^7 ions, like gadolinium(III), $L = 0$ and $S = 7/2$ and the orbital momentum is completely quenched in the ground state.

The Landé's g_J factor of a given J multiplet is expressed by

$$g_J = \frac{3}{2} + \frac{S(S+1) - L(L+1)}{2J(J+1)}. \quad (2.43)$$

In general, the lowest lying J multiplet is well separated from the excited ones. The most notable exceptions are europium(III) and samarium(III). The former has a ground 7F_0 state, with 7F_1 at ca. 350 cm^{-1} , and the latter a ground ${}^6H_{5/2}$ with ${}^6H_{7/2}$ at ca. 700 cm^{-1} .

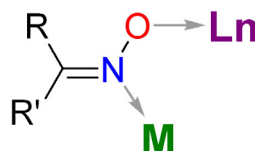
For magnetic study, total momentum J is introduced in place of S . The Brillouin function $B_J(x)$ is defined as eqs 2.14 and 2.15. Similarly, g should be replaced with g_J in eqs 2.13 – 2.18.

2.13 Oximate Ligands

Ligands containing N and O atoms with lone pairs are synthesized with the aim of capturing and linking different types of paramagnetic centers to produce magnetically interesting systems. Thus, for example, a ligand can be designed to provide a coordination environment favored by a 3d metal ion such as copper(II) or nickel(II) ion (relatively N-rich), as well as a site more favored by a “hard” metal ion such as any lanthanoid(III) ions (relatively O^- rich).

Oximate ($RR'C=N-O^-$), as an anionic form of oxime, is very useful ligand because it has an N-site and an O-site, which can be coordinated with a transition-metal ion and a lanthanoid ion, respectively (Scheme 2.1).

Scheme 2.1. Structural Formula of an Oxime Ligand (Ln; Lanthanoid Ion, M; Transition-Metal ion)



References

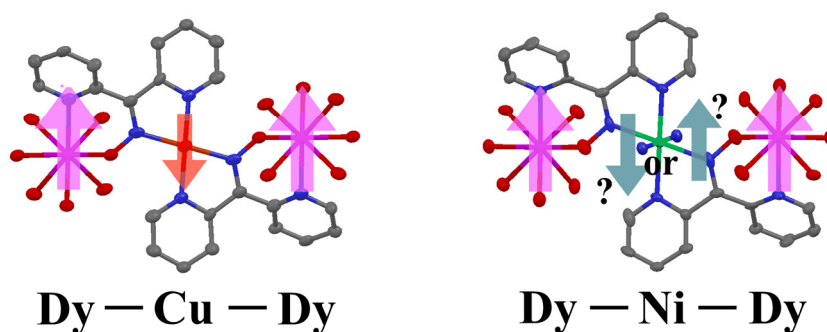
- (1) Kahn, O. *Molecular Magnetism*; VCH: Weinheim, Germany, 1993.
- (2) Itoh, K.; Kinoshita, M. *Molecular Magnetism*; Kodansha, Tokyo, Japan, 2000.
- (3) van Vleck, J. H. *The Theory of Electric and Magnetic Susceptibilities*; Oxford University Press: Oxford, UK, 1932.
- (4) O'Connor, C. J. *Research Frontiers in Magnetochemistry*; World Scientific: Singapore, 1993.
- (5) Heisenberg, W. Z. *Physik.* **1926**, 38, 411.
- (6) Dirac, P. A. M. *Proc. Roy. Soc.* **1926**, 112A, 661.
- (7) Gatteschi, D.; Sessoli, R.; Villain, J. *Molecular Nanomagnets*; Oxford University Press: New York, USA, 2006.
- (8) Miller, J. S.; Drillon, M. *Magnetism: Molecules to Materials III*; Wiley-VCH: Weinheim, Germany, 2002.
- (9) Sessoli, R.; Gatteschi, D.; Caneschi, A.; Novak, M. A. *Nature* **1993**, 365, 141.
- (10) McConnell, J. *Rotational Brownian Motion and Dielectric Theory*; Academic Press: New York, USA, 1980.
- (11) Cole, K. S.; Cole, R. H. *J. Chem. Phys.* **1941**, 9, 341.
- (12) Dekker, C.; Arts, A. F. M.; Wijn, H. W.; van Duyneveldt, A. J.; Mydosh, J. A. *Phys. Rev. B* **1989**, 40, 11243.
- (13) Mydosh, J. A. *Spin Glasses: An Experimental Introduction*; Taylor & Francis Ltd, London, UK, 1993.
- (14) Lis, T. *Acta Cryst. B* **1980**, 30, 2042.
- (15) Benelli, C.; Gatteschi, D. *Chem. Rev.* **2002**, 102, 2369.

Chapter 3

Magnetic Properties and Exchange Couplings in Single-Molecule Magnets [Dy₂Ni] and [Dy₂Cu]

Abstract

Lanthanide ions seem suitable for development of SMMs, since the barrier of magnetization reversal is caused by strong magnetic anisotropy and large spins. Linear trinuclear Ln–M–Ln-type SMMs were prepared. The exchange couplings in [$\{\text{Dy}(\text{hfac})_3\}_2\text{Cu}(\text{dpk})_2$] and [$\{\text{Dy}(\text{hfac})_3\}_2\text{Ni}(\text{dpk})_2(\text{py})_2$] were precisely evaluated by high-frequency EPR and pulsed-field magnetization studies, giving $J_{\text{Dy–Cu}}/k_{\text{B}} = -0.126$ K and $J_{\text{Dy–Ni}}/k_{\text{B}} = -0.031$ K. The Dy signal itself was unobservable in EPR, but the bias field at the 3d metal ions was detected, affording the information of exchange couplings. We have established a standard method to evaluate the exchange couplings.

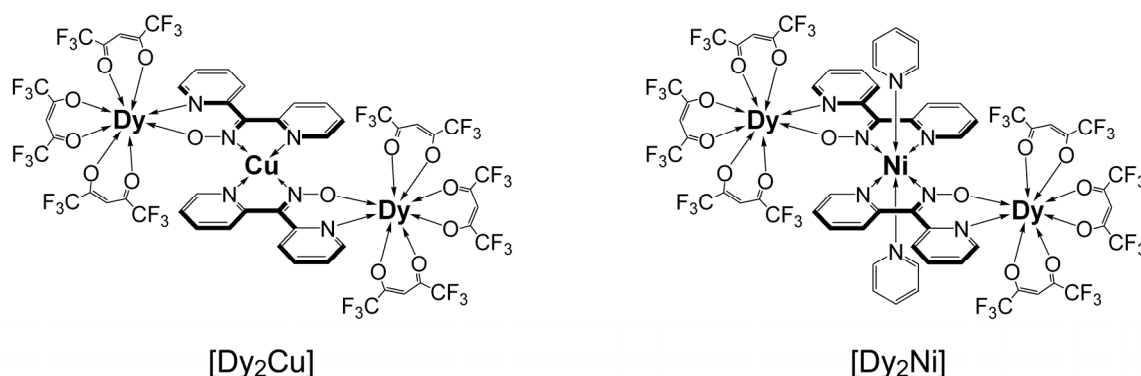


3.1 Introduction

Discrete complexes with bridging ligands are of increasing interest for development of molecule-based magnets since the discovery of SMMs.¹ SMMs exhibit magnetic hysteresis from the single-molecular origin; namely, extremely slow magnetization reversal due to a high energy-barrier. Lanthanide ions seem suitable for development of SMMs because the barrier is caused by strong magnetic anisotropy and large spins.² Our idea was that 4f–3d heterometallic compounds would have larger spins whichever ferro- or antiferromagnetic coupling is operative between 4f and 3d spins. Actually, several Dy–Cu and Dy–Ni compounds showed slow magnetization reversal and distinct hysteresis, as clarified by ac susceptibility and/or pulsed-field magnetization measurements.³ QTM, observable as magnetization steps, is also characteristic of SMMs.¹ In this chapter, we investigated the exchange couplings and energy-level structures of linear trinuclear 4f–3d-heterometallic compounds by means of HF-EPR⁴ together with pulsed-field magnetization.⁵ A number of 4f–3d

heterometallic SMMs are known to date,^{3b,3d,6} but the magnitude of intramolecular exchange coupling has rarely been determined so far.⁷ The advantages of HF-EPR are the extremely high resolution,⁸ the ability to identify quantum numbers of energy levels by the EPR selection rule, and the observation of the energy level splitting in the excited states. The last point complements the magnetization measurements which clarify the alternation of the ground state (level crossing) from magnetization steps. The EPR technique and related analysis scheme have been established in the determination of spin Hamiltonian parameters of 3d-based SMMs and SCMs, such as the ZFS anisotropy on $[\text{Mn}_{12}]$.⁹ On the other hand, EPR techniques have been hardly applied to 4f-3d heterometallic systems so far, mostly because of the difficulty of experiments and the lack in analysis methodology. The present case is the first application of EPR for the evaluation of exchange coupling in this type of compound, and therefore this work will provide a standard method for the systematic study on exchange couplings in 4f-3d heterometallic compounds.

Scheme 3.1. Structural Formulas of $[\text{Dy}_2\text{Cu}]$ and $[\text{Dy}_2\text{Ni}]$



3.2 Results

Complexes $[\{\text{Dy}^{\text{III}}(\text{hfac})_3\}_2\text{Cu}^{\text{II}}(\text{dpk})_2]^{3b}$ and $[\{\text{Dy}^{\text{III}}(\text{hfac})_3\}_2\text{Ni}^{\text{II}}(\text{dpk})_2(\text{py})_2]^{3f}$ (abbreviated as $[\text{Dy}_2\text{Cu}]$ and $[\text{Dy}_2\text{Ni}]$, respectively) were prepared according to the literature method (for the molecular structures, see Scheme 3.1). They crystallized in a monoclinic $P2_1/n$ space group. The molecular structures are similar to each other except for the additional axial pyridine ligands in $[\text{Dy}_2\text{Ni}]$. There is a unique J_{4f-3d} exchange parameter in each compound, owing to a molecular centrosymmetry.

The pulse-field magnetization measurements on a polycrystalline specimen of $[\text{Dy}_2\text{Ni}]$ clarified hysteresis behavior with magnetization jumps (Figure 3.1a). The position of jumps indicated by the peaks of the differential magnetization show no appreciable field-sweeping rate or temperature dependence, being compatible with the QTM. The slow magnetization reversal has already been demonstrated from ac magnetic susceptibility.^{3f} Preliminary Arrhenius analysis on $[\text{Dy}_2\text{Ni}]$ gave T_B

$= 2.5$ K, $E_a/k_B = 66$ K, and $\tau_0 = 1.0 \times 10^{-7}$ s. Combining the results on [Dy₂Cu] previously reported,^{3b} we can conclude that [Dy₂Cu] and [Dy₂Ni] are isomorphous SMMs. Evaluation of J_{4f-3d} and of the energy level for each compound is now the next problem, which seems difficult to solve solely from magnetization studies.

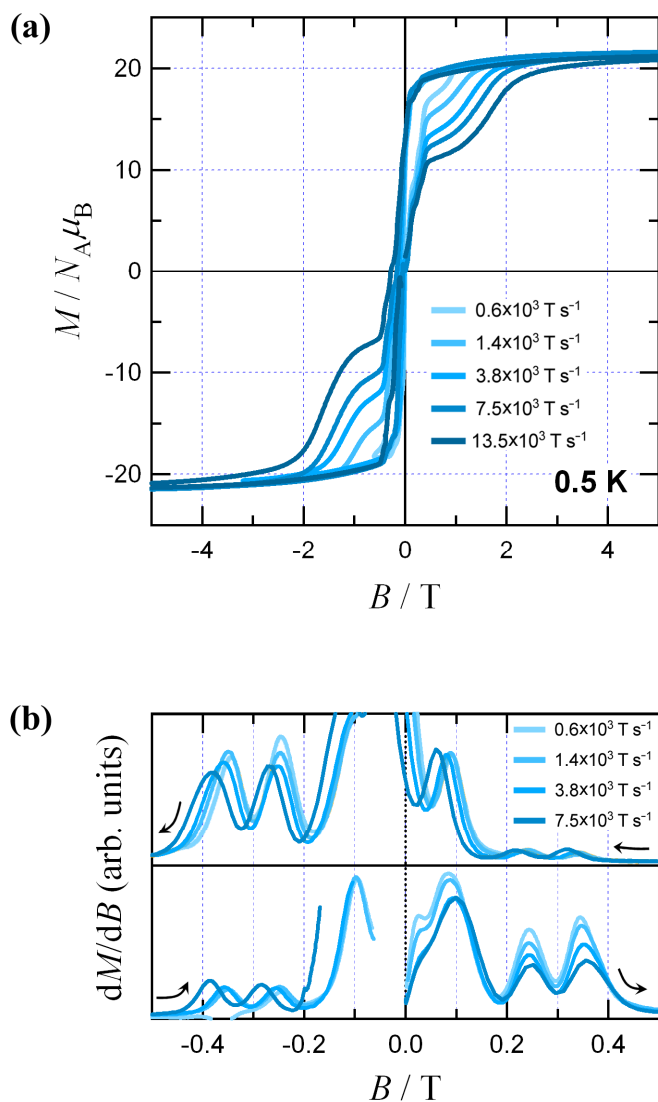


Figure 3.1. (a) Hysteresis curves for [Dy₂Ni] measured at 0.5 K. The field-sweeping rates were $(0.6 - 13.5) \times 10^3 \text{ T s}^{-1}$. (b) Differential magnetization curves as a function of a sweeping rate.

HF-EPR spectra of powder [Dy₂Cu] were collected in a wide frequency range between 41.2 and 190 GHz at 4.2 K (Figure 3.2a). We found a series of major signals shifted to a higher field with an increase of frequency. The g value was 2.07(1) from the slope of the frequency-field plot, being consistent with the Cu signal satisfying a conventional EPR selection rule of $\Delta m_s = \pm 1$. There is no single-ion type anisotropy in Cu spins, and thus the observed characteristic frequency-field relation

shows the presence of internal fields on the Cu sites mediated by sizable exchange couplings between Dy and Cu ions. In other words, the observed EPR is attributed to the reversal of the Cu $S = 1/2$ spin biased by the exchange field from the Dy ions. Extrapolation gives a critical field of 1.36 T. The pulsed-field magnetization measurements on $[\text{Dy}_2\text{Cu}]$ have been reported to show a $2 \mu_B$ jump around 1.7 T, which is ascribable to the Cu spin-flip.^{3b} The critical field of 1.36 T determined by the EPR measurements is identical to the position of the $2 \mu_B$ jump around 1.7 T in the magnetization curves.

The temperature dependence of the EPR signal intensity indicates that this absorption band was ascribable to the transition from the ground state (Figure 3.2b). Owing to the level cross at 1.36 T, the ferromagnetic state $[\text{Dy}(\uparrow)\text{-Cu}(\uparrow)\text{-Dy}(\uparrow)]$ becomes the lowest in this region, and excitation to a ferrimagnetic state $[\text{Dy}(\uparrow)\text{-Cu}(\downarrow)\text{-Dy}(\uparrow)]$ was observed. The ground state of $[\text{Dy}_2\text{Cu}]$ at zero field is ferrimagnetic (Figure 3.3).

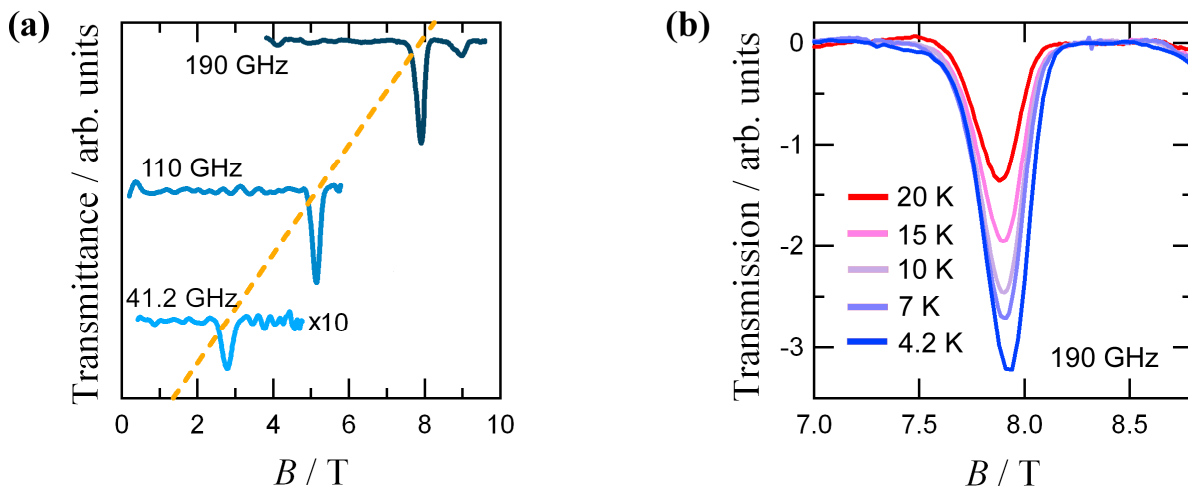


Figure 3.2. (a) Selected EPR spectra measured at 4.2 K as a function of frequency for $[\text{Dy}_2\text{Cu}]$. The spectra are offset in a linear scale of the frequency. Dotted lines are drawn for a guide to the eye. (b) EPR spectra recorded in a temperature range of 4.2 – 20 K at 190 GHz.

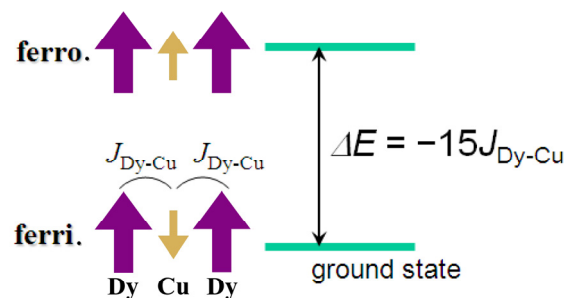


Figure 3.3. Energy diagram at zero-field for $[\text{Dy}_2\text{Cu}]$. Spin structures for two related states (ferrimagnetic state and ferromagnetic state) are drawn with arrows. Large purple and small orange arrows show Dy and Cu moments, respectively.

HF-EPR spectra of powder [Dy₂Ni] were recorded in a frequency range of 92.4 – 352 GHz at 4.2 K (Figure 3.4a). We found three “allowed” $g \approx 2$ lines and three “forbidden” $g \approx 4$ lines. This finding indicates that the local symmetry of the Ni²⁺ single-ion-type anisotropy is orthorhombic with ZFS D and E terms. No Dy signal was observed like the [Dy₂Cu] case.

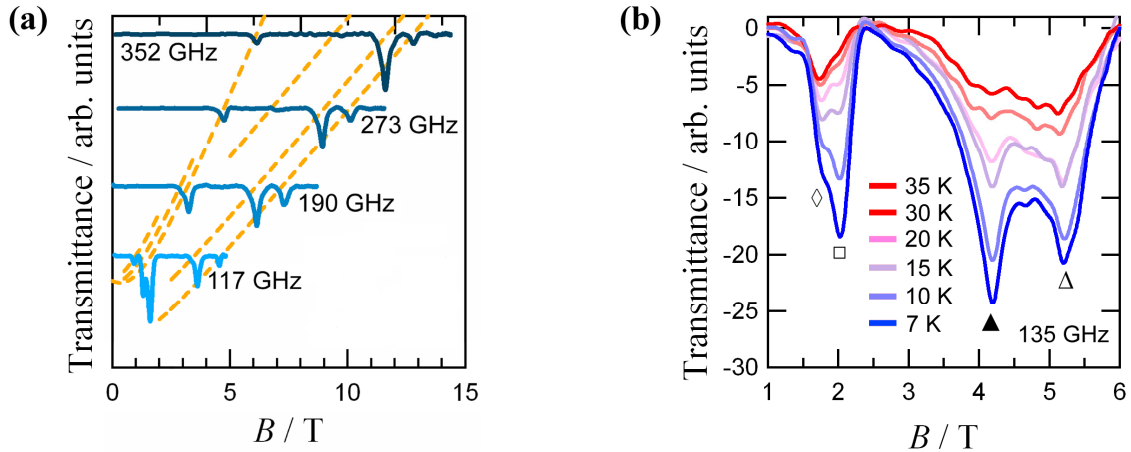


Figure 3.4. (a) Selected EPR spectra measured at 4.2 K as a function of frequency for [Dy₂Ni]. The spectra are offset in a linear scale of the frequency. Dotted lines are drawn for a guide to the eye. (b) EPR spectra recorded in a temperature range of 7 – 35 K at 135 GHz.

3.3 Discussion

By treatment of the Dy moments as Ising spins with $|J| = 15/2$ and $g_{\text{Dy}} = 4/3$, an Ising-type spin Hamiltonian (eq 3.1) for [Dy₂Cu] can be built as an exchange coupling model here.^{3b} The first term implies exchange interaction and the second the Zeeman effect. There is a single adjustable parameter $J_{\text{Dy-Cu}}$, and accordingly $J_{\text{Dy-Cu}}/k_{\text{B}}$ can be easily determined to be $-0.126(3)$ K by fitting the EPR result. This value is close to that from the magnetization study (-0.155 K),^{3b} but the present value has a much better precision because of the high-resolution of HF-EPR and the variable-frequency technique. We note here that the exchange energy is as large as 0.47 K because of the long Dy moment.

$$\mathcal{H} = -J_{\text{Dy-Cu}}(\hat{J}_{\text{Dy1}}^z \cdot \hat{S}_{\text{Cu}} + \hat{J}_{\text{Dy2}}^z \cdot \hat{S}_{\text{Cu}}) + \mu_{\text{B}}H^z(g_{\text{Dy}}J_{\text{Dy1}}^z + g_{\text{Dy}}J_{\text{Dy2}}^z + g_{\text{Cu}}S_{\text{Cu}}) \quad (3.1)$$

The EPR frequency-field relations of Ni²⁺ compounds with orthorhombic symmetry are well-known,¹⁰ and Figure 3.4a demonstrates a typical transverse-field pattern for Ni ions. Two intense bands (denoted with \blacktriangle and \triangle in Figure 3.4b) out of three $g \approx 2$ lines are ascribable to absorption bands for the Ni second easy axis. The other minor band is assigned to that for the first. The powder sample was loosely packed, and each microcrystal underwent reorientation to the easy

axis in a sample room. If the easy axes of Dy and Ni were close to each other, the sample could be oriented along those axes. Then Ni EPR spectra of the easy axis would be expected, which is different from the present result. Therefore, the easy-axis directions of the Ni and Dy are different from each other, and the sample powder is reoriented so that the Dy moments align along the field direction. As a result, the Ni spin experiences a transverse field.

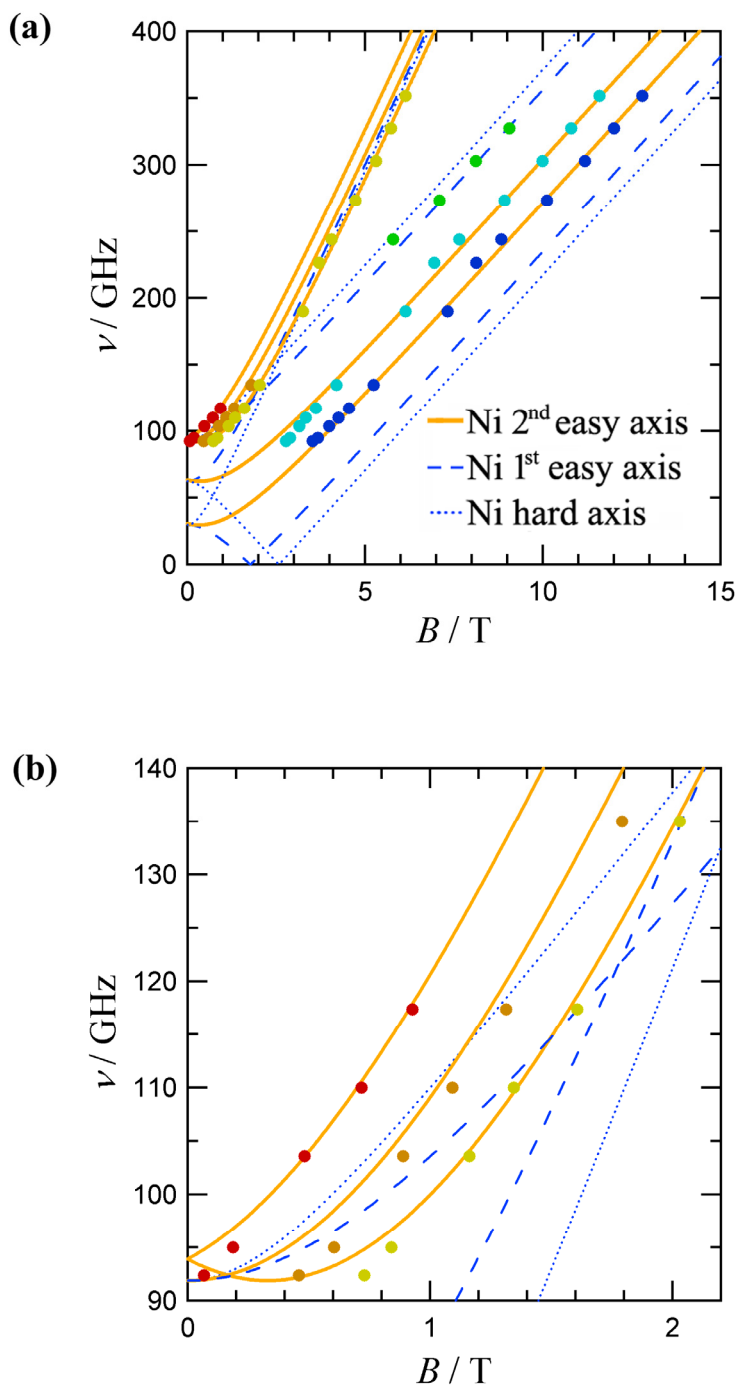


Figure 3.5. Frequency-field diagrams for (a) $[\text{Dy}_2\text{Ni}]$ and (b) its magnification in a small magnetic field region. Circles: data. Lines: calculation from the energy-level diagram (Figure 3.4).

Though the spectra are somewhat complex in comparison with those of [Dy₂Cu], the basic concept holds for [Dy₂Ni]. We extend the Ising model as follows (eq 3.2).

$$\mathcal{H} = -J_{\text{Dy-Ni}} (\hat{J}_{\text{Dy1}}^z \cdot \hat{S}_{\text{Ni}}^z + \hat{J}_{\text{Dy2}}^z \cdot \hat{S}_{\text{Ni}}^z) + D_{\text{Ni}} \left(\hat{S}_{\text{Ni}}^{z^2} - \frac{1}{3} S_{\text{Ni}} (S_{\text{Ni}} + 1) \right) + E_{\text{Ni}} (\hat{S}_{\text{Ni}}^{x^2} - \hat{S}_{\text{Ni}}^{y^2}) + \mu_{\text{B}} H^z (g_{\text{Dy}} J_{\text{Dy1}}^z + g_{\text{Dy}} J_{\text{Dy2}}^z) + \mu_{\text{B}} g_{\text{Ni}} \hat{S}_{\text{Ni}} \cdot \hat{H} \quad (3.2)$$

where $J_{\text{Dy-Ni}}$ is an exchange coupling. The ZFS terms defined by D_{Ni} and E_{Ni} are incorporated in eq 3.2. The last term implies the Zeeman effect on the Heisenberg Ni spin. The coordinate is defined as z along the Dy easy axis and y along the Ni first easy axis. The fitting result is given in Figure 3.5.

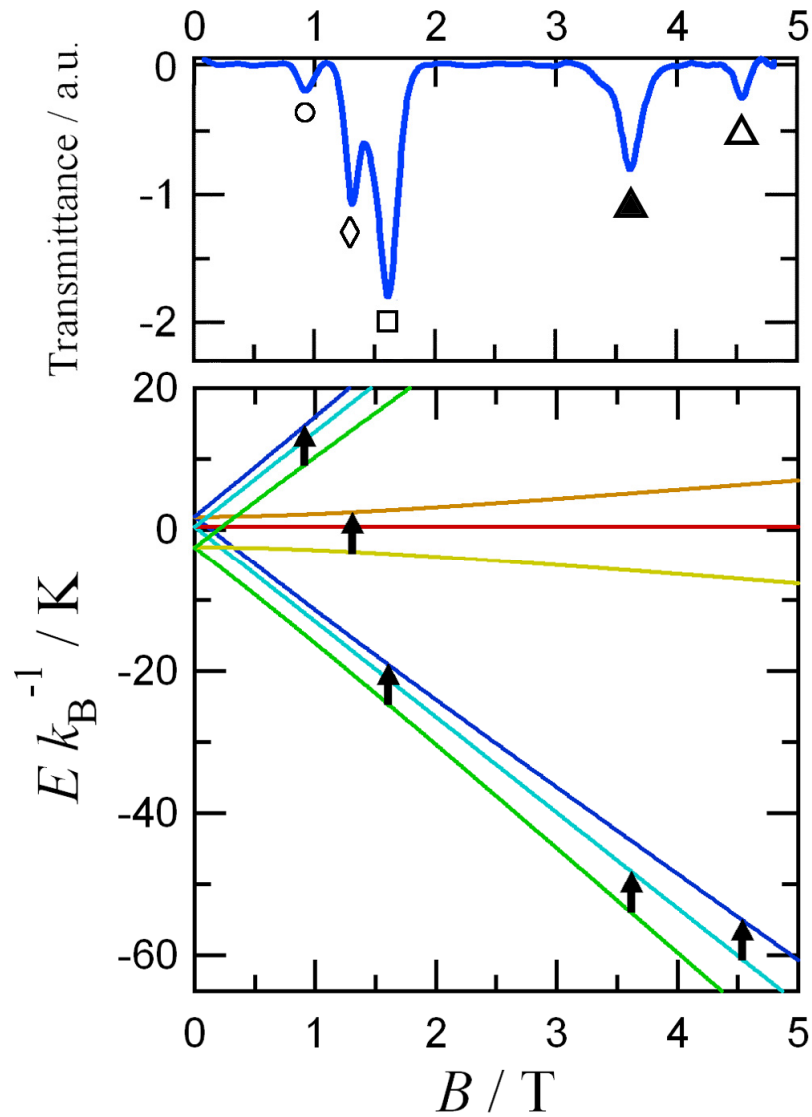


Figure 3.6. Schematic Zeeman diagrams of [Dy₂Ni]. The EPR absorption spectrum at 117.4 GHz and 4.2 K is also shown in the top. Arrows denote the EPR absorption at 117.4 GHz.

The forbidden line is usually single, but there were three $g \approx 4$ lines (denoted as \circ , \square , and \diamond in Figure 3.6) in the present study. This finding can be plausibly interpreted only when the sublevels due to the Dy–Ni exchange interaction is taken into consideration in addition to the usual ZFS. For simplicity, the exchange term is replaced by the exchange bias field in the fitting. Finally, we obtained $J_{\text{Dy-Ni}}/k_{\text{B}} = -0.031$ K, $D_{\text{Ni}}/k_{\text{B}} = +3.7$ K, and $E_{\text{Ni}}/k_{\text{B}} = -0.73$ K with $g_{\text{Ni}} = 2.10$. Though $J_{\text{Dy-Ni}}$ is small, the fitting was impossible without this coupling.

The sign of D_{Ni} was determined from the intensity ratio of the allowed bands (\blacktriangle and Δ in Figure 3.6). The ground state was confirmed by the variable-temperature experiments. Such a technique has been widely applied to the determination of D values in 3d-based SMMs.¹¹ Note that the present application of HF-EPR to evaluate the exchange coupling is quite unique. The profile of the forbidden bands is sensitive to the sign of $J_{\text{Dy-Ni}}$. The Ni forbidden band due to the excitation from $\text{Dy}(\uparrow)\text{-Ni}(\downarrow)\text{-Dy}(\uparrow)$ to $\text{Dy}(\uparrow)\text{-Ni}(\uparrow)\text{-Dy}(\uparrow)$ (\square in Figure 3.6) is the strongest because of a transition from the ground state. On the other hand, the band from $\text{Dy}(\downarrow)\text{-Ni}(\downarrow)\text{-Dy}(\downarrow)$ to $\text{Dy}(\downarrow)\text{-Ni}(\uparrow)\text{-Dy}(\downarrow)$ is the weakest (\circ in Figure 3.6) because this transition takes place between higher-energy states. The stronger band appears in the higher field when $J_{\text{Dy-Ni}}$ is negative. If $J_{\text{Dy-Ni}}$ were positive, the stronger band would appear in the lower field. We confirmed this by simulation works.

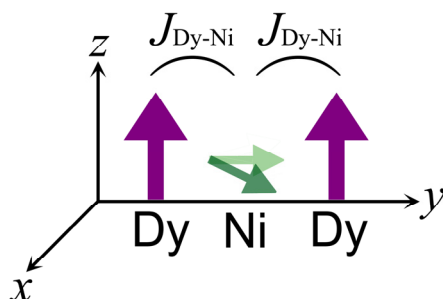


Figure 3.7. Schematic spin structure of ground state (large purple and small dark green arrows stand for Dy and Ni moments, respectively). Small light green arrow denotes Ni moment when the exchange interaction are ignored. Orientation of the Cartesian axes used for directions of the tensor of ZFS parameters in the spin Hamiltonian.

The above description with arrows is valid only in very high fields. The Dy and Ni spins are antiferromagnetically coupled, and at the same time, the Ni single-ion anisotropy directs the Ni spin perpendicular to the z axis (i.e., $\text{Dy}(\uparrow)\text{-Ni}(\rightarrow)\text{-Dy}(\uparrow)$). Consequently, the Ni spin is tilted from the z axis at the ground state in zero field. The magnitude of tilting is regulated by the balance between the exchange coupling and the Ni single-ion anisotropy (Figure 3.7).

The present $[\text{Dy}_2\text{Ni}]$ energy-level structure completely agrees with the EPR signal positions, taking the 117.4 GHz data, for example, in Figure 3.6. As for several level crossings in a small field

region (Figure 3.8), they clearly coincide with the positions of the magnetization jumps. Thus, the present model is totally consistent with both the magnetization and EPR results.

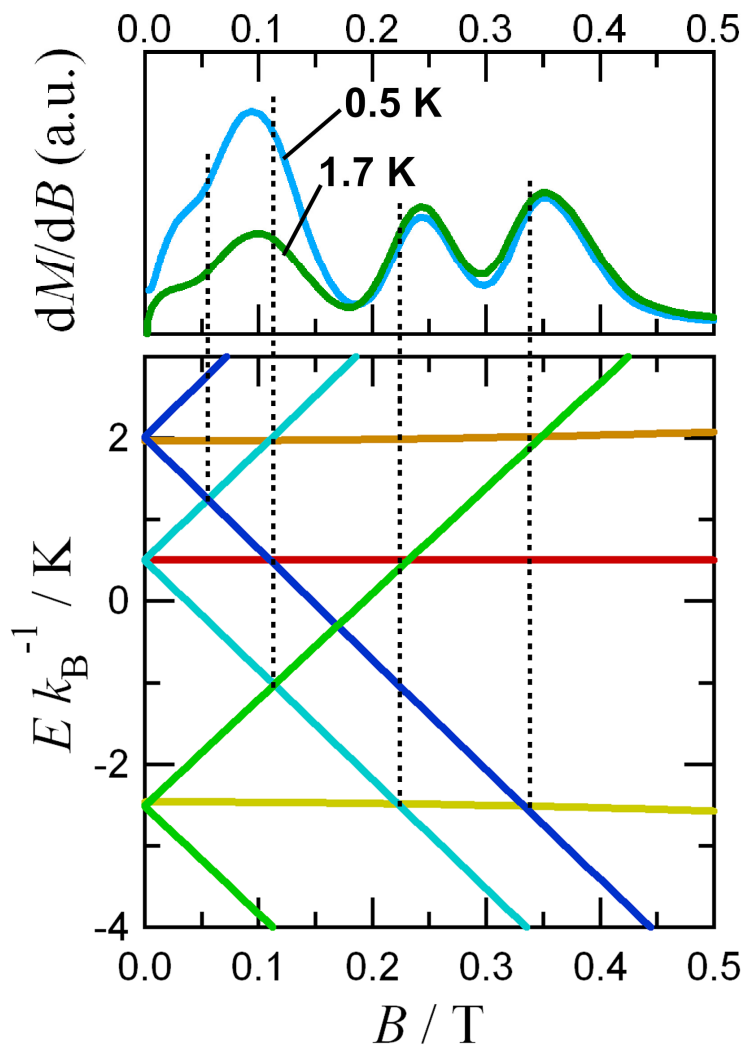


Figure 3.8. Magnification of schematic Zeeman diagrams of [Dy₂Ni] in a small magnetic region (0 – 0.5 T). The differential magnetization curves measured at 0.5 and 1.7 K with a field-sweeping rate of $3.6 \times 10^3 \text{ T s}^{-1}$ are also shown in the top.

There are ample reports on ferromagnetic $J_{\text{Dy-Cu}}$ as well as $J_{\text{Gd-Cu}}$.^{12–14} Antiferromagnetic couplings are explained in terms of the violation of the ferromagnetic interaction between the 4f spin portion and 3d spin,¹² owing to torsion along the Ln(4f)–O–N–M(3d) linkage.¹⁵ The nickel(II) ion has two 3d spin in $3d_{z^2}$ and $3d_{x^2-y^2}$. Antiferromagnetic coupling between $3d_{x^2-y^2}$ and Dy 4f orbitals are present in [Dy₂Ni] and therefore we can comprehend that both [Dy₂Cu] and [Dy₂Ni] possess negative J_{4f-3d} .

3.4 Conclusion

The advantages of HF-EPR are its extremely high resolution and its ability to identify quantum numbers of energy levels by the EPR selection rule. In the present work, the Dy signal itself was unobservable, but the bias field at the 3d metal ions was detected, affording the information of exchange couplings. To the best of our knowledge, the present work is the first example on determination of 4f-3d exchange parameters by means of EPR. We have precisely evaluated J_{4f-3d} and depicted energy levels for $[\text{Dy}_2\text{Cu}]$ and $[\text{Dy}_2\text{Ni}]$. The present methodology would be applicable to other 4f-3d heterometallic SMM compounds.

3.5 Experimental Section

3.5.1 Preparation

The compounds $[\text{Dy}_2\text{Ni}]$ and $[\text{Dy}_2\text{Cu}]$ were prepared by following a previously described procedure.^{3b} They were identified by means of elemental analysis and X-ray crystallographic measurement. $[\text{Dy}_2\text{Ni}]$: Anal. Calcd.: C, 34.15; H, 1.48; N, 5.14% for $\text{C}_{62}\text{H}_{32}\text{Dy}_2\text{F}_{36}\text{N}_8\text{NiO}_{14}$. Found: C, 33.98; H, 1.98; N, 4.96%. $[\text{Dy}_2\text{Cu}]$: Anal. Calcd.: C, 30.81; H, 1.09; N, 4.15% for $\text{C}_{52}\text{H}_{22}\text{CuDy}_2\text{F}_{36}\text{N}_6\text{O}_{14}$. Found: C, 30.33; H, 1.39; N, 4.22%.

3.5.2 Physical Measurements

Low-temperature magnetization was measured by a conventional inductive probe in pulsed-magnetic fields, and the temperature was reached as low as 0.5 K using a ^3He cryostat.⁴ Figure 3.9 shows the schematic view of the apparatus. Polycrystalline specimens (typically 15 mg) were mounted in a capillary made of polyimide Kapton (duPont). The sample was not fixed within the sample tube and then it aligned along the magnetic field direction. After we applied the magnetic field several times, the orientation effect was saturated, and the magnetization curves obtained in further shots were found to be identical.

HF-EPR spectrum for polycrystalline samples were obtained on the same pulsed-field generator.⁵ The sample was packed in a case made of polyethylene. The radiation was produced by Gunn oscillators, backward traveling wave oscillators, and an optically pumped far-infrared laser.

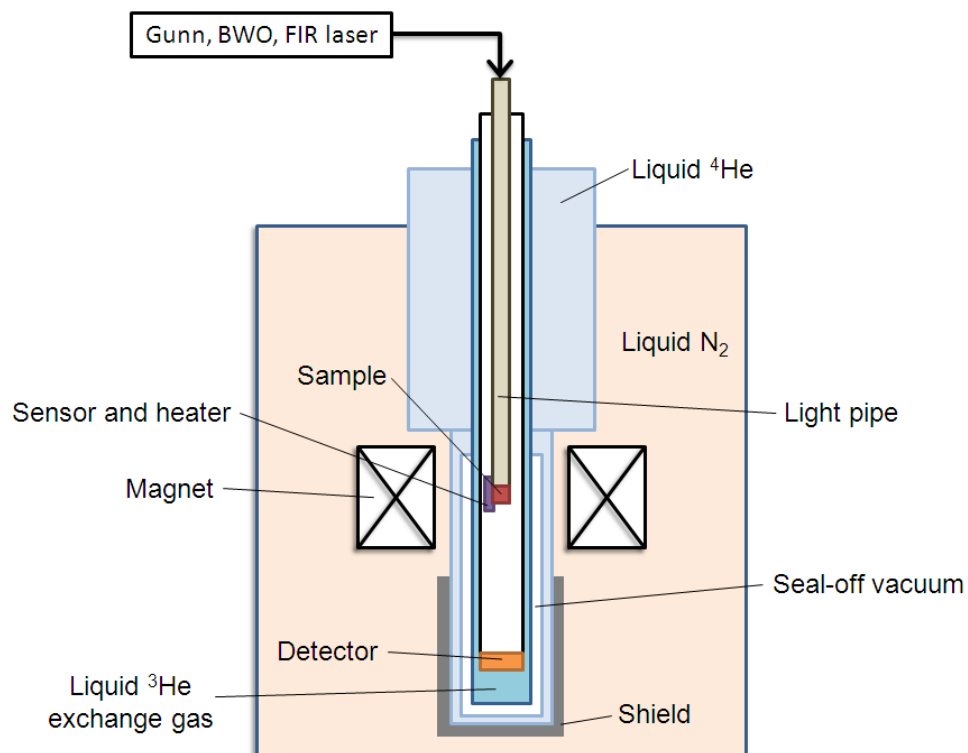


Figure 3.9. The schematic view of the pulsed-field magnetization/HF-EPR apparatus. The light sources and guides are shown for the HF-EPR measurements. The cryostat for ³He temperature is shown. Insulation vacuum layers of liquid ⁴He and of liquid N₂ are omitted for clarity.

References

- (1) (a) Gatteschi, D.; Sessoli, R.; Villain, J. *Molecular Nanomagnets*, Oxford University Press: New York, 2006. (b) Sessoli, R.; Gatteschi, D.; Caneschi, A.; Novak, M.A. *Nature* **1993**, *365*, 141. (c) Gatteschi, D.; Caneschi, A.; Pardi, L.; Sessoli, R. *Science* **1994**, *265*, 1054. (d) Christou, G.; Gatteschi, D.; Hendrickson, D. N.; Sessoli, R. *MRS Bull.* **2000**, *25*, 66. (e) Gatteschi, D.; Sessoli, R. *Angew. Chem., Int. Ed.* **2003**, *42*, 268.
- (2) (a) Ishikawa, N.; Sugita, M.; Ishikawa, T.; Koshihara, S.-y.; Kaizu, Y. *J. Am. Chem. Soc.* **2003**, *125*, 8694. (b) Ishikawa, N.; Sugita, M.; Wernsdorfer, W. *J. Am. Chem. Soc.* **2005**, *127*, 3650.
- (3) Dy-Cu compounds: (a) Osa, S.; Kido, T.; Matsumoto, N.; Re, N.; Pochaba, A.; Mrozinski, J. *J. Am. Chem. Soc.* **2004**, *126*, 420. (b) Mori, F.; Nyui, T.; Ishida, T.; Nogami, T.; Choi, K.-Y.; Nojiri, H. *J. Am. Chem. Soc.* **2006**, *128*, 1440. (c) Aronica, C.; Pilet, G.; Chastanet, G.; Wernsdorfer, W.; Jacquot, J.-F.; Luneau, D. *Angew. Chem., Int. Ed.* **2006**, *45*, 4659. (d) Ueki, S.; Ishida, T.; Nogami, T.; Choi, K.-Y.; Nojiri, H. *Chem. Phys. Lett.* **2007**, *440*, 263. (e) Hamamatsu, T.; Yabe, K.; Towatari, M.; Matsumoto, N.; Re, N.; Pochaba, A.; Mrozinski, J. *Bull. Chem. Soc. Jpn.* **2007**, *80*, 523. Dy-Ni compounds: (f) Mori, F.; Ishida, T.; Nogami, T. *Polyhedron* **2005**, *24*, 2588. (g) Pointillart, F.; Bernot, K.; Sessoli, R.; Gatteschi, D. *Chem.-Eur. J.* **2007**, *13*, 1602. (h) Chandrasekhar, V.; Pandian, B. M.; Boomishankar, R.; Steiner, A.; Viftal, J. J.; Hourii, A.; Clérac, R. *Inorg. Chem.* **2008**, *47*, 4918. (i) Costes, J. P.; Shova, S.; Wernsdorfer, W. *Inorg. Chem.* **2008**, 1843.
- (4) Nojiri, H.; Choi, K.-Y.; Kitamura, N. *J. Magn. Magn. Mater.* **2007**, *310*, 1468.
- (5) Nojiri, H.; Ajiro, Y.; Asano, T.; Boucher, J.-P. *New J. Phys.* **2006**, *8*, 218.
- (6) (a) Mishra, A.; Wernsdorfer, W.; Abboud, K. A.; Christou, G. *J. Am. Chem. Soc.* **2004**, *126*, 15648. (b) Zaleski, C. M.; Depperman, E. C.; Kampf, J. W.; Kirk, M. L.; Pecoraro, V. L. *Angew. Chem., Int. Ed.* **2004**, *43*, 3912. (c) Mishra, A.; Wernsdorfer, W.; Parsons, S.; Christou, G.; Brechin, E. K. *Chem. Commun.* **2005**, 2086. (d) Costes, J.-P.; Dahan, F.; Wernsdorfer, W. *Inorg. Chem.* **2006**, *45*, 5. (e) Murugesu, M.; Mishra, A.; Wernsdorfer, W.; Abboud, K. A.; Christou, G. *Polyhedron* **2006**, *25*, 613. (f) Chandrasekhar, V.; Pandian, B. M.; Azhakar, R.; Vittal, J. J.; Clérac, R. *Inorg. Chem.* **2007**, *46*, 5140. (g) Costes, J.-P.; Shova, S.; Wernsdorfer, W. *Dalton Trans.* **2008**, 1843.
- (7) (a) Ferbinteanu, M.; Kajiwara, T.; Choi, K.-Y.; Nojiri, H.; Nakamoto, A.; Kojima, N.; Cimpoesu, F.; Fujimura, Y.; Takaishi, S.; Yamashita, M. *J. Am. Chem. Soc.* **2006**, *128*, 9008. (b) Mereacre, V.; Ako, A. M.; Clérac, R.; Wernsdorfer, W.; Hewitt, I. J.; Anson, C. E.; Powell, A. K. *Chem.-Eur. J.* **2008**, *14*, 3577.
- (8) Eaton, G. R.; Eaton, S. S. *Appl. Magn. Reson.* **1999**, *16*, 161.
- (9) Barra, A. L.; Caneschi, A.; Cornia, A.; De Biani, F. F.; Gatteschi, D.; Sangregorio, C.; Sessoli, R.; Sorace, L. *J. Am. Chem. Soc.* **1999**, *121*, 5302.

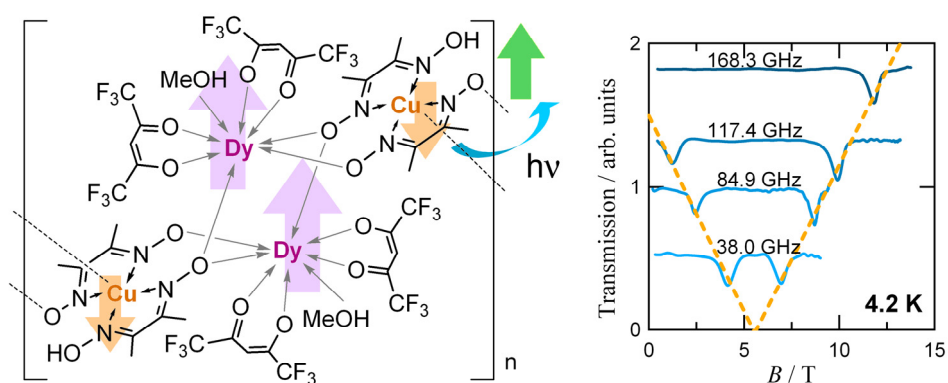
- (10) Rebilly, J.-N.; Charron, G.; Riviere, E.; Guillot, R.; Barra, A.-L.; Serrano, M. D.; van Slageren, J.; Mallah, T. *Chem.–Eur. J.* **2008**, *14*, 1169.
- (11) (a) Barra, A. L.; Gatteschi, D.; Sessoli, R. *Phys. Rev. B* **1997**, *56*, 8192. (b) Bouwen, A.; Caneschi, A.; Gatteschi, D.; Goovaerts, E.; Schoemaker, D.; Sorace, L.; Stefan, M. *J. Phys. Chem. B* **2001**, *105*, 2658.
- (12) Andruh, M.; Ramade, I.; Coddjovi, E.; Guillou, O.; Kahn, O.; Trombe, J. C. *J. Am. Chem. Soc.* **1993**, *115*, 1822.
- (13) (a) Costes, J.-P.; Dahan, F.; Dupuis, A. *Inorg. Chem.* **2000**, *39*, 5994. (b) Costes, J.-P.; Dahan, F.; Dupuis, A.; Laurent, J.-P. *Inorg. Chem.* **2000**, *39*, 169. (c) Costes, J.-P.; Dahan, F.; Dupuis, A.; Laurent, J.-P. *Chem.–Eur. J.* **1998**, *4*, 1616.
- (14) (a) Kido, T.; Ikuta, Y.; Sunatsuki, Y.; Ogawa, Y.; Matsumoto, N.; Re, N. *Inorg. Chem.* **2003**, *42*, 398. (b) Evangelisti, M.; Kahn, M. L.; Bartolome, J.; de Jongh, L. J.; Meyers, C.; Leandri, J.; Leroyer, Y.; Mathoniere, C. *Phys. Rev. B* **2003**, *68*, 184405.
- (15) (a) Kobayashi, Y.; Ueki, S.; Ishida, T.; Nogami, T. *Chem. Phys. Lett.* **2003**, *378*, 337. (b) Ueki, S.; Kobayashi, Y.; Ishida, T.; Nogami, T. *Chem. Commun.* **2005**, 5223.

Chapter 4

A 4f-3d Heterometallic Chain $[\text{Dy}_2\text{Cu}_2]_n$ Compound Showing Single-Molecule Magnet Behavior

Abstract

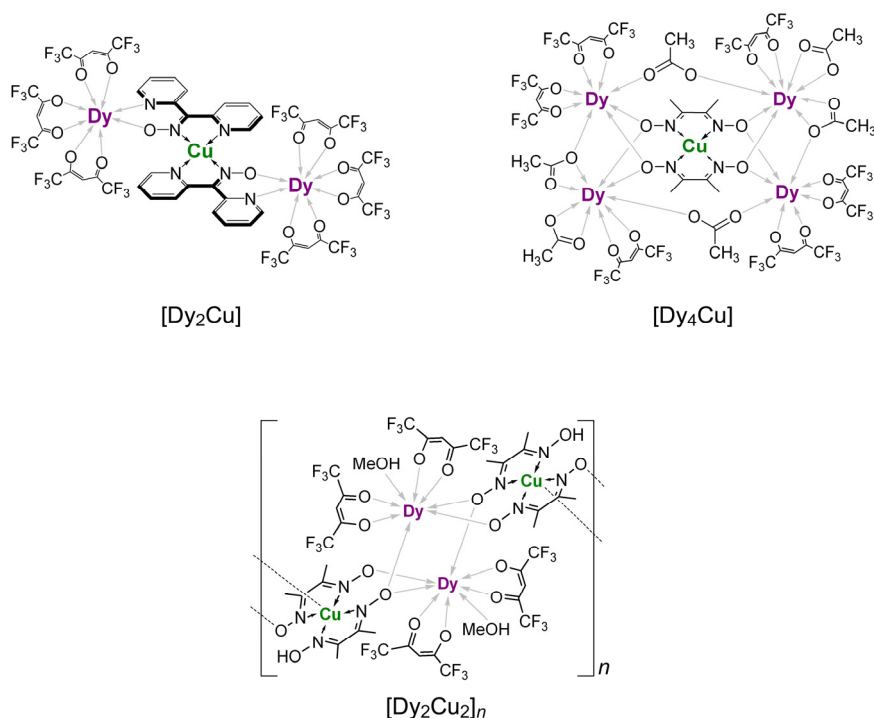
A 4f-3d heterometallic compound $[\{\text{Dy}(\text{hfac})_2(\text{CH}_3\text{OH})\}_2\{\text{Cu}(\text{dmg})(\text{Hdmg})\}_2]_n$ (denoted by $[\text{Dy}_2\text{Cu}_2]_n$) was synthesized. A centrosymmetric diamond-arrayed ferrimagnetic unit involving the oximate bridge, Dy-O-N-Cu, is repeated to form a discrete chain. An onset of the frequency dependence was found in the ac magnetic susceptibility measurements down to 1.8 K. Low-temperature magnetization measurements on $[\text{Dy}_2\text{Cu}_2]_n$ exhibited magnetic hysteresis with magnetization steps. To examine the energy level structure and the exchange coupling between the Dy and Cu ions, HF-EPR spectra of a polycrystalline sample of $[\text{Dy}_2\text{Cu}_2]_n$ were recorded at various frequencies and temperatures. We analyzed the spectra by treating the Dy moments as Ising spins and built an exchange-coupling model for a diamond-arrayed tetranuclear macrocycle $[\text{Dy}_2\text{Cu}_2]$. The Dy-Cu exchange couplings were precisely evaluated, owing to the high resolution of HF-EPR; $J/k_B = -0.895(8)$ and $-0.061(8)$ K for two independent Dy-Cu relations, where the exchange parameter is defined as $-J$. The Cu...Cu coupling among the macrocycles was estimated to be ferromagnetic with approximately 1 K. The present study has established the definitive methodology to examine the energy level in 4f-3d heterometallic systems by using HF-EPR. The magnetic properties of the $[\text{Dy}_2\text{Cu}_2]_n$ chain were plausibly described as a perturbed system of a SMM. The QTM is based on a different principle compared with those of the 3d-based SMMs, since the energy level structure of $[\text{Dy}_2\text{Cu}_2]_n$ is regulated by the exchange couplings.



4.1 Introduction

Low-dimensional coordination compounds with bridging ligands are of increasing interest for development of molecule-based magnets since the discovery of SMMs¹ and related systems such as SCMs.^{2,3} We have employed a strategy using oximate coordination compounds for a nonserendipitous synthesis of oligo-nucleating compounds, since the N–O groups are versatile to bridge in heterometallic systems.^{3,4} Actually, a variety of compounds have been rationally synthesized such as the linear trinuclear $[\text{DyCuDy}]$ complex using dpk^5 and centrosymmetric pentanuclear complex $[\text{Dy}_4\text{Cu}]$ bridged by dmg^{2-} (Scheme 4.1).⁶ Distinct SMM behaviors are found in those compounds, and moreover, the exchange couplings have been evaluated based on an Ising model. Such quantitative analysis is quite rare but an essential ingredient of the systematic research of molecule-based magnets including lanthanide ions. The next direction may be the synthesis of one-dimensional compounds, and in fact much effort has been paid to metal–radical alternating coordination compounds^{2,7,8} and heterometallic chain compounds,^{3,9} for example. We have also applied the dmg -bridging architecture to 4f–3d heterometallic SCMs and have successfully obtained the $[\text{Gd}_2\text{Cu}_2]_n$ ferrimagnetic chain.¹⁰

Scheme 4.1. Structural Formulas of 4f–3d Heterospin System



In this chapter, we report the synthesis and detailed structural characterization of $[\text{Dy}_2\text{Cu}_2]_n$. The results of ac/dc magnetic susceptibility, magnetization, and HF-EPR are presented. The analysis

of EPR is given by using our effective Ising model, and the exchange couplings between Dy and Cu ions are precisely evaluated. This work will certify the generality of the basic idea on the exchange-coupled QTM mechanism originally proposed for $[\text{Dy}_4\text{Cu}]$.⁶

A number of 4f-based SMMs and 4f-3d heterometallic SMMs are known to date, but the magnitude of intramolecular exchange coupling has rarely been determined to our knowledge.^{5,6} In the previous chapter, we applied the measurements by HF-EPR and pulsed-field magnetization to determinate exchange coupling constants on $[\text{Dy}_2\text{Cu}]$ and $[\text{Dy}_2\text{Ni}]$ SMMs. Next, we demonstrated here the magnitude of 4f-3d exchange couplings on $[\text{Dy}_2\text{Cu}_2]_n$. We have established a standard method to evaluate the exchange couplings. Additionally, we can determine 4f-3d exchange couplings by magnetization steps in a pulsed field magnetization curve measurements. However, the exchange coupling constants in this compound are still uncertain because there are two types of exchange paths in the quasi-diamond-arranged motif. To breakthrough this difficulty, we applied a HF-EPR technique.

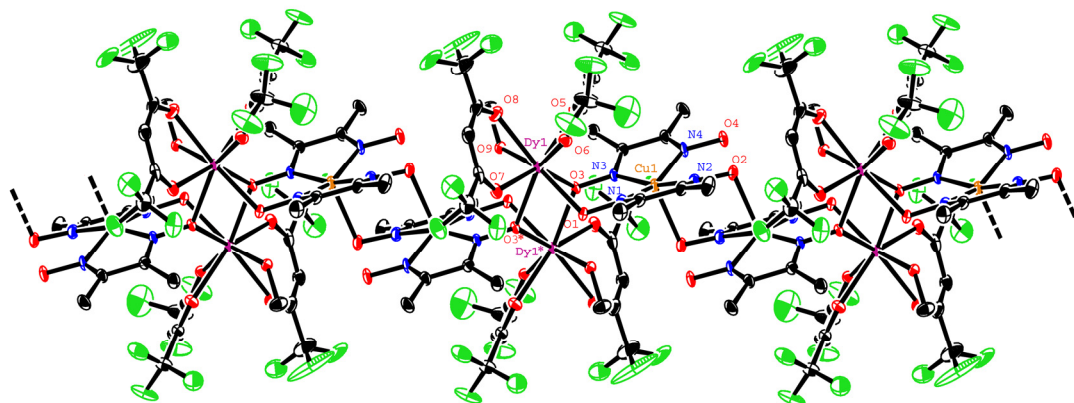


Figure 4.1. Crystal structure of $[\{\text{Dy}(\text{hfac})_2(\text{CH}_3\text{OH})\}_2\{\text{Cu}(\text{dmg})(\text{Hdmg})\}_2]_n$ ($[\text{Dy}_2\text{Cu}_2]_n$) with the thermal ellipsoids at the 50% probability level. Three repeating units are shown. Hydrogen atoms are omitted for clarity. Selected atoms are labeled. The symmetry operation code of * is $2-x, 1-y, -z$.

4.2 Results

4.2.1 Crystal Structure

The molecular and crystal structures of $[\text{Dy}_2\text{Cu}_2]_n$ (Figure 4.1) are practically identical with the known $[\text{Gd}_2\text{Cu}_2]_n$,¹⁰ except for the absence of any crystal solvent molecules. Thus, $[\text{Dy}_2\text{Cu}_2]_n$ is isomorphous to $[\text{Gd}_2\text{Cu}_2]_n$, as supported by the cell parameters (Table 4.1). The complex crystallizes in a $P\bar{1}$ space group. A partially deprotonated $[\text{Cu}(\text{dmg})(\text{Hdmg})]^-$ unit is coordinated to two Dy^{3+} ions through the oximate oxygen atoms, and thus the oximate bridge ($\text{Dy}-\text{O}-\text{N}-\text{Cu}$) is found in every

nearest Dy...Cu geometry. A discrete polymeric chain, constructed with a Cu...Cu linkage, runs along the crystallographic *b* axis. The Dy³⁺ ion is eight-coordinated by oxygen atoms from one MeOH molecule, two bridging oxime groups, and two hfac ligands, forming an approximate *D*_{4d} SAPR coordination sphere with an axial compression. The two SAPR polyhedra are fused with two oxygen atoms (O3 and O3*) shared. The Dy1–O1, Dy–O3, and Dy1*–O3 distances are 2.331(6), 2.427(5), and 2.356(5) Å, respectively. Other Dy–O distances range from 2.313(6) to 2.409(7) Å.

Table 4.1. Selected Crystallographic Data for [Ln₂Cu₂]_n (Ln = Gd and Dy)

compounds	[Gd ₂ Cu ₂] _n	[Dy ₂ Cu ₂] _n
formula	C ₂₀ H ₂₂ CuF ₁₂ GdN ₄ O ₁₀	C ₁₉ H ₁₉ CuDyF ₁₂ N ₄ O ₉
formula weight	927.19	901.43
habit	brown platelet	brown platelet
dimension/mm³	0.30 × 0.30 × 0.25	0.25 × 0.20 × 0.15
<i>T</i>/K	95	118
crystal system	triclinic	triclinic
space group	<i>P</i> $\bar{1}$	<i>P</i> $\bar{1}$
<i>a</i>/Å	10.556(7)	10.5791(9)
<i>b</i>/Å	11.115(9)	11.0987(13)
<i>c</i>/Å	14.15(1)	14.1662(12)
α/°	71.78(6)	71.530(4)
β/°	75.76(6)	75.669(3)
γ/°	84.77(6)	84.702(5)
<i>V</i>/Å³	1527(1)	1528.4(3)
<i>Z</i>	2	2
<i>D</i>_{calc}/g cm⁻³	2.015	1.959
unique data	7005	7318
μ(MoKα)/mm⁻¹	2.983	3.249
<i>R</i> (<i>F</i>)^a (<i>I</i> > 2σ(<i>I</i>))	0.061	0.0615
<i>R</i>_w(<i>F</i>²)^b (all data)	0.106	0.0889
reference	ref. 10	this work

^a $R = \sum ||F_o| - |F_c|| / \sum |F_o|$. ^b $R_w = [\sum w(F_o^2 - F_c^2)^2 / \sum w(F_o^2)^2]^{1/2}$.

The $[\text{Dy}_2\text{Cu}_2]$ unit is centrosymmetric, and another inversion center resides at the middle of the two Cu ions in neighboring units. Dy1 and Cu1 are doubly-bridged with oximate groups (O1–N1 and O3–N3), while Dy1* and Cu1 are singly-bridged with an oximate group (O3–N3). The Dy1⋯Dy1*, Dy1⋯Cu1, and Dy1*⋯Cu1 separations are 3.9945(5), 4.0247(9), and 4.5995(11) Å, respectively. The torsion angles of Dy–O–N–Cu are considerably large ($-62.3(5)$, $56.5(5)$, and $-93.3(6)^\circ$ for Dy1–O1–N1–Cu1, Dy1–O3–N3–Cu1, and Dy1*–O3–N3–Cu1, respectively). The non-planar Dy–O–N–Cu structure is related with the magnetic coupling operative here.^{6,10,25}

The Cu^{2+} ion has a square-pyramidal geometry. The $[\text{Cu}(\text{dmg})(\text{Hdmg})]$ moiety forms a sandwich dimer correlated with an inversion symmetry. The basal plane consists of four nitrogen atoms from dmg or Hdmg ligands with the Cu–N bond lengths of 1.969(7) – 2.005(8) Å. A neighboring oximate oxygen atom is located at the axial position with a longer distance (2.248(5) Å). The magnetic orbital $3d_{x^2-y^2}$ is located on the basal plane, and accordingly the spin-polarized lone-pair of the oxygen atom of a neighboring molecule is located in an orthogonal manner. This structure favors ferromagnetic coupling.²⁶ The Cu1⋯Cu1* separation is 3.8978(14) Å.

To describe the following magnetic properties, we define a repeating unit as a quasi-diamond macrocycle $[\text{CuDy}_2\text{Cu}]$ as shown in the bottom of Scheme 4.1. Intermacrocycle coupling is thus assigned to an interaction between two neighboring Cu ions.

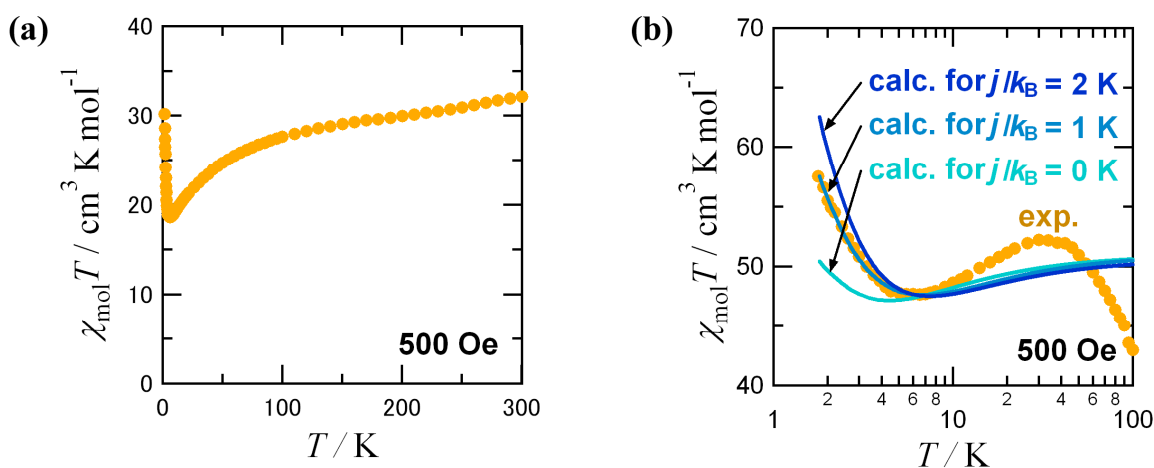


Figure 4.2. Temperature dependence of $\chi_{\text{mol}}T$ for (a) a randomly oriented polycrystalline sample and (b) a field-oriented polycrystalline sample of $[\text{Dy}_2\text{Cu}_2]_n$ at 500 Oe. Orange filled circles: experimental data. Blue solid lines: simulation curves for a dimeric octanuclear model $[\text{CuDy}_2\text{Cu}]_2$ with $J_A/k_B = -0.895$ K, $J_B/k_B = -0.061$ K, and $j/k_B = 0, +1.0, +2.0$ K.

4.2.2 Magnetic Properties

The dc magnetic susceptibility measurement on a randomly oriented polycrystalline specimen of $[\text{Dy}_2\text{Cu}_2]_n$ was investigated down to 1.8 K (Figure 4.2a). At room temperature, the $\chi_{\text{mol}}T$ value of

$32.11 \text{ cm}^3 \text{ K mol}^{-1}$ is close to the calculated value $29.11 \text{ cm}^3 \text{ K mol}^{-1}$ expected for two Cu^{2+} ($0.375 \text{ cm}^3 \text{ K mol}^{-1}$ per a Cu^{2+} ; $S = 1/2$ and $g = 2.0$) plus two Dy^{3+} ions ($14.18 \text{ cm}^3 \text{ K mol}^{-1}$ per a Dy^{3+} ; $S_{\text{Dy}} = 5/2$, $L_{\text{Dy}} = 5$, $J_{\text{Dy}} = 15/2$ and $g_J = 4/3$). Upon cooling, the $\chi_{\text{mol}}T$ value once decreased and turned to increase like the $[\text{Gd}_2\text{Cu}_2]_n$ case.¹⁰ The sharp increase in lower temperatures is due to the ferromagnetic assembly of the large $[\text{Dy}_2\text{Cu}_2]$ moments. We have further investigated the magnetic properties of a field-oriented polycrystalline sample of $[\text{Dy}_2\text{Cu}_2]_n$ (Figure 4.2b). On cooling, the $\chi_{\text{mol}}T$ value once decreased down to 6.5 K, reached a minimum value of $47.6 \text{ cm}^3 \text{ K mol}^{-1}$, and then turned to increase. The $\chi_{\text{mol}}T$ value was $57.5 \text{ cm}^3 \text{ K mol}^{-1}$ at 1.8 K. The upsurge in a low temperature region is similar to that of a randomly oriented specimen, but the present $\chi_{\text{mol}}T$ value is almost twice as large as the randomly oriented data. The magnitude of $\chi_{\text{mol}}T$ indicates that a ground state of the Dy ions is given by the maximal value of $|J| = 15/2$, being well separated from the first excited-state in the $2J+1$ multiplet series.

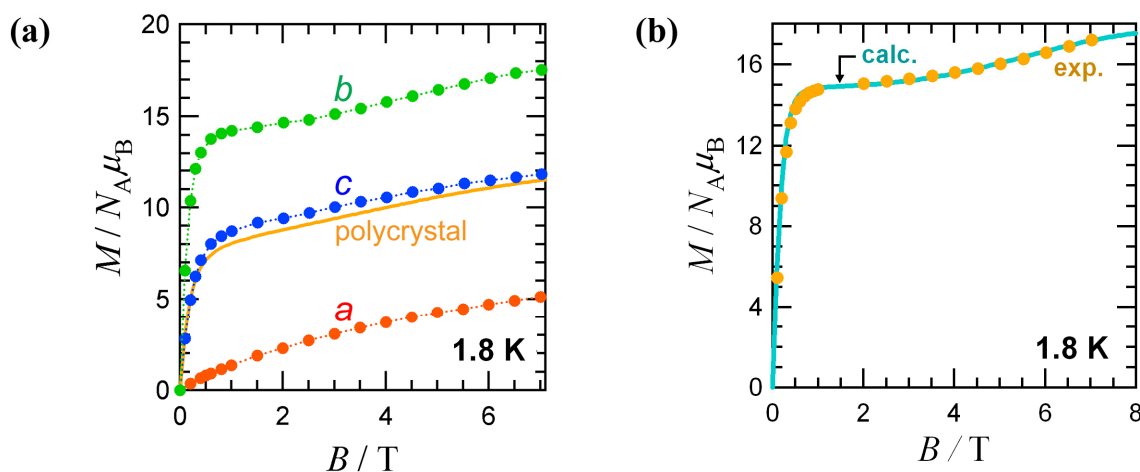


Figure 4.3. (a) Magnetization curves of a randomly oriented polycrystalline sample (orange solid line) and a single crystal specimen of $[\text{Dy}_2\text{Cu}_2]_n$ measured at 1.8 K. The marks *a*, *b*, and *c* indicate the magnetization curves with the applied field parallel to the *a*, *b*, and *c* axes, respectively. Dotted lines are shown for a guide to the eye. (b) Magnetization curves of a field-oriented polycrystalline sample of $[\text{Dy}_2\text{Cu}_2]_n$ measured at 1.8 K (orange filled circles) and calculation curve for a tetranuclear model $[\text{CuDy}_2\text{Cu}]$ (light blue solid line).

The magnetization curves of a randomly oriented polycrystalline specimen of $[\text{Dy}_2\text{Cu}_2]_n$ were recorded at 1.8 K (Figure 4.3a). No hysteresis was observed with usual field-scan rates on a SQUID magnetometer. To clarify the magnetic anisotropy, we measured magnetization curves on a single crystal. The measurements show that the magnetic easy axis is almost parallel to the crystallographic *b* direction. The magnetization along the *b* axis was almost saturated at 7 T, and this value is smaller than a theoretical saturated one from two Dy^{3+} and Cu^{2+} , suggesting that the Dy^{3+} moment lies in a direction between the *b* and *c* axes (the former is arranged closer). The magnetization curve showed

a step in the measurements along the b axis, which can be assigned to the reorientation of the two Cu^{2+} spins. The energy level cross between the ferrimagnetic $[\text{Dy}(\uparrow)_2\text{Cu}(\downarrow)_2]_n$ and the ferromagnetic $[\text{Dy}(\uparrow)_2\text{Cu}(\uparrow)_2]_n$ states occurs here with an aid of the Zeeman energy. The curvature averaged over the a , b , and c axis data was practically identical to that of the polycrystalline data. Furthermore, the magnetization curve on a field-oriented specimen (Figure 4.3b) was also quite similar to that of the b axis data on a single-crystal specimen (Figure 4.3a). The saturation value was as large as $17.7 \mu_B$, which is about 80% of the full saturation of $22 \mu_B$, owing to incomplete field-orientation. When the saturation value is calibrated as $22 \mu_B$, we found that the jump approximately corresponds to $4 \mu_B$. The reversal of one Cu spin gives a $2 \mu_B$ jump, and thus the $4 \mu_B$ step is caused by the simultaneous flip of two Cu ions per a repeating unit.

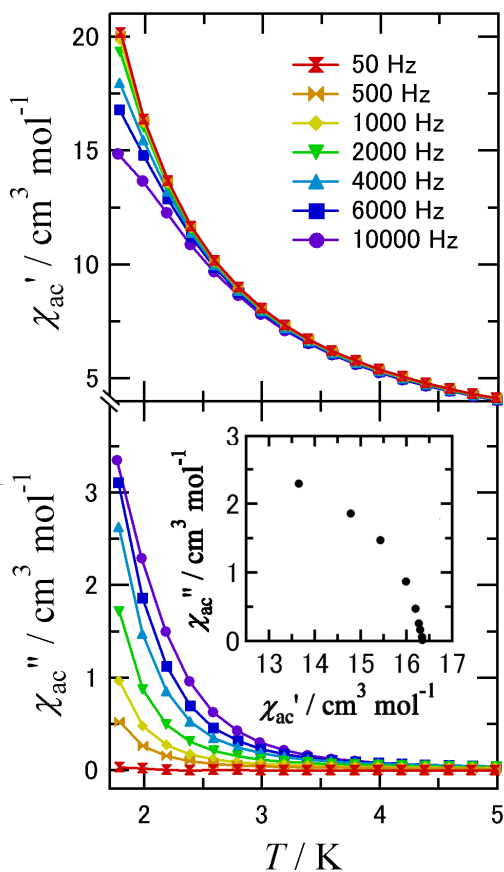


Figure 4.4. ac magnetic susceptibilities (χ'_{ac} and χ''_{ac} for in-phase and out-of-phase parts, respectively) for a randomly oriented polycrystalline sample of $[\text{Dy}_2\text{Cu}_2]_n$. The amplitude of the applied ac magnetic field was 5 Oe. Lines are shown for a guide to the eye. Inset shows the Cole–Cole diagram at 1.8 K.

Ac magnetic susceptibilities, χ'_{ac} and χ''_{ac} for the in-phase and out-of-phase components, respectively, are plotted as a function of temperature and frequency (Figure 4.4). We can observe

frequency-dependence of the ac susceptibilities. With an increase of frequency, a χ_{ac}' decrease and a concomitant χ_{ac}'' increase were clearly observed. We confirmed that the magnetization relaxation became relatively slow, compared with the timescale of these experiments. However, no χ_{ac}'' peak appeared above 1.8 K in our apparatus, and the activation energy of the magnetization reorientation could not be estimated. A Cole–Cole plot²⁷ displayed an only partial semicircle (the inset of Figure 4.4). The activation energy of the magnetization reorientation will be estimated by an appropriate model (see below), instead of the Arrhenius analysis.

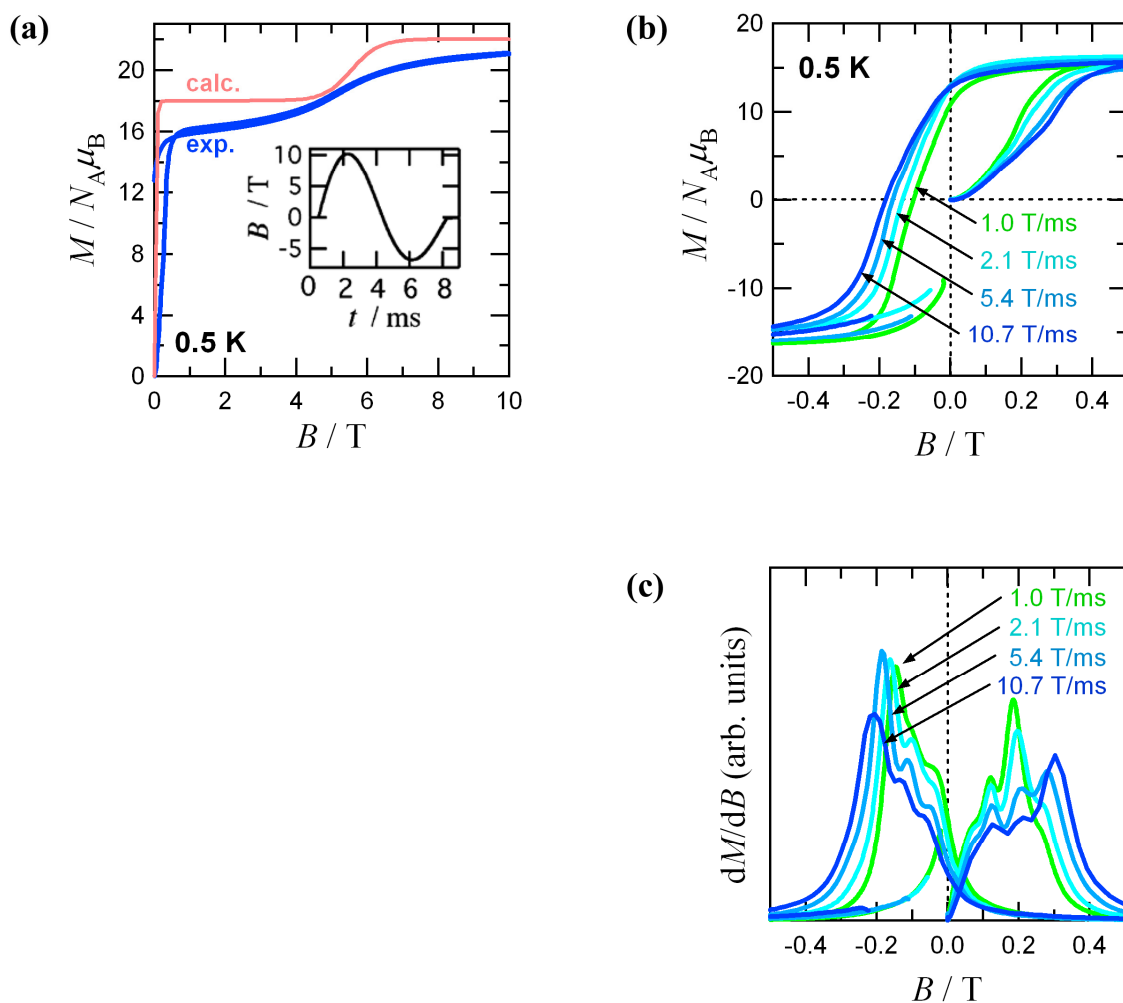


Figure 4.5. (a) Pulsed-field magnetization curve of $[\text{Dy}_2\text{Cu}_2]_n$ measured at 0.5 K (blue solid line). A red solid line represents a simulation curve for a model $[\text{CuDy}_2\text{Cu}]$ at 0.5 K. (b) Hysteresis curve in a low-field region. (c) Differential magnetization curves as a function of a field-sweeping rate measured at 0.5 K.

The pulsed-field technique gave more detailed information on the magnetization process. Figure 4.5a shows a distinct magnetization step at 5.5 T measured on a polycrystalline sample of $[\text{Dy}_2\text{Cu}_2]_n$ at 0.5 K, which is much clearer than that measured at 1.8 K (Figure 4.3b), owing to the

suppression of population on thermally activated states. The magnetization also exhibits a relatively narrow hysteresis within ± 0.4 T (Figure 4.5b). In a small field region, the dM/dB vs. B plot (Figure 4.5c) clarifies mainly four fine magnetization jumps at 0.06, 0.12, 0.19, and 0.26 T at a field scan rate of 1.0 T/ms. This behavior is related with QTM caused by the level crossing among excited states, which is characteristic of SMMs¹ and SCMs.² The positions of two former steps (0.06 and 0.12 T) are independent of the sweep rate. As for the latter (0.19 and 0.26 T), the positions shift as a function of the sweep rate, presumably because of a non-adiabatic effect. It is also found that hysteresis curves are slightly asymmetric; in the negative field each step was shifted with respect to the positive one, indicating the presence of a dipolar-coupling bias that affects the field at which magnetization tunneling takes place. The origin of the magnetization step and the fine structure will be discussed together with the results of EPR experiments.

4.2.3 HF-EPR Spectra

HF-EPR spectra for crystalline samples were collected in a wide frequency range between 34.7 and 525.4 GHz and in the corresponding magnetic field range of 0 – 25 T. Figure 4.6a shows typical EPR spectra recorded at 4.2 K. The spectrum of 117.4 GHz exhibited two intense peaks at 1.2 and 9.9 T. The band position of the former was abnormally shifted to a lower field with an increase of frequency. On the other hand, the latter moved to a higher field, obeying the Zeeman effect. At 305 GHz, only the higher-field peak was found. On decreasing frequency, the two peaks seem to merge around 5.5 T at zero frequency.

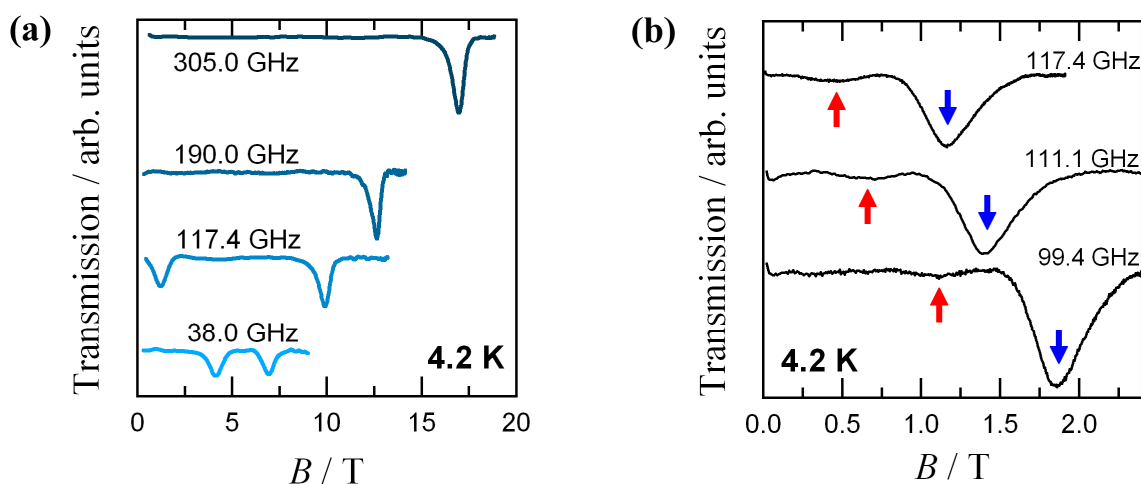


Figure 4.6. (a) Selected HF-EPR spectra of $[\text{Dy}_2\text{Cu}_2]_n$ measured at 4.2 K as a function of frequency. The spectra are offset in a linear scale of the frequency. (b) Expanded HF-EPR spectra at 4.2 K showing a minor absorption band (denoted with red up arrows) together with a major one (blue down arrows).

Figure 4.6b shows an expansion of a low field part of the spectra. We found additional weak absorptions indicated by red arrows in the lower-field side. The intensities of the two major peaks decreased rapidly with elevating temperature, while that of the minor peak was more gradual above 4.2 K. Moreover, the minor peak disappeared at lower temperatures. Those behaviors indicate that the major peaks can be assigned to excitation from the ground state and the minor peak to that from excited states.

The frequency dependence of the absorption positions is summarized in Figure 4.7. The peak positions of the major peaks showed a V-shaped pattern. The minor peak was observed only in a low magnetic field region. From linear fits of the slopes for the major and minor bands, we obtained $g = 1.919(3)$ and $2.07(2)$, respectively. The turning point of the former was $5.56(3)$ T at zero frequency. The g -values are very close to 2, implying that the observed EPR is caused by the reversal of a Cu $S = 1/2$ spin in consistent with a conventional EPR selection rule of $\Delta m_s = \pm 1$. There is no single-ion type anisotropy in Cu spins, and thus the observed characteristic frequency-field relation shows the presence of internal fields on Cu sites mediated by sizable exchange couplings between Dy and Cu ions.

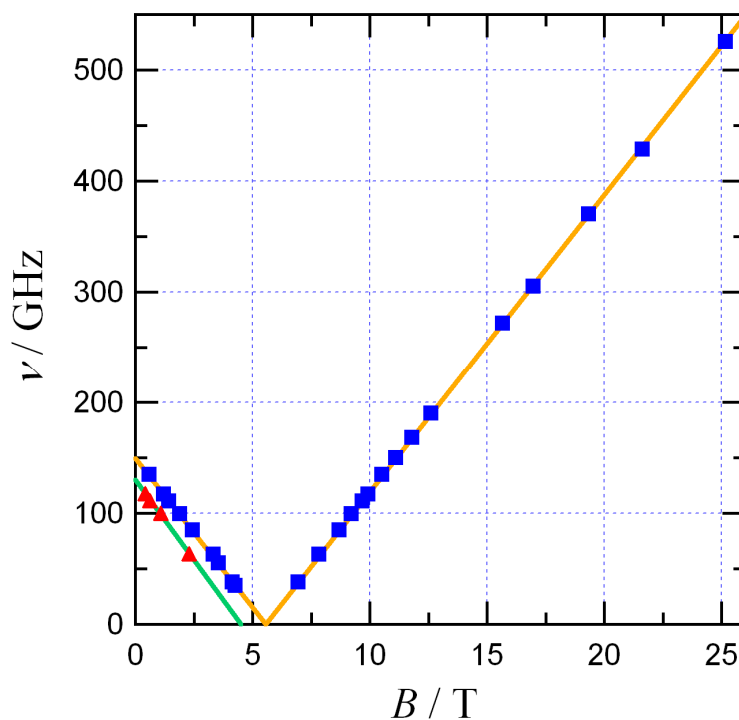


Figure 4.7. Frequency-field diagram of two EPR absorption bands (major, blue filled squares; minor, red filled triangles) observed at 4.2 K for $[\text{Dy}_2\text{Cu}_2]_n$. Solid lines represent the best linear fittings. See the text for the optimized parameters.

We can illustrate an energy level diagram together with exchange couplings by analyzing the EPR data. The intercept of the frequency-field diagram usually corresponds to an energy level crossing. In fact, the magnetization step is found in the magnetization curves (Figures 4.3b and 4.4a for 1.8 and 0.5 K, respectively) at 5.5 T. The critical fields of two independent methods agree well with each other. The HF-EPR experiments have an advantage in precise determination of the position of the energy level crossing.

4.3 Discussion

4.3.1 Magnetic Anisotropy

The single-crystal magnetic study on $[\text{Dy}_2\text{Cu}_2]_n$ (Figure 4.3a) revealed that the magnetic easy-axis lies almost along the chain direction (the crystallographic b axis). Note that the easy-axis direction of the single ion is unique in the crystal, because there are two Dy^{3+} ion in a unit cell and they are related by an inversion symmetry in the space group $P\bar{1}$. We can define the unique Ising axis for the whole system.

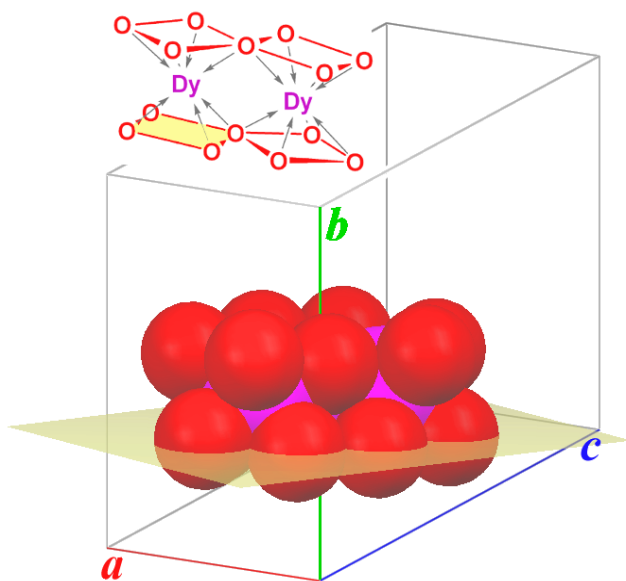


Figure 4.8. Coordination sphere of the oxygen atoms around the Dy ions and mutual direction with respect to the unit cell in the crystal of $[\text{Dy}_2\text{Cu}_2]_n$. A yellow plane represents a basal plane of the SAPR coordination structure defined by O1, O3, O5, and O6.

The saturation behavior of the data parallel to the b axis supports that the easy axis is correctly found in a real crystal. However, a considerable portion of the magnetization parallel to the c axis

was also observed, in contrast to the reports on the uniaxial magnetic anisotropy located just in the chain direction for metal–radical SCMs² and heterometallic SCMs.³ The magnetization easy axis was mapped on the X-ray crystal structure for $[\text{Dy}_2\text{Cu}_2]_n$ to explain the dislocation of the magnetic easy axis of $[\text{Dy}_2\text{Cu}_2]_n$ from the chain direction. The coordination sphere of the Dy^{3+} ion is an axially compressed SAPR structure. Figure 4.8 depicts edge-shared double SAPRs of the Dy_2O_{14} moiety based on the crystallographic analysis. A uniaxial anisotropy has been characterized for the $[\text{Dy}(\text{pc})_2]$ -type SMM having an N_8 compressed SAPR coordination (pc stands for phthalocyanate);¹⁴ the magnetic easy axis coincides the SAPR axial direction. Similarly, in the present compound, the uniaxial anisotropy seems to be related to the SAPR axis, which is inclined from the chain direction (i.e., the b axis direction) to the c direction by ca. 10° . Furthermore, the α angle is $71.530(4)^\circ$ in the triclinic cell (Figure 4.8), and consequently almost a half amount of the Dy^{3+} moments would be detected along the c axis compared with that of the b axis. The experimental results shown in the inset of Figure 4.3a are fully compatible with this picture. The strong uniaxial anisotropy guarantees that each Dy^{3+} moment can be treated as an Ising spin in the following discussion.

4.3.2 Ferrimagnetic Ground State and Exchange Coupling

We can find a magnetization step in Figure 4.5a which corresponds to the Cu spin-flip by $4 \mu_{\text{B}}$, definitely indicating the ground ferrimagnetic state of $[\text{Dy}(\uparrow)_2\text{Cu}(\downarrow)_2]$ for a unit. Very similarly, the corresponding monomeric prototypes $[\{\text{Dy}(\text{hfac})_2(\text{ROH})\}_2\{\text{Cu}(\text{emg})(\text{Hemg})(\text{ROH})\}_2]$ ($\text{R} = \text{CH}_3$ and C_2H_5) have been established to be ground ferrimagnetic compounds as $[\text{Dy}(\uparrow)_2\text{Cu}(\downarrow)_2]$.²⁸ We measured the $\chi_{\text{mol}}T - T$ data and magnetization curves on a field-oriented specimen of $[\text{Dy}_2\text{Cu}_2]_n$. The upturn of the $\chi_{\text{mol}}T$ value observed below 6.5 K (Figure 4.2b) is consistent with the fact that the ground state is ferrimagnetic.

It is not clear whether the Dy–O–Dy bridge transmits a ferromagnetic coupling, but it is reasonably acceptable that two Dy spins with an intervening Cu spin are ferrimagnetically correlated as $\text{Dy}(\uparrow)\text{--Cu}(\downarrow)\text{--Dy}(\uparrow)$. Although there have been several examples showing ferromagnetic coupling of heavier lanthanide ions (including Gd and Dy) with Cu ions, the antiferromagnetic coupling between Dy and Cu ions across the oximate O–N bridge have been discussed^{5,6,10} based on the twisted geometry²⁹ defined by the Dy–O–N–Cu torsion and comparison with the Gd and heavier lanthanide analogs.³⁰ The non-planar Dy–O–N–Cu structures in $[\text{Dy}_2\text{Cu}_2]_n$ favor antiferromagnetic coupling.

On the other hand, the $\text{Cu}\cdots\text{Cu}$ coupling is ferromagnetic according to a superexchange mechanism. Hatfield et al. also reported the ferromagnetic coupling in the synthetic precursor $[\text{Cu}(\text{dmgH})_2]_2$.²⁶ Several dinuclear copper(II) compounds having out-of-plane-bridged structures are known to show ferromagnetic interaction between the two Cu ions.³¹ In the Gd analog, it has been already proved that the $\{\text{Cu}(\text{dmg})_2\}_2$ dimerization gives rise to ferromagnetic coupling therein.¹⁰ Experimentally, the ferromagnetic coupling was confirmed in the initial steep raise of the magnetization as well as the hysteresis loop in the low-temperature magnetization curves. If an

antiferromagnetic coupling was present between Cu ions, a gradual increase of magnetization would be recorded.

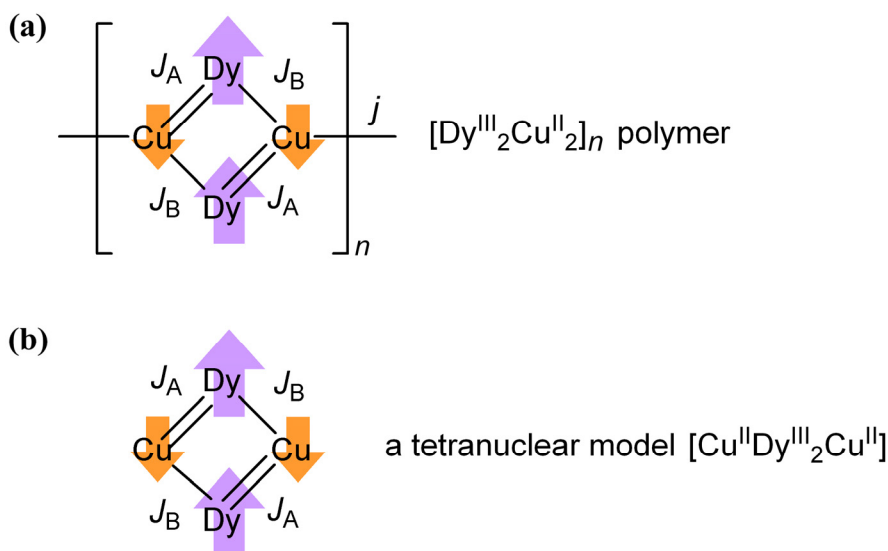


Figure 4.9. (a) Exchange coupling scheme for $[\text{Dy}_2\text{Cu}_2]_n$ polymer. (b) A tetranuclear model $[\text{CuDy}_2\text{Cu}]$.

Each chain is sufficiently isolated in the crystal packing owing to the bulky substituents such as CF_3 . The exchange coupling between 4f metal ions are much smaller than the 4f-3d and 3d-3d interactions.³² We propose models of the exchange couplings in $[\text{Dy}_2\text{Cu}_2]_n$ as shown in Figure 4.9a. Interaction of a diagonal $\text{Cu}\cdots\text{Cu}$ is disregarded from viewing of the long distance. In a tetranuclear model, two exchange couplings between Dy and Cu ions are considered (J_A and J_B), which are crystallographically independent. This magnetic model may be better described as a rectangle rather than a diamond. When the diamond-arrayed units form a chain, an additional coupling j across the $\text{Cu}\cdots\text{Cu}$ linkage should be taken into account. As long as the j is small and ferromagnetic, it gives a shift of the energy of the ferrimagnetic ground state as a whole, but an energy diagram around low-lying states is only slightly modified when infinite systems are constructed.³³ We can easily corroborate it by calculating the energy levels for a finite chain with periodic boundary conditions including two or three units (see below). The spin structure overlaid in Figure 4.9a is qualitatively plausible.

4.3.3 Effective Ising Model

A Dy moment with total $J (= L + S)$ splits into $2J+1$ multiplets owing to the strong anisotropy. If the temperature is sufficiently below the energy separation between the ground state and the excited states in our experiments, the J of each Dy ion can take only the ground state value. It means that the

full Hamiltonian of the system can be reduced to an effective Hamiltonian, in which the J value is fixed to that of the ground state. When the symmetry of the ground state is reasonably high, the ground state may be one of the doublets such as $|\mathcal{F}| = 15/2, 13/2, 11/2$, etc.; in other words, the Dy moment can be treated as an Ising spin. Note that the present experiments were done at low temperatures, and thus this simplification is realistic even if there is some distortion of symmetry. Such Ising models were recently proposed by us in the analysis of 4f-3d heterometallic SMMs, and the exchange couplings have been successfully evaluated.^{5,6} Those models involved only one exchange coupling as an adjustable parameter, but we have to extend the model to include two different exchange couplings in the present work. We propose the following Hamiltonian for the tetranuclear [CuDy₂Cu] unit.

$$\mathcal{H} = -J_A(\hat{J}_2^z \cdot \hat{S}_1 + \hat{J}_3^z \cdot \hat{S}_4) - J_B(\hat{J}_3^z \cdot \hat{S}_1 + \hat{J}_2^z \cdot \hat{S}_4) + \mu_B H^z (g_1 S_1 + g_2 J_2^z + g_3 J_3^z + g_4 S_4) \quad (4.1)$$

Symbols J_2 and J_3 represent the total moments of Dy ions, while S_1 and S_4 the spins of Cu ions. The first and second terms stand for the Ising-type exchange interactions between Dy and Cu ions, where the coupling parameters are defined as $-J_A$ and $-J_B$, and the third term represents the Zeeman interaction. As mentioned previously, it suffices to consider a coupling between a ground doublet state of the Dy ions having the largest $|\mathcal{F}| = 15/2$, being consistent with the fact that Dy³⁺ is a Kramers ion having 4f⁹ electrons. Here the exchange coupling term is an originally isotropic Heisenberg-type formula; however, the resultant energy level in the Hamiltonian is that of the Ising model. The dipolar interactions are disregarded.

One may point out possibility of admixture of \mathcal{F} levels or the ground $|\mathcal{F}|$ value other than $15/2$.³⁴ There are some supports for the ground state of $|\mathcal{F}| = 15/2$. We found the normalized saturation magnetization to be 22 μ_B when the normalization factor was determined from the jump of 4 μ_B for the reversal of two Cu²⁺ spins, although we measured the magnetization mostly with polycrystals. The second point is the g -value close to 2 and the straight frequency-field relation found in the EPR experiments. If the ground state is different from $|\mathcal{F}| = 15/2$, the g value cannot be close to 2. Moreover, admixture of different $|\mathcal{F}|$ values would result in the additional ZFS of the doublet. In this case, the energy level should bend around zero field, but such feature is totally absent in the experiments.

4.3.4 Evaluation of Exchange Parameters

Figure 4.10a shows the energy levels of the [CuDy₂Cu] model calculated on the basis of eq 4.1. Here we use the values $J_A/k_B = -0.895$ K, $J_B/k_B = -0.061$ K, $J_2^z = J_3^z = 15/2$, $S_1 = S_4 = 1/2$, $g_2 = g_3 = g_{Dy} = 4/3$ and $g_1 = g_4 = g_{Cu} = 1.919$ or 2.07. Those parameters are chosen to fit the EPR and magnetization data as we discuss below.

The exchange interaction energy of a neighboring Dy–Cu is defined with $-J(\mathcal{F}\cdot S)$. In the tetranuclear unit, each Dy or Cu moments can point up or down, and consequently the total number of states is $2^4 = 16$. Since the Landé g_J factors for lanthanide ions do not equal to 2, it is a convenient way to use a quantum number M to be equivalent to $g_J J$, i.e., a Dy ion has $10 \mu_B$. Thus, in zero field, the energy of the ground ferrimagnetic $|M^f| = 18 \mu_B$ state ($[\text{Cu}(\downarrow)\text{Dy}(\uparrow)\text{Dy}(\uparrow)\text{Cu}(\downarrow)]$) is lower than that of an $|M^f| = 20 \mu_B$ state ($[\text{Cu}(\uparrow)\text{Dy}(\uparrow)\text{Dy}(\uparrow)\text{Cu}(\downarrow)]$ for example) by $-2(J_A + J_B)\mathcal{F}\cdot S$. Similarly, the energy of an excited ferromagnetic $|M^f| = 22 \mu_B$ state ($[\text{Cu}(\uparrow)\text{Dy}(\uparrow)\text{Dy}(\uparrow)\text{Cu}(\uparrow)]$) is higher than that of an $|M^f| = 20 \mu_B$ state by the same gap. Spin arrangements are schematically drawn by arrows in Figures 4.10a and 4.10b. Each of those states splits to two states owing to the Zeeman effect. Considering the selection rule of EPR ($\Delta m_s = \pm 1$), we can expect the transitions between the states of $M^f = -18$ and $-20 \mu_B$ and between those of $M^f = -20$ and $-22 \mu_B$. Those two transitions show the identical field dependence. Namely, the zero-field offsets of two modes decrease on applying a magnetic field, and become zero at the same field. Therefore, the two EPR signals intrinsically overlap at any frequency, and the levels are crossing at the same position (P_1). On further increasing a magnetic field from P_1 , the energy of the transition increases linearly, being fully consistent with the V-shaped frequency-field relation for the major peaks.

The experiments revealed the energy level cross among the three states ($M^f = -18, -20$ and $-22 \mu_B$) at 5.56(3) T and the g_{Cu} value of 1.919(3), leading to the energy gap $-2(J_A + J_B)\mathcal{F}\cdot S$ of 7.17(4) K. Since three states are separated equally, the determination of the level crossing field tells only the sum of J_A and J_B . We cannot separate J_A and J_B at this stage, even when the results of the magnetic study are combined.

There is another EPR absorption satisfying the selection rule; i.e., transitions from $M^f = 0$ to $-2 \mu_B$ and $M^f = +2$ to $0 \mu_B$. We can deduce that the minor band is attributed to the absorption of these transitions. As shown in Figure 4.10, there are three states at zero field. The zero-field energy of the $|M^f| = 2 \mu_B$ state ($[\text{Cu}(\uparrow)\text{Dy}(\uparrow)\text{Dy}(\downarrow)\text{Cu}(\uparrow)]$ for example) is exactly zero for the cancellation of J_A and J_B , and this state undergoes the Zeeman splitting. In case of the singlet states ($M^f = 0 \mu_B$), the zero-field offsets from the $|M^f| = 2 \mu_B$ level are given by the difference of two exchange couplings as $-2(J_A - J_B)\mathcal{F}\cdot S$. Since the three states are equally spaced at zero field and two transitions show the identical field-dependence. The zero-field offset is calculated to be 6.25(8) K from 4.50(6) T with $g_{\text{Cu}} = 2.07(2)$. From a combination of the equations, $-(15/2)(J_A + J_B)/k_B = 7.17(4)$ K and $-(15/2)(J_A - J_B)/k_B = 6.25(8)$ K, we successfully obtain $J_A/k_B = -0.895(8)$ K and $J_B/k_B = -0.061(8)$ K.

We can assign the minor band to absorptions between the excited states. The intensity ratio of minor/major EPR signals is quantitatively consistent with the estimation by using Boltzman's function. Assuming that the signal intensity is proportional to the Boltzman distribution at each state, we calculated the ratio of the minor/major bands, giving 8.9×10^{-2} , 3.5×10^{-2} , and 4.2×10^{-3} at 4.2 K with the frequencies of 117.4, 111.1, and 99.4 GHz, respectively. The observed ratios were 5.5×10^{-2} , 2.7×10^{-2} and 8.6×10^{-3} (Figure 4.6b), respectively, in agreement with the calculation within an

appreciable error in reading the intensity. Furthermore, with an increase of the field we could not follow the minor band because of the negligible intensity. It is consistent with the Zeeman effect leading to the $M^f = -2, 0, \text{ and } 2 \mu_B$ states much stabilized than the $M^f = -18, -20, \text{ and } -22 \mu_B$ ones in higher fields (Figure 4.10a).

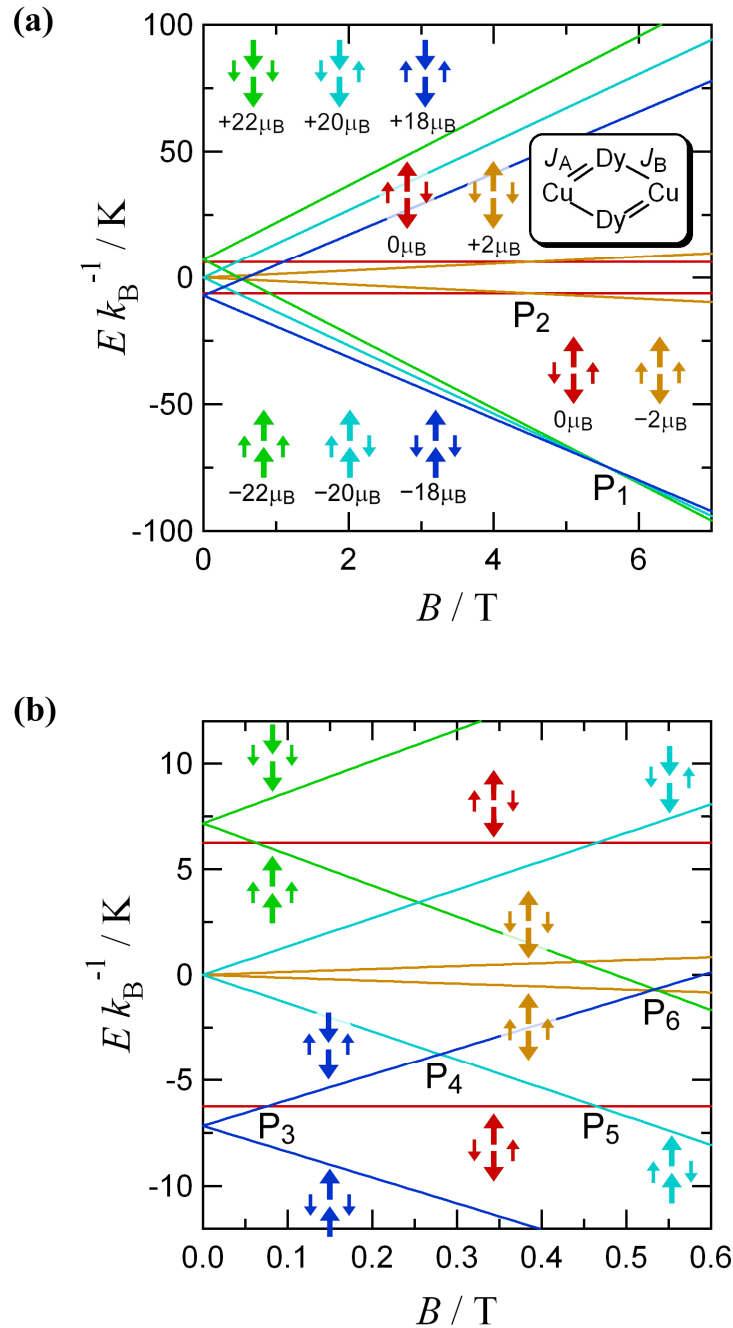


Figure 4.10. (a) Energy levels of tetranuclear model $[\text{CuDy}_2\text{Cu}]$ in a ground-state manifold calculated by the spin Hamiltonian (see the text). (b) Magnification of the plot in a low field region. Spin structures are drawn with arrows (Large and small arrows denote the Dy and Cu moments, respectively). One of the degenerate states is shown; for example, the $M^f = 0$ and $-2 \mu_B$ states are 2-fold degenerate.

These g values are close to 2, supporting the assignment of this absorption to the flip of a Cu^{2+} spin. In detailed discussion, the g value of the minor band (2.07(2)) is somewhat larger than that of the major band (1.919(3)), being consistent with the fact that the former is purely originated from the Cu^{2+} g value when the Dy^{3+} spins are completely cancelled in the corresponding states. The principal axis direction of the Cu^{2+} ion differs from the Dy^{3+} one. Namely, the Dy^{3+} easy axis is approximately parallel to the Cu^{2+} basal plane (Figure 4.1). When the Cu^{2+} spin is exchange-coupled with the Ising Dy^{3+} spins in the states of $M^f = -18, -20$ and $-22 \mu_B$, the g value should be observed as g_{\perp} , which is smaller than g_{\parallel} for typical Cu^{2+} coordination compounds having a magnetic $3d_{x^2-y^2}$ orbital.³⁵ The slightly smaller g value for the major band supports the presence of exchange coupling with adjacent Dy^{3+} ions.

The exchange parameters in the present compound are comparable to those of the previous compounds; -0.64 K for $[\text{Dy}_4\text{Cu}]^6$ and -0.115 K for $[\text{DyCuDy}]^5$. The former has double oximate bridges, while the latter a single oximate bridge. Only from the analysis on the present compound never can we tell a priori which value, J_A or J_B , would be assigned to each crystallographically independent Dy–O–N–Cu relation. However, the negatively larger one (J_A) is likely ascribable to the coupling across double oximate bridges, because of the same order of the J values, and the smaller one (J_B) to the coupling across a single bridge.

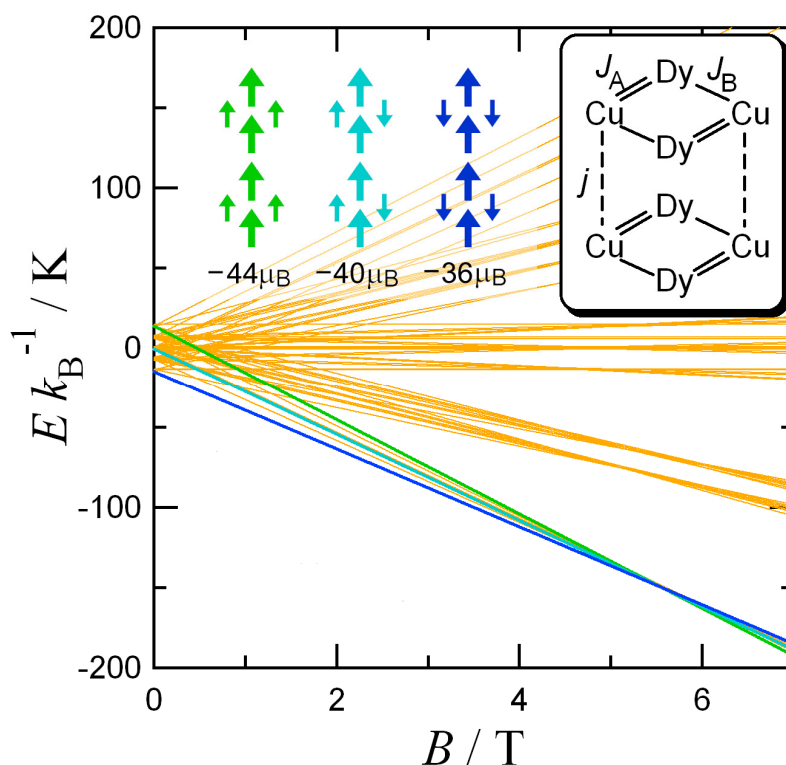


Figure 4.11. Calculated energy levels of an octanuclear model $[\text{CuDy}_2\text{Cu}]_2$. Selected spin structures are drawn with arrows.

We make a brief comment on blocking. As Figure 4.10b shows, the first excited state is located at only 0.92 K higher than the ground state level at zero field. This value can be regarded as a least activation energy for the magnetization reorientation. A possible blocking seems to occur much below 1.8 K (Figure 4.4). The activation energy could not be determined by the Arrhenius analysis from the χ_{ac} data, simply because it is as small as 0.92 K.

4.3.5 Estimation of Inter-macrocycle Interaction

To clarify the magnitude of the inter-macrocycle interaction (j), we proposed here a dimeric octanuclear model [CuDy₂Cu]₂, introducing periodic boundary conditions. Figure 4.11 shows the energy diagram for [CuDy₂Cu]₂ with $J_A/k_B = -0.895$ K, $J_B/k_B = -0.061$ K, and $j/k_B = +1.0$ K. Though there are many levels due to eight doublets, we concentrate on a few low-lying lines, because the observed magnetization is dominantly contributed by low-lying states. The energy structure near the ground state was hardly changed, and the level-crossing field was not shifted (5.56 T). Calculated magnetization curves of [CuDy₂Cu] and [CuDy₂Cu]₂ at 0.5 or 1.8 K were practically identical to each other and reproduced well the experimental curve of [Dy₂Cu₂]_n (Figure 4.5a). It should be noted that, since the calculations on the tetra- and octanuclear models exhibited practically no size effect in the magnetization, extrapolation to an infinite polymer would also give a similar result.

It was rather difficult to determine the magnitude of j solely from the magnetization and EPR analyses. On the other hand, the $\chi_{mol}T$ vs T plot in a lowest temperature region is very sensitive to j , because the ground ferrimagnetic moment remarkably increases with an increase of j . Actually, a simulation work tells us that the larger j value leads to the sharper upsurge of the $\chi_{mol}T$ value around 2 K, as shown by calculated curves for the octanuclear model with $j/k_B = 0, +1$ and $+2$ K (Figure 4.2b). A fit to the experimental $\chi_{mol}T$ value approximately gave $j/k_B = +1.0$ K. The experimental value was somewhat smaller than the calculated curves by a factor of 0.689, because of the incomplete field-orientation. A broad minimum typical of ferrimagnetic chains is found around 6 K. The Ising character of the Dy spins cannot be held at higher temperatures, the easy-axis component of the moments is decreased, and accordingly the $\chi_{mol}T$ value in this direction is deviated downward on heating above ca. 50 K.

There are many examples of dinuclear Cu²⁺ complexes involving out-of-plane oximate bridges which showed ferromagnetic coupling, and the magnitude of the coupling depends on the geometry.³¹ The present value falls in a typical range of the Cu–Cu coupling,^{26,31} indicating that the present simulation is reliable.

4.3.6 Fine Structure in the Magnetization

Finally we will discuss the energy level crosses taking place in a small field region. The magnetization jumps were found in the pulsed-field experiments (Figure 4.5c). The calculated

energy level crossings are shown in Figure 4.10b. Important crossings are: P_3 (0.08 T), P_4 (0.28 T), P_5 (0.46 T), and P_6 (0.53 T). For example, the P_3 crossing leads to an interchange from a $[\text{Cu}(\uparrow)\text{Dy}(\downarrow)\text{Dy}(\downarrow)\text{Cu}(\uparrow)]$ state to a $[\text{Cu}(\downarrow)\text{Dy}(\uparrow)\text{Dy}(\downarrow)\text{Cu}(\uparrow)]$ state with a certain probability. Four dM/dB peaks appeared at 0.06, 0.12, ca. 0.19, and ca. 0.26 T. Some of them depended on the field-sweeping rate. In the adiabatic limit, the peak positions should be independent of the sweeping rate. This dependence on the sweeping rate might be ascribed to the non-adiabatic feature arising from very fast sweeping or mixing of residual thermal relaxation.³⁶ The number of the level crossing points and their positions are not so different from the theoretical prediction. The deviation may be caused by some small perturbation such as inter-macrocycle coupling j or dipolar interaction. On the other hand, the level structure determined by P_1 and P_2 is not affected by such perturbations.

In the present model, level crossings are classified into two regimes. The first group involves those at higher fields such as P_1 and P_2 . The other group includes those at lower fields. This characteristic feature can be regarded as a fingerprint of the Ising-type model for heterometallic molecular magnets including lanthanide ions, in sharp contrast to the nearly equally spaced steps in SMMs such as $[\text{Mn}_{12}]$ ³⁷ and $[\text{Fe}_{10}]$.³⁸ Since the Dy ions bring about very strong magnetic anisotropy and weak exchange couplings, the level crossing fields inform us the magnitude of exchange couplings. On the other hand, the level crosses in 3d-based SMMs are regulated by the ZFS parameter D and not J , because the D values are much smaller than the intramolecular J . We can regard the present Dy-Cu-based magnets, $[\text{Dy}_2\text{Cu}_2]_n$ as well as $[\text{DyCuDy}]$ ⁵ and $[\text{Dy}_4\text{Cu}]$,⁶ as a new class of SMMs and SCMs, whose QTMs are based on a completely different principle.

4.4 Conclusion

The magnetic studies on $[\text{Dy}_2\text{Cu}_2]_n$ clarified the slow magnetization orientation and magnetization steps usually related to a SMM and SCM. We have reported here the precise evaluation of exchange coupling and energy levels by using a HF-EPR technique. The magnitude of J_{4f-3d} has rarely been determined for 4f-3d SMMs. By combining the magnetization and EPR results, we can precisely determine the exchange couplings in $[\text{Dy}_2\text{Cu}_2]_n$. The magnetic behavior of polymer $[\text{Dy}_2\text{Cu}_2]_n$ can be explained as a perturbed system of the monomeric SMM model $[\text{CuDy}_2\text{Cu}]$. The introduction of intermolecular interaction has been discussed for a dimer of the $[\text{Mn}_4]$ -based SMM³⁹ and polymers of the $[\text{Mn}_2\text{Ni}]$ -based SMMs.³⁹ We are now investigating what is the advantage of magnetically correlated SMMs compared with isolated SMMs in the Dy-Cu system.

The mechanism for the magnetization steps is quite different from that of the 3d-based SMMs;¹ the magnetization reorientation occurs through the internal flip of the elemental spins one by one, which finally brings about the reorientation as a whole. To exploit novel SMMs and SCMs showing such QTM, the present synthetic and EPR-analytic methodologies can be applied for isomorphous compounds of $[\text{Dy}_2\text{Cu}_2]_n$ and other Dy-Cu-based SMMs with replacing 4f and 3d metal ions. We believe that this work will lead to further designed magnets and functional magnetic materials.

4.5 Experimental Section

4.5.1 Preparation

Complex $[\text{Dy}_2\text{Cu}_2]_n$ was synthesized by the complexation of $[\text{Dy}(\text{hfac})_3(\text{H}_2\text{O})_2]^{41}$ and partially deprotonated $[\text{Cu}(\text{Hdmg})_2]^{26}$ in methanol/acetone. $[\text{Cu}(\text{Hdmg})_2]$ (15 mg, 0.050 mmol) was dissolved in 1 mL of MeOH containing 0.1 mmol of KOH. An acetone solution (2 mL) of $[\text{Dy}(\text{hfac})_3(\text{H}_2\text{O})_2]$ (107 mg, 0.130 mmol) was slowly added to the above solution. The resultant dark brown solution was allowed to stand at room temperature for a day, to give dark brown prismatic crystals that were collected on a filter, washed with a small amount of MeOH, and dried in air. The yield was 27 mg (0.015 mmol; 60% on the repeating unit basis). The elemental analysis (C, H, N) of the complex on a Fisons EA-1108 by a usual combustion method supported the chemical composition. Anal. Calcd.: C, 25.32; H, 2.12; N, 6.22% for $\text{C}_{19}\text{H}_{19}\text{CuDyF}_{12}\text{N}_4\text{O}_9$. Found: C, 25.05; H, 2.10; N, 6.10%. IR (KBr disc) 486, 586, 661, 741, 800, 964, 1078, 1103, 1147, 1205, 1257, 1491, 1531, 1522, 1655, 3431 cm^{-1} .

4.5.2 X-ray Crystallographic Study

Single-crystal X-ray diffraction data of the specimen were collected on a Rigaku R-Axis RAPID IP and Saturn70 CCD diffractometers with graphite monochromated Mo $K\alpha$ ($\lambda = 0.71069 \text{ \AA}$) radiation and the oscillation scans technique in the range $0 < 2\theta < 56.6^\circ$. The structures were solved by a direct method using the program SIR92⁴² and expanded using Fourier techniques in CRYSTALSTRUCTURE program package.⁴³ Full-matrix least-squares methods were applied using all of the unique data. Numerical absorption correction was used. Non-hydrogen atoms were refined anisotropically, while hydrogen atoms were located at calculated positions and their parameters were refined as “riding”.

4.5.3 Physical Measurements

The dc magnetic susceptibilities of $[\text{Dy}_2\text{Cu}_2]_n$ in a range of 1.8 – 300 K were measured on a Quantum Design SQUID magnetometer (MPMS-7). Polycrystalline samples were suspended in a small amount of mineral oil “Nujol” (Aldrich). Typical sample masses were 20 – 50 mg. The magnetization curves were recorded from -70 to $+70$ kOe. Magnetizations and susceptibilities on randomly oriented polycrystalline specimens were collected after the sample suspension was solidified on cooling without any applied magnetic field. Field-oriented data were obtained after the sample suspension was solidified in the applied field of 7 T. As for single-crystal magnetization measurements, a dark brown prismatic crystal ($0.60 \times 0.33 \times 0.18 \text{ mm}^3$) was fixed with a small amount of vacuum silicon grease.

The ac measurements were obtained on a Quantum Design PPMS ac/dc magnetometer on polycrystalline samples fixed in mineral oil. The ac frequency varied from 50 to 10000 Hz with an amplitude of 5 Oe.

Low-temperature magnetization curves and HF-EPR spectra on $[\text{Dy}_2\text{Cu}_2]_n$ were measured in a manner similar to those of $[\text{Dy}_2\text{Ni}]$ (in Experimental Section of Chapter 3).

References

- (1) (a) Gatteschi, D.; Sessoli, R.; Villain, J. *Molecular Nanomagnets*; Oxford University Press: New York, USA, 2006. (b) Sessoli, R.; Gatteschi, D.; Caneschi, A.; Novak, M.A. *Nature* **1993**, *365*, 141. (c) Gatteschi, D.; Caneschi, A.; Pardi, L.; Sessoli, R. *Science* **1994**, *265*, 1054. (d) Christou, G.; Gatteschi, D.; Hendrickson, D. N.; Sessoli, R. *MRS Bull.* **2000**, *25*, 66. (e) Gatteschi, D.; Sessoli, R. *Angew. Chem., Int. Ed.* **2003**, *42*, 268.
- (2) (a) Caneschi, A.; Gatteschi, D.; Lalioti, N.; Sangregorio, C.; Sessoli, R.; Venturi, G.; Vindigni, A.; Rettori, A.; Pini, M. G.; Novak, M. A. *Angew. Chem., Int. Ed.* **2001**, *40*, 1760. (b) Caneschi, A.; Gatteschi, D.; Lalioti, N.; Sessoli, R.; Sorace, L.; Tangoulis, V.; Vindigni, A. *Chem.–Eur. J.* **2002**, *8*, 286. (c) Caneschi, A.; Gatteschi, D.; Lalioti, N.; Sangregorio, C.; Sessoli, R.; Venturi, G.; Vindigni, A.; Rettori, A.; Pini, M. G.; Novak, M. A. *Europhys. Lett.* **2002**, *58*, 771.
- (3) Clérac, R.; Miyasaka, H.; Yamashita, M.; Coulon, C. *J. Am. Chem. Soc.* **2002**, *124*, 12837.
- (4) Lloret, F.; Ruiz, R.; Cervera, B.; Castro, I.; Julve, M.; Faus, J.; Real, J. A.; Sapiña, F.; Journaux, Y.; Colin, J. C.; Verdaguer, M. *J. Chem. Soc., Chem. Commun.* **1994**, 2615.
- (5) Mori, F.; Nyui, T.; Ishida, T.; Nogami, T.; Choi, K.-Y.; Nojiri, H. *J. Am. Chem. Soc.* **2006**, *128*, 1440.
- (6) Ueki, S.; Ishida, T.; Nogami, T.; Choi, K.-Y.; Nojiri, H. *Chem. Phys. Lett.* **2007**, *440*, 263.
- (7) Miyasaka, H.; Madanbashi, T.; Sugimoto, K.; Nakazawa, Y.; Wernsdorfer, W.; Sugiura, K.-I.; Yamashita, M.; Coulon, C.; Clérac, R. *Chem.–Eur. J.* **2006**, *12*, 7028.
- (8) (a) Ishii, N.; Ishida, T.; Nogami, T. *Inorg. Chem.* **2006**, *45*, 3837. (b) Ishii, N.; Okamura, Y.; Chiba, S.; Nogami, T.; Ishida, T. *J. Am. Chem. Soc.* **2008**, *130*, 24.
- (9) (a) Prado, E.; Ruiz-García, R.; Lloret, F.; Faus, J.; Julve, M.; Journaux, Y.; Delgado, F.; Ruiz-Pérez, C. *Adv. Mater.* **2004**, *16*, 1597. (b) Prado, E.; Ruiz-García, R.; Lloret, F.; Faus, J.; Julve, M.; Journaux, Y.; Novak, M. A.; Delgado, F. S.; Ruiz-Pérez, C. *Chem.–Eur. J.* **2007**, *13*, 2054. (c) Toma, L. M.; Lescouëzec, R.; Pasán, J.; Ruiz-Pérez, C.; Vaissermann, J.; Cano, J.; Carrasco, R.; Wernsdorfer, W.; Lloret, F.; Julve, M. *J. Am. Chem. Soc.* **2006**, *128*, 4842.
- (10) Ueki, S.; Kobayashi, Y.; Ishida, T.; Nogami, T. *Chem. Commun.* **2005**, 5223.
- (11) (a) Osa, S.; Kido, T.; Matsumoto, N.; Re, N.; Pochaba, A.; Mrozinski, J. *J. Am. Chem. Soc.* **2004**, *126*, 420. (b) Hamamatsu, T.; Yabe, K.; Towatari, M.; Osa, S.; Matsumoto, N.; Re, N.; Pochaba, A.; Mrozinski, J.; Gallani, J.-L.; Barla, A.; Imperia, P.; Paulsen, C.; Kappler, J.-P. *Inorg. Chem.* **2007**, *46*, 4458.
- (12) (a) Zaleski, C. M.; Depperman, E. C.; Kampf, J. W.; Kirk, M. L.; Pecoraro, V. L. *Angew. Chem., Int. Ed.* **2004**, *43*, 3912. (b) Zaleski, C. M.; Depperman, E. C.; Kampf, J. W.; Kirk, M. L.; Pecoraro, V. L. *Inorg. Chem.* **2006**, *45*, 10022. (c) Zaleski, C. M.; Kampf, J. W.; Mallah, T.; Kirk, M. L.; Pecoraro, V. L. *Inorg. Chem.* **2007**, *46*, 1954.
- (13) (a) Mishra, A.; Wernsdorfer, W.; Abboud, K. A.; Christou, G. *J. Am. Chem. Soc.* **2004**, *126*, 15648. (b) Mishra, A.; Wernsdorfer, W.; Parsons, S.; Christou, G.; Brechin, E. K. *Chem.*

- Commun.* **2005**, 2086. (c) Murugesu, M.; Mishra, A.; Wernsdorfer, W.; Abboud, K. A.; Christou, G. *Polyhedron* **2006**, *25*, 613. (d) Mishra, A.; Tasiopoulos, A. J.; Wernsdorfer, W.; Abboud, K. A.; Christou, G. *Inorg. Chem.* **2007**, *46*, 3105.
- (14) (a) Ishikawa, N.; Sugita, M.; Ishikawa, T.; Koshihara, S.-Y.; Kaizu, Y. *J. Am. Chem. Soc.* **2003**, *125*, 8694. (b) Ishikawa, N.; Sugita, M.; Tanaka, N.; Ishikawa, T.; Koshihara, S.-Y.; Kaizu, Y. *Inorg. Chem.* **2004**, *43*, 5498. (c) Ishikawa, N.; Sugita, M.; Wernsdorfer, W. *J. Am. Chem. Soc.* **2005**, *127*, 3650.
- (15) (a) Costes, J. P.; Dahan, F.; Wernsdorfer, W. *Inorg. Chem.* **2006**, *45*, 5. (b) Costes, J. P.; Auchel, M.; Dahan, F.; Peyrou, V.; Shova, S.; Wernsdorfer, W. *Inorg. Chem.* **2006**, *45*, 1924.
- (16) Tang, J.; Hewitt, I.; Madhu, N. T.; Chastanet, G.; Wernsdorfer, W.; Ansen, C. E.; Benelli, C.; Sessoli, R.; Powell, A. K. *Angew. Chem., Int. Ed.* **2006**, *45*, 1729.
- (17) (a) Bogani, L.; Sangregorio, C.; Sessoli, R.; Gatteschi, D. *Angew. Chem., Int. Ed.* **2005**, *44*, 5817. (b) Bernot, K.; Bogani, L.; Caneschi, A.; Gatteschi, D.; Sessoli, R. *J. Am. Chem. Soc.* **2006**, *128*, 7947.
- (18) (a) Aronica, C.; Pilet, G.; Chastanet, G.; Wernsdorfer, W.; Jacquot, J.-F.; Luneau, D. *Angew. Chem., Int. Ed.* **2006**, *45*, 4659. (b) Aronica, C.; Chastanet, G.; Pilet, G.; Le Guennic, B.; Robert, V.; Wernsdorfer, W.; Luneau, D. *Inorg. Chem.* **2007**, *46*, 6108.
- (19) He, F.; Tong, M.-L.; Chen, X.-M. *Inorg. Chem.* **2005**, *44*, 8285.
- (20) (a) Mori, F.; Ishida, T.; Nogami, T. *Polyhedron* **2005**, *24*, 2588. (b) Ueki, S.; Sahlan, M.; Ishida, T.; Nogami, T. *Synth. Met.* **2005**, *154*, 217.
- (21) Ueki, S.; Ishida, T.; Nogami, T.; Tamura, M. *Mol. Cryst. Liq. Cryst.* **2006**, *455*, 129.
- (22) Ferbinteanu, M.; Kajiwara, T.; Choi, K.-Y.; Nojiri, H.; Nakamoto, A.; Kojima, N.; Cimpoesu, F.; Fujimura, Y.; Takaishi, S.; Yamashita, M. *J. Am. Chem. Soc.* **2006**, *128*, 9008.
- (23) Pointillart, F.; Bernot, K.; Sessoli, R.; Gatteschi, D. *Chem.-Eur. J.* **2007**, *13*, 1602.
- (24) Chandrasekhar, V.; Pandian, B. M.; Azhakar, R.; Vittal, J. J.; Clérac, R. *Inorg. Chem.* **2007**, *46*, 5140.
- (25) Kobayashi, Y.; Ueki, S.; Ishida, T.; Nogami, T. *Chem. Phys. Lett.* **2003**, *378*, 337.
- (26) Villa, J. F.; Hatfield, W. E. *J. Chem. Phys.* **1971**, *55*, 4758.
- (27) Cole, K. S.; Cole, H. R. *J. Chem. Phys.* **1941**, *9*, 341.
- (28) Ueki, S.; Okazawa, A.; Ishida, T.; Nogami, T.; Nojiri, H. *Polyhedron* **2007**, *26*, 1970.
- (29) (a) Costes, J.-P.; Dahan, F.; Dupuis, A.; Laurent, J.-P. *Inorg. Chem.* **2000**, *39*, 169. (b) Costes, J.-P.; Dahan, F.; Dupuis, A. *Inorg. Chem.* **2000**, *39*, 5994.
- (30) Kahn, M. L.; Mathoniere, C.; Kahn, O. *Inorg. Chem.* **1999**, *38*, 3692.
- (31) Cervera, B.; Ruiz, R.; Lloret, F.; Julve, M.; Cano, J.; Faus, J.; Bois, C.; Mrozinski, J. *J. Chem. Soc., Dalton Trans.* **1997**, 395.
- (32) Panagiotopoulos, A.; Zafirooulos, T. F.; Perlepes, S. P.; Bakalbassis, E.; Masson-Ramade, I.; Kahn, O.; Terzis, A.; Raptopoulou, C. P. *Inorg. Chem.* **1995**, *34*, 4918.

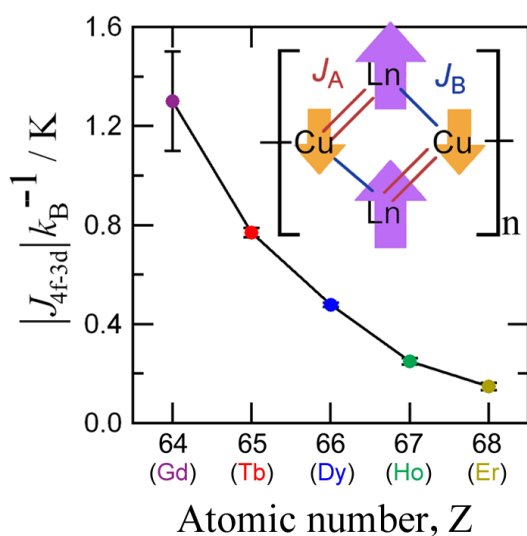
- (33) Oshima, Y.; Nojiri, H.; Asakura, K.; Sakai, T.; Yamashita, M.; Miyasaka, H. *Phys. Rev. B* **2006**, *73*, 214435.
- (34) Sugita, M.; Ishikawa, N.; Ishikawa, T.; Koshihara, S.-Y.; Kaizu, Y. *Inorg. Chem.* **2006**, *45*, 1299.
- (35) (a) ShklyaeV, A. A.; Anufrienko, V. F.; Ogorodnikov, V. D. *Zh. Strukt. Khim.* **1973**, *14*, 994. (b) Hathaway, B. J.; Tomlinson, A. A. G. *Coord. Chem. Rev.* **1970**, *5*, 1.
- (36) (a) Landau, L. *Phys. Z. Sowjetunion* **1932**, *2*, 46. (b) Zener, C. *Proc. R. Soc. London, Ser. A* **1932**, *137*, 696. (c) Stukelberg, E. C. G. *Helv. Phys. Acta* **1932**, *5*, 369.
- (37) Thomas, L.; Lionti, F.; Ballou, R.; Gatteschi, D.; Sessoli, R.; Barbara, B. *Nature* **1996**, *383*, 145.
- (38) Wernsdorfer, W.; Ohm, T.; Sangregorio, C.; Sessoli, R.; Mailly, D.; Paulsen, C. *Phys. Rev. Lett.* **1999**, *82*, 3903.
- (39) Wernsdorfer, W.; Aliaga-Alcalde, N.; Hendrickson, D. N.; Christou, G. *Nature* **2002**, *416*, 406.
- (40) (a) Ferbinteanu, M.; Miyasaka, H.; Wernsdorfer, W.; Nakata, K.; Sugiura, K.; Yamashita, M.; Coulon, C.; Clérac, R. *J. Am. Chem. Soc.* **2005**, *127*, 3090. (b) Miyasaka, H.; Nezu, T.; Sugimoto, K.; Sugiura, K.; Yamashita, M.; Clérac, R. *Chem.–Eur. J.* **2005**, *11*, 1592.
- (41) Richardson, M. F.; Wagner, W. F.; Sands, D. E. *J. Inorg. Nucl. Chem.* **1968**, *30*, 1275.
- (42) Altomare, A.; Cascarano, G.; Giacovazzo, C.; Guagliardi, A.; Burla, M.; Polidori, G.; Camalli, M. *J. Appl. Crystallogr.* **1994**, *27*, 435.
- (43) CRYSTALSTRUCTURE, *Crystal Structure Analysis Package*, version 3.8; Rigaku/MS: The Woodlands, TX, USA, 2000–2006.

Chapter 5

Exchange Couplings of 4f-3d Heterometallic Chain $[\text{Ln}_2\text{Cu}_2]_n$ Compounds Evaluated by High-Frequency Electron Paramagnetic Resonance

Abstract

Heterometallic polymeric coordination compounds $[\text{Ln}_2\text{Cu}_2]_n$ ($\text{Ln} = \text{Tb}, \text{Ho}, \text{and Er}$) were synthesized, and the X-ray crystallographic analysis shows that their structures are isomorphous to those of the known ferrimagnetic $[\text{Gd}_2\text{Cu}_2]_n$ and $[\text{Dy}_2\text{Cu}_2]_n$ analogs. The exchange couplings in $[\text{Tb}_2\text{Cu}_2]_n$, $[\text{Ho}_2\text{Cu}_2]_n$, and $[\text{Er}_2\text{Cu}_2]_n$ were precisely evaluated by HF-EPR and pulsed-field magnetization studies, giving $J_{\text{Tb-Cu}}/k_{\text{B}} = -0.77(2)$ K, $J_{\text{Ho-Cu}}/k_{\text{B}} = -0.250(12)$ K, and $J_{\text{Er-Cu}}/k_{\text{B}} = -0.149(15)$ K. They were comparable to those of the Gd and Dy analogues. The absolute value of the exchange coupling parameter monotonically decreases in the order of Gd, Tb, Dy, Ho, and Er.



5.1 Introduction

SMMs exhibit magnetic hysteresis from the single-molecular origin;¹ namely, extremely slow magnetization reversal due to a high energy-barrier. Lanthanide ions seem suitable for development of SMMs, since the barrier is caused by strong magnetic anisotropy and large spins.² Several Dy–Cu compounds showed slow magnetization reversal and distinct hysteresis, as clarified by ac susceptibility and pulsed-field magnetization measurements.^{3–8} We have investigated the exchange couplings and energy-level structures of them^{3–5} by means of HF-EPR⁹ together with pulsed-field magnetization.¹⁰

In Chapter 4, we reported the HF-EPR study on a 4f–3d heterometallic chain compound [Dy₂Cu₂]_n.¹¹ The crystallographic analysis was satisfactorily performed to show the isomorphous structure to [Gd₂Cu₂]_n. The energy-level crossing and QTM were described in terms of the well-defined Dy–Cu exchange couplings. Though the structure is infinitely one-dimensional, the magnetism was interpreted as a SMM with slight perturbation due to the one-dimensionally arrayed structure. In this chapter, we will report the characterization of various isomorphous [Ln₂Cu₂]_n complexes and their magnetic properties, where Ln is Tb, Ho, and Er. Comparison of the exchange interactions between the 4f- and 3d-spins (J_{4f-3d}) is of great interest. One of the advantages of HF-EPR is the ability of precise determination of J_{4f-3d} owing to the extremely high resolution and variable-frequency technique.¹²

5.2 Results

Complexes [Tb₂Cu₂]_n, [Ho₂Cu₂]_n, and [Er₂Cu₂]_n (for the molecular structures, see Figure 5.1) were prepared according to the similar method (see Chapter 4) using the corresponding Ln salt as a starting material in place of the Dy one. They crystallized in a triclinic $P\bar{1}$ space group. Their molecular structures are isomorphous to each other and also to those of [Dy₂Cu₂]_n (Table 4.1 in Chapter 4) and [Gd₂Cu₂]_n.¹¹ Selected crystallographic parameters of [Tb₂Cu₂]_n, [Ho₂Cu₂]_n, and [Er₂Cu₂]_n are listed in Table 5.1. Figure 5.1 shows the ORTEP drawing of [Tb₂Cu₂]_n for an instance. The tetranuclear unit was a diamond-arrayed Tb₂Cu₂ and the symmetrical inversion center is located in the center of a diamond; a half of a diamond is crystallographically independent. There are two Tb–Cu relations. The Tb ion has a SAPR structure with eight oxygen atoms coordinated. Inter-unit coupling is very weak along the elongated axial O··Cu bond in a square-pyramid coordination sphere of the Cu ion. A chain runs in the crystallographic *b* direction. No appreciable interchain interaction was found, and accordingly the chains are magnetically isolated.

Ac magnetic susceptibilities, χ_{ac}' and χ_{ac}'' for the in-phase and out-of-phase components, respectively, are plotted as a function of temperature and frequency for [Tb₂Cu₂]_n, [Ho₂Cu₂]_n, and [Er₂Cu₂]_n. We observed practically no frequency dependence of the ac susceptibilities above $T = 2.0$ K and up to $f = 10$ kHz. SMM behavior could not be observed in our ordinary apparatuses, and therefore further research work requires temperatures below 2 K to investigate SMM behavior. On the other hand, research on J_{4f-3d} can afford fruitful results at the present stage without observation of SMM behavior. We focus our attention on determination of J_{4f-3d} 's and their comparison among the analogs. Magnetic study below 2 K is not necessarily required, but we measured the pulsed-field magnetization curves at 0.5 K, because the experiments at lower temperatures could exhibit better step-shaped magnetization curves.

The pulse-field magnetization measurements on a polycrystalline specimen of [Tb₂Cu₂]_n were collected at 0.5 K (Figure 5.2a). The saturation magnetization (M_s) of 15.7 μ_B at 10 T was close to the calculated value 17 μ_B with $|\mathcal{J}| = 5$ and $g_J = 3/2$, and did not reach the calculated one with maximal

$|\mathcal{F}| = 6$. A parallel study on the same specimen using a SQUID magnetometer supported this result. This finding indicates that a ground state of the Tb ions may be given by the value of $|\mathcal{F}| = 5$. The field-oriented data were usually obtained in these measurements (see Experimental section), but the M_s value may not be a full-saturation value because of incomplete orientation.

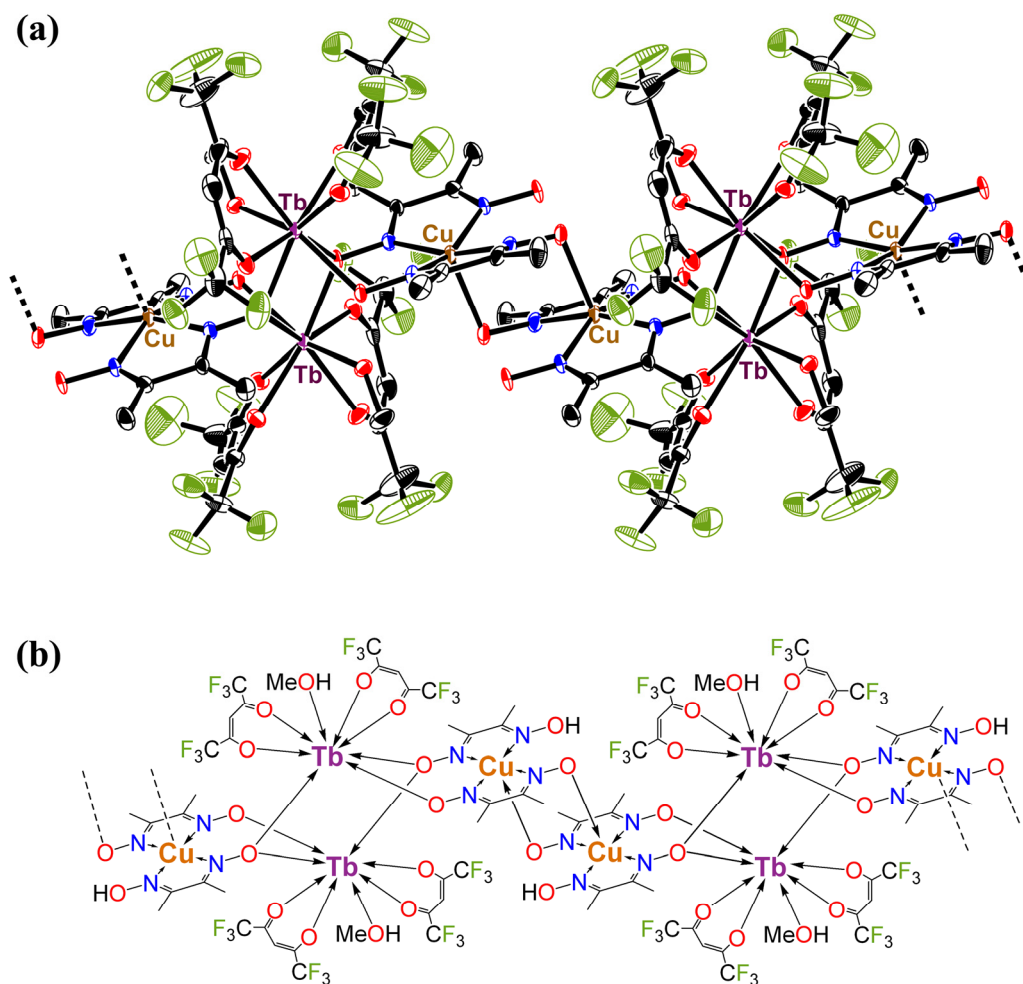


Figure 5.1. Crystal structure of $[\text{Tb}_2\text{Cu}_2]_n$ with the thermal ellipsoids at the 50% probability level. Two repeating units are shown. Hydrogen atoms are omitted for clarity. (b) Structure formula of $[\text{Tb}_2\text{Cu}_2]_n$. Note that Gd, Dy, Ho, and Er derivatives exhibited an isomorphous structure.

The differentiated magnetization curve on $[\text{Tb}_2\text{Cu}_2]_n$ is shown in the bottom of Figure 5.2a, clarifying that the magnetic field at the dM/dB peak is 5.6 T. The gap of the jump corresponds to $4 \mu_B$ from two copper spins. Consequently, the jump is ascribable to the transition from the ground ferrimagnetic state ($[\text{Tb}(\uparrow)_2\text{Cu}(\downarrow)_2]_n$) to the ferromagnetic one ($[\text{Tb}(\uparrow)_2\text{Cu}(\uparrow)_2]_n$). In other words, the energy-level crossing takes place around 5.6 T in a Zeeman picture.

Table 5.1. Selected Crystallographic Data for [Ln₂Cu₂]_n (Ln = Tb, Ho, and Er)

compounds	[Tb ₂ Cu ₂] _n	[Ho ₂ Cu ₂] _n	[Er ₂ Cu ₂] _n
formula	C ₁₉ H ₁₉ CuF ₁₂ N ₄ O ₉ Tb	C ₁₉ H ₁₉ CuF ₁₂ HoN ₄ O ₉	C ₁₉ H ₁₉ CuErF ₁₂ N ₄ O ₉
formula weight	897.83	903.84	906.17
habit	brown platelet	brown prism	brown prism
dimension/mm³	0.08 × 0.07 × 0.03	0.05 × 0.04 × 0.03	0.04 × 0.04 × 0.03
T/K	110	100	90
crystal system	triclinic	triclinic	triclinic
space group	<i>P</i> $\bar{1}$	<i>P</i> $\bar{1}$	<i>P</i> $\bar{1}$
<i>a</i>/Å	10.537(5)	10.528(13)	10.517(12)
<i>b</i>/Å	11.087(3)	11.048(8)	11.059(6)
<i>c</i>/Å	14.151(10)	14.161(14)	14.130(4)
α°	71.65(5)	71.57(10)	71.55(7)
β°	75.87(5)	75.57(10)	75.47(7)
γ°	85.20(6)	84.85(11)	84.75(8)
<i>V</i>/Å³	1521.7(14)	1513(3)	1509(2)
<i>Z</i>	2	2	2
<i>D</i>_{calc}/g cm⁻³	1.959	1.984	1.994
unique data	6900	6855	6845
μ(MoKα)/mm⁻¹	3.123	3.426	3.857
<i>R</i> (<i>F</i>)^a (<i>I</i> > 2σ(<i>I</i>))	0.0414	0.0513	0.0602
<i>R</i>_w(<i>F</i>²)^b (all data)	0.0613	0.0844	0.0802

^a $R = \sum ||F_o| - ||F_c|| / \sum |F_o|$. ^b $R_w = [\sum w(F_o^2 - F_c^2)^2 / \sum w(F_o^2)^2]^{1/2}$.

Similarly, the pulsed-field magnetization measurements on a polycrystalline specimen of [Ho₂Cu₂]_n were collected at 0.5 K (Figure 5.2c). The *M*_s value 13.8 μ_B at 15 T, which did not reach the calculated value 22 μ_B with maximal $|J^f| = 8$ and $g_J = 5/4$. Assuming that the observed *M*_s is intrinsic, the ground state of the Ho ions would have a smaller moment such as $|J^f| = 6$ (the calculated *M*_s value 17 μ_B) or 5 (14.5 μ_B). The magnetic field at the d*M*/d*B* peak is 2.5 T (the bottom of Figure 5.2c). The energy-level crossing between the ferrimagnetic ([Ho(\uparrow)₂Cu(\downarrow)₂]_n) and ferromagnetic ([Ho(\uparrow)₂Cu(\uparrow)₂]_n) states occurs around 2.5 T.

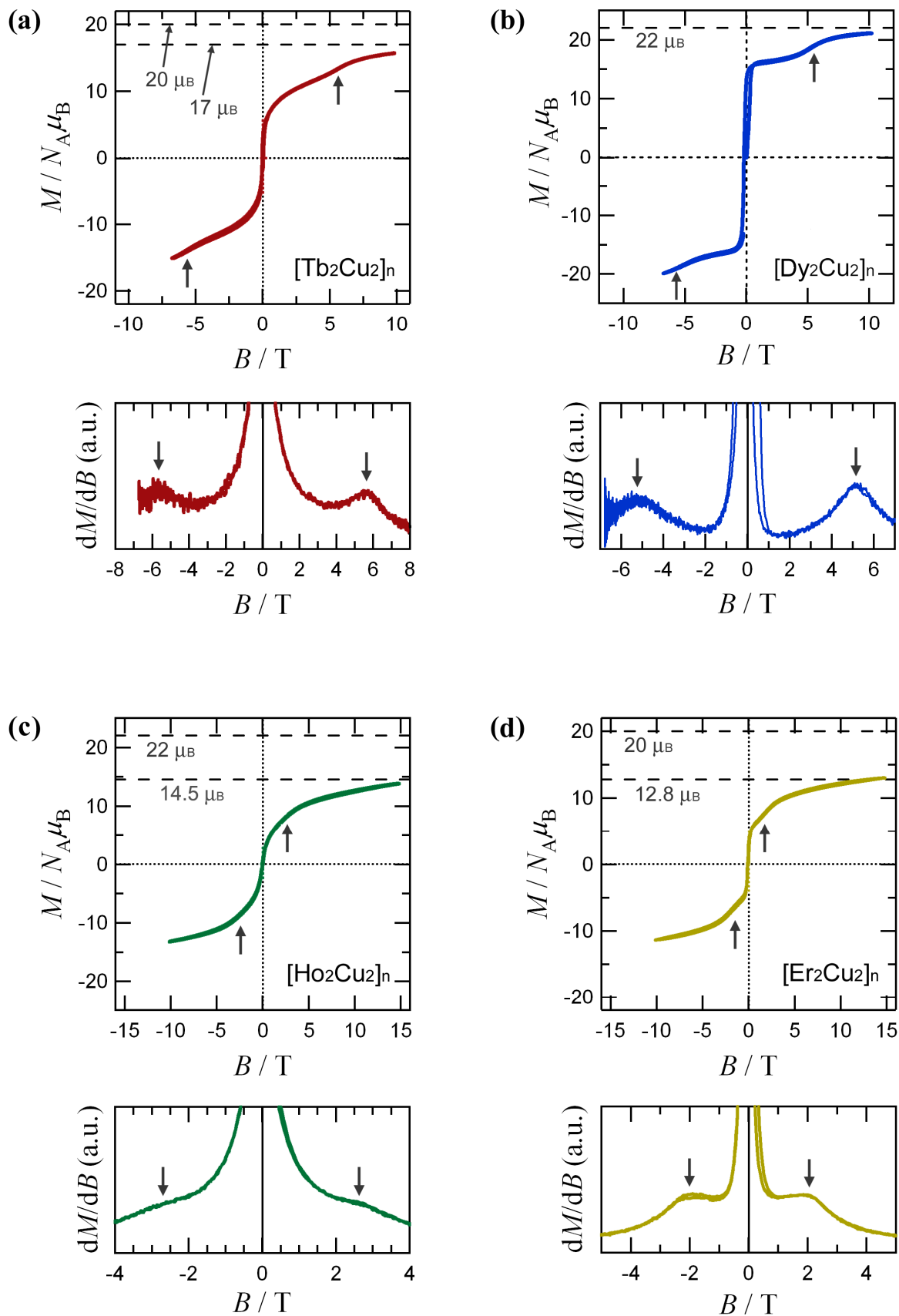


Figure 5.2. Magnetization curves for measured at 0.5 K, where Ln = (a) Tb, (b) Dy, (c) Ho, and (d) Er. Derivative curves are also shown in the bottom figure. The arrows show the positions of the magnetization jumps.

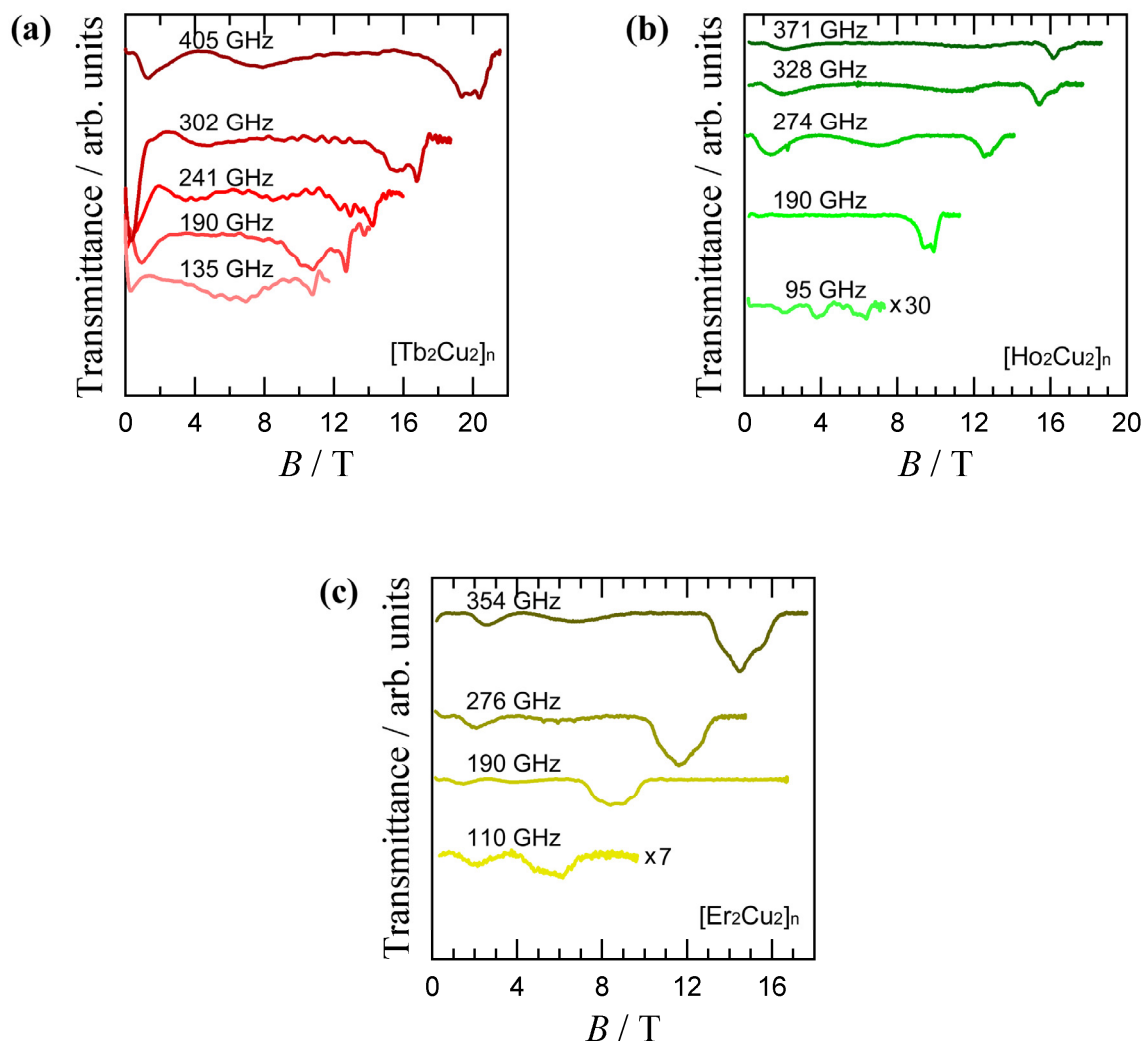


Figure 5.3. Selected EPR spectra measured at 4.2 K as a function of frequency for (a) $[\text{Tb}_2\text{Cu}_2]_n$, (b) $[\text{Ho}_2\text{Cu}_2]_n$, and (c) $[\text{Er}_2\text{Cu}_2]_n$. The spectra are offset in a linear scale of the frequency.

In the case of $[\text{Er}_2\text{Cu}_2]_n$ (Figure 5.2d), the M_s value was $13.0 \mu_B$ at 15 T, which did not reach the calculated value $20 \mu_B$ with maximal $|\mathcal{F}| = 15/2$ and $g_J = 6/5$. The ground state of the Er ions may have a smaller moment such as $|\mathcal{F}| = 11/2$ (the calculated M_s value $15.2 \mu_B$) or $9/2$ ($12.8 \mu_B$). The energy-level crossing between the ferrimagnetic and ferromagnetic states occurs around 2.5 T (the bottom of Figure 5.2d). The magnetization curves for $[\text{Gd}_2\text{Cu}_2]_n$ and $[\text{Dy}_2\text{Cu}_2]_n$ exhibited a similar copper(II) spin-flip transition at ca. 7.0 and 5.56 T, respectively (Figure 5.2b, see also ref 11). Therefore, the series of $[\text{Ln}_2\text{Cu}_2]_n$ involve 4f–3d antiferromagnetic couplings for all heavier-lanthanide ions investigated (Ln = Gd, Tb, Dy, Ho, and Er).

The precise level-crossing field is finally determined from the HF-EPR experiments. HF-EPR spectra of powder $[\text{Tb}_2\text{Cu}_2]_n$ were collected in a wide frequency range 95 – 405 GHz at 4.2 K (Figure 5.3a). We found several series of signals shifted to a higher field with an increasing frequency ($\alpha - \varepsilon$ in Figure 5.4a). The g value of the signals (ε) was 1.99(2) from the slope of the frequency-field plot.

It is consistent with the Cu signal satisfying a conventional EPR selection rule of $\Delta m_s = \pm 1$. The g value slightly smaller than 2 was previously reported and discussed on $[\text{Dy}_2\text{Cu}_2]_n$ in chapter 4. Extrapolation gives a critical field of 5.80(8) T, which implies the level-crossing of two states with respect to the Cu spin-flip. It is identical to the position of the magnetization jump in the magnetization curve, and the value from the HF-EPR is more precise than that of the magnetization measurements.

The g values of the other signals ($\alpha - \delta$) were ca. 10, ca. 15, 2.65(11) and 1.92(5), respectively. Some of them seem to be caused by transitions among $2J+1$ multiplets of the Tb ion. For example, a transition of $\Delta m_J = \pm 10$ with $g_J = 3/2$ gives an apparent g value of 15; namely, the transition with $g = \text{ca. } 15$ (β) may be attributed to a forbidden transition with $\Delta m_J = \pm 10$ (e.g. $\mathcal{F} = -5 \leftrightarrow +5$).

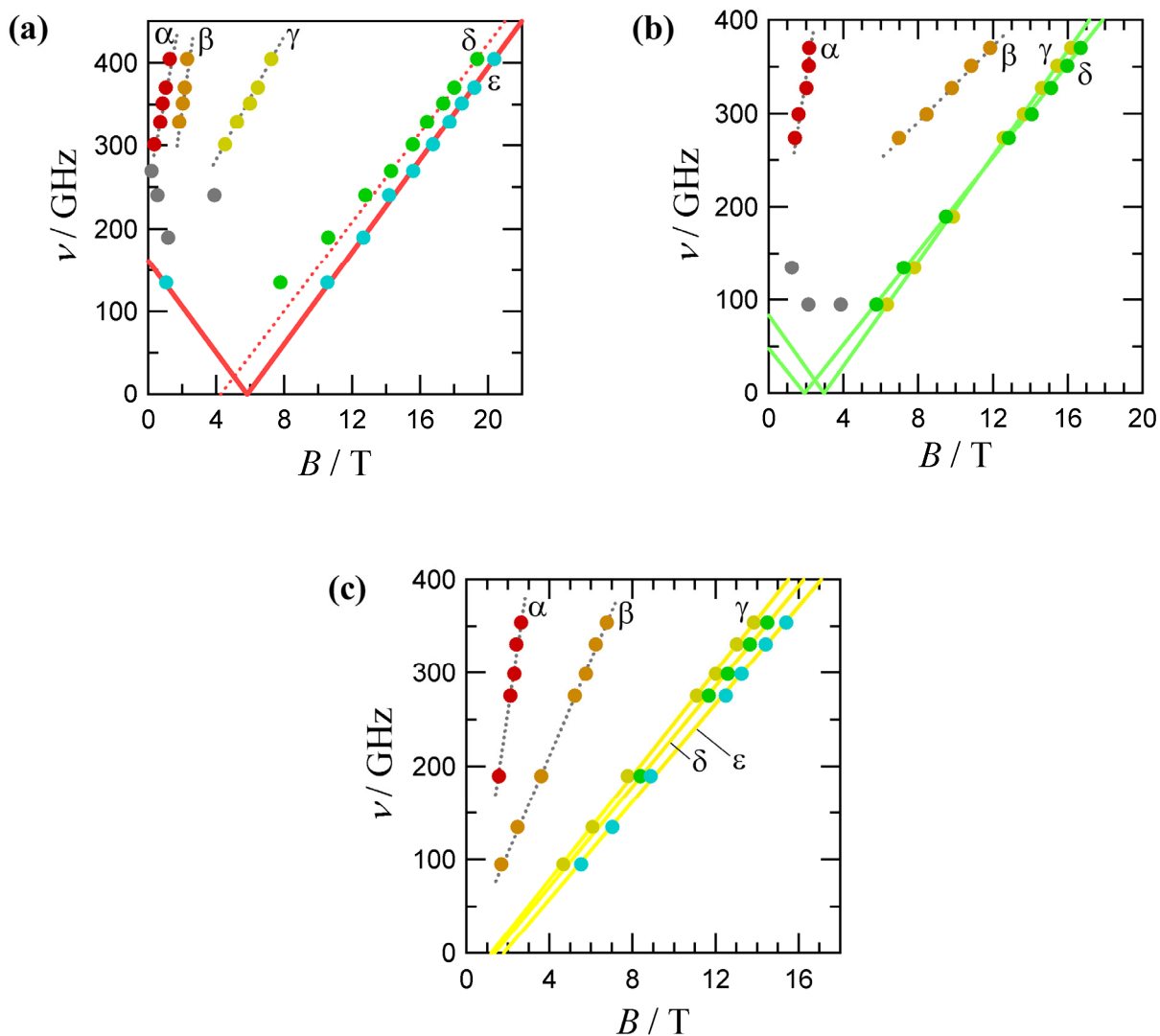


Figure 5.4. Frequency-field diagrams (a) $[\text{Tb}_2\text{Cu}_2]_n$, (b) $[\text{Ho}_2\text{Cu}_2]_n$, and (c) $[\text{Er}_2\text{Cu}_2]_n$. Dotted lines are shown for a guide to the eye. Solid lines represent the best linear fittings.

HF-EPR spectra of powder [Ho₂Cu₂]_n were collected in a frequency range 95 – 371 GHz at 4.2 K (Figure 5.3b). We found several series of signals shifted to a higher field with an increasing frequency ($\alpha - \delta$ in Figure 5.4b). The g values of the γ and δ series were 2.01(2) and 1.79(4), respectively, from the slope of the frequency-field plot. They are assigned to the Cu signals, similarly to the [Tb₂Cu₂]_n case. Extrapolations of their peaks give different critical fields of 1.9(2) T and 2.96(11) T. They may originate from different transitions. The Ho ions affect the internal field at the adjacent Cu ions in terms of exchange-bias fields. Accordingly, the position of the critical fields is in proportion to \mathcal{F} . If the stronger peaks (γ) on higher field is attributed to Ho ions with maximal $\mathcal{F} = \pm 8$, the weaker peaks (δ) might be to Ho ions with $\mathcal{F} = \pm 5$. The peaks of the δ series were stronger than those of the γ series in a small field region, indicating that a state with $\mathcal{F} = \pm 5$ for Ho ions is the ground state among $2J+1$ multiplets of the Ho ion while the first excited state has $\mathcal{F} = \pm 8$ for Ho ions. This finding is consistent with the small M_s value of the magnetization measurements. The resonance-field positions of the α and β series were bent in a small field region, and their g values could not be calculated accurately. The g value of α is roughly estimated to be 8 or larger, and that of β to be 1.5 or larger. The origins of the α signals is ascribable to a forbidden transition among $2J+1$ multiplets of the Ho ion. The β signals may be attributed to a transition with a smaller Δm_J value

HF-EPR spectra of powder [Er₂Cu₂]_n were collected in a frequency range 95 – 354 GHz at 4.2 K (Figure 5.3c). We found several series of signals shifted to a higher field with an increasing frequency ($\alpha - \varepsilon$ in Figure 5.4c). The g values of the γ , δ and ε series were 1.99(4), 1.88(6), and 1.87(3), respectively, which are ascribed to the Cu signals. Extrapolations of their peaks give different critical fields of 1.10(10) T, 1.35(15) T and 1.79(15) T. The presence of the various critical fields may be caused by different \mathcal{F} values at Er ions ($\mathcal{F} = \pm^{15}/2, \pm^{13}/2, \pm^{11}/2$, etc.). If the highest-field series (ε) is attributed to Er ions with $\mathcal{F} = \pm^{15}/2$, the other peaks (γ and δ) might be to Er ions with $\mathcal{F} = \pm^{11}/2$ and $\pm^9/2$, respectively. The g values of the α and β series were 10.8(7) and 3.66(4), respectively. The former seems to be caused by transitions of the Er ion itself with a somewhat large \mathcal{J}^z and possibly be assigned to a forbidden transition with $\Delta m_J = \pm 9$, because $\Delta m_J = \pm 9$ ($\mathcal{F} = -^9/2 \leftrightarrow +^9/2$) with $g_J = ^6/5$ gives an apparent g value of 10.8. The latter seems to be caused by transition between $\mathcal{F} = -^{15}/2 \leftrightarrow -^9/2$, because $\Delta m_J = \pm 3$ with $g_J = ^6/5$ gives an apparent g value of 3.6.

5.3 Discussion

For all compounds investigated here, 4f-3d couplings were antiferromagnetic, giving the ferrimagnetic ground state. The magnetization and HF-EPR measurements consistently indicate the critical field (B_C), ascribable to an energy-level crossing from the ferri- to ferromagnetic states. The present exchange-coupling model holds for [Ln₂Cu₂]_n as well as [Ln₄Cu]⁴ and [Ln₂M]³. Assuming

the Ising character of Ln ions, the following general spin Hamiltonian is available for the repeating unit $[\text{Ln}_2\text{Cu}_2]$:

$$\mathcal{H} = -J_A(\hat{J}_2^z \cdot \hat{S}_1 + \hat{J}_3^z \cdot \hat{S}_4) - J_B(\hat{J}_3^z \cdot \hat{S}_1 + \hat{J}_2^z \cdot \hat{S}_4) + \mu_B H^z (g_1 S_1 + g_2 J_2^z + g_3 J_3^z + g_4 S_4) \quad (5.1)$$

Symbols J_2 and J_3 represent the total moments of Ln ions, while S_1 and S_4 the spins of Cu ions. The first and second terms stand for the Ising-type exchange interactions between Ln and Cu ions, where the coupling parameters are defined as $-J_A$ and $-J_B$, and the third term represents the Zeeman interaction (Figure 5.5).

The EPR signals due to Ln ions were observed for the Tb, Ho, and Er analogs. These signals are originally “forbidden,” but possible admixture of the states might violate the EPR selection rule and their signals become observable. In addition, in some case, the \mathcal{F} value does not have a maximal value of $J = L + S$. Along this context, the Ising character is somewhat weakened, in contrast to the typical Ising character found in the Dy analog (see Chapter 4). However, the anisotropic character of lanthanide ions is usually strong, and the moments are still large. The effective Ising-spin model seems to be valid in the analysis on J_{4f-3d} .

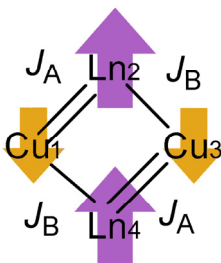


Figure 5.5. Exchange coupling scheme for $[\text{Ln}_2\text{Cu}_2]$. The ground ferromagnetic spin structure is drawn with arrows.

The parameter J_{4f-3d} was estimated using the above Hamiltonian; namely the energy gap between the ground ferrimagnetic state and first excited ferromagnetic state was derived directly from the magnitude of the level-crossing field. Since the level-crossing field found in the HF-EPR data has more accuracy than that of the magnetization data, we utilized the HF-EPR data. The results are summarized in Table 5.2. In the present analysis, we can estimate an average value on J_A and J_B . Separation of J_A and J_B requires more detailed analysis, according to the method already described in Chapter 4.

We obtained antiferromagnetic 4f-3d couplings in all compounds investigated here. A possible reason is stated as follows. Kahn et al. explained the magnetic couplings in 4f-3d

compounds as follows.¹³ When the number of 4f electrons is more than seven, the orbital and spin momenta of Ln are parallel, and the ferromagnetic spin coupling gives rise to an overall ferromagnetic interaction. There are ample reports on ferromagnetic $J_{\text{Dy-Cu}}$ as well as $J_{\text{Gd-Cu}}$.^{13–15} Antiferromagnetic couplings are explained in terms of the violation of the ferromagnetic interaction between the 4f spin portion and 3d spins.^{11,16} In the present compounds, the severe torsion along the Ln–O–N–M linkage was found in common, and such out-of-plane geometry favors antiferromagnetic coupling, as previously discussed in [Gd₂Cu₂]_n.¹¹

Table 5.2. Exchange parameter J_{4f-3d} for [Ln₂Cu₂]_n determined from the HF-EPR study.

Ln	Gd ^{a)}	Tb	Dy	Ho	Er
$J_{4f-3d}k_B^{-1} / \text{K}$	–1.3(2) ^{b)}	–0.77(2)	–0.478(8) ^{c)}	–0.250(12)	–0.149(15)
reference	ref 11	this work	Chapter 4	this work	this work

a) The Gd moments are treated as Heisenberg spins. b) Estimated from the dc magnetic susceptibility as a function of temperature. c) Averaged from the reported values J_A and J_B for two crystallographically independent exchange couplings.

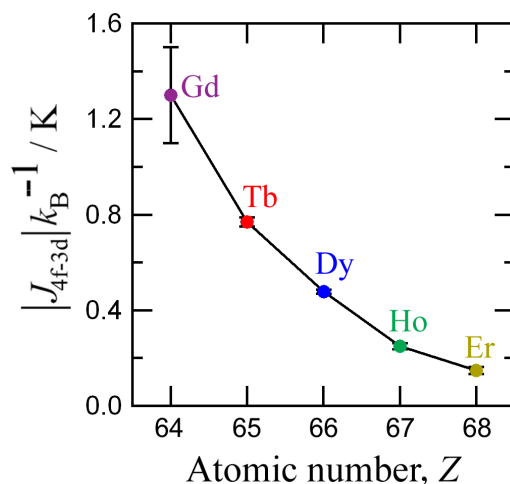


Figure 5.6. Plot of the 4f–3d exchange parameters in [Ln₂Cu₂]_n as a function of the atomic number of the Ln ions. Solid line is shown for a guide to the eye.

Furthermore, the exchange coupling parameters monotonically decrease with the atomic number from ₆₄Gd to ₆₈Er, as depicted in Figure 5.6. The present simple relation is different from the typical

trend of magnetic anisotropy as $\text{Dy} > \text{Tb} > \text{Ho} > \text{Er} \gg \text{Gd}$.¹⁷ On the other hand, the nominal number of 4f-electrons increases from $4f^7$ to $4f^{11}$, and accordingly the number of the 4f-spins decreases from seven to three, in the order from Gd^{3+} to Er^{3+} . This finding indicates that the exchange coupling takes place between the copper $3d_{x^2-y^2}$ -spin and the lanthanide 4f-spin portion, regardless of the angular contribution or magnetic anisotropy from Ln ions. The observed antiferromagnetic coupling is approximately proportion to the overlap between the 4f and 3d magnetic orbitals, and the combination for the orbital overlap would increase with an increase of the number of magnetic 4f orbitals.

5.4 Conclusion

The advantages of HF-EPR are the extremely high resolution and the ability to identify quantum numbers of energy-levels by the EPR selection rule. The bias field at the copper(II) ions was detected, affording the information of exchange couplings. We have precisely evaluated J_{4f-3d} for $[\text{Ln}_2\text{Cu}_2]_n$, (Ln = Tb, Ho, and Er). These J_{4f-3d} values are comparable to those for Ln = Gd¹¹ and Dy (chapter 4), and the magnetic couplings in all compounds investigated here were antiferromagnetic. Furthermore, the $|J_{4f-3d}|$ value monotonically decreases in the order of Gd, Tb, Dy, Ho, and Er. The present methodology would be applicable to other 4f-3d heterometallic compounds. We are now investigating J_{4f-3d} in the $[\text{Ln}_2\text{Cu}_2]_n$ derivatives involving lighter lanthanide ions.

5.5 Experimental Section

5.5.1 Preparations

Complexes $[\text{Ln}_2\text{Cu}_2]_n$ (Ln = Tb, Ho, and Er) were synthesized by the complexation of $[\text{Ln}(\text{hfac})_3(\text{H}_2\text{O})_2]$ ¹⁸ and partially deprotonated $[\text{Cu}(\text{Hdmg})_2]$ ¹⁹ in methanol. $[\text{Cu}(\text{Hdmg})_2]$ (15 mg, 0.050 mmol) was dissolved in 1.5 mL of MeOH containing 0.1 mmol of KOH. A methanol solution (1 mL) of $[\text{Tb}(\text{hfac})_3(\text{H}_2\text{O})_2]$ (82 mg, 0.050 mmol) was slowly added to the above solution. The resultant dark brown solution was allowed to stand at room temperature for a day, to give dark brown prismatic crystals that were collected on a filter, washed with a small amount of MeOH, and dried in air. The yield of $[\text{Tb}_2\text{Cu}_2]_n$ was 23 mg (0.025 mmol; 50% on the repeating unit basis). Similarly, $[\text{Ho}_2\text{Cu}_2]_n$ and $[\text{Er}_2\text{Cu}_2]_n$ were prepared as brown prismatic crystals in 70% and 65% yield. The elemental analysis (C, H, N) of their complexes on a Fisons EA-1108 by a usual combustion method supported the chemical composition. $[\text{Tb}_2\text{Cu}_2]_n$: Anal. Calcd.: C, 25.42; H, 2.13; N, 6.24% for $\text{C}_{19}\text{H}_{19}\text{CuF}_{12}\text{N}_4\text{O}_9\text{Tb}$. Found: C, 22.60; H, 2.52; N, 5.65%. $[\text{Ho}_2\text{Cu}_2]_n$: Anal. Calcd.: C, 25.25; H, 2.12; N, 6.20% for $\text{C}_{19}\text{H}_{19}\text{CuF}_{12}\text{HoN}_4\text{O}_9$. Found: C, 23.35; H, 2.46; N, 5.78%. $[\text{Er}_2\text{Cu}_2]_n$: Anal. Calcd.: C, 25.18; H, 2.11; N, 6.18% for $\text{C}_{19}\text{H}_{19}\text{CuErF}_{12}\text{N}_4\text{O}_9$. Found: C, 24.94; H, 2.24; N, 5.81%.

5.5.2 X-ray Crystallographic Studies

Single-crystal X-ray diffraction analyses of $[\text{Ln}_2\text{Cu}_2]_n$ ($\text{Ln} = \text{Tb}, \text{Ho}, \text{and Er}$) were performed in a manner similar to those of $[\text{Dy}_2\text{Ni}]$ (in Experimental Section of Chapter 3).

5.5.3 Physical Measurements

The dc and ac magnetic susceptibilities, low-temperature magnetization curves, and HF-EPR measurements of $[\text{Ln}_2\text{Cu}_2]_n$ were performed in a manner similar to those of $[\text{Dy}_2\text{Cu}_2]_n$ (in Experimental Section of Chapter 4).

References

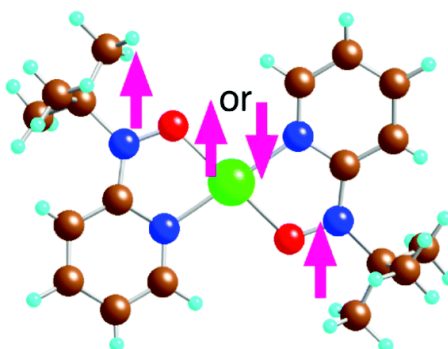
- (1) (a) Gatteschi, D.; Sessoli, R.; Villain, J. *Molecular Nanomagnets*, Oxford University Press, New York, 2006. (b) Gatteschi, D.; Sessoli, R. *Angew. Chem. Int. Ed.* **2003**, *42*, 268.
- (2) (a) Ishikawa, N.; Sugita, M.; Ishikawa, T.; Koshihara, S.-Y.; Kaizu, Y. *J. Am. Chem. Soc.* **2003**, *125*, 8694. (b) Ishikawa, N.; Sugita, M.; Wernsdorfer, W. *J. Am. Chem. Soc.* **2005**, *127*, 3650.
- (3) (a) Mori, F.; Nyui, T.; Ishida, T.; Nogami, T.; Choi, K.-Y.; Nojiri, H. *J. Am. Chem. Soc.* **2006**, *128*, 1440. (b) Mori, F.; Ishida, T.; Nogami, T. *Polyhedron* **2005**, *24*, 2588.
- (4) Ueki, S.; Ishida, T.; Nogami, T.; Choi, K.-Y.; Nojiri, H. *Chem. Phys. Lett.* **2007**, *440*, 263.
- (5) Ueki, S.; Okazawa, S.; Ishida, T.; Nogami, T.; Nojiri, H. *Polyhedron* **2007**, *26*, 1970
- (6) Osa, S.; Kido, T.; Matsumoto, N.; Re, N.; Pochaba, A.; Mrozinski, J. *J. Am. Chem. Soc.* **2004**, *126*, 420.
- (7) Aronica, C.; Pilet, G.; Chastanet, G.; Wernsdorfer, W.; Jacquot, J. F.; Luneau, D. *Angew. Chem., Int. Ed.* **2006**, *45*, 4659.
- (8) Costes, J. P.; Shova, S.; Wernsdorfer, W. *Dalton Trans.* **2008**, 1843.
- (9) Nojiri, H.; Choi, K.-Y.; Kitamura, N. *J. Magn. Magn. Mater.* **2007**, *310*, 1468.
- (10) Nojiri, H.; Ajiro, Y.; Asano, T.; Boucher, J.-P. *New J. Phys.* **2006**, *8*, 218.
- (11) Ueki, S.; Kobayashi, Y.; Ishida, T.; Nogami, T. *Chem. Commun.* **2005**, 5223.
- (12) Krzystek, J.; Zvyagin, S. A.; Ozarowski, A.; Trofimenko, S.; Telsner, J. *J. Mag. Res.* **2006**, *178*, 174.
- (13) Andruh, M.; Ramade, I.; Codjovi, E.; Guillou, O.; Kahn, O.; Trombe, J. C. *J. Am. Chem. Soc.* **1993**, *115*, 1822.
- (14) (a) Costes, J.-P.; Dahan, F.; Dupuis, A. *Inorg. Chem.* **2000**, *39*, 5994. (b) Costes, J.-P.; Dahan, F.; Dupuis, A.; Laurent, J.-P. *Inorg. Chem.* **2000**, *39*, 169. (c) Costes, J.-P.; Dahan, F.; Dupuis, A.; Laurent, J.-P. *Chem.-Eur. J.* **1998**, *4*, 1616.
- (15) (a) Kido, T.; Ikuta, Y.; Sunatsuki, Y.; Ogawa, Y.; Matsumoto, M.; Re, N. *Inorg. Chem.* **2003**, *42*, 398. (b) Evangelisti, M.; Kahn, M. L.; Bartolome, J.; de Jongh, L. J.; Meyers, C.; Leandri, J.; Leroyer, Y.; Mathoniere, C. *Phys. Rev. B* **2003**, *68*, 184405.
- (16) Kobayashi, Y.; Ueki, S.; Ishida, T.; Nogami, T. *Chem. Phys. Lett.* **2003**, *378*, 337.
- (17) Bernot, K.; Bogani, L.; Caneschi, A.; Gatteschi, D.; Sessoli, R. *J. Am. Chem. Soc.* **2006**, *128*, 7974.
- (18) Richardson, M. F.; Wagner, W. F.; Sands, D. E. *J. Inorg. Nucl. Chem.* **1968**, *30*, 1275.
- (19) Villa, J. F.; Hatfield, W. E. *J. Chem. Phys.* **1971**, *55*, 4758.

Chapter 6

tert-Butyl 2-Pyridyl Nitroxide Available as Paramagnetic Chelate Ligands for Strongly Exchange-Coupled Metal–Radical Compounds

Abstract

A paramagnetic ligand 2pyNO (*tert*-butyl 2-pyridyl nitroxide) was trapped with transition-metal ions, giving stable metal–radical compounds. Complex $[\text{Ni}^{\text{II}}(2\text{pyNO})_2(\text{H}_2\text{O})_2](\text{ClO}_4)_2$ showed intramolecular strong ferromagnetic coupling, while $[\text{Cu}^{\text{II}}(2\text{pyNO})_2(\text{ClO}_4)_2]$ did antiferromagnetic coupling, through the direct metal–radical coordination bonds.

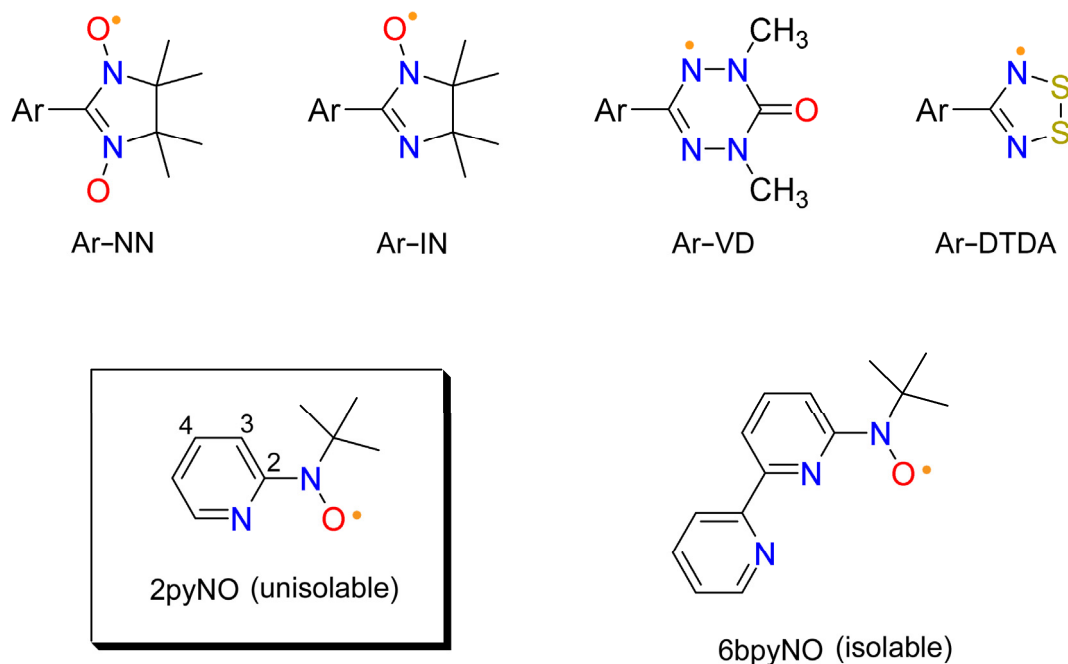


6.1 Introduction

Metal–radical hybrid solids have been well investigated toward molecule-based magnets, where a radical center is directly bonded to the metal ion, affording appreciable magnetic exchange coupling.¹ Various 2-pyridyl-substituted ligands containing a paramagnetic center such as nitronyl nitroxide (NN),^{2,3} imino nitroxide (IN),⁴ oxoverdazyl (VD),⁵ and dithiadiazolyl (DTDA)⁶ groups have been known to form chelate rings (see Scheme 6.1 for their structural formulas). We propose here *tert*-butyl 2-pyridyl nitroxide (2pyNO; NO stands for the *tert*-butyl nitroxide group) as a promising candidate for strongly correlated metal–radical materials. The spin density on the ligating oxygen atom of Ar–NO is assumed to be almost twice as large as that of the other conventional radicals such as Ar–NN, owing to an almost half size of the spin-delocalizable π -conjugation in the radical groups, which also leads to the undesired instability of Ar–NO. There have been no reports on the chelate compounds involving 2pyNO despite many efforts because of synthetic difficulty; the simple pyridyl–NOs are not isolable.⁷ Thanks to the stabilization from an extended aromatic ring, 6bpyNO has been available for synthesis of $[\text{Ni}^{\text{II}}(6\text{bpyNO})_2]_2(\text{PF}_6)_2$ and $[\text{Cu}^{\text{II}}(6\text{bpyNO})\text{Cl}_2]$.⁸ Complexation with metal ions stabilizes the radicals, as demonstrated by the isolation of H–IN,^{1d,9} 3pyNO, and

4pyNO¹⁰ compounds. This technique has been widely utilized for unstable functional groups by means of steric protection as well as electronic perturbation.¹¹ We supposed that the synthesis of 2pyNO complexes would be challenging, and actually we have succeeded in the preparation of [Ni^{II}(2pyNO)₂(H₂O)₂](ClO₄)₂ (**1**) and [Cu^{II}(2pyNO)₂(ClO₄)₂] (**2**).

Scheme 6.1. Structural Formulas of 2-Pyridyl-Substituted Radicals with Chelating Ability



6.2 Results and Discussion

A precursory hydroxylamine (2pyNOH) was prepared from 2-bromopyridine and 2-methyl-2-nitrosobutane via the conventional organo-lithium method. Crude 2pyNO, obtained from oxidation of 2pyNOH with Ag₂O, was introduced to a subsequent complexation without isolation, giving **1** and **2** by use of a stoichiometric amount of nickel(II) and copper(II) perchlorates, respectively. The present complexes are sufficiently stable during storage under ambient conditions for several months.

Table 6.1 summarizes selected crystallographic data of **1** and **2**. The chelate rings involving 2pyNO are clearly depicted in Figure 6.1. The dicationic moiety of **1** (abbreviated as **1**²⁺) has a twofold symmetry around the O2–Ni1–O3 bond (Figure 6.1a). Two water molecules occupy the axial position with respect to the chelate plane, while the counter ClO₄[−] anions are located in clearance of the crystal. An octahedron is characterized by the O1–Ni1, N1–Ni1, O2–Ni1, and O3–Ni1 distances of 2.008(2), 2.018(3), 2.080(4), and 2.052(4) Å, respectively, suggesting the high spin center

with $S_{Ni} = 1$. The chelate ring is highly planar as indicated with the small C1–N2–O1–Ni1 torsion angle ($3.9(3)^\circ$). We have proposed the C_{2py}–N–O–M torsion as a convenient indicator for orthogonal arrangement of metal 3d σ and oxygen 2p $_z$ orbitals.³

Table 6.1. Selected Crystallographic Data for **1** and **2**

compounds	1: [Ni(2pyNO) ₂ (H ₂ O) ₂](ClO ₄) ₂	2: [Cu(2pyNO) ₂ (ClO ₄) ₂]
formula	C ₁₈ H ₃₀ Cl ₂ N ₄ O ₁₂ Ni	C ₁₈ H ₂₆ Cl ₂ CuN ₄ O ₁₀
formula weight	624.05	592.87
habit	black block	black platelet
dimension/mm³	0.70 × 0.60 × 0.50	0.35 × 0.30 × 0.10
T/K	100	90
crystal system	orthorhombic	monoclinic
space group	<i>Pcca</i>	<i>P2₁/n</i>
a/Å	21.697(8)	6.176(3)
b/Å	8.534(3)	20.503(10)
c/Å	14.165(6)	9.516(4)
α/°	90	90
β/°	90	104.33(4)
γ/°	90	90
V/Å³	2622.8(17)	1167.4(10)
Z	4	2
D_{calc}/g cm⁻³	1.580	1.686
unique data	2992	3349
μ(Mo Kα)/mm⁻¹	1.009	1.227
R (F)^a (I > 2σ(I))	0.0540	0.0592
R_w(F²)^b (all data)	0.0667	0.1085

^a $R = \frac{\sum ||F_o| - |F_c||}{\sum |F_o|}$. ^b $R_w = \left[\frac{\sum w(F_o^2 - F_c^2)^2}{\sum w(F_o^2)^2} \right]^{1/2}$.

Compound **2** has a centrosymmetry (Figure 6.1b). The copper(II) ion forms an elongated octahedron with the somewhat long axial Cu1–O2 distance (2.478(4) Å) compared with the equatorial bonds (1.942(4) and 1.935(3) Å for O1–Cu1 and N1–Cu1, respectively). The axial direction is

considerably canted from the normal of the basal plane as indicated by the O1–Cu1–O2 and N1–Cu1–O2 angles (85.6(2) and 83.4(2)°, respectively), probably owing to the steric effect from the perchlorate ligand. The C1–N2–O1–Cu1 torsion angle is 25.9(5)°, which may violate orthogonality between the copper(II) and nitroxide magnetic orbitals (see below).

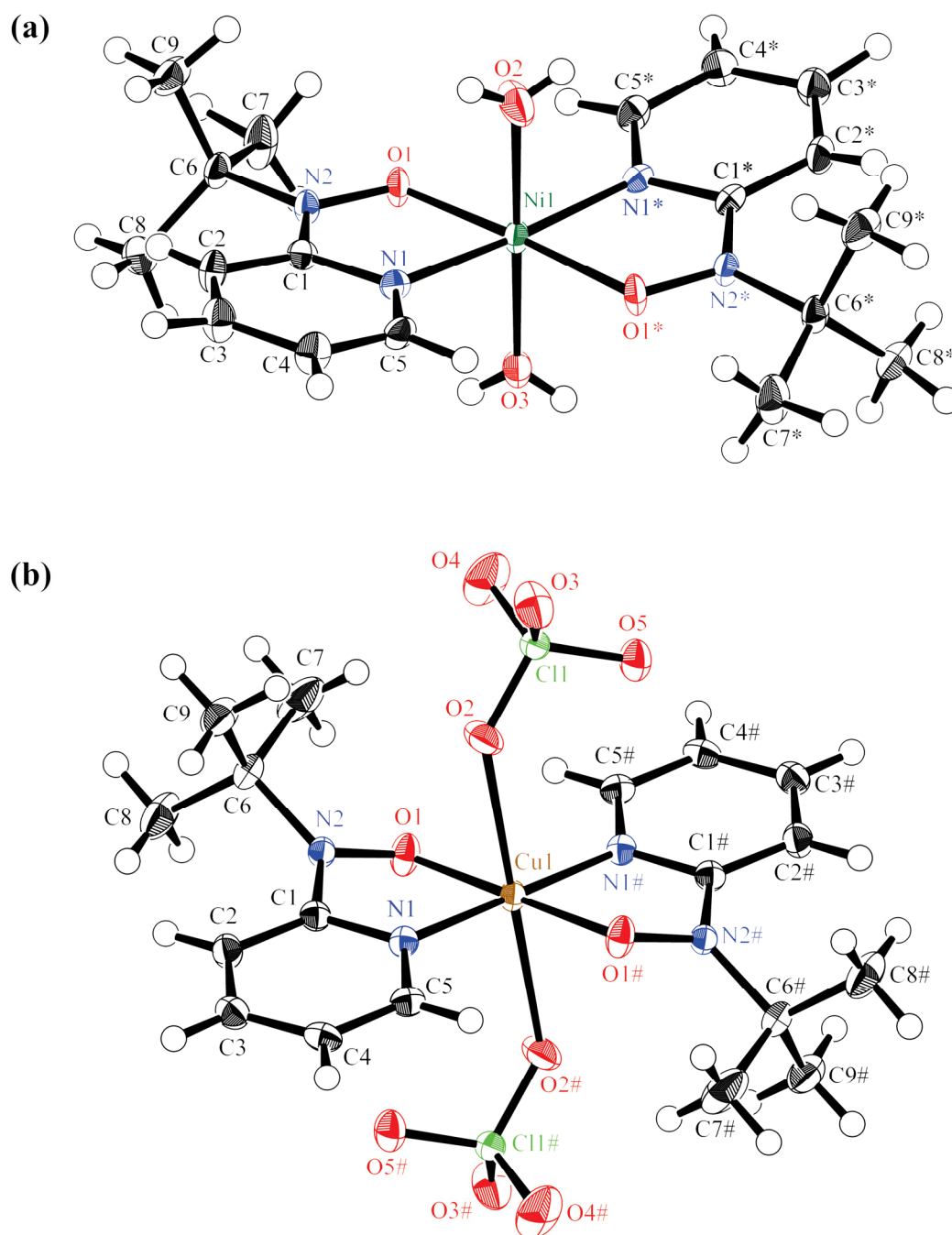


Figure 6.1. Ortep drawings for (a) $[\text{Ni}(\text{2pyNO})_2(\text{H}_2\text{O})_2]^{2+}$ in **1** and (b) $[\text{Cu}(\text{2pyNO})_2(\text{ClO}_4)_2]$ (**2**). Thermal ellipsoids are drawn at the 50% probability level for non-hydrogen atoms. Symmetry operation codes for * and # are $(-x, +y, 1/2 - z)$ and $(-x, -y, -z)$, respectively.

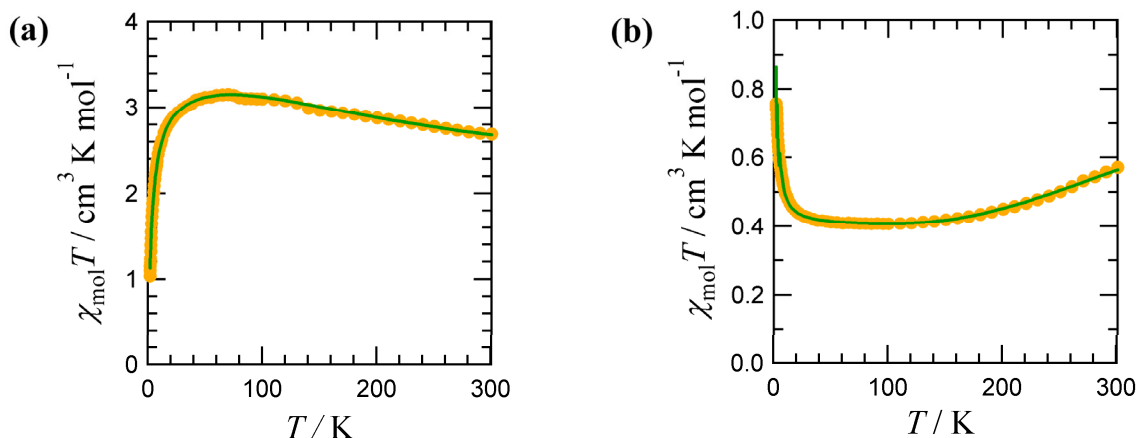


Figure 6.2. Temperature dependence of $\chi_{\text{mol}}T$ (orange circles) for (a) **1** and (b) **2** measured at 500 and 5000 Oe, respectively. The green solid lines represent calculated curves. See the text for the equations and optimized parameters.

Magnetic susceptibilities of **1** and **2** were measured on a SQUID magnetometer (Figure 6.2). Upon cooling from 300 to 70 K, the $\chi_{\text{mol}}T$ value of **1** increased up to $3.2 \text{ cm}^3 \text{ K mol}^{-1}$, indicating the presence of intramolecular ferromagnetic interaction. A linear-arrayed three-centered model¹² (the spin Hamiltonian $H = -2J(\hat{S}_1 \cdot \hat{S}_2 + \hat{S}_2 \cdot \hat{S}_3)$) was applied to the analysis of **1** together with a Weiss mean field parameter θ . Fitting to the resultant expression (eq 6.1) afforded the optimized parameters $J/k_B = +126(3) \text{ K}$ and $\theta = -3.45(5) \text{ K}$ with $g_{\text{avg}} = 2.112(4)$. A final drop of the $\chi_{\text{mol}}T$ value can be assigned to Ni^{II} ZFS as well as intermolecular antiferromagnetic couplings, both of which were confined to θ .

$$\chi_{\text{mol}} = \frac{2N_{\text{A}}g^2\mu_{\text{B}}^2}{k_{\text{B}}(T - \theta)} \frac{\exp(-2J/k_{\text{B}}T) + 1 + 5\exp(2J/k_{\text{B}}T)}{\exp(-4J/k_{\text{B}}T) + 3\exp(-2J/k_{\text{B}}T) + 3 + 5\exp(2J/k_{\text{B}}T)} \quad (6.1)$$

In sharp contrast to the results on **1**, the $\chi_{\text{mol}}T$ value of **2** decreased and reached a plateau at $0.4 \text{ cm}^3 \text{ K mol}^{-1}$ on cooling, indicating the presence of intramolecular antiferromagnetic interaction. A final upsurge can be ascribed to intermolecular ferromagnetic interaction. We applied a doublet-quartet model based on a linear array (eq 6.2),¹³ with a modification using a Weiss temperature (θ), to give the parameters $J/k_B = -274(2) \text{ K}$, $\theta = +1.88(2) \text{ K}$, and $g_{\text{avg}} = 2.064(2)$. The calculated curves well-reproduced the experimental data for both **1** and **2**.

$$\chi_{\text{mol}} = \frac{N_{\text{A}}g^2\mu_{\text{B}}^2}{4k_{\text{B}}(T - \theta)} \frac{\exp(-2J/k_{\text{B}}T) + 1 + 10\exp(J/k_{\text{B}}T)}{\exp(-2J/k_{\text{B}}T) + 1 + 2\exp(J/k_{\text{B}}T)} \quad (6.2)$$

A DFT calculation supported the above analysis. We applied an unrestricted DFT method (UB3LYP/6-31G(d,p)) in the Gaussian03 program¹⁴ to the molecular geometries determined above. The converged self-consistent field energies of the singlet and quintet of **1**²⁺ showed the gap of $3.41 \times$

10^{-3} au with the ground quintet state. On the other hand, the doublet state of **2** was lower in energy than the quartet one by 3.46×10^{-3} au. The intramolecular magnetic coupling constants of $\mathbf{1}^{2+}$ and **2** were estimated as $J/k_B = +179$ and -364 K, respectively. Though the calculated J values were somewhat overestimated, the ground spin states were correctly predicted. The spin density surfaces of the ground states of $\mathbf{1}^{2+}$ and **2** are shown in Figure 6.3. Qualitatively the same results were obtained using the LanL2DZ basis set.

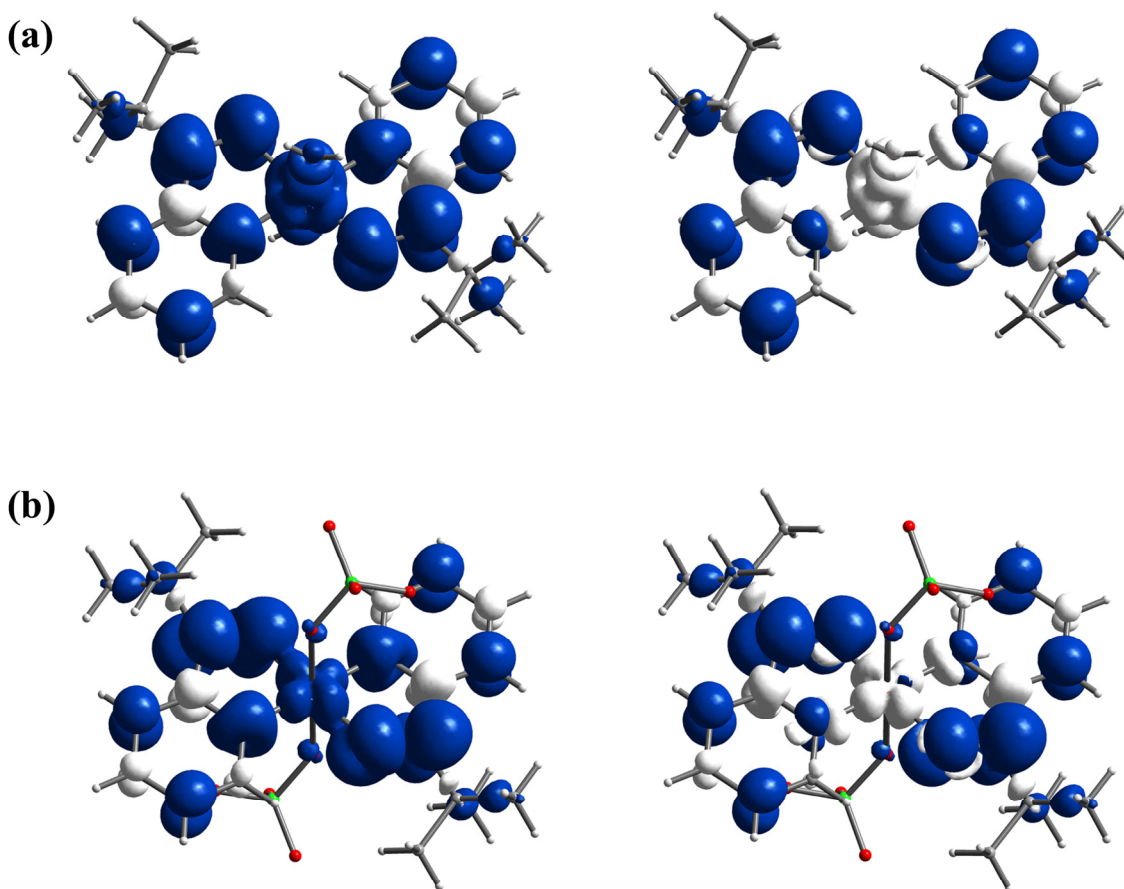


Figure 6.3. (a) Spin density surfaces of the quintet state (left) and the singlet (right) of $\mathbf{1}^{2+}$. (b) Spin density surfaces of the quartet state (left) and the doublet (right) of **2**. They were calculated on the UB3LYP/6-31G(d,p) level. Blue, positive spin; light gray, negative spin. See Figure 6.1 for the atom labels.

These spin density maps approximately represent the SOMOs, which carry a σ character at the metal ions and a π^* character at the nitroxide groups. As previously proposed,^{2-4,15} the metal-radical ferromagnetic couplings observed can be explained in terms of the orbital orthogonality between them (Figure 6.4a). Compound **1** showed the ferromagnetic coupling owing to the small torsion angle around $C_{2py}-N-O-M$ (3.9°). Similarly, the nickel(II)- and copper(II)-6bpyNO complexes having

the small torsion ($4.6 - 5.5^\circ$ and 10.7° , respectively) exhibited the strong ferromagnetic couplings.⁸ On the other hand, **2** has a considerably large torsion (25.9°), and accordingly the antiferromagnetic coupling was operative (Figure 6.4b).

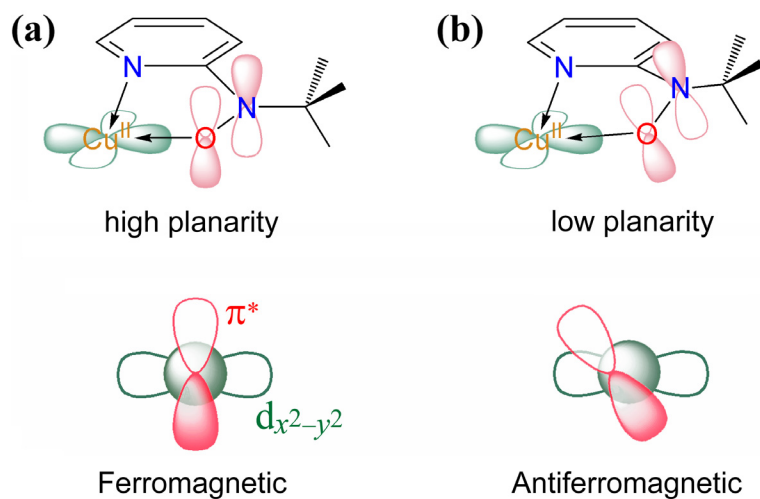


Figure 6.4. Schematic drawings for (a) a ferromagnetic and (b) an antiferromagnetic coupling arrangements between the copper(II) magnetic orbital $3d_{x^2-y^2}$ and the radical magnetic orbital π^* .

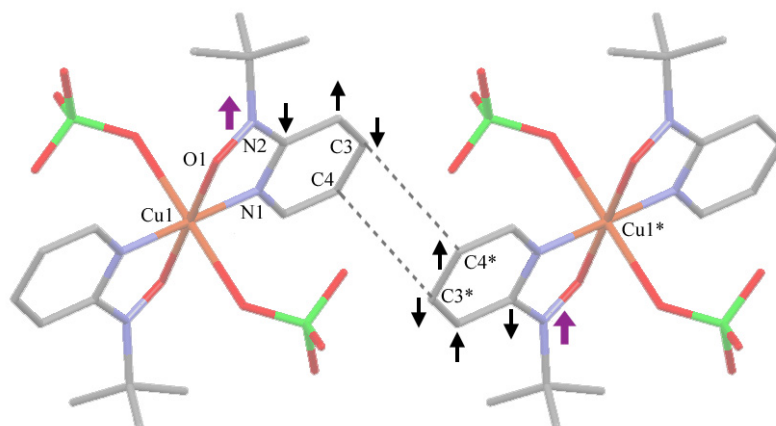


Figure 6.5. Molecular arrangement in the crystal of **2**. The hydrogen atoms are omitted for clarity. Dotted lines indicate the interatomic contacts of $3.274(8)$ Å between C3 and C4* (or between C4 and C3*), where the symmetry operation code of * is $1 - x, -y, 1 - z$. The possible spin polarization scheme is shown with arrows.

We can also find that polarized spin densities on the pyridine ring are appreciable (Figure 6.3). A possible mechanism of the intermolecular ferromagnetic coupling in the crystal of **2** should be noticed. The C3 and C4 carry negative (-0.0445) and positive ($+0.0928$) spin densities, respectively

(Figure 6.3b), in good agreement with the spin-polarization scheme on an aromatic ring (Figure 6.5).¹⁶ The relatively short intermolecular distances of 3.274(8) Å are found between C3...C4* and C4...C3*, which is smaller than the sum of the van der Waals radii (3.40 Å)¹⁷ (the symmetry operation code for * is $1 - x, -y, 1 - z$). McConnell proposed the intermolecular exchange coupling in the π -stacking dimer where the spin density was polarized.^{18,19} The intermolecular ferromagnetic coupling of **2** was observed as expected from this model. In the crystal of **1**, we can find hydrogen bonds between water and pyridine hydrogen atoms and perchlorate oxygen atoms. The intermolecular antiferromagnetic coupling observed seems consistent with these intermolecular contacts.

6.3 Conclusion

In summary, we have reported here the first examples of Ni^{II} and Cu^{II} complexes having 2pyNO chelate rings, both of which showed considerably strong exchange couplings. The spin is polarized from the NO group onto the pyridine ring (Figure 6.3), in contrast to the case of nitronyl nitroxide and other radicals,²⁰ leading to magnetic coupling in an intermolecular fashion. This work encourages us to develop more studies on metal-radical hybrid materials using fragile radicals which have been set aside so far because of the preconceived notion that they were unavailable.

6.4 Experimental Section

6.4.1 Preparations

Materials

Unless otherwise noted, starting materials were obtained from commercial supplies and used without further purification. 2-Bromopyridine was dried over molecular sieves. Ether was purified by distillation from sodium and benzophenone. *Caution! Perchlorate salts are potentially explosive and should only be handled with care in small quantities.*

***N*-tert-Butyl-*N*-2-pyridylhydroxylamine (2pyNOH)**

A hexane solution of *n*-butyllithium (1.6 mol/L; 28.5 mL; 46 mmol) was added to a dry ether solution (80 mL) of 2-bromopyridine (4.3 mL; 45 mmol) at -78°C , and the mixture was stirred for 30 min under dry N_2 . A dry ether solution (80 mL) containing 2-methyl-2-nitrosopropane (4.0 g, 46 mmol) was added to the above solution over 1 h. The cooling bath was removed, and the reaction vessel was allowed to stand at room temperature. After quenching with aqueous saturated ammonium chloride, aqueous sodium bicarbonate was added and the mixture was extracted with dichloromethane. The organic layer was dried over anhydrous magnesium sulfate, filtered, and concentrated. The products were separated by silica-gel column chromatography eluted with 1/2 dichloromethane/ether to give 2pyNOH as a colorless solid (3.04 g; 18.3 mmol) in 41% yield. Mp $40 - 42^{\circ}\text{C}$. ^1H NMR (CDCl_3 , 270 MHz) 1.24 (s, 9H), 7.02 (ddd, $J = 7.3, 4.9, 1.1$ Hz, 1H), 7.11 (dt, $J = 8.1, 1.1$ Hz, 1H) 7.60 (ddd, $J = 8.1, 7.3, 1.6$ Hz, 1H), 7.74 (broad, 1H), 8.33 (ddd, $J = 4.9, 1.6, 1.1$ Hz,

1H). ^{13}C NMR (CDCl_3 , 68 MHz; in the presence of a trace amount of phenylhydrazine)²¹ 26.4, 61.8, 117.5, 119.3, 136.6, 146.2, 161.4. IR (KBr disc) 802, 1200, 1360, 1431, 1587, 2987, 3230 cm^{-1} . MS (EI, 70 eV) m/z 166.1(M^+), 135.0, 110.0, 109.0, 92.0, 79.0, 57.0.

[Ni(2pyNO)₂(H₂O)₂](ClO₄)₂ (1)

Freshly prepared Ag_2O (278 mg, 1.20 mmol) was added to a dichloromethane solution (5 mL) containing 2pyNOH (67 mg, 0.40 mmol), and the suspension was stirred at room temperature for 1 h. After the solids were centrifuged and filtered off, the filtrate was concentrated to give a volume of ca. 1 mL under reduced pressure at room temperature. Immediately $\text{Ni}(\text{ClO}_4)_2 \cdot 6\text{H}_2\text{O}$ (73 mg, 0.20 mmol) in ethanol (2 mL) was added to the above solution and the resultant mixture was allowed to stand in a refrigerator for 1 day. After ether (3 mL) was added to the solution, dark red powder of **1** was precipitated and collected on a filter (106 mg; 0.170 mmol; yield 85%). Dark red crystals of **1** were obtained by slow ether-vapor diffusion into an acetonitrile solution. Anal. Calcd.: C, 34.46; H, 4.85; N, 8.98% for $\text{C}_{18}\text{H}_{30}\text{Cl}_2\text{N}_4\text{O}_{12}\text{Ni}$. Found: C, 34.89; H, 4.92; N, 8.82%. IR (KBr disc) 627, 771, 1090, 1144, 1437, 1589, 2991, 3429 cm^{-1} .

[Cu(2pyNO)₂(ClO₄)₂] (2)

According to a similar procedure for **1**, crude 2pyNO (prepared from 2pyNOH (33 mg; 0.20 mmol)) and $\text{Cu}(\text{ClO}_4)_2 \cdot 6\text{H}_2\text{O}$ (37 mg, 0.10 mmol) were mixed in dichloromethane (1 mL) and ethanol (3 mL), and the mixture was allowed to stand in a refrigerator for 1 day. Black block crystals of **2** were precipitated and collected on a filter (18 mg; 0.031 mmol; yield 31%). They were suitable X-ray diffraction and magnetic studies. Anal. Calcd.: C, 36.47; H, 4.42; N, 9.45% for $\text{C}_{18}\text{H}_{26}\text{Cl}_2\text{CuN}_4\text{O}_{10}$. Found: C, 36.78; H, 4.19; N, 9.63%. IR (KBr disc) 623, 787, 1055, 1103, 1439, 1591, 2993 cm^{-1} .

6.4.2 X-ray Crystallographic Studies

X-Ray diffraction data of single crystals of **1** and **2** were collected on a Rigaku R-axis RAPID diffractometer with graphite monochromated $\text{Mo K}\alpha$ ($\lambda = 0.71069 \text{ \AA}$) radiation. The structures were solved by direct methods and expanded using Fourier techniques in CRYSTALSTRUCTURE program package.²² Numerical absorption correction was used. Full-matrix least-squares methods were applied using all of the unique reflection data. All of the hydrogen atoms in **1** were found experimentally, and their parameters were included in the refinement. The thermal displacement parameters of non-hydrogen atoms were refined anisotropically and those of hydrogen atoms were refined isotropically. As for **2**, all of the hydrogen atoms were located at calculated positions and the parameters were refined as “riding”.

6.4.3 Physical Measurements

Magnetic susceptibilities of the polycrystalline samples of **1** and **2** were measured on a Quantum Design MPMS SQUID magnetometer at an applied magnetic field of 500 or 5000 Oe in a temperature range down to 1.8 K. The magnetic response was corrected with diamagnetic blank data of the

sample holder obtained separately. The diamagnetic contribution of the sample itself was estimated from Pascal's constant.

6.4.4 Molecular Orbital Calculations

Molecular orbital calculations were performed on the Gaussian03 program.¹⁴ We applied unrestricted DFT UB3LYP methods with the Becke²³ exchange functional and the Lee–Yang–Parr correlation functional.²⁴ The 6–31G(d,p) basis set was chosen. The convergence criterion for the energy was set at 10^{-9} a.u. The SCF energies of the singlet states were obtained according to the broken symmetry method.²⁵ The structural parameters were given from the crystallographic data. The spin density surfaces were drawn in Figure 6.3 at the isovalue of 0.0025. The SCF energies of the singlet and quintet states of **1**²⁺ were converged to -2730.59618231 and -2730.59959420 a.u., respectively, and those of the doublet and quartet states of **2** were -4232.31131549 and -4232.30785564 a.u., respectively. To check a basis-set dependence, we also selected the LanL2DZ basis set. The SCF energies of the singlet and quintet states of **1**²⁺ were converged to -1391.50325085 and -1391.50657389 a.u., respectively, and those of the doublet and quartet states of **2** were -1896.64866293 and -1896.64528295 a.u., respectively. Both calculations (UB3LYP/6–31(d,p) and UB3LYP/LanL2DZ) indicated the quintet (high-spin) ground state for **1**²⁺ and the doublet (low-spin) ground state for **2**.

References

- (1) (a) Caneschi, A.; Gatteschi, D.; Sessoli, R. *Acc. Chem. Res.* **1989**, *22*, 392. (b) Manriquez, J. M.; Yee, G. T.; McLean, R. S.; Epstein, A. J.; Miller, J. S. *Science* **1991**, *252*, 1415. (c) Inoue, K.; Hayamizu, T.; Iwamura, H.; Hashizume, D.; Ohashi, Y. *J. Am. Chem. Soc.* **1996**, *118*, 1803. (d) Ise, T.; Ishida, T.; Hashizume, D.; Iwasaki, F.; Nogami, T. *Inorg. Chem.* **2003**, *42*, 6106.
- (2) (a) Romero, F. M.; Luneau, D.; Ziessel, R. *Chem. Commun.* **1998**, 551. (b) Luneau, D.; Risoan, G.; Rey, P.; Grand, A.; Caneschi, A.; Gatteschi, D.; Laugier, J. *Inorg. Chem.* **1993**, *32*, 5616.
- (3) Aoki, C.; Ishida, T.; Nogami, T. *Inorg. Chem.* **2003**, *42*, 7616.
- (4) (a) Luneau, D.; Rey, P.; Laugier, J.; Fries, P.; Caneschi, A.; Gatteschi, D.; Sessoli, R. *J. Am. Chem. Soc.* **1991**, *113*, 1245. (b) Luneau, D.; Rey, P.; Laugier, J.; Belorizky, E.; Conge, A. *Inorg. Chem.* **1992**, *31*, 3578.
- (5) (a) Hicks, R. G.; Lemaire, M. T.; Thompson, L. K.; Barclay, T. M. *J. Am. Chem. Soc.* **2000**, *122*, 8077. (b) Barclay, T. M.; Hicks, R. G.; Lemaire, M. T.; Thompson, L. K. *Chem. Commun.* **2000**, 2141.
- (6) (a) Hearn, N. G. R.; Preuss, K. E.; Richardson, J. F.; Bin-Salamon, S. *J. Am. Chem. Soc.* **2004**, *126*, 9942. (b) Jennings, M.; Preuss, K. E.; Wu, J. *Chem. Commun.* **2006**, 341.
- (7) Keana, J. F. W. *Chem. Rev.* **1978**, *78*, 37.
- (8) Osanai, K.; Okazawa, A.; Nogami, T.; Ishida, T. *J. Am. Chem. Soc.* **2006**, *128*, 14008.
- (9) (a) Ise, T.; Ishida, T.; Nogami, T. *Bull. Chem. Soc. Jpn.* **2002**, *75*. (b) Ise, T.; Ishida, T.; Nogami, T. *Mol. Cryst. Liq. Cryst.* **2002**, *379*, 147.
- (10) Kitano, M.; Ishimaru, Y.; Inoue, K.; Koga, N.; Iwamura, H. *Inorg. Chem.* **1994**, *33*, 6012.
- (11) Fischer, H.; Stumpf, R.; Roth, G. *Adv. Organomet. Chem.* **1999**, *43*, 125.
- (12) Gruber, S. J.; Harris, C. M.; Sinn, E. *J. Chem. Phys.* **1968**, *49*, 2183.
- (13) Jotham, R. W.; Kettle, S. F.; Marks, J. A. *J. Chem. Soc., Faraday Trans. 2* **1976**, 125.
- (14) Frisch, M. J.; Trucks, G. W.; Schlegel, H. B.; Scuseria, G. E.; Robb, M. A.; Cheeseman, J. R.; Montgomery, J. A., Jr.; Vreven, T.; Kudin, K. N.; Burant, J. C.; Millam, J. M.; Iyengar, S. S.; Tomasi, J.; Barone, V.; Mennucci, B.; Cossi, M.; Scalmani, G.; Rega, N.; Petersson, G. A.; Nakatsuji, H.; Hada, M.; Ehara, M.; Toyota, K.; Fukuda, R.; Hasegawa, J.; Ishida, M.; Nakajima, T.; Honda, Y.; Kitao, O.; Nakai, H.; Klene, M.; Li, X.; Knox, J. E.; Hratchian, H. P.; Cross, J. B.; Bakken, V.; Adamo, C.; Jaramillo, J.; Gomperts, R.; Stratmann, R. E.; Yazyev, O.; Austin, A. J.; Cammi, R.; Pomelli, C.; Ochterski, J. W.; Ayala, P. Y.; Morokuma, K.; Voth, G. A.; Salvador, P.; Dannenberg, J. J.; Zakrzewski, V. G.; Dapprich, S.; Daniels, A. D.; Strain, M. C.; Farkas, O.; Malick, D. K.; Rabuck, A. D.; Raghavachari, K.; Foresman, J. B.; Ortiz, J. V.; Cui, Q.; Baboul, A. G.; Clifford, S.; Cioslowski, J.; Stefanov, B. B.; Liu, G.; Liashenko, A.; Piskorz, P.; Komaromi, I.; Martin, R. L.; Fox, D. J.; Keith, T.; Al-Laham, M. A.; Peng, C. Y.; Nanayakkara, A.; Challacombe, M.; Gill, P. M. W.; Johnson, B.; Chen, W.; Wong, M. W.; Gonzalez, C.; Pople, J. A. *Gaussian03*, revision C.02; Gaussian, Inc.: Wallingford, CT, USA, 2004.

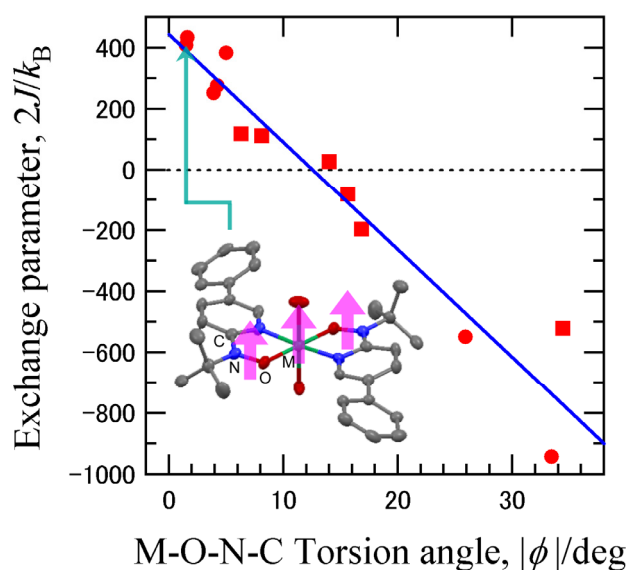
- (15) Kahn, O.; Prins, R.; Reedijk, J.; Thompson, J. S. *Inorg. Chem.* **1987**, *26*, 3557.
- (16) (a) Iwamura, H. *Adv. Phys. Org. Chem.* **1990**, *26*, 179. (b) Rajca, A. *Chem. Rev.* **1994**, *94*, 871.
(c) Ishida, T.; Iwamura, H. *J. Am. Chem. Soc.* **1991**, *113*, 4238.
- (17) Bondi, A. *J. Phys. Chem.* **1964**, *68*, 441.
- (18) McConnell, H. M. *J. Chem. Phys.* **1963**, *39*, 1910.
- (19) Imachi, R.; Ishida, T.; Suzuki, M.; Yasui, M.; Iwasaki, F.; Nogami, T. *Chem. Lett.* **1997**, 743.
- (20) (a) Zheludev, A.; Barone, V.; Bonnet, M.; Delley, B.; Grand, A.; Ressouche, E.; Rey, P.; Subra, R.; Schweizer, J. *J. Am. Chem. Soc.* **1994**, *116*, 2019. (b) Awaga, K.; Inabe, T.; Maruyama, Y. *Chem. Phys. Lett.* **1992**, *190*, 349.
- (21) Lee, T. D.; Keana, J. F. W. *J. Org. Chem.* **1975**, *40*, 3145.
- (22) CRYSTALSTRUCTURE, *Crystal Structure Analysis Package*, version 3.7.0; Rigaku/MSK: The Woodlands, TX, USA, 2003.
- (23) Becke, A. D. *J. Chem. Phys.* **1993**, *98*, 5648.
- (24) Lee, C.; Yang, W.; Parr, R. G. *Phys. Rev. B* **1998**, *37*, 785.
- (25) (a) Ruiz, E.; Cano, J.; Alvarez, S.; Alemany, P. *J. Comput. Chem.* **1999**, *20*, 1391. (b) Noodleman, L.; Peng, C. Y.; Case, D. A.; Mouesca, J. M. *Coord. Chem. Rev.* **1995**, *144*, 199.

Chapter 7

Magneto-Structure Relationship in Copper(II) and Nickel(II) Complexes Chelated with Stable *tert*-Butyl 5-Phenyl-2-pyridyl Nitroxide and Related Radicals

Abstract

We have isolated and characterized a new paramagnetic bidentate ligand, *tert*-butyl 5-phenyl-2-pyridyl nitroxide (phpyNO). Complexation of phpyNO with nickel(II) and copper(II) ions gave ML_2 -type chelated compounds. The magnetic measurements of $[Ni(phpyNO)_2(H_2O)_2](ClO_4)_2$ and $[Cu(phpyNO)_2(H_2O)](ClO_4)_2 \cdot C_6H_4Cl_2$ revealed that the metal–radical exchange couplings were strongly ferromagnetic with $2J/k_B = +409(10)$ and $+434(12)$ K, respectively. The torsion angle (ϕ) around $M-O-N-C_{2py}$ can be regarded as a reliable indicator for the plane geometry of chelates; namely, highly planar chelates defined by small ϕ exhibit ferromagnetic coupling. An approximate linear relation was found in the J versus ϕ plot using the data of the present complexes and related known compounds. The critical angle of ϕ , at which the sign of the metal–radical exchange changes from positive to negative, was $12.6(9)^\circ$. This finding could be almost reproduced by DFT calculation on a model copper(II)–nitroxide dyad. The exchange couplings in equatorially coordinated copper(II)– and nickel(II)–nitroxide complexes are very strongly ferromagnetic by nature.



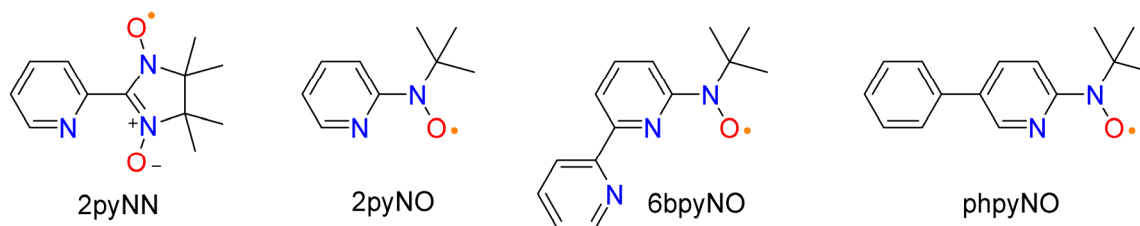
7.1 Introduction

Metal-radical hybrid solids have been well investigated for molecule-based magnets, where a radical center is directly bonded to the metal ion, affording considerably large magnetic exchange coupling.¹ Various 2-pyridyl-substituted ligands containing a paramagnetic $S = 1/2$ center such as nitronyl nitroxide (NN) groups²⁻⁴ have been known to form chelate rings (see Scheme 7.1 for their structural formulas). We have proposed *tert*-butyl 2-pyridyl nitroxide (2pyNO) as a promising candidate for such purpose. However, the simple pyridyl-NOs have been reported to be unisolable⁵ as already described in Chapter 6.

The ferromagnetic couplings are explained in terms of the orthogonality between the π^* -type SOMO of the radical and the $d\sigma$ -type SOMO(s) of nickel(II) ($3d^8$; $S_{Ni} = 1$) and copper(II) ions ($3d^9$; $S_{Cu} = 1/2$).^{2-4,6,7} The mother skeleton 2pyNO should be handled much more delicately than 6bpyNO. The 2pyNO-chelated compounds were successfully synthesized by a trapping method with suitable transition metal ions, without isolation of 2pyNO.

We propose here a new candidate, *tert*-butyl 5-phenyl-2-pyridyl nitroxide (abbreviated as phpyNO), as a paramagnetic ligand. An additional phenyl group at the pyridine 5-position will facilitate isolation because substitution at the para position with respect to the nitroxide radical group is quite effective for stabilization.^{5,8} Actually, this modification enabled us to utilize phpyNO as an isolable synthetic intermediate. After a chelation reaction of phpyNO with copper(II) or nickel(II) ions, we determined the molecular structures by means of X-ray crystallographic analysis and evaluated magnetic couplings between nitroxide radical spins and copper(II) or nickel(II) spins. The relationship between the geometry and intramolecular metal-radical magnetic coupling will be discussed. There are many geometrical freedoms of the atoms involved in the chelate structure, and one may wonder what would be a good parameter for describing the orthogonal geometry. No simple magnetostructure relationship has been reported to date, including the works on nitronyl nitroxide ligands as well as nitroxide ones, before our work demonstrated in Chapter 6.⁷ We will show a satisfactory relation by choosing a single geometrical parameter.

Scheme 7.1. Structural Formulas of 2-Pyridyl-Substituted Radicals with Chelating Ability



7.2 Results

7.2.1 Characterization of phpyNO

We synthesized and isolated a paramagnetic ligand, phpyNO. The precursory hydroxylamine phpyNOH was prepared according to the conventional method,^{6,8} and the oxidation with Ag₂O gave phpyNO, which could be purified by passing through silicagel column chromatography. The spectroscopic measurements of phpyNO satisfied the molecular formula. This compound crystallizes at room temperature under air, and the crystal structure was determined by means of X-ray diffraction study (Figure 7.1a). The nitroxide nitrogen atom is highly planar, whereas the hydroxylamine nitrogen atom pyramidalized. The N–O bond distance in phpyNO is 1.2900(15) Å, which is in a typical range for aromatic *tert*-butyl nitroxide,⁹ and much shorter than the corresponding bond length in phpyNOH (1.4550(12) Å). Such a change of the N–O distance is important when we determine the nominal charge of the N–O group in the complexes of phpyNO and related compounds. The nitroxide oxygen atom is located at the transoid position with respect to the pyridine nitrogen atom, but the C1–N2 bond freely rotates during the complexation reaction.

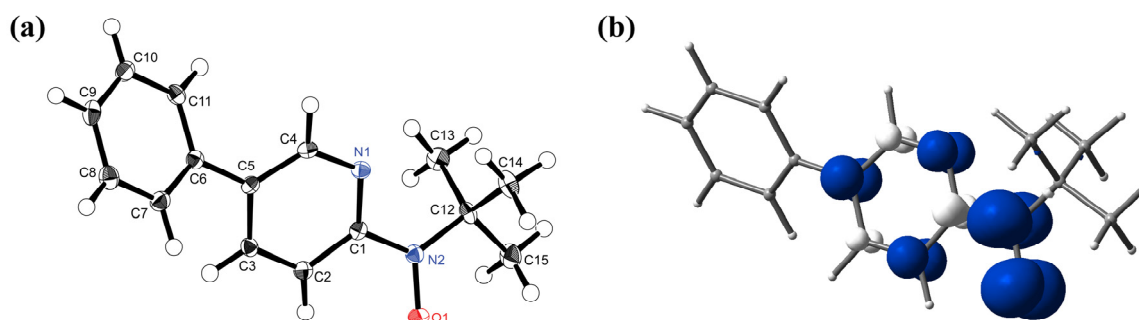


Figure 7.1. (a) Molecular structure of phpyNO with thermal ellipsoids at the 50% probability level non-hydrogen atoms. (b) Spin density surface of phpyNO calculated at the DFT UB3LYP/6–311G(d,p) level. Blue, positive spin; light gray, negative spin. The isocontour value is set to 0.004.

The solution EPR spectra of phpyNO and 2pyNO are shown in Figure 7.2. The phenyl group in phpyNO masks one of the proton splittings, but the EPR spectrum of phpyNO was not simplified, because additional hyperfine splittings took place from the phenyl protons. We analyzed the hyperfine splitting constants of phpyNO as well as those of 2pyNO (Figure 7.2b).

We estimated the spin distribution on the pyridine ring from the McConnell relation, $a_H = Q_C \rho_C$,¹⁰ where ρ_C stands for spin density at the aromatic carbon atom connected with the proton (Table 7.1). We applied $\rho_C = -2.45$ mT proposed for azaaromatic rings.¹¹ As for the pyridine nitrogen, a similar equation, $a_N = Q_N \rho_N$ with $Q_N = +2.5$ mT,¹² is available to estimate directly the spin density at

the nitrogen atom (ρ_N). The sign could not be determined solely from the EPR data, but there have been many examples describing the spin-polarization¹³ leading to alternating spin density on the aromatic groups including pyridines.¹⁴ DFT calculations supported the determination of the sign (Figure 7.1b for phpyNO), in which the geometry was optimized because the experimental data were obtained in a solution, and the magnitudes are also consistent with the experiments (Table 7.1). The polarized spin density calculated by DFT was slightly overestimated compared with those of the EPR results.

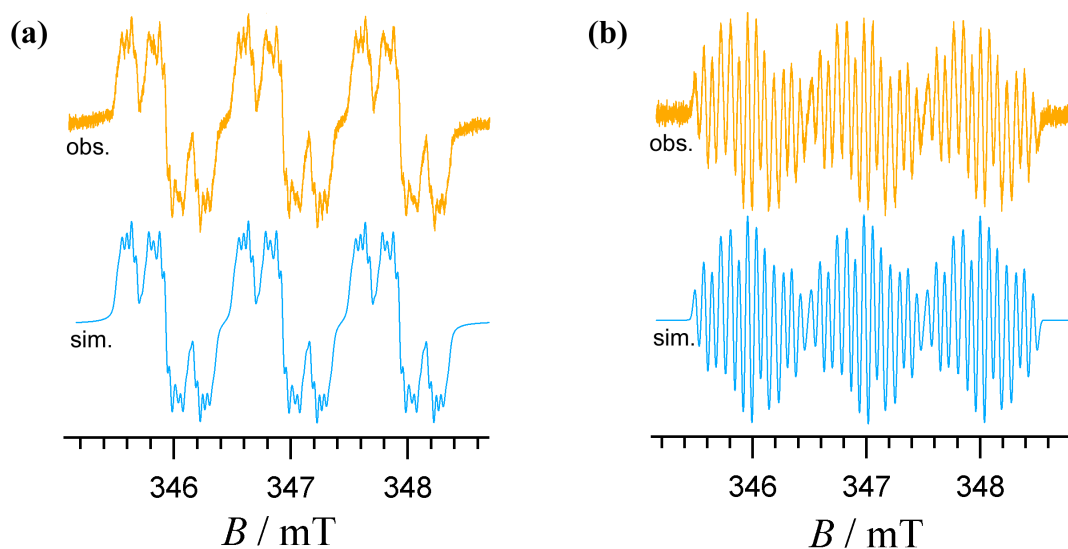


Figure 7.2. X-band EPR spectra of (a) phpyNO and (b) 2pyNO in toluene at room temperature (orange line). Simulated spectra are also shown (blue line).

7.2.2 Crystal Structure Analysis of the Copper(II) and Nickel(II) Complexes

Because phpyNO has a π^* -type SOMO as illustrated in Figure 7.1b, we focused our attention on transition metal ions having $d\sigma$ -type magnetic orbitals, such as nickel(II) and copper(II) ions, to bestow the orthogonal arrangement between them at the direct nitroxide–metal bond. Actually, we prepared several chelated compounds with phpyNO according to a method similar to those of the 2pyNO and 6bpyNO complexes.⁶ Simply mixing of phpyNO with divalent metal salts in appropriate organic solvents gave polycrystals of ML_2 -type compounds: $[\text{Ni}(\text{phpyNO})_2(\text{H}_2\text{O})_2](\text{ClO}_4)_2$ (**1**), $[\text{Cu}(\text{phpyNO})_2(\text{ClO}_4)_2]\cdot\text{CH}_2\text{Cl}_2$ (**2**), $[\text{Cu}(\text{phpyNO})_2(\text{H}_2\text{O})](\text{ClO}_4)_2\cdot\text{C}_6\text{H}_4\text{Cl}_2$ (**3**), and $[\text{Cu}(\text{phpyNO})_2(\text{CF}_3\text{SO}_3)_2]\cdot 0.35\text{H}_2\text{O}$ (**4**). They were characterized by means of elemental analysis and IR spectroscopy, and finally their molecular structures were successfully determined by means of X-ray crystallographic analysis (Figure 7.3 and Tables 7.2 and 7.3).

Table 7.1. Observation Hyperfine Splitting Constants, Spin Densities, and Calculated Spin Densities for phpyNO and 2pyNO

compounds	a_x/mT^{a}	ρ_C, ρ_N (experiments) ^{b)}	ρ_C, ρ_N (calculation) ^{c)}	
phpyNO	$a_{\text{N(NO)}}$	1.000	0.340	
	$a_{\text{N(py)}}$	0.143	$\rho_{\text{N(py)}}$ 0.057	0.113
	$a_{\text{H3(py)}}$	0.240	$\rho_{\text{C3(py)}}$ 0.099	0.125
	$a_{\text{H4(py)}}$	0.080	$\rho_{\text{C4(py)}}$ (-)0.033	-0.056
	$a_{\text{H6(py)}}$	0.080	$\rho_{\text{C6(py)}}$ (-)0.033	-0.059
	$a_{\text{H(o,p-ph)}}$	0.037	$\rho_{\text{C(o,p-ph)}}$ 0.015	0.020 ^{d)}
2pyNO	$a_{\text{N(NO)}}$	1.023	0.345	
	$a_{\text{N(py)}}$	0.143	$\rho_{\text{N(py)}}$ 0.057	0.090
	$a_{\text{H3(py)}}$	0.243	$\rho_{\text{C3(py)}}$ 0.099	0.114
	$a_{\text{H4(py)}}$	0.070	$\rho_{\text{C4(py)}}$ (-)0.031	-0.054
	$a_{\text{H5(py)}}$	0.243	$\rho_{\text{C5(py)}}$ 0.099	0.119
	$a_{\text{H6(py)}}$	0.070	$\rho_{\text{C6(py)}}$ (-)0.031	-0.057

a) Measured in toluene at room temperature. The g values were 2.0060 and 2.0061 for phpyNO and 2pyNO, respectively. b) Estimated from the McConnell relations, $a_{\text{N}} = Q_{\text{N}}\rho_{\text{N}}$ with $Q_{\text{N}} = +2.5$ mT for pyridine nitrogen atoms and $a_{\text{H}} = Q_{\text{C}}\rho_{\text{C}}$ with $Q_{\text{C}} = -2.45$ mT for pyridine carbon atoms. Negative signs are assumed from the spin-polarization scheme. c) DFT calculation at the UB3LYP/6-311G(d,p) level after geometries were optimized at the UB3LYP/6-31G(d,p) level. d) Averaged on those of two ortho and one para positions.

We can find five-membered chelate rings involving a nitroxide group in every compound. In the molecule of **1** (Figure 7.3a), two water molecules occupy the axial position with respect to the chelate plane, and the counteranion ClO_4 is located in the clearance of the crystal. A 2_1 screw axis runs through O2-Ni1-O3 . The N1-O1 bond length is 1.306(3) Å, supporting that the phpyNO ligand is paramagnetic. The Ni-O and $-\text{N}$ distances of 1.981(2) – 2.078(3) Å imply an octahedral structure with $S_{\text{Ni}} = 1$. The planar chelate ring guarantees the orthogonal arrangement between nickel d_{or} orbitals (i.e., $3d_{x^2-y^2}$ and $3d_{z^2}$) and nitroxide π^* -orbital. We have proposed that the torsion angle along $\text{M-O-N-C}_{2\text{py}}$ is convenient as an indicator of the planar character.³ The Ni1-O1-N2-C1 torsion angle in **1** is very small (1.5(3)°).

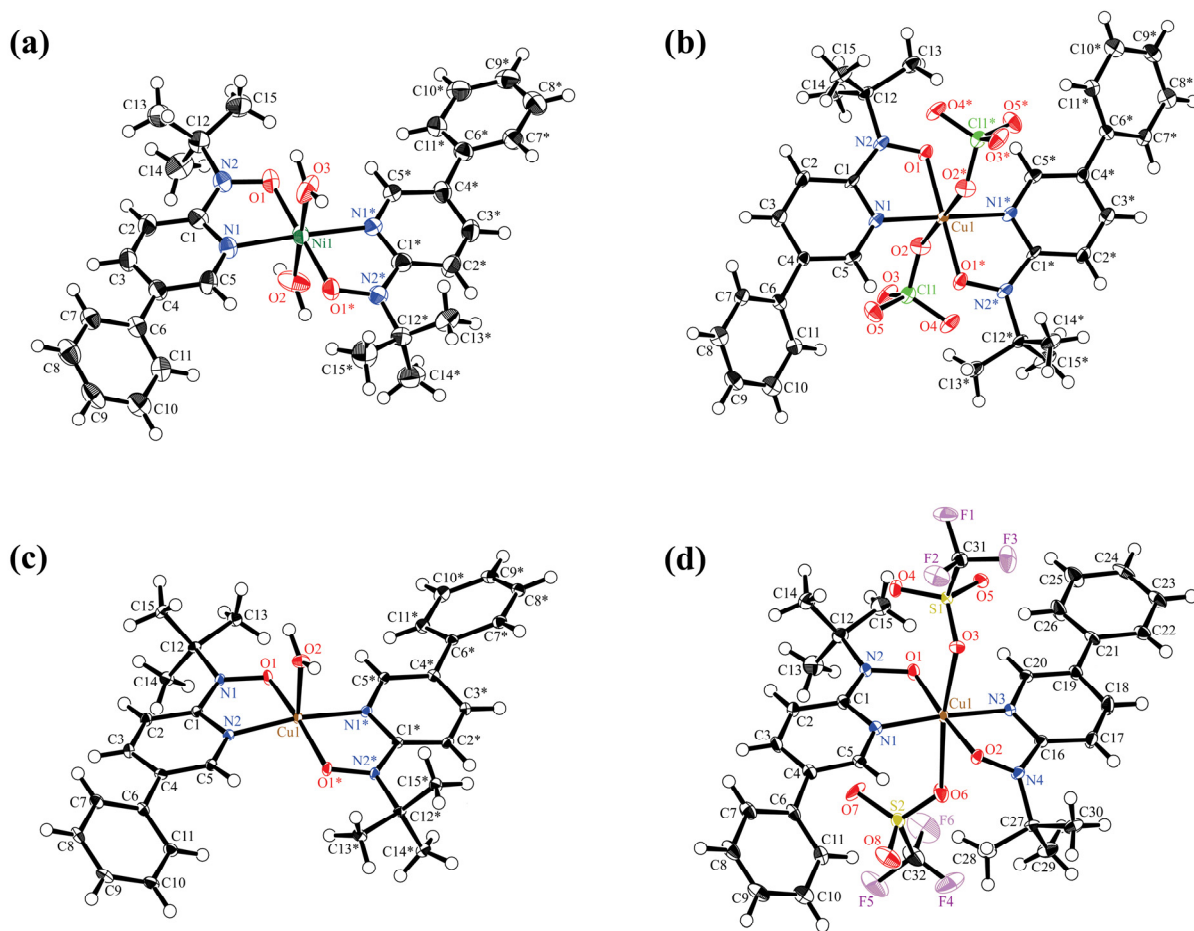


Figure 7.3. Molecular structure of (a) $[\text{Ni}(\text{phpyNO})_2(\text{H}_2\text{O})_2]^{2+}$ in **1**, (b) $[\text{Cu}(\text{phpyNO})_2(\text{ClO}_4)_2]$ in **2**, (c) $[\text{Cu}(\text{phpyNO})_2(\text{H}_2\text{O})_2]^{2+}$ in **3**, and (d) $[\text{Cu}(\text{phpyNO})_2(\text{CF}_3\text{SO}_3)_2]$ in **4** with thermal ellipsoids at the 50% probability level for non-hydrogen atoms. Atom numbering schemes are also shown. Only a major conformer is shown in (d).

The molecule of **2** has an inversion center at the metal ion in the space group $P\bar{1}$ (Figure 7.3b). The crystal solvent molecules (dichloromethane) were incorporated in the clearance. Two perchlorate ions are coordinated at the axial positions, like $[\text{Cu}(\text{2pyNO})_2(\text{ClO}_4)_2]$. The Jahn–Teller distortion is found as usual; the copper(II) ion forms an elongated octahedron with the somewhat long axial Cu1–O2 distance (2.492(6) Å), compared with the equatorial Cu1–O1 and Cu1–N1 bonds. The Cu1–O1–N2–C1 torsion angle remains relatively small ($-4.2(8)^\circ$), in comparison with that of $[\text{Cu}(\text{2pyNO})_2(\text{ClO}_4)_2]$ ($25.9(5)^\circ$). This geometry indicates the approximate orthogonal arrangement between copper $d\sigma$ orbital ($3d_{x^2-y^2}$) and nitroxide π^* orbital in **2**.

In the preparation of **2**, a minor impurity was found from one batch, and accordingly pure **2** could be manually picked up under a microscope and subjected to crystallographic analysis. From the elemental analysis on a bulk specimen, the ML_2 -composition was unequivocally confirmed, but the ratio of the solvated molecules depended on the preparation batches. A preliminary crystal structure analysis of the impurity portion indicated the formula of $[\text{Cu}(\text{phpyNO})_2(\text{ClO}_4)_2] \cdot 0.24\text{CH}_2\text{Cl}_2$ (**2'**)

crystallized in a monoclinic $C2/c$ space group as a pseudopolymorph. A somewhat distorted chelate ring was found as $\phi = 12.9(7)^\circ$ after the refinement down to $R(F)$ ($I > 2\sigma(I)$) of 0.158.

To avoid the polymorph problem of **2** and **2'**, we tried to prepare and purify specimens from other solvents and finally found a good crystalline product (**3**) from 1,2-dichlorobenzene (Figure 7.3c). The copper ion in **3** has a square pyramid structure with a water molecule at an axial position. The Cu1–O2 distance (2.146(2) Å) is longer than those of Cu1–O1 and Cu1–N1, and a 2-fold axis is located on the Cu1–O2 bond. The copper ion is slightly deviated from the basal plane as indicated with the O1–Cu1–O1* and N1–Cu1–N1* angles of 166.76(7) and 167.70(8)°, respectively. The chelate ring is highly planar with $\phi = 1.6(2)^\circ$.

Table 7.2. Selected Bond Lengths (Å) and Angles (degree) for **1–3**

compounds	1 (M = Ni)	2 (M = Cu)	3 (M = Cu)
M1–O1	1.981(2)	1.934(3)	1.9481(13)
M1–N1	2.035(2)	1.939(4)	1.961(2)
M1–O2	2.078(3)	2.492(6)	2.146(2)
M1–O3	2.071(3)		
O1–N2	1.306(3)	1.301(6)	1.309(3)
N2–C1	1.403(4)	1.404(5)	1.399(3)
O1–M1–N1	79.64(10)	81.69(16)	80.81(7)
M1–O1–N2	114.56(18)	113.2(2)	114.66(11)
O1–N2–C1	118.0(2)	117.7(4)	128.918(3)
O1–M1–O2	90.35(8)	92.24(18)	96.62(5)
N1–M1–O2	87.69(8)	87.7(2)	96.15(5)
O1–M1–O3	89.65(8)		
N1–M1–O3	92.31(8)		
M1–O1–N2–C1	1.5(3)	–4.2(8)	–1.6(2)
N1–M1–O1–N1	–4.7(2)	0.4(4)	1.65(14)
O2–M1–O1–N2	82.9(2)	87.7(4)	–93.54(13)
O3–M1–O1–N2	–97.1(2)		

Table 7.3. Selected Bond Lengths (Å) and Angles (degree) for **4**

Cu1–O1	1.9316(19)	Cu1–O2	1.9491(18)
Cu1–N1	1.9281(19)	Cu1–N3	1.9459(19)
Cu1–O3	2.4314(16)	Cu1–O6	2.5922(18)
N2–O1	1.304(2)	N4–O2	1.303(2)
N2–C1	1.391(3)	N4–C16	1.400(3)
N1–Cu1–O1	81.83(8)	N3–Cu1–O2	80.69(7)
Cu1–O1–N2	113.96(15)	Cu1–O2–N4	110.32(14)
O1–N2–C1	116.62(2)	O2–N4–C16	114.54(19)
O1–Cu1–O3	89.92(6)	O2–Cu1–O3	88.04(6)
O1–Cu1–O6	96.54(6)	O2–Cu1–O6	85.23(6)
Cu1–O1–N2–C1	–4.9(2)	Cu1–O2–N4–C16	33.4(2)
N1–Cu1–O1–N2	2.42(14)	N3–Cu1–O2–N4	–23.78(13)
O3–Cu1–O1–N2	–95.32(14)	O3–Cu1–O2–N4	–114.55(13)
O6–Cu1–O1–N2	89.96(14)	O6–Cu1–O2–N4	60.54(13)

The molecular structure of **4** is unsymmetrical, and accordingly two nitroxide groups are crystallographically independent (Figure 7.3d). The space group is $P\bar{1}$, but the inversion center resides at the middle of two neighboring molecules. We found a disorder in the trifluoromethanesulfonate group involving S2 and C32. Their positions are related by a rotation around the Cu1–O6 with the optimized occupancy factors of 0.526(3)/0.474(3). Figure 7.3d shows a major conformation. The geometry of the chelate core does not show any disorder. The bond lengths around the copper ion (1.9281(19) – 1.9491(18) Å) are close to those for **2** and **3**. Two torsion angles are $-4.9(2)$ and $33.4(2)^\circ$ for Cu1–O1–N2–C1 and Cu1–O2–N4–C16, respectively. The sterically bulky axial groups seem responsible for the deformation of the latter chelate ring, giving the severe torsion, while the former chelate ring remains highly planar. There is a solvated water molecule in a clearance with the optimized occupancy of 0.354(8).

7.2.3 Intermolecular Magnetic Coupling

Magnetic susceptibilities of polycrystalline **1–4** were measured on a SQUID magnetometer. Upon cooling from 300 to 2 K, the $\chi_{\text{mol}}T$ values of **1–3** increased once, indicating the presence of

intramolecular ferromagnetic interactions (Figure 7.4a). The spin-only values are 3.0 and 1.875 cm³ K mol⁻¹ for **1** ($S_{\text{total}} = 2$) and for **2** and **3** ($S_{\text{total}} = 3/2$), respectively. The $\chi_{\text{mol}}T$ values at their maximum clearly indicate that they have high spin ground states. The final drops of the $\chi_{\text{mol}}T$ values are assigned to intermolecular antiferromagnetic couplings.

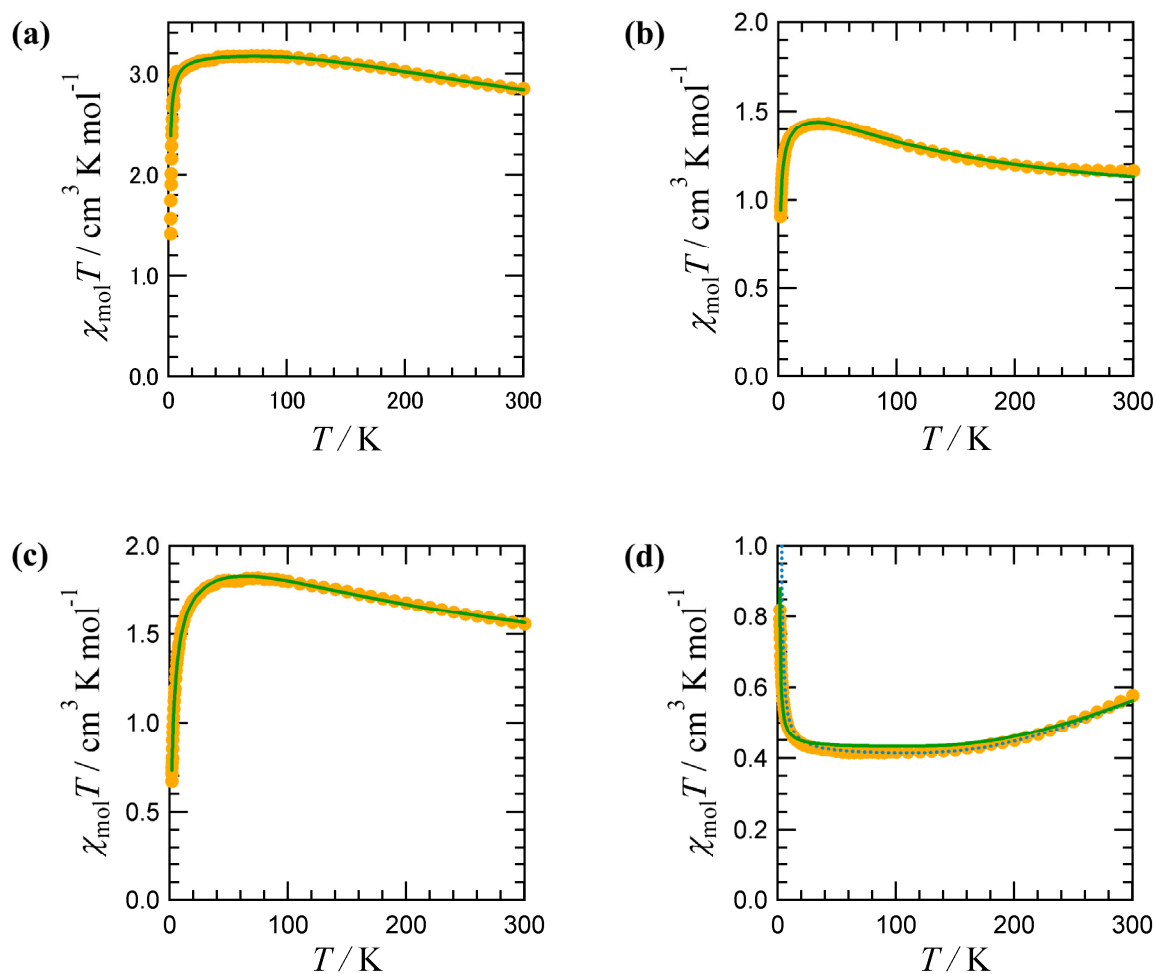


Figure 7.4. (a) Temperature dependence of $\chi_{\text{mol}}T$ (orange circles) for (a) **1**, (b) **2**, (c) **3**, and (d) **4**. The applied magnetic field were 500Oe. The green solid and blue dotted lines represent curves. See the text for the equations and optimized parameters.

For **1–3**, the metal–radical interaction is unique owing to the 2-fold or inversion symmetry, and accordingly the Heisenberg spin Hamiltonian was defined as $\mathcal{H} = -2J(\hat{S}_1 \cdot \hat{S}_2 + \hat{S}_2 \cdot \hat{S}_3)$ for a three-centered system, in which coupling between the terminal ions was disregarded.^{15,16} Thus, we applied the van Vleck equation to our systems, giving the following expressions, eqs 7.1 and 7.2 for the nickel(II) and copper(II) complexes, respectively.¹⁷

$$\chi_{\text{mol}} = \frac{2N_{\text{A}}g_{\text{avg}}^2\mu_{\text{B}}^2}{k_{\text{B}}(T-\theta)} \frac{\exp(-2J/k_{\text{B}}T) + 1 + 5\exp(2J/k_{\text{B}}T)}{\exp(-4J/k_{\text{B}}T) + 3\exp(-2J/k_{\text{B}}T) + 3 + 5\exp(2J/k_{\text{B}}T)} \quad (7.1)$$

$$\chi_{\text{mol}} = \frac{N_{\text{A}}g_{\text{avg}}^2\mu_{\text{B}}^2}{4k_{\text{B}}(T-\theta)} \frac{\exp(-2J/k_{\text{B}}T) + 1 + 10\exp(J/k_{\text{B}}T)}{\exp(-2J/k_{\text{B}}T) + 1 + 2\exp(J/k_{\text{B}}T)} \quad (7.2)$$

The experimental data were fitted to these equations, and the parameters were optimized as summarized in Table 7.4. A Weiss mean field parameter θ was introduced for intermolecular antiferromagnetic couplings and also for the ZFS of the nickel(II) ion in **1**. Because **2** (space group $P\bar{1}$) was contaminated with **2'** ($C2/c$), the purity factor ρ was defined and used for the molar fraction of **2**, on the assumption of the presence of a ground doublet species from **2'** as an $S = 1/2$ paramagnetic impurity.¹⁸ The parameter ρ was optimized to be 0.844(2) with the g_{avg} value fixed to 2. The impurity contribution was relatively small in this measurement. The calculation fit was satisfactory (Figure 7.4b). The J value hardly depended on the variation of ρ , implying that obtained J value of **2** is reliable. There is no impurity problem in **3**, and we simply applied eq 7.2, giving the largest class of the J value ($2J/k_{\text{B}} = +434(12)$ K).

On the other hand, we characterized a ground low-spin state for **4** (Figure 7.4d). The experimental $\chi_{\text{mol}}T$ value of **4** decreased on cooling and reached to a plateau at $\chi_{\text{mol}}T = \sim 0.4$ cm³ K mol⁻¹ around 100 K, which is close to the spin only $S_{\text{total}} = 1/2$ value. A final $\chi_{\text{mol}}T$ upsurge is assigned to intermolecular ferromagnetic coupling. We have to adopt an unsymmetrical model, $\mathcal{H} = -2J_{12}\hat{S}_1 \cdot \hat{S}_2 - 2J_{23}\hat{S}_2 \cdot \hat{S}_3$, because the two terminal ions are crystallographically independent. We at first used eq 7.3 for the analysis of the magnetic data.¹⁶

$$\chi_{\text{mol}} = \frac{N_{\text{A}}g_{\text{avg}}^2\mu_{\text{B}}^2}{4k_{\text{B}}(T-\theta)} \times \frac{\text{A}}{\text{B}} \quad (7.3)$$

where

$$\text{A} = \exp(-2\sqrt{J_{12}^2 + J_{23}^2 - J_{12}J_{23}}/k_{\text{B}}T) + 1 + 10\exp((J_{12} + J_{23} - \sqrt{J_{12}^2 + J_{23}^2 - J_{12}J_{23}})/k_{\text{B}}T)$$

$$\text{B} = \exp(-2\sqrt{J_{12}^2 + J_{23}^2 - J_{12}J_{23}}/k_{\text{B}}T) + 1 + 2\exp((J_{12} + J_{23} - \sqrt{J_{12}^2 + J_{23}^2 - J_{12}J_{23}})/k_{\text{B}}T)$$

We obtained negative J_{12} and positive J_{23} values for **4** from fitting with eq 7.3 and found the obtained J_{23} value accompanied by a large statistical error. The reason may reside in the strong S_1 - S_2 pairing, leading to a trivial magnetic coupling between a doublet S_3 and a ground singlet S_1 - S_2 . In other words, J_{23} is insensitive to the $\chi_{\text{mol}}T$ versus T profile. Therefore, we utilized another equation consisting of a sum of a doublet term and a singlet-triplet equilibrium term¹⁹ (eq 7.4), assuming the condition of $J_{23} \ll |J_{12}|$. The Weiss mean field parameter was introduced. The optimized $2J_{12}$ was $-940(30)$ K with $\theta = +0.909(1)$ K (Table 7.4). The calculated $\chi_{\text{mol}}T$ versus T curve reproduced well

the experimental data as shown with the solid line in Figure 7.4d. Although we cannot tell a priori which exchange interaction, J_{12} or J_{23} , of **4** would be assigned to each crystallographically independent copper–radical relation solely from the magnetic analysis, the negative one (J_{12}) is inferred to correspond to the largely twisted side (see below).

$$\chi_{\text{mol}} = \frac{N_{\text{A}} g_{\text{avg}}^2 \mu_{\text{B}}^2}{k_{\text{B}}(T - \theta)} \left(\frac{1}{4} + \frac{2}{3 + \exp(-2J_{12}/k_{\text{B}}T)} \right) \quad (7.4)$$

We have to mention briefly the intermolecular ferromagnetic coupling in the crystal of **4**. Figure 7.5 depicts a relatively short π – π type interaction between pyridine rings in neighboring molecules, which are related with centrosymmetry. The distance of C17 and C18# (3.594(3) Å) is close to the sum of the van der Waals radii,²⁰ and the ferromagnetic coupling can be explained by the spin-polarization scheme^{13,14,21,22} throughout the py–py contact (the arrows in Figure 7.5), since the pyridine ring in phpyNO is appreciably spin-polarized, as evidenced by the EPR experiments. The weak intermolecular contact seems responsible for the small magnitude of the θ value.

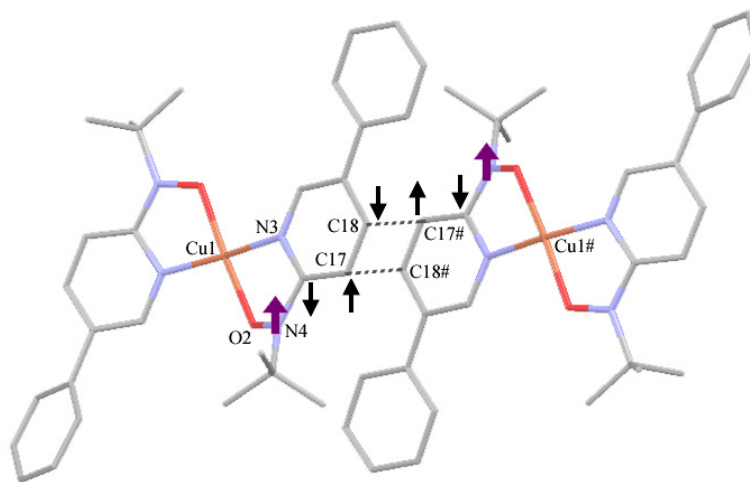


Figure 7.5. Molecular arrangement in the crystal of **4**. The axial ligands (triflate) and hydrogen atoms are omitted for clarity. Dotted lines indicate the interatomic contacts of 3.594(3) Å between C17 and C18#, where the symmetry operation code of # is $1 - x, 1 - y, z$. A possible spin polarization scheme is shown with arrows.

7.3 Discussion

7.3.1 Magneto-Structure Relationship

We have found intramolecular metal–radical magnetic couplings varying in a considerably wide range from relatively small structural modifications. This family will lead to an insight into a detailed magneto-structure relationship. There are many parameters defining the mutual geometry

around the radical N–O group and transition metal center. To simplify the discussion, we disregard several features commonly possessed by all of the compounds investigated here. The M–O distances range from 1.9316(19) – 1.981(2) Å, and the M–O–N angles vary from 110.32(14) – 114.66(11)°. The deviation of the axial ligand from the normal of the basal plane is indicated by the $O_{\text{eq}}\text{--M--}O_{\text{ax}}$ angles (85.23(6) – 96.62(5)°). These parameters are basically important in the exchange coupling between the metal and nitroxide spins. However, they made practically no difference in the magnetic coupling within a series of the present compounds. As we described above, the most important parameter is an indicator for the out-of-plane dislocation from the chelate ring with respect to the N–O–M moiety. We can regard the torsion around the M–O–N–C_{2py} skeleton as a representative of the geometry. The N_{py}–M–O–N torsion seems to be another candidate, but the former is more sensitive to the dislocation of the nitroxide O and N atoms from the chelate plane.

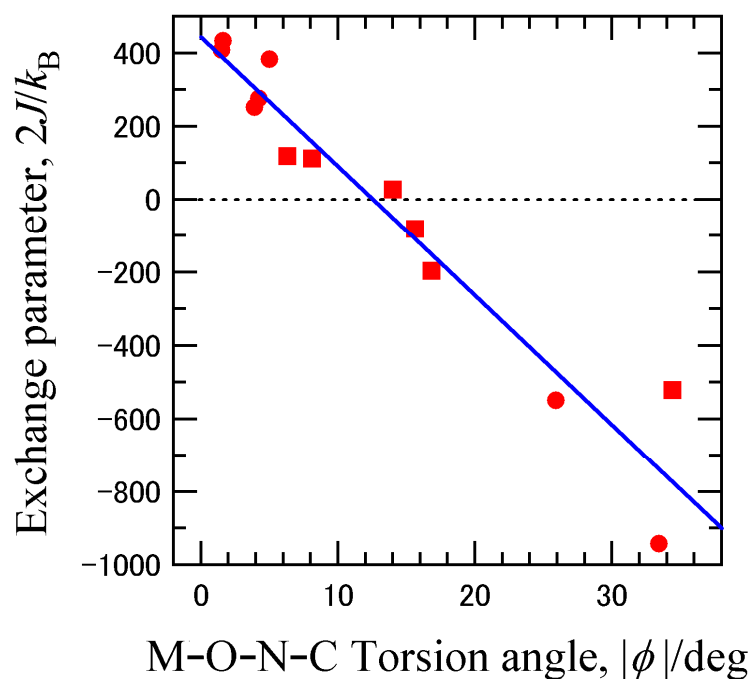


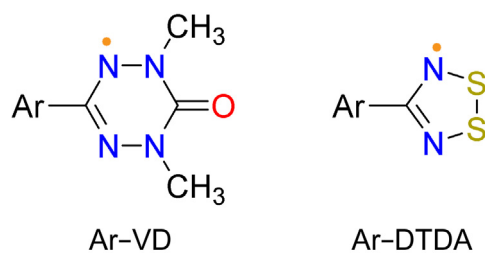
Figure 7.6. Plot of the observed exchange coupling parameter ($2J$) versus M–O–N–C_{2Ar} torsion angle ($|\phi|$) as a magneto-structure relationship in the nickel(II) or copper(II) complexes listed in Table 7.4. Circles and squares denote the data on the Ar–NO and Ar–NN complexes, respectively. The reported $2J$ for Ar–NN complexes are multiplied by a factor of 1.4 (see text).

We can draw a plot of J versus $|\phi|$ for the copper(II) and nickel(II) complexes exhibiting equatorial chelation by nitroxide ligands (Figure 7.6). The copper(II) ion has a paramagnetic spin at $3d_{x^2-y^2}$, while the nickel(II) ion has two paramagnetic spins at $3d_{x^2-y^2}$ and $3d_{z^2}$. The $3d_{x^2-y^2}\text{--}\pi^*$ interaction dominantly contributes to the observed J , although $3d_{z^2}$ is orthogonal to π^* as well, viewing

from the short distance and mutual lobe direction between interacting SOMOs. Therefore the interaction of $3d_{x^2-y^2}-\pi^*$ in the nickel(II) complexes is comparable to that of the copper(II) complexes, and their data are superposed in one plot. A significant pyramidalization around the copper(II) ion was observed in $[\text{Cu}(\text{6bpyNO})\text{Cl}_2]$, and its data point was omitted.

Furthermore, the present argument holds also for the chelates of nitronyl nitroxide radicals. The spin density on the oxygen atom of Ar-NO is assumed to be much larger than that of the Ar-NN, owing to an almost half size spin delocalizable π -conjugation in the radical groups. More quantitative discussion needs the aid of the EPR study. The spin density at the ligating N-O oxygen atom is assumed to be approximately proportional to the a_{N} value of the nitroxide group. Typical a_{N} values of Ar-NO are 1.2 ± 0.2 mT,^{23,24} while those of Ar-NN are 0.74 ± 0.03 mT^{24a,25} (0.743 mT for phenyl NN in benzene²⁵ and 0.759 mT for 4-imidazolyl NN in toluene³). To superpose the data of the Ar-NN-based complexes in Figure 7.6, we multiplied the reported J values by a factor of 1.4 because the magnetic exchange coupling is proportional to the spin densities at the interacting atoms.²¹ An advantage of the Ar-NO system over not only the Ar-NN system²⁷ but also the Ar-VD²⁷ and Ar-DTDA²⁸ ones (Scheme 7.2 for the molecular structures) can be pointed out. Their spins are delocalized mainly onto conjugated N_2O_2 , N_4 , and N_2S_2 systems, respectively, as clarified by the EPR hyperfine data (a_{N} etc.), while the spin in the NO group is highly localized in two atoms. Thus, strong exchange couplings were realized in the present Ar-NO system.

Scheme 7.2. Structural Formulas of Aryl-Substituted Oxoverdazyl (VD) and Dithiadiazolyl (DTDA)



Antiferromagnetic couplings were often observed in the copper(II) and nickel(II) coordination compounds chelated with 2-azaaromatic NN ligands.^{3,26} The nickel(II) complex containing 2,2'-bipyridine-6,6'-diyl-bis (NN) (abbreviated as bpyNN₂ here after) exceptionally exhibited ferromagnetic coupling.²⁶ The tension operative in the fused 5- and 6-membered rings would regulate the M-O-N-C_{2Ar} structure to be more planar, like the case of the 6bpyNO complexes.⁶ Luneau et al. discussed the coplanarity between the radical and metal equatorial planes but did not report the torsion angle (ϕ) around M-O-N-C_{2Ar}. We calculated these angles from their Supporting Information data; $[\text{Ni}(\text{bpyNN}_2)(\text{H}_2\text{O})_2](\text{ClO}_4)_2$ showing $2J/k_{\text{B}} = -140$ and $+114$ K has M-O-N-C_{2Ar}

torsion angles of 16.8 and 0.3° (the latter exhibited a severe structural disorder), and [Ni(bpyNN₂)(H₂O)(ClO₄)](ClO₄) showing $2J/k_B = +80.0$ and $+19.8$ K has M–O–N–C_{2Ar} torsion angles of 8.1 and 14.0° (Table 7.4). These data totally obeyed the relation presented here, as indicated with the superposition in Figure 7.6.

The magneto-structural relationship is simply formulated as $2J/k_B = a + b|\phi|$ with $a = 440(50)$ K and $b = -35(3)$ K deg⁻¹ from Figure 7.6. The critical $|\phi|$, at which the sign of the metal–radical exchange coupling changes from positive to negative, is 12.6(9)°. Because an approximation (disregarding J_{23} in eq 7.4) was introduced in the analysis of the magnetic properties of **4** (see above), we reanalyze here the magnetic properties of **4** involving J_{23} in eq 7.3. The torsion of 4.9° leads to $2J_{23}/k_B = +270$ K from the relationship. The other parameters were optimized as $g_{\text{avg}} = 2.115(5)$, $2J_{12}/k_B = -964(14)$ K, and $\theta = +1.06(2)$ K, and the calculated $\chi_{\text{mol}}T$ versus T curve satisfactorily reproduced the experimental result (a dotted line in Figure 7.4b). The independently calculated values ($-940(30)$ and $-964(14)$ K) agree well with each other within a statistical error.

Table 7.4. Optimized Parameters, g_{ave} , J , θ , Together with the Torsion Angle $|\phi|$ for **1–4** and Related Compounds

compounds ^{a)}	g_{ave}	$2J/k_B^{-1}/\text{K}$	θ/K	$ \phi /\text{deg}$	reference ^{b)}
1	2.067(2)	+409(10)	-0.61(3)	1.5(3)	this work
2	2 ^{c)}	+276(4)	-1.18(1)	4.2(8)	this work
3	2.035(4)	+434(12)	-2.92(4)	1.6(2)	this work
4	2.139(8)	-940(30) ^{d)}	+0.909(1)	33.4(2), 4.9(2)	this work
[Ni(2pyNO) ₂ (H ₂ O) ₂](ClO ₄) ₂	2.112(4)	+252(6)	-3.45(5)	3.9(3)	Chapter 6
[Cu(2pyNO) ₂ (ClO ₄) ₂]	2.064(2)	-548(4)	+1.88(2)	25.9(5)	Chapter 6
[Ni(6bpyNO) ₂](PF ₆) ₂	2.082(1)	+384(4)	-0.67(1)	5.0(5) ^{e)}	ref 7
[Cu(6bpyNO)Cl ₂]	2.062(4)	+400(20)	-3.52(6)	10.7(2)	ref 7
[Ni(4ImNNH) ₂ (NO ₃) ₂]	2.06(1)	+85(3)	+1.04(3)	6.3(4)	ref 3
[Cu(4ImNNH) ₂ (NO ₃) ₂]	2.08(1)	-58(4)	0	15.6(4)	ref 3
[Cu(4ImNNH) ₂ Br ₂]	2.05(1)	-372(5)	+1.69(7)	34.4(6)	ref 3
[Ni(bpyNN ₂) ₂ (H ₂ O) ₂](ClO ₄) ₂	2.12	-140	-0.4	16.8	ref 27
[Ni(bpyNN ₂)(H ₂ O)(ClO ₄)](ClO ₄)	2.15	+80.0, +19.8	+1.0	8.1, 14.0	ref 27

a) 4ImNNH and bpyNN₂ stand for 4-imidazolyl nitronyl nitroxide and 2,2'-bipyridine-6,6'-diyl bis(nitronyl nitroxide), respectively. b) See Reference in the main text. c) A purity factor was optimized to be 0.844(2) with g_{ave} value fixed. d) Another parameter was estimated as $2J/k_B = \sim +270$ K from the J vs $|\phi|$ relations with 4.9(2)°. e) An averaged value on the geometries of four crystallographically independent units.

Finally, we confirmed this relation with a DFT MO calculation. A model molecule was proposed (Figure 7.7), in which peripheral substituents were simplified because of the reduction of the calculation cost, namely, a singlet–triplet equilibrium of $[\text{Cu}^{\text{II}}(2\text{pyNO})(\text{NH}_3)(\text{H}_2\text{O})]^{2+}$ was subjected to calculation. The molecular geometry was fully optimized, except for only one constraint (ϕ for the dihedral angle $\text{Cu}-\text{O}-\text{N}-\text{C}_{2\text{py}}$), at the HF/3–21G level. The energies of the singlet and triplet states were calculated at the UB3LYP/6–311G(d,p) level. The singlet–triplet energy gap ΔE_{ST} is plotted in Figure 7.7a, which corresponds to the experimental $2J$. We can find a monotonic decrease of ΔE_{ST} with an increase of ϕ . The critical angle of ϕ was calculated to be 10.9° .

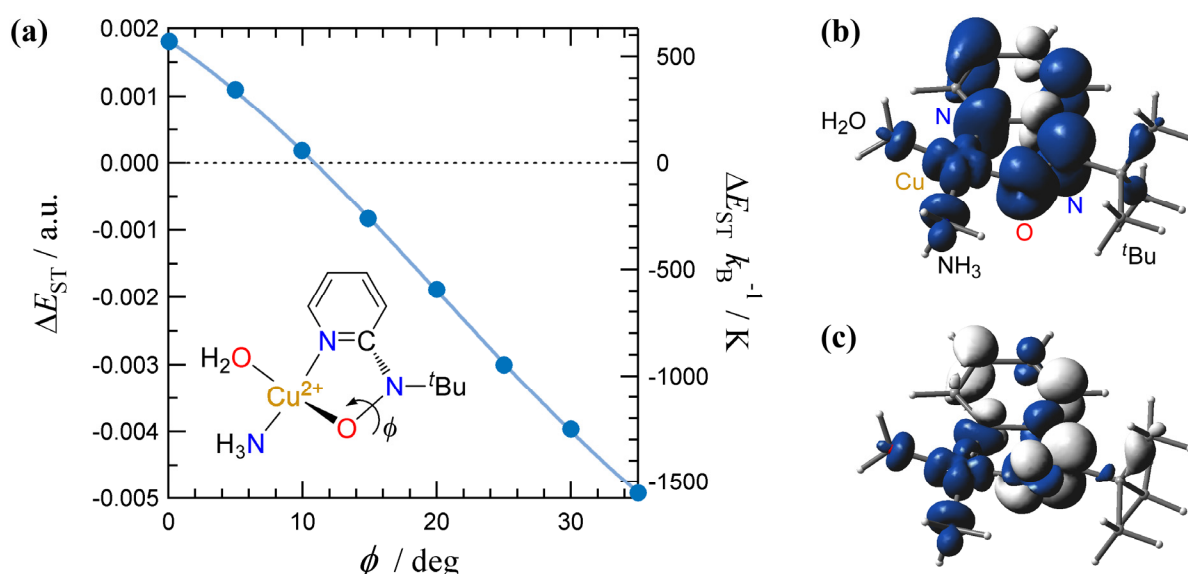


Figure 7.7. (a) DFT calculation result at the UB3LYP/6–311G(d,p)//HF/3–21G level of the single–triplet energy gap (ΔE_{ST}) as a function of the dihedral angle of $\text{Cu}-\text{O}-\text{N}-\text{C}_{2\text{py}}$ (ϕ). A line is drawn as a guide to the eye. See the text for details. A model compound is also shown. (b) Spin density surfaces for the ground triplet state at $\phi = 0^\circ$ and (c) for the ground singlet state at $\phi = 30^\circ$. Blue, positive spin; light gray, negative spin.

Figures 7.7b and 7.7c display the spin density surfaces for the ground triplet model at $\phi = 0^\circ$ and the ground singlet one at $\phi = 30^\circ$, respectively. They qualitatively correspond to the SOMOs, and we confirm the σ - and π^* -characters for the copper(II) and nitroxide SOMOs, respectively. The orthogonal arrangement of them is clearly demonstrated at $\phi = 0^\circ$, while the violation of the orthogonality is pointed out at $\phi = 30^\circ$ (Figure 6.4 in Chapter 6). Moreover, we can imagine the strict orthogonal arrangement at $\phi = 180^\circ$, as well as at $\phi = 0^\circ$, by taking the symmetry of the oxygen $2p_z$ orbital into consideration. Therefore, the SOMO–SOMO overlap obeys $\cos 2\phi$ (or $\cos^2 \phi$) dependence.²⁹ The curvature found in Figure 7.7a implies that an antiferromagnetic contribution

(J_{AF}) in $J = J_F + J_{AF}$ ³⁰ mainly results from the SOMO-SOMO overlap. The calculation curve does not exactly obey the $\cos 2\phi$ law. The DFT optimized geometry of $[\text{Cu}^{\text{II}}(2\text{pyNO})(\text{NH}_3)(\text{H}_2\text{O})]^{2+}$ at $\phi = 0^\circ$ was not planar at the copper center, as indicated with the N(py)-Cu-N(ammonia) and O(nitroxide)-Cu-O(water) angles of 167.8 and 168.3°, respectively. The J vs ϕ plot is not symmetrical with respect to $\phi = 0^\circ$. The auxiliary coupling contribution due to the M-N(py) interaction to the total J is also responsible for the deviation from the pure $\cos 2\phi$ dependence.

Table 7.5. Selected Crystallographic Data for phpyNOH and phpyNO

compounds	phpyNOH	phpyNO
formula	C ₁₅ H ₁₈ N ₂ O	C ₁₅ H ₁₇ N ₂ O
formula weight	242.32	241.31
habit	colorless prism	red platelet
dimension/mm ³	0.50 × 0.50 × 0.35	0.60 × 0.50 × 0.40
<i>T</i> /K	110	100
crystal system	triclinic	monoclinic
space group	$P\bar{1}$	$P2_1/c$
<i>a</i> /Å	6.435(4)	10.8007(3)
<i>b</i> /Å	9.750(6)	11.3559(3)
<i>c</i> /Å	11.898(8)	11.2283(3)
α°	66.99(5)	90
β°	87.11(5)	110.6004(13)
γ°	77.42(5)	90
<i>V</i> /Å ³	670.2(7)	1289.11(6)
<i>Z</i>	2	4
$D_{\text{calc}}/\text{g cm}^{-3}$	1.201	1.243
unique data	3038	2941
$\mu(\text{Mo K}\alpha)/\text{mm}^{-1}$	0.076	0.079
$R(F)^a (I > 2\sigma(I))$	0.04830	0.0383
$R_w(F^2)^b$ (all data)	0.0622	0.0351

^a $R = \sum ||F_o| - |F_c|| / \sum |F_o|$. ^b $R_w = [\sum w(F_o^2 - F_c^2)^2 / \sum w(F_o^2)^2]^{1/2}$.

Table 7.6. Selected Crystallographic Data for 1–4

compounds	1	2	3	4
formula	C ₃₀ H ₃₈ Cl ₂ N ₄ NiO ₁₂	C ₃₂ H ₃₈ Cl ₆ CuN ₄ O ₁₀	C ₃₆ H ₄₀ Cl ₄ CuN ₄ O ₁₁	C ₃₂ H _{34.7} CuF ₆ N ₄ O _{8.35} S ₂
formula weight	776.24	914.93	910.08	850.61
habit	dark-red platelet	black platelet	black platelet	black block
dimension/mm³	0.50 × 0.30 × 0.20	0.50 × 0.30 × 0.05	0.24 × 0.16 × 0.16	0.17 × 0.14 × 0.10
T/K	104	110	90	90
crystal system	orthorhombic	triclinic	monoclinic	triclinic
space group	C222 ₁	<i>P</i> $\bar{1}$	C2	<i>P</i> $\bar{1}$
a/Å	11.5278(7)	9.1578(2)	20.637(17)	10.762(6)
b/Å	15.7492(10)	11.1366(15)	7.641(3)	11.551(5)
c/Å	18.7820(14)	11.2967(13)	15.541(8)	14.984(13)
α/°	90	65.765(5)	90	87.84(4)
β/°	90	87.145(7)	128.918(3)	83.95(4)
γ/°	90	68.691(5)	90	82.14(4)
V/Å³	3409.9(4)	972.03(17)	1906.8(19)	1834.4(20)
Z	4	1	2	2
D_{calc}/g cm⁻³	1.512	1.563	1.585	1.540
unique data	3923	4199	4132	8335
μ(Mo Kα)/mm⁻¹	0.793	1.033	0.919	0.797
R (F)^a (I > 2σ(I))	0.0483	0.0727	0.0280	0.0438
R_w(F²)^b (all data)	0.0480	0.1043	0.0431	0.0667

$$^a R = \frac{\sum ||F_o| - |F_c||}{\sum |F_o|} \quad ^b R_w = \left[\frac{\sum w(F_o^2 - F_c^2)^2}{\sum w(F_o^2)^2} \right]^{1/2}$$

Note that the distances Cu–O, N–O and angles Cu–O–N, O–N–C_{2py} are entirely optimized under the condition of the single constraint of ϕ . Consequently this plot simply suggests that the dihedral angle is a good indicator for the magnetic coupling. The magnitude is a function of the interatomic Cu–O distances³¹ which depend on bulkiness of the substituents. The DFT calculation tends to overestimate the exchange parameter,³² in the present work, the calculation brought about *J* values larger than the experimental data by about 20% in the ferromagnetic region. The slope is not so reproducible with the experimental results. However, the critical angle between ferro- and

antiferromagnetic couplings seems to be defined independent of the magnitude of J . The calculated value of 10.9° is close to the experimental one ($12.6(9)^\circ$).

7.4 Conclusion

It is well-known that axially coordinated copper(II)–nitroxide complexes exhibit ferromagnetic coupling,^{1a,33} whereas equatorially coordinated copper(II)–nitroxide complexes are often claimed to show antiferromagnetic coupling.^{26,27} However, the present work informs us that the latter situation is potentially ferromagnetic as well; on the contrary, it is much more strongly ferromagnetic. A simple magneto-structure relationship has been proposed plausibly indicating that the critical ϕ value is $12.6(9)^\circ$. We can point out an advantage of the 5-membered chelation structure. Ferromagnetic coupling can often be obtained in the copper(II) and nickel(II) complexes involving 2pyNO-type radicals because of the highly planar 5-membered rings, in comparison with 6-membered rings. Intramolecular ferromagnetic couplings are thus designed on the basis of the SOMO–SOMO orthogonality.

The spin is appreciably polarized onto the pyridine ring, in contrast to the case of nitronyl nitroxide and other radicals.³⁴ The $N_{\text{py}}\text{--}M$ coordination may play an auxiliary role in ferromagnetic interaction because the pyridine nitrogen atom is spin-polarized and the $2p_z(N)$ orbital is orthogonal to $3d\sigma(M)$. A few compounds are known to exhibit intermolecular ferromagnetic coupling³ like **4**. We can expect intramolecular, as well as intermolecular, magnetic couplings through the pyridine rings being regarded as an advantage of the Ar–NO system over the NN system. Introduction of π -conjugated radicals seems promising, and the replacement of the bulky *tert*-butyl group with aromatic groups is now underway.

7.5 Experimental Section

7.5.1 Preparation

Materials

Unless otherwise noted, starting materials were obtained from commercial supplies and used without further purification. *Caution! Perchlorate salts are potentially explosive and should only be handled with care in small quantities.*

***N-tert*-Butyl-*N*-(5-phenyl-2-pyridyl)hydroxylamine (phpyNOH)**

The precursor 2-bromo-5-phenylpyridine³⁵ was prepared from 2-bromo-5-pyridylboric acid and iodobenzene by the Suzuki coupling reaction. To the dry toluene solution (150 mL) containing 2-bromo-5-phenylpyridine (2.67 g; 11.4 mmol) was added a hexane solution (1.61 mol/L) of *n*-butyllithium (7.8 mL; 13 mmol) at -78°C under nitrogen atmosphere. After the mixture was stirred at -78°C for 0.5 h, a dry toluene solution (20 mL) containing 2-methyl-2-nitrosopropane (1.19 g; 13.7 mmol) was added to the above mixture at -78°C . The mixture was stirred, being allowed to

warm gradually up to room temperature. The reaction mixture was quenched by aqueous ammonium chloride and neutralized with aqueous sodium bicarbonate at room temperature, and the organic layer was separated. After the mixture was dried over anhydrous magnesium sulfate, filtered, and concentrated under reduced pressure. A main product was purified by passing through a short column (silica gel) with 1/1 dichloromethane-ether as an eluent. Recrystallization from dichloromethane/hexane gave 1.42 g of a colorless solid of phpyNOH (5.87 mmol; 52%). Mp. 99 – 101°C. ^1H NMR (270 MHz, CDCl_3) δ 1.30 (s, 9H), 7.19 (dd, 1H, $J = 9, 1$ Hz), 7.38 – 7.58(m, 6H), 7.81 (dd, 1H, $J = 9, 3$ Hz), 8.57 (dd, 1H, $J = 3, 1$ Hz). ^{13}C NMR (68 MHz, CDCl_3) δ 26.5, 61.8, 117.0, 126.6, 127.5, 128.9, 132.0, 135.1, 137.3, 144.4, 160.9. These NMR data were recorded in the presence of a trace amount of phenylhydrazine.³⁶ MS (EI, 70 eV) m/z 241.9 ($\text{M} + \text{H}$)⁺, 225.9, 210.9, 185.9 ($\text{M} - t\text{-Bu} + \text{H}$)⁺, 169.9, 154.9. IR (KBr disk) 696, 758, 860, 1200, 1265, 1469, 1593, 2993, 3205 cm^{-1} .

***tert*-Butyl (5-phenyl-2-pyridyl) nitroxide (phpyNO)**

Freshly prepared Ag_2O (579 mg) was added to a dichloromethane solution (20 mL) containing 121 mg (0.50 mmol) of phpyNOH and the mixture was stirred at room temperature for 1 h. The supernatant immediately turned red. The solution phase was filtered and concentrated under reduced pressure. A main product was purified by passing a short column (silica gel; dichloromethane as an eluent). Red platelet crystals of phpyNO were obtained after the removal of the solvent. The yield was 88 mg (0.37 mmol; 73%). Mp. 87.5 – 88.5°C. ESR (X-band, toluene, room temperature) $g = 2.0060$. MS (ESI+) m/z 264.1 ($\text{M} + \text{Na}$)⁺, 208.1 ($\text{M} - t\text{-Bu} + \text{Na}$)⁺. IR (KBr disk) 698, 768, 849, 1190, 1265, 1377, 1462, 2989 cm^{-1} .

$[\text{Ni}(\text{phpyNO})_2(\text{H}_2\text{O})_2](\text{ClO}_4)_2$ (1**)**

A dichloromethane solution (1 mL) containing 48 mg (0.20 mmol) of phpyNO was combined to an ethanol solution (1 mL) containing 36 mg (0.10 mmol) of $\text{Ni}(\text{ClO}_4)_2 \cdot 6\text{H}_2\text{O}$, and the resultant solution was stirred for 1 min. A slow diffusion with ether gave dark purple crystals of **1**. After being kept in a refrigerator for 2 days, the crystals were separated on a filter and washed with ether. The yield was 62 mg (0.080 mmol; 80%). Single crystals suitable for the X-ray diffraction study were obtained by slow diffusion of ether into an acetone solution of **1**. Mp. 149 – 152°C (decomp.). Anal. Calcd.: C, 46.42; H, 4.93; N, 7.22% for $\text{C}_{30}\text{H}_{38}\text{Cl}_2\text{N}_4\text{NiO}_{12}$. Found: C, 46.36; H, 4.82; N, 7.21%. IR (KBr disk) 627, 696, 766, 1090, 1117, 1144, 1456, 2993, 3392 cm^{-1} .

$[\text{Cu}(\text{phpyNO})_2(\text{ClO}_4)_2] \cdot 2\text{CH}_2\text{Cl}_2$ (2**)**

According to a similar procedure for **1**, phpyNO (48 mg; 0.20 mmol) and $\text{Cu}(\text{ClO}_4)_2 \cdot 6\text{H}_2\text{O}$ (37 mg, 0.10 mmol) were mixed in dichloromethane (0.5 mL) and ethanol (1 mL), and the mixture was allowed to stand in a refrigerator for 1 day. Black needle-like crystals of **2** were precipitated and collected on a filter (58 mg; 0.063 mmol; yield 63%). They were suitable X-ray diffraction and magnetic studies. Mp. 140 – 141°C (decomp.). Anal. Calcd.: C, 45.18; H, 4.39; N, 6.82% for $\text{C}_{30.9}\text{H}_{35.8}\text{Cl}_{3.8}\text{CuN}_4\text{O}_{10}$ (i.e., $[\text{Cu}(\text{phpyNO})_2(\text{ClO}_4)_2] \cdot 0.9\text{CH}_2\text{Cl}_2$). Found: C, 45.02; H, 4.52; N, 7.11%. IR (KBr disk) 627, 698, 768, 1090, 1117, 1146, 1458, 2985 cm^{-1} . The ratio of the solvated

molecules depended on batches, owing to the presence of **2'** ($[\text{Cu}(\text{phpyNO})_2(\text{ClO}_4)_2] \cdot 0.24\text{CH}_2\text{Cl}_2$) as an impurity.

$[\text{Cu}(\text{phpyNO})_2(\text{H}_2\text{O})](\text{ClO}_4)_2 \cdot \text{C}_6\text{H}_4\text{Cl}_2$ (3**)**

According to a similar procedure for **1**, phpyNO (48 mg; 0.20 mmol) and $\text{Cu}(\text{ClO}_4)_2 \cdot 6\text{H}_2\text{O}$ (37 mg, 0.10 mmol) were mixed in *o*-dichlorobenzene (0.5 mL) and acetonitrile (1 mL), and the mixture was allowed to stand in a refrigerator for 1 day. Black platelet crystals of **3** were precipitated and collected on a filter (52 mg; 0.057 mmol; yield 57%). They were suitable X-ray diffraction and magnetic studies. Mp. 158 – 160°C (decomp.). Anal. Calcd.: C, 47.51; H, 4.43; N, 6.16% for $\text{C}_{36}\text{H}_{40}\text{Cl}_4\text{CuN}_4\text{O}_{11}$ (i.e., $[\text{Cu}(\text{phpyNO})_2(\text{H}_2\text{O})](\text{ClO}_4)_2 \cdot \text{C}_6\text{H}_4\text{Cl}_2$). Found: C, 47.51; H, 4.43; N, 6.39%. IR (KBr disk) 627, 698, 768, 1090, 1115, 1146, 1458, 2987, 3437 cm^{-1} .

$[\text{Cu}(\text{phpyNO})_2(\text{CF}_3\text{SO}_3)_2] \cdot 0.35\text{H}_2\text{O}$ (4**)**

According to a similar procedure for **1**, phpyNO (48 mg; 0.20 mmol) and $\text{Cu}(\text{CF}_3\text{SO}_3)_2$ (36 mg, 0.10 mmol) were mixed in chloroform (0.5 mL) and acetonitrile (0.5 mL), and the mixture was allowed to stand in a refrigerator for 1 day. Black block crystals of **4** were precipitated and collected on a filter (52 mg; 0.071 mmol; yield 71%). They were suitable X-ray diffraction and magnetic studies. Mp. 148 – 149°C (decomp.). Anal. Calcd.: C, 45.18; H, 4.11; N, 6.59; S, 7.54% for $\text{C}_{32}\text{H}_{34.7}\text{CuF}_6\text{N}_4\text{O}_{8.35}\text{S}_2$ (i.e., $[\text{Cu}(\text{phpyNO})_2(\text{CF}_3\text{SO}_3)_2] \cdot 0.35\text{H}_2\text{O}$). Found: C, 45.02; H, 4.02; N, 6.79; S, 7.56%. IR (KBr disk) 638, 766, 1032, 1165, 1263, 1279, 1456, 2991, 3523 cm^{-1} .

7.5.2 X-ray Crystallographic Studies

X-Ray diffraction analyses of single crystals of the specimens were performed as described in Experimental Section of Chapter 6. All of the hydrogen atoms were found experimentally for phpyNOH and phpyNO. Thermal displacement parameters were refined anisotropically for non-hydrogen atoms and those of hydrogen atoms were treated isotropically. The hydrogen atoms in **1–4** were placed at calculated positions, and their parameters were refined as “riding”. Selected crystallographic data are summarized in Table 7.5 and 7.6.

7.5.3 Physical Measurements

EPR spectra of 2pyNO and phpyNO were recorded on Bruker ESP300E X-band (9.7 GHz) spectrometer. After the sample solution in toluene was thoroughly purged with nitrogen, the EPR spectra were recorded immediately at room temperature. Simulated spectra were calculated in the WinEPR Simfonia.⁵

The dc magnetic susceptibilities of polycrystalline samples of the present complexes were measured in a manner similar to those of the complexes containing 2pyNO ligand (in Experimental Section of Chapter 6).

7.5.4 Molecular Orbital Calculation

Molecular orbital calculations were performed as described in Experimental Section of Chapter 6. The 6–311G(d,p) basis set was chosen. For the calculation on a model compound (Figure 7.7),

we applied a conformation analysis routine in the Spartan'02 program.³⁷ The molecular geometry was fully optimized on the restricted HF/3-21G level except for the constraint of the Cu-O-N-C_{2py} dihedral angle. The calculation points were set to $\phi = 0 - 35^\circ$ with an interval of 5° . The energies of the triplet and broken-symmetry singlet³⁸ states were calculated at the UB3LYP/6-311G(d,p) level with the Gaussian03 program.

References

- (1) (a) Caneschi, A.; Gatteschi, D.; Sessoli, R.; Rey, P. *Acc. Chem. Res.* **1989**, *22*, 392. (b) Manriquez, J. M.; Yee, G. T.; McLean, R. S.; Epstein, A. J.; Miller, J. S. *Science* **1991**, *252*, 1415. (c) Inoue, K.; Hayamizu, T.; Iwamura, H.; Hashizume, D.; Ohashi, Y. *J. Am. Chem. Soc.* **1996**, *118*, 1803. (d) Lemaire, M. T. *Pure Appl. Chem.* **2004**, *76*, 277.
- (2) Romero, F. M.; Luneau, D.; Ziessel, R. *Chem. Commun.* **1998**, 551.
- (3) Aoki, C.; Ishida, T.; Nogami, T. *Inorg. Chem.* **2003**, *42*, 7616.
- (4) (a) Luneau, D.; Rey, P.; Laugier, J.; Fries, P.; Caneschi, A.; Gatteschi, D.; Sessoli, R. *J. Am. Chem. Soc.* **1991**, *113*, 1245. (b) Luneau, D.; Rey, P.; Laugier, J.; Belorizky, E.; Conge, A. *Inorg. Chem.* **1992**, *31*, 3578.
- (5) Keana, J. F. W. *Chem. Rev.* **1978**, *78*, 37.
- (6) Osanai, K.; Okazawa, A.; Nogami, T.; Ishida, T. *J. Am. Chem. Soc.* **2006**, *128*, 14008.
- (7) Kahn, O.; Prins, R.; Reedijk, J.; Thompson, J. S. *Inorg. Chem.* **1987**, *26*, 3557.
- (8) (a) Calder, A.; Forrester, A. R. *J. Chem. Soc. C* **1969**, 1459. (b) Forrester, A. R.; Hepburn, S. P. *J. Chem. Soc., Perkin I* **1974**, 2208.
- (9) (a) Nishimaki, H.; Mashiyama, S.; Yasui, M.; Nogami, T.; Ishida, T. *Chem. Mater.* **2006**, *18*, 3602. (b) Inoue, K.; Iwamura, H. *Adv. Mater.* **1992**, *4*, 801. (c) Fujita, J.; Tanaka, M.; Suemune, H.; Koga, N.; Matsuda, K.; Iwamura, H. *J. Am. Chem. Soc.* **1996**, *118*, 9347.
- (10) (a) McConnell, H. M.; Strathdee, J. *Mol. Phys.* **1959**, *2*, 129. (b) McConnell, H. M. *J. Chem. Phys.* **1958**, *28*, 1188.
- (11) Talcott, C. L.; Myers, R. J. *Mol. Phys.* **1967**, *12*, 549.
- (12) Carrington, A.; dos Santos-Veiga, J. *Mol. Phys.* **1962**, *5*, 21.
- (13) (a) Iwamura, H. *Adv. Phys. Org. Chem.* **1990**, *26*, 179. (b) Rajca, A. *Chem. Rev.* **1994**, *94*, 871. (c) Ishida, T.; Iwamura, H. *J. Am. Chem. Soc.* **1991**, *113*, 4238. (d) Mataga, N. *Theor. Chim. Acta* **1967**, *10*, 372. (e) Longuet-Higgins, J. C. *J. Chem. Phys.* **1950**, *18*, 265.
- (14) (a) Kumada, H.; Sakane, A.; Koga, N.; Iwamura, H. *J. Chem. Soc., Dalton Trans.* **2000**, 911. (b) Shimada, T.; Ishida, T.; Nogami, T. *Polyhedron* **2005**, *24*, 2593. (c) Kitano, M.; Ishimaru, Y.; Inoue, K.; Koga, N.; Iwamura, H. *Inorg. Chem.* **1994**, *33*, 6012. (d) Ishimaru, Y.; Kitano, M.; Kumada, H.; Koga, N.; Iwamura, H. *Inorg. Chem.* **1998**, *37*, 2273.
- (15) (a) Bu, X.-H.; Tong, M.-L.; Xie, Y.-B.; Li, J.-R.; Chang, H.-C.; Kitagawa, S.; Ribas, J. *Inorg. Chem.* **2005**, *44*, 9837. (b) Lescouezec, R.; Lloret, F.; Julve, M.; Vaissermann, J.; Verdagner, M. *Inorg. Chem.* **2002**, *41*, 818.
- (16) (a) Bencini, A.; Benelli, C.; Dei, A.; Gatteschi, D. *Inorg. Chem.* **1985**, *24*, 695. (b) Tanaka, M.; Matsuda, K.; Iwamura, H. *J. Am. Chem. Soc.* **1998**, *120*, 7168.
- (17) Gruber, S. J.; Harris, C. M.; Sinn, E. *J. Chem. Phys.* **1968**, *49*, 2183.
- (18) The impurity **2'** might have a ground doublet state, because the torsion of **2'** was large (preliminarily 12.9(9)°). A negligibly interacting copper–radical relation seems possible as

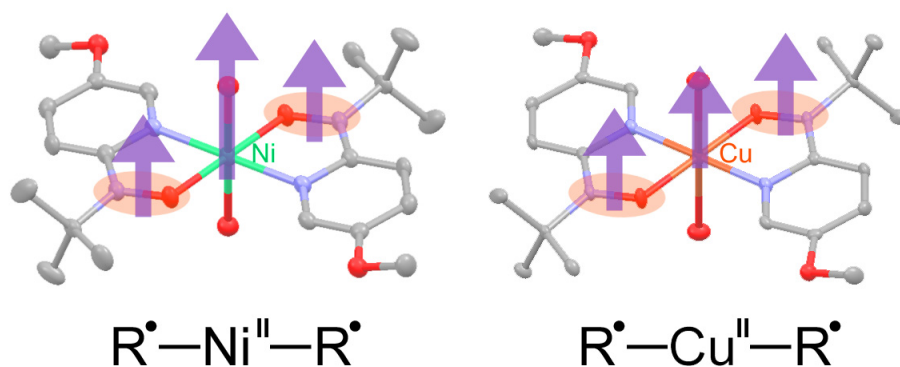
- well. However, the ground quartet state of **2'** would give rise to an unrealistic g value smaller than 2 as estimated from the somewhat small $\chi_{\text{mol}}T$ value.
- (19) Bleaney, B.; Bowers, K. D. *Proc. R. Soc. London, Ser. A* **1952**, *214*, 451.
- (20) Bondi, A. *J. Phys. Chem.* **1964**, *68*, 441.
- (21) McConnell, H. M. *J. Chem. Phys.* **1963**, *39*, 1910.
- (22) (a) Izuoka, A.; Murata, S.; Sugawara, T.; Iwamura, H. *J. Am. Chem. Soc.* **1985**, *107*, 1786. (b) Imachi, R.; Ishida, T.; Suzuki, M.; Yasui, M.; Iwasaki, F.; Nogami, T. *Chem. Lett.* **1997**, 743.
- (23) (a) Calder, A.; Forrester, A. R.; Hepburn, S. P. *J. Chem. Soc., Perkin I* **1973**, 456. (b) Forrester, A. R.; Hepburn, S. P.; McConnachie, G. *J. Chem. Soc., Perkin I* **1974**, 2213.
- (24) (a) Goldman, J.; Petersen, T. E.; Torrsell, K.; Becher, J. *Tetrahedron* **1973**, *29*, 3833. (b) Lemaire, H.; Marechal, Y.; Ramasseul, R.; Rassat, A. *Bull. Soc. Chim. Fr.* **1965**, 372.
- (25) Ullman, E. F.; Osiecki, J. H.; Boocock, G. B.; Darcy, R. *J. Am. Chem. Soc.* **1972**, *94*, 7049.
- (26) Luneau, D.; Risoan, G.; Rey, P.; Grand, A.; Caneschi, A.; Gatteschi, D.; Laugier, J. *Inorg. Chem.* **1993**, *32*, 5616.
- (27) (a) Hicks, R. G.; Lemaire, M. T.; Thompson, L. K.; Barclay, T. M. *J. Am. Chem. Soc.* **2000**, *122*, 8077. (b) Barclay, T. M.; Hicks, R. G.; Lemaire, M. T.; Thompson, L. K. *Chem. Commun.* **2000**, 2141. (c) Gilroy, J. B.; Koivisto, B. D.; McDonald, R.; Ferguson, M. J.; Hicks, R. G. *J. Mater. Chem.* **2006**, *16*, 2618.
- (28) (a) Hearn, N. G. R.; Preuss, K. E.; Richardson, J. F.; Bin-Salamon, S. *J. Am. Chem. Soc.* **2004**, *126*, 9942. (b) Jennings, M.; Preuss, K. E.; Wu, J. *Chem. Commun.* **2006**, 341.
- (29) Venkataraman, L.; Klare, J. E.; Nuckolls, C.; Hyberstsen, M. S.; Steigerwald, M. L. *Nature* **2006**, *442*, 904.
- (30) Kahn, O. *Molecular Magnetism*; VCH: New York, 1993; Chapter 8, p 145.
- (31) Cervera, B.; Ruiz, R.; Lloret, F.; Julve, M.; Cano, J.; Faus, J.; Bois, C.; Mrozinski, J. *J. Chem. Soc., Dalton Trans.* **1997**, 395.
- (32) (a) Dai, D.; Whangbo, M.-H.; Koo, H.-J.; Rocquefelte, X.; Jobic, S.; Villesuzanne, A. *Inorg. Chem.* **2005**, *44*, 2407. (b) Grau-Crespo, R.; de Leeuw, N. H.; Catlow, C. R. *J. Mater. Chem.* **2003**, *13*, 2848.
- (33) (a) Benelli, C.; Gatteschi, D.; Carnegie, D. W., Jr.; Carlin, R. L. *J. Am. Chem. Soc.* **1985**, *107*, 2560. (b) Caneschi, A.; Gatteschi, D.; Laugier, J.; Rey, P. *J. Am. Chem. Soc.* **1987**, *109*, 2191.
- (34) (a) Zheludev, A.; Barone, V.; Bonnet, M.; Delley, B.; Grand, A.; Ressouche, E.; Rey, P.; Subra, R.; Schweizer, J. *J. Am. Chem. Soc.* **1994**, *116*, 2019. (b) Awaga, K.; Inabe, T.; Maruyama, Y. *Chem. Phys. Lett.* **1992**, *190*, 349.
- (35) Parry, P. R.; Wang, C.; Batsanov, A. S.; Bryce, M. R.; Tarbit, B. *J. Org. Chem.* **2002**, *67*, 7541.
- (36) Lee, T. D.; Keana, J. F. W. *J. Org. Chem.* **1975**, *40*, 3145.
- (37) SPARTAN'02; Wavefunction Inc.: Irvine, CA, USA, 2002.
- (38) (a) Ruiz, E.; Cano, J.; Alvarez, S.; Alemany, P. *J. Comput. Chem.* **1999**, *20*, 1391. (b) Noodleman, L.; Peng, C. Y.; Case, D. A.; Mouesca, J. M. *Coord. Chem. Rev.* **1995**, *144*, 199.

Chapter 8

Strong Intramolecular Ferromagnetic Coupling in Nickel(II) and Copper(II) Complexes Chelated with *tert*-Butyl 5-Methoxy-2-pyridyl Nitroxide

Abstract

We successfully isolated a new paramagnetic bidentate ligand *tert*-butyl 5-methoxy-2-pyridyl nitroxide (meopyNO). Complexation of nickel(II) and copper(II) perchlorates with meopyNO gave the corresponding ML_2 -type bis-chelated compounds. The magnetic studies showed that they were ground high-spin molecules with $2J/k_B = +288(5)$ and $+178(3)$ K for $[M(\text{meopyNO})_2(\text{H}_2\text{O})_2](\text{ClO}_4)_2$ ($M = \text{Ni}$ and Cu , respectively), where the spin Hamiltonian is defined as $\mathcal{H} = -2J(\hat{S}_1 \cdot \hat{S}_2 + \hat{S}_2 \cdot \hat{S}_3)$. From the crystallographic analysis, the torsion angles (ϕ) around $M\text{-O-N-C}_{2\text{py}}$ were $4.2(3)^\circ$ and $6.87(19)^\circ$, respectively, being so small that the orthogonality between the magnetic radical π^* and the metal $d\sigma$ orbitals would be guaranteed.

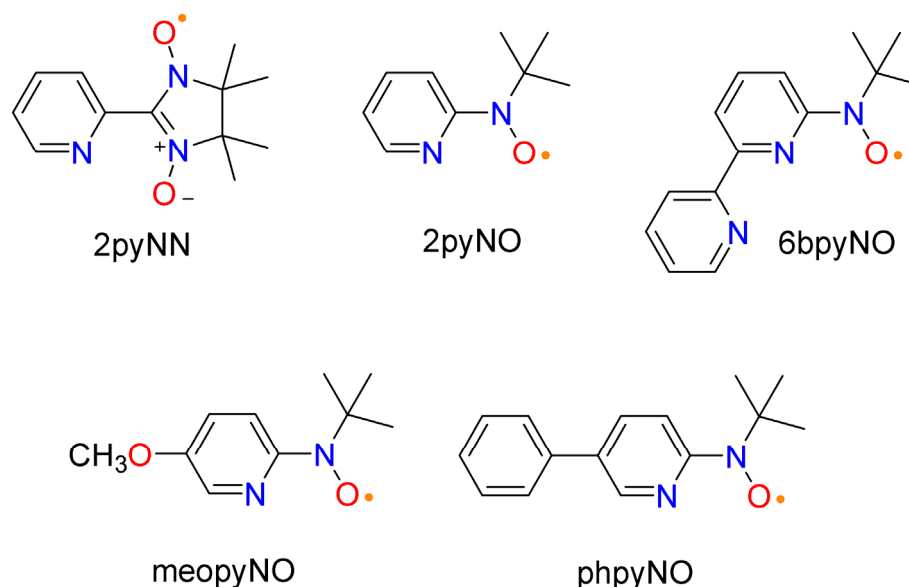


8.1 Introduction

Metal-radical hybrid solids have been well investigated toward molecule-based magnets, where a radical center is directly bonded to the metal ion, affording appreciable magnetic exchange coupling.¹ Various 2-pyridyl-substituted ligands containing a paramagnetic center such as nitronyl nitroxide (NN) groups²⁻⁴ have been known to form chelate rings (see Scheme 8.1 for their structural formulas). On the other hand, 2pyNO and its complexes have hardly been studied, because the simple pyridyl-NOs are unisolable.⁵ In Chapter 6, it was shown that the 2pyNO-chelated compounds were synthesized by a trapping method without isolation of 2pyNO. The phpyNO ligand, which was described in Chapter 7, was also developed as a member of this family.

A new candidate of isolable paramagnetic ligands, *tert*-butyl 5-methoxy-2-pyridyl nitroxide (meopyNO) seem promising, because substitution of a methoxy group at the para position with respect to the nitroxide radical group is quite effective for stabilization.^{5,7,8} We will describe the preparation of $[M^{II}(\text{meopyNO})_2(\text{H}_2\text{O})_2](\text{ClO}_4)_2$ ($M = \text{Ni}$ (**1**) and Cu (**2**)) and their molecular structures determined by means of X-ray crystallographic analysis. The magnetic couplings between nitroxide radical spins and copper(II) or nickel(II) spins for the present compounds will be discussed here.

Scheme 8.1. Structural Formulas of 2-Pyridyl-Substituted Radicals with Chelating Ability



8.2 Results

8.2.1 Characterization of meopyNO

We successfully synthesized and isolated a paramagnetic ligand, meopyNO. The precursor meopyNOH was prepared according to the conventional method,^{6,7} and the oxidation with Ag_2O gave meopyNO, which could be purified and isolated by passing through silica-gel column chromatography. The spectroscopic measurements of meopyNO satisfied the molecular formula, but unfortunately it did not give good crystalline solids because of the low melting point (ca. 10°). The EPR spectra of meopyNO measured in toluene at room temperature showed a typical 1/1/1 triplet signal with $a_N = 1.076$ mT at $g = 2.0059$. The spin density at the nitrogen atom is suggested to be larger than those of 6bpyNO (1.05 mT),⁶ phpyNO (1.000 mT), and 2pyNO (1.023 mT). This finding seems to be an advantage from the viewpoint of the magnitude of magnetic interaction, because the magnetic coupling is proportional to the spin density at the contacting atoms.⁹

Table 8.1. Selected Crystallographic Data for **1** and **2**

compounds	1	2
formula	C ₂₀ H ₃₄ Cl ₂ N ₄ NiO ₁₄	C ₂₀ H ₃₄ Cl ₂ CuN ₄ O ₁₄
formula weight	684.11	688.96
habit	dark-red platelet	black block
dimension/mm ³	0.45 × 0.30 × 0.20	0.80 × 0.50 × 0.40
<i>T</i> /K	108	108
crystal system	triclinic	triclinic
space group	<i>P</i> $\bar{1}$	<i>P</i> $\bar{1}$
<i>a</i> /Å	8.3898(11)	8.8931(9)
<i>b</i> /Å	8.5392(15)	8.7447(8)
<i>c</i> /Å	10.1289(13)	9.2046(11)
α°	84.661(4)	84.640(4)
β°	85.308(3)	85.986(6)
γ°	89.921(7)	90.420(4)
<i>V</i> /Å ³	720.07(18)	710.86(13)
<i>Z</i>	1	1
<i>D</i> _{calc} /g cm ⁻³	1.577	1.609
unique data	3250	3193
μ (Mo K α)/mm ⁻¹	0.932	1.029
<i>R</i> (<i>F</i>) ^a (<i>I</i> > 2 σ (<i>I</i>))	0.0476	0.0300
<i>R</i> _w (<i>F</i> ²) ^b (all data)	0.0731	0.0343

$$^a R = \frac{\sum ||F_o| - |F_c||}{\sum |F_o|}, \quad ^b R_w = \left[\frac{\sum w(F_o^2 - F_c^2)^2}{\sum w(F_o^2)^2} \right]^{1/2}.$$

8.2.2 Crystal Structure Analysis of the Nickel(II) and Copper(II) Complexes

Since meopyNO has a π^* -type SOMO at the nitroxide group, we utilized transition metal ions having $d\sigma$ -type magnetic orbitals to bestow the orthogonal arrangement between them at the direct nitroxide–metal bond. Therefore, we focused metal ions, nickel(II) (3d⁸) and copper(II) (3d⁹), which have only $d\sigma$ -spins. Actually, we prepared some chelated compounds with meopyNO according to a method similar to those of the 2pyNO, 6bpyNO,⁶ and phpyNO complexes (see also in Chapters 6 and 7). Simply mixing of meopyNO with metal(II) perchlorates in appropriate organic solvents gave

ML₂-type compounds of **1** and **2**. They were characterized by means of elemental analysis and IR spectroscopy, and finally their molecular structures were successfully determined by means of X-ray crystallographic analysis. Table 8.1 summarizes selected crystallographic data of **1** and **2**, and their molecular structures are shown in Figure 8.1.

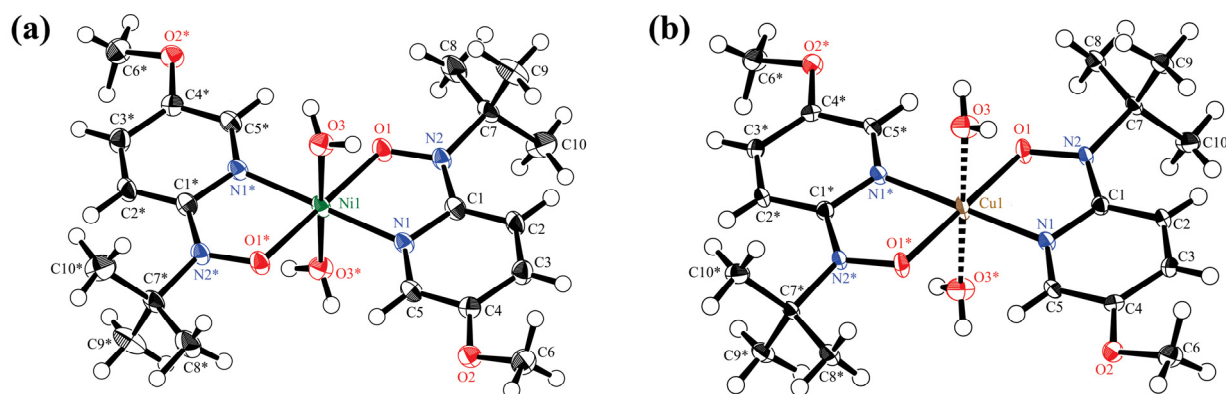


Figure 8.1. Molecular structures of (a) **1** and (b) **2** with the thermal ellipsoids at the 50% probability level for non-hydrogen atoms. Atom numbering schemes are also shown. Counter anions are not shown for the sake of clarity.

We can find five-membered chelate rings involving a metal center and nitroxide group. Water molecules occupy the axial positions. Compounds **1** and **2** are isomorphous in the space group $P\bar{1}$, except for the following: the coordination structure of the nickel(II) ion in **1** is an almost octahedron (the Ni1–O1, Ni1–N1, and Ni1–O3 distances are 2.020(2), 2.011(2), and 2.091(2) Å, respectively). The octahedral structure of nickel(II) coordination sphere implies $S_{Ni} = 1$. On the other hand, copper(II) ion in **2** shows the Jahn–Teller distortion as indicated with the somewhat longer Cu1–O3 distance of 2.4292(17) Å than those of the Cu1–O1 and Cu1–N1 distances (1.9688(13) and 1.9404(15), respectively). The five-membered chelate rings are very planar for both, which guarantees the orthogonal arrangement between the metal $d\sigma$ orbitals (i.e., $3d_{x^2-y^2}$ and $3d_{z^2}$) and nitroxide π^* orbital. We have proposed that the torsion angle along M–O–N–C_{2py} is convenient for an indicator of the orthogonality. The M1–O1–N1–C1 torsion angles are 4.2(3)° and 6.87(19)° for **1** and **2**, respectively. The small size of water seems responsible for such a planar geometry. Perchlorate anions are relatively bulky, and the perchlorate oxygen atom has a considerably bent angle of M–O–Cl and accordingly the large M–O–N–C_{2py} torsion in [Cu(phpyNO)₂(ClO₄)₂] and [Cu(2pyNO)₂(ClO₄)₂].

8.2.3 Intramolecular Magnetic Coupling in the Nickel(II) and Copper(II) Complexes

Magnetic susceptibilities of **1** and **2** were measured on a SQUID magnetometer. Upon cooling from 300 to 2 K, the $\chi_{\text{mol}}T$ values of them once increased, indicating the presence of intramolecular ferromagnetic interactions, and then decreased (Figure 8.2). The spin-only values are 3.0 and 1.88 $\text{cm}^3 \text{K mol}^{-1}$ for **1** ($S_{\text{total}} = 2$) and for **2** ($S_{\text{total}} = 3/2$), respectively. The experimental $\chi_{\text{mol}}T$ values at their maximum clearly indicate that they have high-spin states. Final drops of the $\chi_{\text{mol}}T$ values are assigned to intermolecular antiferromagnetic couplings, as well as ZFS for the nickel(II) ions in **1**.

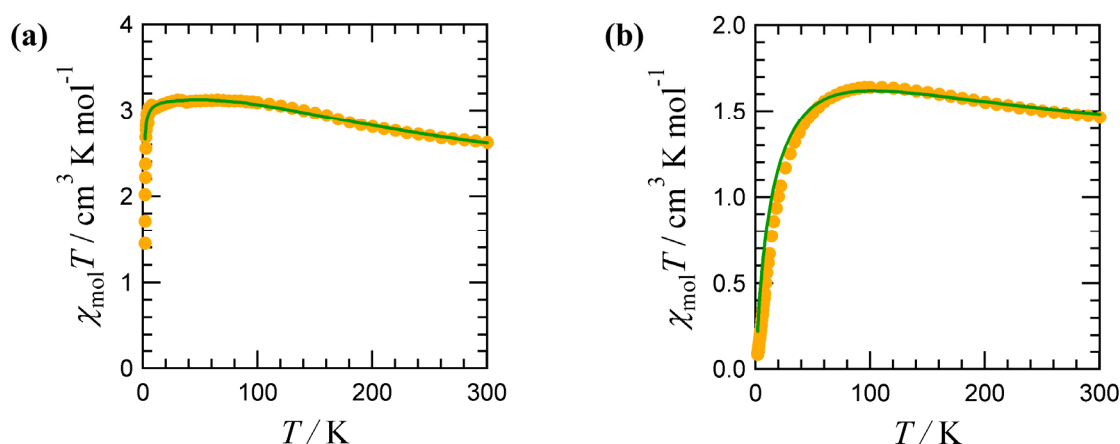


Figure 8.2. Temperature dependence of $\chi_{\text{mol}}T$ for (a) **1** and (b) **2**. Applied magnetic fields were 500 Oe for **1** and 1000 Oe for **2**. The solid lines represent calculated curves. See the text for the equations and optimized parameters.

For all the complexes investigated here, the metal–radical geometry is unique due to the two-fold or inversion symmetry, and accordingly the spin Hamiltonian was defined as $\mathcal{H} = -2J(\hat{S}_1 \cdot \hat{S}_2 + \hat{S}_2 \cdot \hat{S}_3)$ for the three-centered system, in which coupling between the terminal ions was disregarded. Thus, we applied the van Vleck equation to our systems, giving the following expressions, eqs 8.1 and 8.2 for the nickel(II) and copper(II) complexes, respectively.¹⁰

$$\chi_{\text{mol}} = \frac{2N_{\text{A}}g_{\text{avg}}^2\mu_{\text{B}}^2}{k_{\text{B}}(T-\theta)} \frac{\exp(-2J/k_{\text{B}}T) + 1 + 5\exp(2J/k_{\text{B}}T)}{\exp(-4J/k_{\text{B}}T) + 3\exp(-2J/k_{\text{B}}T) + 3 + 5\exp(2J/k_{\text{B}}T)} \quad (8.1)$$

$$\chi_{\text{mol}} = \frac{N_{\text{A}}g_{\text{avg}}^2\mu_{\text{B}}^2}{4k_{\text{B}}(T-\theta)} \frac{\exp(-2J/k_{\text{B}}T) + 1 + 10\exp(J/k_{\text{B}}T)}{\exp(-2J/k_{\text{B}}T) + 1 + 2\exp(J/k_{\text{B}}T)} \quad (8.2)$$

The experimental data were fitted to these equations and the optimized parameters are obtained as $g_{\text{avg}} = 2.050(2)$, $2J/k_{\text{B}} = +288(5)$ K, and $\theta = -0.32(2)$ K for **1**. A final drop of the $\chi_{\text{mol}}T$ value can be assigned to intermolecular antiferromagnetic couplings as well as zero-field splitting for the Ni^{II}

ions in **1**, both of which are confined to θ . On the other hand, we found that the accuracy of J and g_{avg} in **2** was somewhat unsatisfactory with an unrealistic statistical error, though the positive sign of J is meaningful. The large J and small g are partly cancelled in this calculation, possibly giving rise to appreciable errors. Thus, we fixed g_{avg} as a typical value of 2.05 (Table 7.4), and analyzed the data again. The parameters were optimized as $2J/k_B = +178(3)$ K and $\theta = -13.7(3)$ K for **2**.

8.3 Discussion

As we mentioned above and discussed previously, the most important parameter is the M–O–N–C_{2py} torsion angle (ϕ), which indicates the out-of-plane dislocation from the chelate ring with respect to the N–O–M moiety. The ferromagnetic couplings observed here and for the related compounds are well explained in terms of the orbital orthogonality between radical π^* and nickel(II) or copper(II) $3d_{x^2-y^2}$ SOMOs.¹¹ Now we have to check quantitatively the magnitude of J according to the magneto-structure relationship previously proposed.

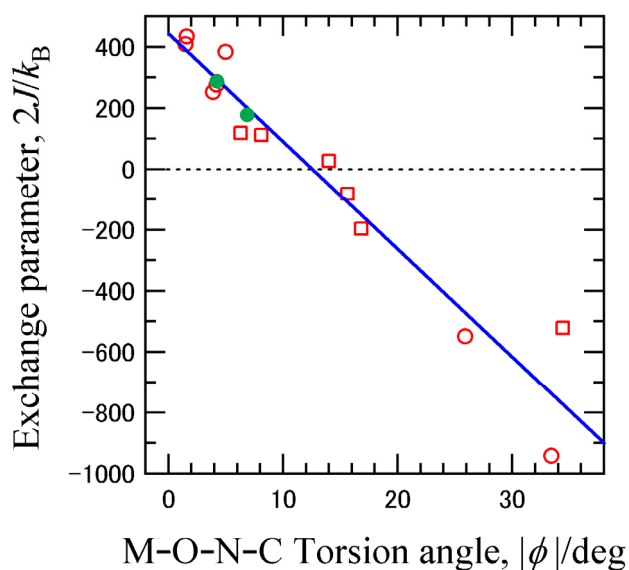


Figure 8.3. A Plot of the observed exchange coupling parameter ($2J$) versus M–O–N–C_{2Ar} torsion angle ($|\phi|$) as a magneto-structure relationship in the hexacoordinated nickel(II) or copper(II) complexes with radical chelating ligand. Green filled circles stand for the data points on **1** and **2**, respectively. The data of Ar–NO compounds were collected from ref 6 and this thesis (in Chapter 6 and 7), and those of Ar–NN complexes were from refs. 3, 12. The line stands for a linear fit.

We have previously drawn a plot of J versus ϕ for the hexacoordinated nickel(II) and copper(II) complexes (Chapter 6). It should be noted that the argument holds also for the chelates of nitronyl nitroxide (NN) radicals.^{3,4,12} The spin density on the oxygen atom of Ar–NO is assumed to be much larger than that of the Ar–NN, owing to an almost half size of the spin-delocalizable π -conjugation in

the radical groups. Here we superposed two points from **1** and **2** on this plot (Figure 8.3). The present results totally obey this relation. It is instructive to test the following equation, $2J/k_B = a + b|\phi|$ with $a = 440(50)$ K and $b = -35(3)$ K deg⁻¹ previously proposed. We calculated $2J/k_B = +293$ and $+200$ K from $\phi = 4.2^\circ$ and 6.87° , respectively, which satisfactorily agree with the experimental values of $2J/k_B = +288(5)$ and $+178(3)$ K. The expression is refined using all the data including those of **1** and **2**; $2J/k_B = a + b|\phi|$ with $a = 440(40)$ K and $b = -35(3)$ K deg⁻¹.

8.4 Conclusion

We successfully utilized the new isolable synthetic intermediacy meopyNO, and complexation of nickel(II) and copper(II) perchlorates gave **1** and **2**, where the torsion angles (ϕ) around M–O–N–C_{2py} were as small as $4.2(3)^\circ$ and $6.87(19)^\circ$, respectively. Both of them exhibit the considerably ferromagnetic metal–radical coupling. The 5-membered chelation in the 2-pyridyl–NO systems has an advantage over the 6-membered chelation in the 2-pyridyl–NN systems, with respect to the planarity and accordingly the $d\sigma-\pi^*$ orbital orthogonality. 2-Pyridyl–NO system has another advantage; strong magnetic coupling owing to the high spin density on the ligating oxygen atoms.

8.5 Experimental Section

8.5.1 Preparations

Materials

Unless otherwise noted, starting materials were obtained from commercial supplies and used without further purification. *Caution! Perchlorate salts are potentially explosive and should only be handled with care in small quantities.*

***N*-tert-Butyl-*N*-(5-methoxy-2-pyridyl)hydroxylamine (meopyNOH)**

The precursor 2-bromo-5-methoxypyridine was prepared from 2-amino-5-methoxypyridine¹³ by the Sandmeyer bromination.¹⁴ To the dry toluene solution (125 mL) containing 2-bromo-5-methoxypyridine (1.89 g; 10.0 mmol) was added a hexane solution (1.61 mol/L) of *n*-butyllithium (6.8 mL; 11 mmol) at -78°C under nitrogen atmosphere. After the mixture was stirred at -78°C for 0.5 h, a dry toluene solution (25 mL) containing 2-methyl-2-nitrosopropane (1.23 g; 14.1 mmol) was added to the above mixture at -78°C . The mixture was stirred, being allowed to warm gradually up to room temperature. The reaction mixture was quenched by aqueous ammonium chloride and neutralized with aqueous sodium bicarbonate at room temperature. The organic layer was separated, dried over anhydrous sodium sulfate, filtered, and concentrated under reduced pressure. A main product was purified by passing through a short column (silica gel) with 1/1 dichloromethane-ether as an eluent. Recrystallization from dichloromethane/hexane gave 0.238 g of a colorless solid of meopyNOH (1.30 mmol; 66%). Mp. $75 - 76^\circ\text{C}$. ¹H NMR (270 MHz, CDCl₃) δ

1.19 (s, 9H), 3.85 (s, 3H), 7.06 (d, 1H, $J = 8.9$ Hz), 7.15 (brs, 1H), 7.19 (dd, 1H, $J = 3.0$ and 8.9 Hz), 8.04 (d, 1H, $J = 3.0$ Hz). ^{13}C NMR (68 MHz, CDCl_3) δ 25.4, 55.8, 62.1, 121.6, 125.2, 127.7, 149.2, 150.3.

***tert*-Butyl 5-methoxy-2-pyridyl nitroxide (meopyNO)**

Freshly prepared Ag_2O (695 mg) was added to a dichloromethane solution (10 mL) containing 196 mg (1.00 mmol) of meopyNOH and the mixture was stirred at room temperature for 0.5 h. The supernatant immediately turned red. The solution phase was filtered and concentrated under reduced pressure. A main product was purified by passing a short column (silica gel; dichloromethane as an eluent). Red viscous oil of meopyNO was obtained after the removal of the solvent. We obtained 194 mg (0.99 mmol) of meopyNO in 99% yield. Mp. ca. 10 °C. EPR (X-band, toluene, room temperature) $g = 2.0059$, $a_{\text{N}} = 1.076$ mT. MS (ESI+) m/z 218.1 ($\text{M} + \text{Na}$) $^+$, 162.0 ($\text{M} - t\text{-Bu} + \text{Na}$) $^+$.

$[\text{Ni}(\text{meopyNO})_2(\text{H}_2\text{O})_2](\text{ClO}_4)_2$ (1**)**

A dichloromethane solution (1 mL) containing 78 mg (0.40 mmol) of meopyNO was combined to an ethanol solution (1 mL) containing 73 mg (0.20 mmol) of $\text{Ni}(\text{ClO}_4)_2 \cdot 6\text{H}_2\text{O}$. A slow diffusion with ether gave dark red crystals of **1** after being kept in a refrigerator for a few days. The crystals were separated on a filter and washed with water. The yield was 108 mg (0.158 mmol; 79%). Single crystals suitable for the X-ray diffraction study were obtained by slow diffusion of ether into an acetone solution of **1**. Mp. 170 – 172°C (decomp.). Anal. Calcd.: C, 35.11; H, 5.01; N, 8.19% for $\text{C}_{20}\text{H}_{34}\text{Cl}_2\text{N}_4\text{NiO}_{14}$. Found: C, 35.03; H, 5.18; N, 8.18%.

$[\text{Cu}(\text{meopyNO})_2(\text{H}_2\text{O})_2](\text{ClO}_4)_2$ (2**)**

According to a similar procedure for **1**, meopyNO (78 mg; 0.40 mmol) and $\text{Cu}(\text{ClO}_4)_2 \cdot 6\text{H}_2\text{O}$ (74 mg, 0.20 mmol) were mixed in dichloromethane (1 mL) and ethanol (1 mL), and the mixture was allowed to stand in a refrigerator for 1 day. Black platelet crystals of **2** were precipitated and collected on a filter (40 mg; 0.061 mmol; yield 61%). They were suitable X-ray diffraction and magnetic studies. Mp. 168 – 170°C (decomp.). Anal. Calcd.: C, 34.87; H, 4.97; N, 8.13% for $\text{C}_{20}\text{H}_{34}\text{Cl}_2\text{CuN}_4\text{O}_{14}$. Found: C, 34.83; H, 4.82; N, 8.13%.

8.5.2 X-ray Crystallographic Studies

X-ray diffraction analyses of single crystals of **1** and **2** were performed in a manner similar to those of the complexes containing 2pyNO ligand (in Experimental Section of Chapter 6). All of the hydrogen atoms were found experimentally for **1** and **2**. Thermal displacement parameters were refined anisotropically for non-hydrogen atoms and those of hydrogen atoms were treated isotropically. Selected crystallographic data are summarized in Table 8.1.

8.5.3 Magnetic Measurements

The dc magnetic susceptibilities of the polycrystalline samples of **1** and **2** were measured in a manner similar to those of the 2pyNO complexes (in Experimental Section of Chapter 6).

References

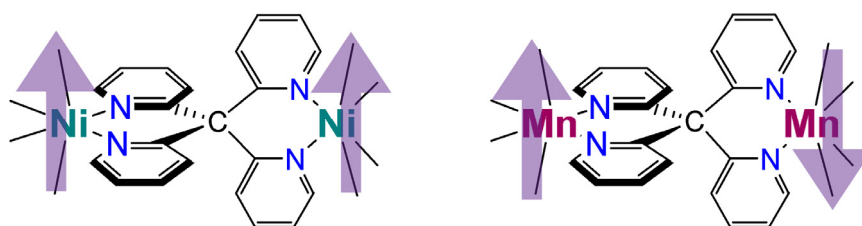
- (1) (a) Caneschi, A.; Gatteschi, D.; Sessoli, R.; Rey, P. *Acc. Chem. Res.* **1989**, *22*, 392. (b) Manriquez, J. M.; Yee, G. T.; McLean, R. S.; Epstein, A. J.; Miller, J. S. *Science* **1991**, *252*, 1415. (c) Inoue, K.; Hayamizu, T.; Iwamura, H.; Hashizume, D.; Ohashi, Y. *J. Am. Chem. Soc.* **1996**, *118*, 1803. (d) Lamaire, M. T. *Pure Appl. Chem.* **2004**, *76*, 277.
- (2) Romero, F. M.; Luneau, D.; Ziessel, R. *Chem. Commun.* **1998**, 551.
- (3) Aoki, C.; Ishida, T.; Nogami, T. *Inorg. Chem.* **2003**, *42*, 7616.
- (4) (a) Luneau, D.; Rey, P.; Laugier, J.; Fries, P.; Caneschi, A.; Gatteschi, D.; Sessoli, R. *J. Am. Chem. Soc.* **1991**, *113*, 1245. (b) Luneau, D.; Rey, P.; Laugier, J.; Belorizky, E.; Conge, A. *Inorg. Chem.* **1992**, *31*, 3578.
- (5) Keana, J. F. W. *Chem. Rev.* **1978**, *78*, 37.
- (6) Osanai, K.; Okazawa, A.; Nogami, T.; Ishida, T. *J. Am. Chem. Soc.* **2006**, *128*, 14008.
- (7) (a) Calder, A.; Forrester, A. R. *J. Chem. Soc. (C)* **1969**, 1459. (b) Forrester, A. R.; Hepburn, S. *P. J. Chem. Soc., Perkin I* **1974**, 2208.
- (8) Kanegawa, S.; Karasawa, S.; Maeyama, M.; Nakano, M. Koga, N. *J. Am. Chem. Soc.* **2008**, *130*, 3079.
- (9) McConnell, H. M. *J. Chem. Phys.* **1963**, *39*, 1910.
- (10) Gruber, S. J.; Harris, C. M.; Sinn, E. J. *Chem. Phys.* **1968**, *49*, 2183.
- (11) Kahn, O.; Prins, R.; Reedijk, J.; Thompson, J.S. *Inorg. Chem.* **1987**, *26*, 3557.
- (12) (a) Luneau, D.; Risoan, G.; Rey, P.; Grand, A.; Caneschi, A.; Gatteschi, D. Laugier, J. *Inorg. Chem.* **1992**, *32*, 5616. (b) Luneau, D.; Romero, F.M.; Ziessel, R. *Inorg. Chem.* **1998**, *37*, 5078.
- (13) Lutzen, A.; Hapke, M.; Staats, H.; Bunzen, J. *Eur. J. Org. Chem.* **2003**, 3948.
- (14) (a) Leeson, P. D.; Emmett, J. C. *J. Chem. Soc., Perkin Trans. I* **1988**, 3085. (b) Effenberer, F.; Krebs, A.; Willrett, P. *Chem. Ber.* **1992**, *125*, 1131.

Chapter 9

Ferromagnetic and Antiferromagnetic Exchange Couplings in Spiro-Fused Dinuclear Nickel(II) and Manganese(II) Complexes with an Approximate D_{2d} Symmetry

Abstract

Dinuclear [$\{\text{Ni}(\text{hfac})_2\}_2(\text{py}_4\text{C})$] (**1**) and [$\{\text{Mn}(\text{hfac})_2\}_2(\text{py}_4\text{C})$] (**2**) complexes were synthesized, where py_4C denotes tetrakis(2-pyridyl)methane. X-ray crystallographic analyses revealed that the dihedral angles were $91.87(9)^\circ$ and $87.4(2)^\circ$ between two chelate rings around the spiro-center in **1** and **2**, respectively. Very weak antiferromagnetic interaction was operative between manganese(II) spins. In contrast, ferromagnetic exchange coupling was operative between nickel(II) spins. Mechanism of the ferromagnetic coupling in **1** was proposed on the basis of the orthogonal $d\sigma$ -type magnetic orbitals, which was supported by DFT calculation.

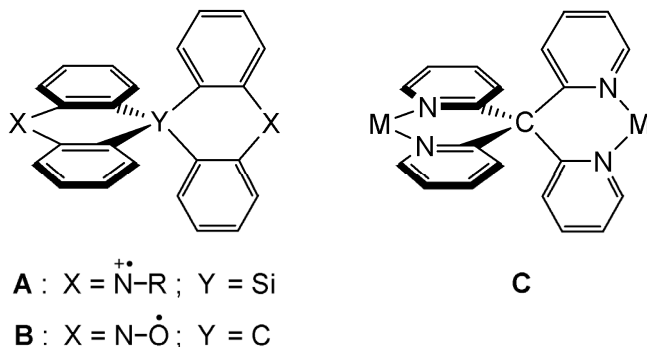


9.1 Introduction

Orthogonally fused π -conjugated systems having a spiro-junction are of great interest for molecular electronic devices, such as a transistor source-drain channel¹⁻³ and light-emitting diodes^{4,5}. The orthogonal arrangement also attracts much attention in magnetochemistry with respect to development of ground high-spin molecules,⁶⁻¹⁰ and, in particular, spirobiacridine-derived biradicals (**A** and **B** in Scheme 9.1)^{6,7} have been studied for ground triplet multiplicity. Synthetic efforts can be drastically decreased when genuine organic spin sources are replaced with transition-metal spin sources, but the application of the strategy of organic high-spin molecules to transition metal complexes is not sufficiently understood with respect to limitation of the π -conjugation regime.¹¹ Di- and polynuclear complex compounds containing a spiro-bridge are rare. Tetrakis(aminomethyl)methanes¹² and spirobi(cyclam)s¹³ have been utilized for bridging ligands but they consist of σ -bond skeletons. The dinuclear spiro-complexes involving four Schiff-bases has been prepared for 40 years ago, but their physical properties have not yet been studied.¹⁴ We planned

to apply the skeleton of **A** and **B** to the coordination compounds (**C**). Here we will report successful preparations and characterizations of nickel(II) and manganese(II) analogs, in which we can expect ferromagnetic couplings from the molecular design.

Scheme 9.1. Spiro-Compounds



9.2 Results

9.2.1 Syntheses

Tetrakis(2-pyridyl)methane (py_4C) was synthesized according to the procedure recently reported by Oda and co-workers.¹⁵ Target dinuclear compound **1** and **2** was obtained from the reaction of $M(hfac)_2$ ($M = Ni$ and Mn , respectively) and py_4C , which acted as a bis-bidentate chelating ligand. We attempted to synthesize the corresponding dinuclear copper(II) derivatives. We could isolate greenish blue $[Cu(hfac)_2(py_4C)]^{16}$ and green $[Cu(hfac)(py_4C)] \cdot [Cu(hfac)_3]^{16}$ as undesired products, but a dinuclear compound could not be obtained. Similarly we tried to prepare oxovanadium(II) derivatives using $VO(hfac)_2$, but no meaningful products were purified.

9.2.2 Crystal Structures

Figure 9.1 shows the molecular structure of **1**. Two Ni ions are crystallographically independent and coordinated with two pyridine nitrogen atoms each. Other coordination sites are occupied with hfac oxygen atoms. The dihedral angle between two chelate rings, defined with C1–C2–N1–Ni1–N2–C7 and C1–C12–N3–Ni2–N4–C17, is $91.87(9)^\circ$, which is very close to the right angle. The $[Ni(py_4C)Ni]$ core has an approximate D_{2d} symmetry. The crystal consists of enantiomerically pure Λ - Λ (or Δ - Δ) configured molecules in a non-centrosymmetric space group $P2_1$. Therefore, the whole molecule has a chiral D_2 symmetry including the stereoisomerism of the periphery.

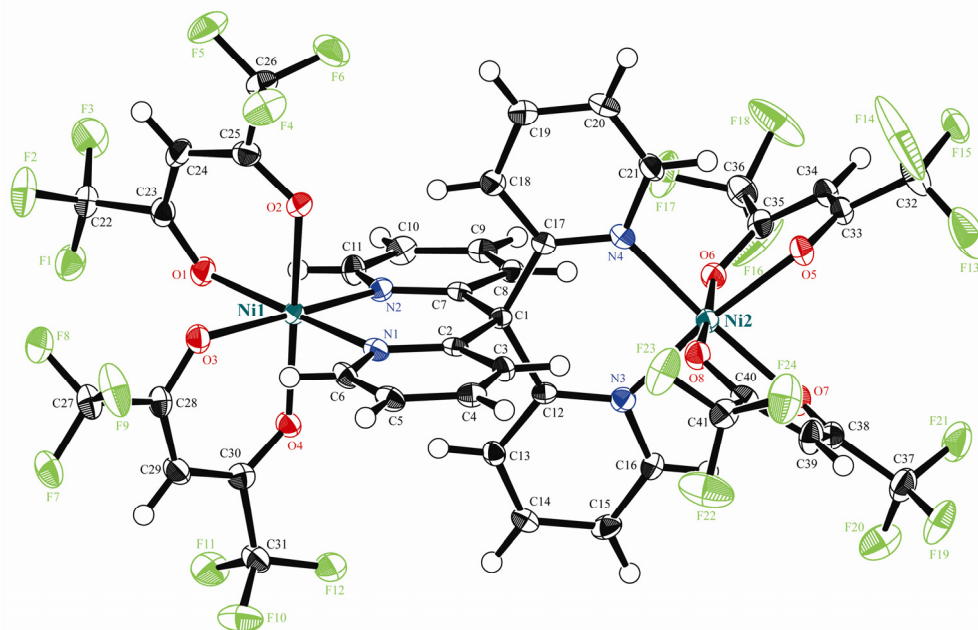


Figure 9.1. ORTEP drawing of $[\{\text{Ni}(\text{hfac})\}_2(\text{py}_4\text{C})]$ (**1**) with thermal ellipsoids at the 50% probability level. Atoms without numbering are hydrogen.

X-ray crystallographic analysis revealed the molecular structure of **2**. The molecular and crystal structures are practically identical to those of the nickel analog. Two Mn ions are crystallographically independent. The dihedral angle between two chelate rings, defined with C1–C2–N1–Mn1–N2–C7 and C1–C12–N3–Mn2–N4–C17, is $87.4(2)^\circ$, which is very close to the right angle. Distortion is very small for both Mn; the Mn–O distances vary from 2.140(5) to 2.180(5) Å and the Mn–N distances from 2.222(6) to 2.234(6) Å. The crystal consists of enantiomerically pure Λ – Λ (or Δ – Δ) configured molecules in a non-centrosymmetric space group $P2_1$.

9.2.3 Magnetic Properties

We measured the magnetic susceptibility of a randomly oriented polycrystalline sample of **1**. Figure 9.2a shows the temperature dependence of the product $\chi_{\text{mol}}T$ and for **1** on the molecular basis. Ferromagnetic interaction was clearly observed, as indicated by the increase of the $\chi_{\text{mol}}T$ value around 20 K with a decrease of temperature. To estimate the magnitude of magnetic interaction, we applied the $S_{\text{Ni}} = 1$ dinuclear model (eq 9.1),¹⁷ where the spin Hamiltonian is defined as $\mathcal{H} = -2J\hat{S}_1 \cdot \hat{S}_2$. The Weiss mean field parameter (θ) was introduced in eq 9.1, since a final drop was found below 5 K on further cooling, suggesting the presence of intermolecular antiferromagnetic coupling among the ground $S_{\text{total}} = 2$ molecules. A term for temperature-independent paramagnetism (χ_{TIP}) was included to eq 9.1. We obtained the following optimized parameters: $J/k_{\text{B}} = +1.85(4)$ K, $\theta = -1.16(1)$ K, $g = 2.217(4)$, and $\chi_{\text{TIP}} = 8.8(12) \times 10^{-4} \text{ cm}^3 \text{ mol}^{-1}$. The calculated curve well reproduced the experimental data (not shown). The intramolecular Ni–Ni coupling dominantly contributes to the

observed magnetic properties because the Ni1...Ni2 distance (7.016(3) Å) is shorter than any other intermolecular Ni...Ni distances (8.865(3) Å or longer). Therefore, the positive J value implies the intramolecular ferromagnetic Ni–Ni coupling.

$$\chi_{\text{mol}} = \frac{2N_{\text{A}}g^2\mu_{\text{B}}^2}{k_{\text{B}}(T-\theta)} \frac{5 + \exp(-4J/k_{\text{B}}T)}{5 + 3\exp(-4J/k_{\text{B}}T) + \exp(-6J/k_{\text{B}}T)} + \chi_{\text{TIP}} \quad (9.1)$$

In the above analysis, the possible ZFS of the ground state of **1** was confined to θ . If we explicitly introduce the ZFS parameter D for the nickel(II) ions in eq 9.1, χ_{mol} should be expressed in a somewhat different and complex manner as derived by Ginsberg (eq 9.2).¹⁸ The parameter optimization gave a positive J value: $J/k_{\text{B}} = +0.57(2)$ K, $D/k_{\text{B}} = -5.01(4)$ K, $g = 2.245(2)$, and $\chi_{\text{TIP}} = 2.6(8) \times 10^{-4} \text{ cm}^3 \text{ mol}^{-1}$. The calculated curve satisfactorily reproduced as well (the solid line in Figure 9.2a). This analysis seems more reliable than that of eq 9.1 from the improvement of calculated deviations, although intermolecular interaction was completely neglected here.¹⁹

$$\chi_{\text{mol}} = \frac{N_{\text{A}}g^2\mu_{\text{B}}^2}{3k_{\text{B}}} \left\{ \frac{F_1(J, D, T)}{T} + \frac{2F_2(J, D, T)}{D} + \frac{6a^2F_3(J, D, T)}{3J - \delta} + \frac{6b^2F_4(J, D, T)}{3J + \delta} \right\} + \chi_{\text{TIP}} \quad (9.2)$$

where

$$\delta = \sqrt{(3J + D)^2 - 8JD}, \quad C_1 = \frac{2\sqrt{2}D}{\sqrt{(9J - D + 3\delta)^2 - 8D^2}}, \quad C_2 = \frac{9J - D + 3\delta}{\sqrt{(9J - D + 3\delta)^2 + 8D^2}}$$

$$F_1(J, D, T) = \frac{1 + e^{4J/k_{\text{B}}T} + 4e^{(4J+D)/k_{\text{B}}T}}{2 + e^{D/k_{\text{B}}T} + e^{(J-\delta)/k_{\text{B}}T} + e^{(J+\delta)/k_{\text{B}}T} + 2e^{4J/k_{\text{B}}T} + 2e^{(4J+D)/k_{\text{B}}T}}$$

$$F_2(J, D, T) = \frac{2e^{(4J+D)/k_{\text{B}}T} + e^{D/k_{\text{B}}T} - 1 - 2e^{4J/k_{\text{B}}T}}{2 + e^{D/k_{\text{B}}T} + e^{(J-\delta)/k_{\text{B}}T} + e^{(J+\delta)/k_{\text{B}}T} + 2e^{4J/k_{\text{B}}T} + 2e^{(4J+D)/k_{\text{B}}T}}$$

$$F_3(J, D, T) = \frac{e^{4J/k_{\text{B}}T} - e^{(J+\delta)/k_{\text{B}}T}}{2 + e^{D/k_{\text{B}}T} + e^{(J-\delta)/k_{\text{B}}T} + e^{(J+\delta)/k_{\text{B}}T} + 2e^{4J/k_{\text{B}}T} + 2e^{(4J+D)/k_{\text{B}}T}}$$

$$F_4(J, D, T) = \frac{e^{4J/k_{\text{B}}T} - e^{(J-\delta)/k_{\text{B}}T}}{2 + e^{D/k_{\text{B}}T} + e^{(J-\delta)/k_{\text{B}}T} + e^{(J+\delta)/k_{\text{B}}T} + 2e^{4J/k_{\text{B}}T} + 2e^{(4J+D)/k_{\text{B}}T}}$$

The magnetization curve in **1** was measured at 5.5 K where the $\chi_{\text{mol}}T$ curve showed a maximum (Figure 9.3). The data fell between the theoretical curves of $S = 1$ and 2, supporting the presence of ferromagnetic interaction between the $S = 1$ centers. The apparent S was optimized to be 1.17(1) with $g = 2.24(1)$. The latter value agrees well with that obtained from the $\chi_{\text{mol}}T$ vs T plot, and the saturation magnetization should be $4.48 N_{\text{A}}\mu_{\text{B}}$.

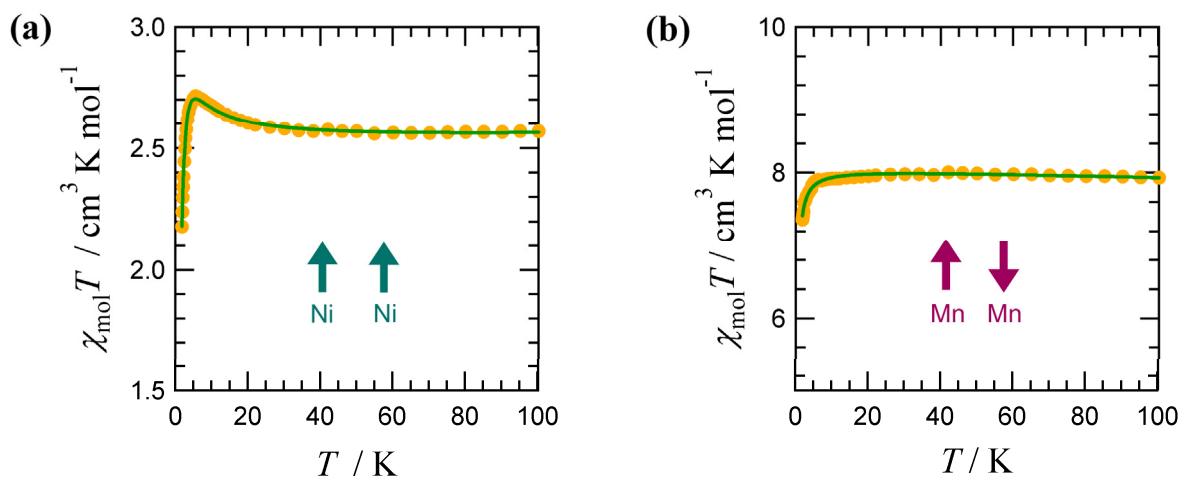


Figure 9.2. Temperature dependence of $\chi_{\text{mol}}T$ (orange circles) for (a) **1** and (b) **2** measured at 5000 Oe. The green solid lines represent calculated curves. See the text for the equations and optimized parameters. The ground spin structures are drawn with arrows.

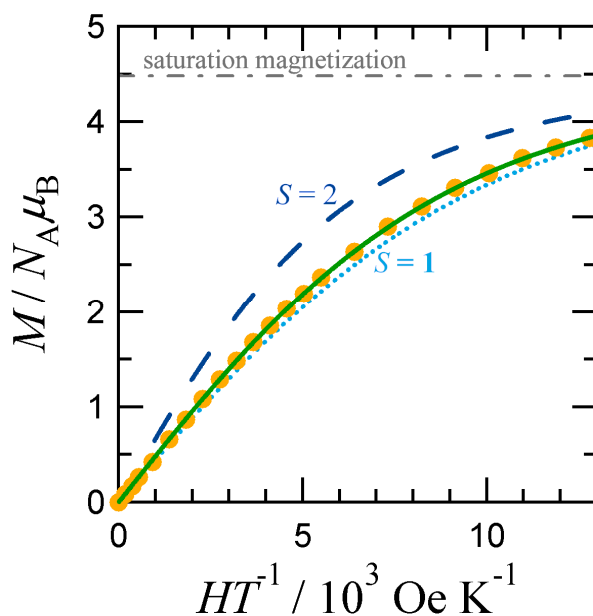


Figure 9.3. Magnetization curve for **1** measured at 5.5 K together with Brillouin functions with $S = 1$ and 2 . Green solid line represents a theoretical fit. For the equation and parameters, see the text.

Figure 9.2b shows the temperature dependence of the product $\chi_{\text{mol}}T$ for **2** on the basis of a molecule. The data were analyzed by the Curie–Weiss equation ($\chi_{\text{mol}} = C/(T - \theta)$) with $C = 8.01 \text{ cm}^3 \text{ K mol}^{-1}$ and $\theta = -0.12 \text{ K}$. The theoretical C value should be $8.75 \text{ cm}^3 \text{ K mol}^{-1}$ from $S_{\text{Mn}} = 5/2$ and $g = 2$. The somewhat smaller C value observed seems due to impurities such as mononuclear compounds (**3**). Very small antiferromagnetic interaction was indicated by the negative θ . A best fit to the $S =$

$^{5/2}$ dinuclear model (eq 9.3)¹⁷ with $x = J/k_B T$ gave the exchange parameter J of -0.023 K, where the spin Hamiltonian is defined as $H = -2J\hat{S}_1 \cdot \hat{S}_2$. The purity factor (ϕ) was estimated to be 92%. The theoretical curve is superposed in Figure 9.2b.

$$\chi_{\text{mol}} = f \frac{2N_A g^2 \mu_B^2}{k_B T} \frac{\exp(-2x) + 5 \exp(-6x) + 14 \exp(-12x) + 30 \exp(-20x) + 55 \exp(-30x)}{1 + 3 \exp(-2x) + 5 \exp(-6x) + 7 \exp(-12x) + 9 \exp(-20x) + 11 \exp(-30x)} \quad (9.3)$$

9.3 Discussion

9.3.1 Intramolecular Ferromagnetic Interaction in **1**

A plausible model for the ground high-spin state of **1** is as follows. SOMOs at the metal ions are degenerated by the molecular geometry of the [Ni(py₄C)Ni] core based on the D_{2d} point group like a triplet oxygen molecule.²⁰ The 3d-electron configuration of Ni^{II} is $(t_{2g})^6(e_g)^2$. Figure 9.4a shows the spatial arrangement of two $d_{x^2-y^2}$ orbitals, indicating the lack of magnetic-orbital overlaps. Even taking the other combination of $d_{z^2}/d_{x^2-y^2}$ into consideration, we can also expect orthogonal arrangement between them (Figure 9.4b). Owing to the orbital lobe direction, the contribution from $d_{x^2-y^2}$ should be dominant in both through-space and through-bond manners. Each spin center is triplet, and accordingly, the resultant spin multiplicity is quintet at the ground state.

Mulliken suggested that the twisted form of ethylene possessed a lowest triplet state,²¹ but modern calculation including ab initio molecular orbital methods predicted that it should have a singlet ground state owing to spin polarization^{22,23} and zwitter ionization.²⁴ Detailed exchange mechanisms in **1** deserve discussion. The most important difference from organic biradicals such as **A** and **B** is the fact that the magnetic orbitals of Ni^{II} have a σ -character with respect to the Ni–N bonds. The π -spin polarization onto the pyridine ring is not effectively operative in the present complex like several pyrimidine complexes,¹¹ whereas the σ -character seems suitable for the orthogonality around the sp³ carbon in terms of the superexchange mechanism originally proposed for M_1-X-M_2 ($X =$ halide, oxide, etc) by Anderson,²⁵ Goodenough,²⁶ Knamori,²⁷ and concisely rewritten by Oshio and Nakano.²⁸ The tetrahedral spiro carbon atom in **1** plays a role of X while the pyridyl–metal groups are assumed as the M_1 and M_2 moieties. In this picture, the through-bond $d_{x^2-y^2}/d_{x^2-y^2}$ interaction around the spiro carbon should be essentially non-bonding, as Figure 9.4a shows.

Furthermore, the role of the π -type t_{2g} orbitals should not be neglected though they are non-magnetic. It has been pointed out that ferromagnetic coupling requires the conditions that the $\langle \text{SOMO} | \text{SOMO} \rangle$ overlap is negligible and at the same time the $\langle \text{SOMO} | \text{NHOMO} \rangle$ overlap is appreciable between two paramagnetic centers.^{29,30} Owing to the twisted Ni \cdots Ni spatial arrangement,

the overlap between $e_g(\text{Ni1})$ SOMO and $t_{2g}(\text{Ni2})$ NHOMO is appreciable instead, as supported from the results of the manganese analog (see below). Therefore, **1** favors intramolecular ferromagnetic coupling.

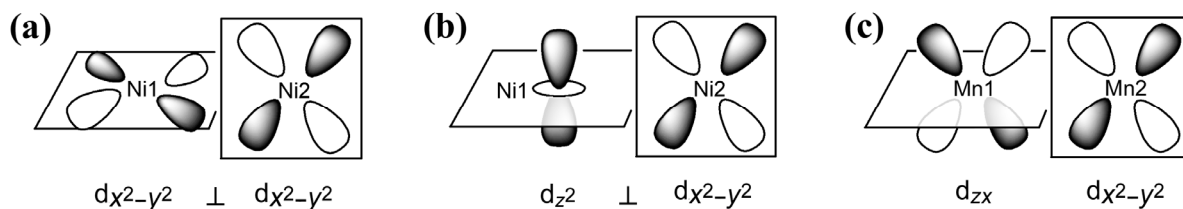


Figure 9.4. Schematic drawings for an orthogonal orbital arrangement between the two nickel(II) magnetic orbitals ((a) $d_{x^2-y^2}$ and $d_{x^2-y^2}$; (b) d_{z^2} and $d_{x^2-y^2}$) leading to ferromagnetic exchange interaction. (c) A schematic drawing for an orbital overlap between manganese(II) magnetic orbitals (d_{zx} and $d_{x^2-y^2}$) leading to antiferromagnetic contribution to the total Mn–Mn exchange interaction.

9.3.2 Intramolecular Antiferromagnetic Interaction in **2**

The intramolecular Mn \cdots Mn coupling dominantly contributes to the observed antiferromagnetic interaction because the Mn1 \cdots Mn2 distance (7.328(1) Å) is shorter than any intermolecular Mn \cdots Mn distances (8.686(1) Å or longer). A possible exchange mechanism for **2** is proposed as follows. The electron configuration (e_g)²(t_{2g})³ of manganese(II) ions has both σ - and π -type spins. As for σ -spins, any combination of magnetic orbitals from two manganese ions gives orthogonal arrangement owing to the spiro-structure. Similarly, any π -spins are orthogonal between the two Mn ions. On the other hand, some combinations of σ -spins and π -spins have substantial through-space orbital contacts. As Figure 9.4c shows, the $3d_{zx}$ orbital on Mn1 and the $d_{x^2-y^2}$ orbital on Mn2 are arranged parallel, for example.

The total magnetic exchange interaction is defined with the sum of ferromagnetic and antiferromagnetic terms.³¹ The experimental result indicates that the latter slightly surpass the former, giving rise to very small antiferromagnetic coupling in the present case.

9.3.3 DFT calculation for **1**

We performed theoretical calculation of a simplified model compound, [(L₂Ni)₂(py₄C)] (HL = malondialdehyde) based on the unrestricted DFT (UB3LYP/6–31G(d,p)). Four SOMOs were calculated at the quintet state which could be attributed mainly to the $3d_{x^2-y^2}$ and $3d_{z^2}$ orbitals. The distribution of the spin density (4e in total) is drawn in Figure 9.4, which clearly represents the

SOMOs carrying a σ -character. It is also clarified that the π -spin polarization does not occur onto the pyridine rings. This finding supports the superexchange mechanism described in Figure 9.3.

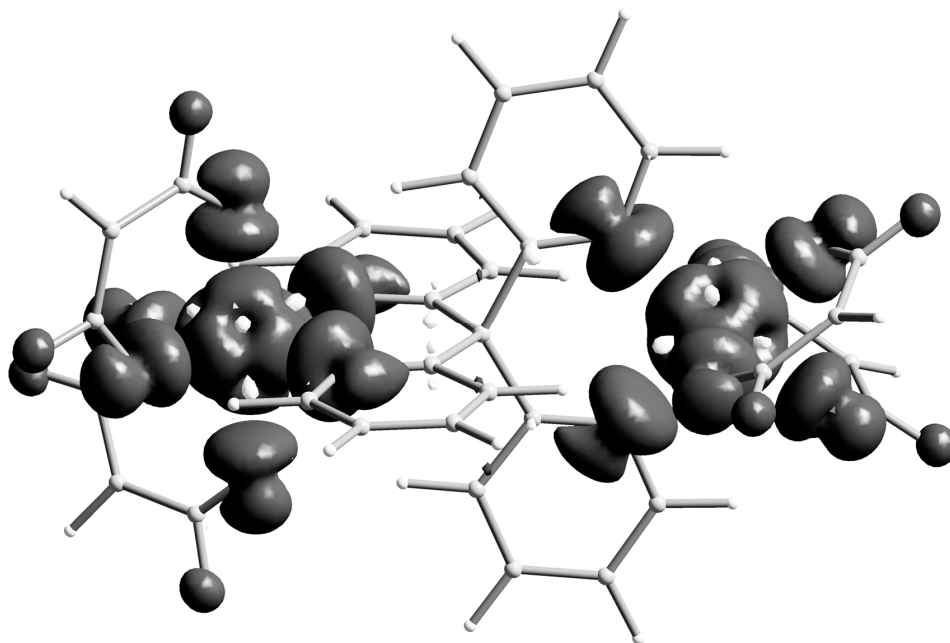


Figure 9.5. Spin density distribution at the quintet state of a model compound $[(\text{NiL}_2)_2(\text{py}_4\text{C})]$ (HL = malondialdehyde) calculated on the UB3LYP/6-31G(d,p) level.

The calculation also indicates that the quintet state is more stable than the singlet state by the energy difference of 0.0505 a.u. To evaluate the basis-set dependence, we performed another UB3LYP calculation using the LanL2DZ basis set. A similar result was derived; the quintet state was more stable than the singlet one by the gap of 0.0525 a.u. The energy gap between the $S = 2$ and $S = 0$ states corresponds to $6J$ (see, eq 9.1), and accordingly the calculated J value was estimated to be 0.0084 a.u. Although the calculation was performed on the simplified model omitting trifluoromethyl groups and accordingly afforded approximate results, the energy gap was rather overestimated compared to the experimental results. Nevertheless, the intramolecular ferromagnetic coupling was confirmed qualitatively.

9.4 Conclusion

In summary, the present spiro-fused structure was easily introduced by means of self-assembly of ligands and metal ions. The magnetic couplings in **1** and **2** have been clarified to be ferromagnetic

and antiferromagnetic, respectively. Since Oda and co-workers reported that the py₄C ligand could be utilized in polynuclear complexes although the metal ions were diamagnetic,³² this strategy may be expanded to two- (or three-) dimensionally networked complexes with paramagnetic metal ions showing ferromagnetic interaction.

Table 9.1. Selected Crystallographic Data for **1** and **2**

compounds	1	2
formula	C ₄₁ H ₂₀ F ₂₄ N ₄ Ni ₂ O ₈	C ₄₁ H ₂₀ F ₂₄ Mn ₂ N ₄ O ₈
formula weight	1269.97	1262.46
habit	green prism	light-yellow needle
dimension/mm ³	0.46 × 0.26 × 0.21	0.15 × 0.12 × 0.03
<i>T</i> /K	90	90
crystal system	monoclinic	monoclinic
space group	<i>P</i> 2 ₁	<i>P</i> 2 ₁
<i>a</i> /Å	9.184(3)	9.1363(3)
<i>b</i> /Å	14.833(6)	15.0475(6)
<i>c</i> /Å	17.070(6)	17.1982(8)
<i>α</i> /°	90	90
<i>β</i> /°	93.09(3)	93.427(2)
<i>γ</i> /°	90	90
<i>V</i> /Å ³	2321(1)	2360.2(2)
<i>Z</i>	1	1
<i>D</i> _{calc} /g cm ⁻³	1.816	1.776
unique data	3250	9876
<i>μ</i> (Mo Kα)/mm ⁻¹	0.965	0.686
<i>R</i> (<i>F</i>) ^a (<i>I</i> > 2σ(<i>I</i>))	0.0366	0.062
<i>R</i> _w (<i>F</i> ²) ^b (all data)	0.0401	0.107

^a $R = \sum ||F_o| - |F_c|| / \sum |F_o|$. ^b $R_w = [\sum w(F_o^2 - F_c^2)^2 / \sum w(F_o^2)^2]^{1/2}$.

9.5 Experimental Section

9.5.1 Preparations

[Ni(hfac)₂]₂(py₄C)] (1)

Dehydrated Ni(hfac)₂ (100 mg from Ni(hfac)₂·2H₂O; 0.20 mmol) in boiling heptane (5 mL) and py₄C¹⁵ (32 mg; 0.10 mmol) dissolved in CH₂Cl₂ (5 mL) were mixed while they were hot, and then the mixture was allowed to stand at room temperature for a few hours. Green prisms were precipitated and separated on a filter, giving **1** in 30% yield, which were subjected to analyses and physical measurements without further purification. Anal. Calcd.: C, 38.78; H, 1.59; N, 4.41% for C₄₁H₂₀F₂₄N₄Ni₂O₈. Found: C, 39.21; H, 1.63; N, 4.27%.

[Mn(hfac)₂]₂(py₄C)] (2)

Dehydrated Mn(hfac)₂ (100 mg from Ni(hfac)₂·2H₂O; 0.20 mmol) and py₄C (32 mg; 0.10 mmol) dissolved in 1/3 CH₂Cl₂/heptanes (20 mL) was refluxed overnight and then allowed to stand at room temperature for a few days. Light-yellow needle-like crystals of **2** were precipitated together with dark yellow platelet crystals of mononuclear [Mn(hfac)₂(py₄C)] (**3**) as an impurity. The solids were separated on a filter. The crystals of **2** and **3** could be isolated manually under a microscope. The yield of **2** and **3** were 28 and ca. 2%, respectively. The 2/1 and 1/1 metal–ligand ratios of **2** and **3**, respectively, were confirmed by means of elemental analysis and X-ray crystallographic analysis. **2**; Anal. Calcd.: C, 39.01; H, 1.60; N, 4.44% for C₄₁H₂₀F₂₄N₄Mn₂O₈. Found: C, 38.84; H, 1.40; N, 4.93%. **3**; Anal. Calcd.: C, 46.93; H, 2.29; N, 7.06% for C₃₁H₁₈F₁₂N₄MnO₄. Found: C, 46.12; H, 2.24; N, 7.05%.

9.5.2 X-ray Crystallographic Studies

X-ray diffraction data of single crystals of **1** and **2** were collected on a Rigaku R-axis RAPID diffractometer with graphite monochromated Mo K α radiation ($\lambda = 0.71069 \text{ \AA}$). The structures were directly solved and the parameters were refined in the CRYSTALSTRUCTURE program package.³³ Numerical absorption correction was used. All of the hydrogen atoms were located at calculated position and the parameters were refined as “riding”. Thermal displacement parameters were refined anisotropically for non-hydrogen atoms. Full-matrix least-squares methods were applied using all of the unique diffraction data. A disorder model was applied around the conformation of the C(36) trifluoromethyl group and the optimized occupancy ratio was 0.68(2)/0.32(2). Although the refinement was much improved, the ellipsoids of these fluorine atoms still remained elongate along the motional track. Figure 9.1 shows a major conformer. Selected crystallographic data are summarized in Table 9.1.

9.5.3 Magnetic Susceptibility and Magnetization Measurements

Magnetic susceptibilities of a polycrystalline specimen of **1** and **2** were measured on a Quantum Design MPMS SQUID magnetometer equipped with a 7 T coil in a temperature range of 1.8 – 100 K.

The magnetic responses were corrected with diamagnetic blank data of the sample holder measured separately. The diamagnetic contribution of the sample itself was estimated from Pascal's constant.

9.5.4 Molecular Orbital Calculations

Molecular orbital calculations were performed on the Gaussian03 program. We applied unrestricted DFT UB3LYP methods with the Becke exchange functional³⁴ and the Lee–Yang–Parr correlation functional.³⁵ The 6–31G(d,p) or LanL2DZ basis set was chosen. The convergence criterion for the energy was set at 10^{-6} a.u. The singlet SCF energy was calculated according to the broken-symmetry method.³⁶ The structural parameters were taken from the crystallographic data and the peripheral trifluoromethyl groups were replaced with hydrogen atoms to reduce computation time. The hydrogen position was optimized at the semi-empirical PM3 level.³⁷

References

- (1) Joachim, C.; Gimzewski, J. K.; Aviram, A. *Nature* **2000**, *408*, 541.
- (2) Tour, J. M.; Wu, R.; Schumm, J. S. *J. Am. Chem. Soc.* **1990**, *112*, 5662.
- (3) Wu, R.; Schumm, J. S.; Pearson, D. L.; Tour, J. M. *J. Org. Chem.* **1996**, *61*, 6906.
- (4) Su, H.-J.; Wu, C.-F.; Shu, C.-F. *Macromolecules* **2004**, *37*, 7197.
- (5) Wu, F.-I.; Dodda, R.; Reddy, D. S.; Shu, C.-F. *J. Mater. Chem.* **2002**, *12*, 2893.
- (6) Ito, A.; Urabe, M.; Tanaka, K. *Angew. Chem., Int. Ed.* **2003**, *42*, 921.
- (7) (a) Ooishi, M.; Seino, M.; Imachi, R.; Ishida, T.; Nogami, T. *Tetrahedron Lett.* **2002**, *43*, 5521.
(b) Ishida, T.; Ooishi, M.; Ishii, N.; Mori, H.; Nogami, T. *Polyhedron* **2007**, *26*, 1793.
- (8) (a) McElwee-White, L.; Goddard III, W. A.; Dougherty, D. A. *J. Am. Chem. Soc.* **1984**, *106*, 3461. (b) McElwee-White, L.; Dougherty, D. A. *J. Am. Chem. Soc.* **1984**, *106*, 3466.
- (9) Frank, N. L.; Clérac, R.; Sutter, J.-P.; Daro, N.; Kahn, O.; Coulon, C.; Green, M. T.; Golhen, S. Ouahab, L. *J. Am. Chem. Soc.* **2000**, *122*, 2053.
- (10) Itkis, M. E.; Chi, X.; Cordes, A. W.; Haddon, R. C. *Science* **2002**, *296*, 1443. (b) Chi, X.; Itkis, M. E.; Patrick, B. O.; Barclay, T. M.; Reed, R. W.; Oakley, R. T.; Cordes, A. W.; Haddon, R. C. *J. Am. Chem. Soc.* **1999**, *121*, 10395.
- (11) Ishida, T.; Kawakami, T.; Mitsubori, S.-i.; Nogami, T.; Yamaguchi, K.; Iwamura, H. *J. Chem. Soc., Dalton Trans.* **2002**, 3177.
- (12) (a) Aukauloo, A.; Ottenwaelder, X.; Ruiz, R.; Journaux, Y.; Pei, Y.; Rivière, E.; Muñoz, M. C. *Eur. J. Inorg. Chem.* **2000**, 951. (b) Smith, T. D.; Martell, A. E. *J. Am. Chem. Soc.* **1972**, *94*, 3029.
- (13) (a) McAuley, A.; Subramanian, S.; Zaworotko, M. J. *J. Chem. Soc., Chem. Commun.* **1992**, 1321.
(b) Bernhardt, P. V.; Comba, P.; Gahan, L. R.; Lawrance, G. A. *Aust. J. Chem.* **1990**, *43*, 2035.
- (14) Oehmke, R. W.; Bailar, Jr., J. C. *J. Inorg. Nucl. Chem.* **1965**, *27*, 2199.
- (15) Matsumoto, K.; Kannami, M.; Oda, M. *Tetrahedron Lett.* **2003**, *44*, 2861.
- (16) Okazawa, A.; Ishida, T.; Nogami, T. *Polyhedron* **2005**, *24*, 2584.
- (17) Wojciechowski, W. *Inorg. Chim. Acta* **1967**, *1*, 319.
- (18) Ginsberg, A. P.; Martin, R. L.; Brookes, R. W.; Sherwood, R. C. *Inorg. Chem.* **1972**, *11*, 2884.
- (19) Journaux, Y.; Lozan, V.; Klingele, J.; Kersting, B. *Chem. Commun.* **2006**, 83.
- (20) Dupeyre, R. M.; Rassat, A.; Ronzaud, J. *J. Am. Chem. Soc.* **1974**, *96*, 6559.
- (21) Mulliken, R. S. *Phys. Rev.* **1932**, *41*, 751.
- (22) Kollmar, H.; Staemmler, V. *Theor. Chim. Acta* **1978**, *48*, 223.
- (23) Silverman, S. K.; Dougherty, D. A. *J. Phys. Chem.* **1993**, *97*, 13273.
- (24) Brooks, B. R.; Schaefer III, H. F. *J. Am. Chem. Soc.* **1979**, *101*, 307.
- (25) Anderson, P. W. *Phys. Rev.* **1959**, *115*, 2.
- (26) Goodenough, J. B. *Phys. Rev.* **1955**, *100*, 564.
- (27) Kanamori, J. *J. Phys. Chem. Solids* **1959**, *10*, 87.

- (28) Oshio, H.; Nakano, M. *Chem.–Eur. J.* **2005**, *11*, 5178.
- (29) Awaga, K. in: Lahti, P. M.; Ed. *Magnetic Properties of Organic Materials*; Marcel Decker: New York, 1999; Chapter 25, p. 519.
- (30) Awaga, K.; Inabe, T.; Maruyama, Y. *Chem. Phys. Lett.* **1992**, *190*, 349.
- (31) Kahn, O. *Molecular Magnetism*; VCH: New York, 1993; Chapter 8, p 145.
- (32) Matsumoto, K.; Kannami, M.; Oda, M. *Chem. Lett.* **2004**, *33*, 1096.
- (33) CRYSTALSTRUCTURE, *Crystal Structure Analysis Package*, version 3.8; Rigaku and Rigaku/MS: The Woodlands, TX, USA, 2000–2006.
- (34) Becke, A. D. *J. Chem. Phys.* **1993**, *98*, 5648.
- (35) Lee, C.; Yang, W.; Parr, R. G. *Phys. Rev. B* **1998**, *37*, 785.
- (36) (a) Ruiz, E.; Cano, J.; Alvarez, S.; Alemany, P. *J. Comput. Chem.* **1999**, *20*, 1391. (b) Noodleman, L.; Peng, C. Y.; Case, D. A.; Mouesca, J. M. *Coord. Chem. Rev.* **1995**, *144*, 199.
- (37) Stewart, J. J. P. *QCPE Bull.* **1989**, *9*, 10.

Chapter 10

Concluding Remarks

In this thesis, the three subjects have been described in detail:

- (i) On exchange couplings between lanthanide ion and transition-metal ion
- (ii) On exchange couplings between transition-metal ion and organic radical
- (iii) On exchange couplings between homo transition-metal ions

Various new materials of hetero-spin and homo-spin systems have been synthesized, purified, and characterized extensively. The synthetic schemes have been rationally designed, so that the mutual geometry among the paramagnetic centers can be constructed as expected. Since the absence or presence of the overlap of magnetic orbitals is a key to the magnetic couplings between them, designable compounds and syntheses are of increasing importance. Novel compounds including organic, inorganic, and organic-inorganic-hybrid compounds are always welcomed by chemists as well as physicists in the field of materials chemistry. Facile synthetic procedures are in particular desired from the viewpoint of wide application for the science, technology, and industry. The self-assemble methods described in this thesis would be a great advantage because of the facile preparation.

The characteristics of the 2p, 3d, and 4f elements have been utilized in an appropriate manner. For example, the 4f elements usually have a large magnetic moments and anisotropy, which is favorable for the developments of SMMs and SCMs. The 2p elements are expected to show large exchange coupling and actually the magnitude of the magnetic coupling came to as much as the order of room temperatures. The 3d elements have moderate magnitudes of moments and exchange interaction. These magnetic orbitals are well defined, thanks to the conventional crystal/ligand field theory and theoretical treatments such as DFT calculations. Hetero-spin materials seem to be promising, when we pay more attention to the role of such talents and synergy effects of these elements.

The exchange couplings in novel compounds and the new methodology to determine the 4f–3d interactions were established. The first examples on determination of 4f–3d exchange parameters by means of EPR were demonstrated in Chapters 3 and 4. The magnetic studies on $[\text{Dy}_2\text{Cu}_2]_n$ clarified the slow magnetization orientation and magnetization steps usually related to a SMM. It is of great interest that $[\text{Dy}_2\text{Cu}_2]_n$ compounds showed distinct SMM behavior originated from a repeating tetranuclear unit $[\text{Dy}_2\text{Cu}_2]$ despite the one-dimensional chain form. Many SMMs have been known so far, but such situation is rare. The HF-EPR technique was expanded to investigate J_{4f-3d} in several $[\text{Ln}_2\text{Cu}_2]_n$ analogs. The $|J_{4f-3d}|$ value monotonically decreases in the order of ${}_{64}\text{Gd}$ to ${}_{68}\text{Er}$, with the number of the 4f-spins decreasing from seven to three. The present methodology would be

applicable to other 4f–3d heterometallic compounds. Magnetic couplings in the $[\text{Ln}_2\text{Cu}]$, $[\text{Ln}_2\text{Ni}]$, and $[\text{Ln}_2\text{Cu}_2]_n$ derivatives involving lighter lanthanide ions are worth of investigation. Some lighter lanthanide ions are broadly available in commercial permanent magnets such as SmCo_5 and $\text{Nd}_2\text{F}_{14}\text{B}$. At the same time, it is important to explore 4f–3d exchange couplings on various derivatives containing other transition-metal ions. We believe that this work will lead to further designable SMMs.

The study on magneto-structure relationship for copper(II) or nickel(II) complexes with *tert*-butyl 2-pyridyl-substituted radical ligands were reported in Chapters 6–8. There have been no reports on the chelate compounds involving 2pyNO so far. We successfully achieved to isolate the radical due to the stabilization by complexation. Three novel radicals were synthesized, and eight novel radical-chelated complexes were identified. The strong π -d interaction simply correlates with the planarity of the chelate ring around a metal ion. Most of them showed intramolecular ferromagnetic coupling between the spins. Furthermore, the compounds having magnetic coupling constants $2J/k_B$ as large as 400 K are notable. The application of metal–radical approaches like this type of compounds would be very useful for the development of room-temperature magnets. The 5-membered chelation in the 2-pyridyl–NO systems has an advantage over the 6-membered chelation in the 2-pyridyl–NN systems, with respect to the planarity and accordingly the $d\sigma$ – π^* orbital orthogonality. 2-Pyridyl–NO system has another advantage; strong magnetic coupling owing to the high spin density on the ligating oxygen atoms. Large three-dimensional exchange interaction among spins will lead to a molecule-based magnet with a higher critical temperature. The molecule-based magnet made of “radical chelating complexes” seems promising in future magnet technology.

We can expect intramolecular, as well as intermolecular, magnetic couplings through the pyridine rings where an appreciable spin is delocalized, being regarded as an advantage of the Ar–NO system over the NN system. Introduction of π -conjugated radicals seems promising along this line, and the replacement of the bulky *tert*-butyl group with aromatic groups is a next target.¹

In Chapter 9, magnetic interactions between 3d–3d spins were discussed. Homometallic dinuclear complexes containing a spiro-bridge, which are rare, were synthesized and the magnetic measurements revealed that exchange couplings were ferro- and antiferromagnetic between two nickel(II) and manganese(II) ions, respectively. The py_4C ligand works as a bridge and accordingly is suitable for constructing polynuclear complexes. This strategy may be expanded to two- and three-dimensionally networked complexes with paramagnetic metal ions showing ferromagnetic interaction, though the magnitude of the exchange couplings are relatively small. Magnetic materials involving a single paramagnetic species would reduce the cost of preparation.

The magnet technology is indispensable for our daily life of today and future. I hope that this study will be one of the guidelines for the developments of molecular magnetic materials.

1) Okazawa, A.; Ishida, T.; Nogami, T. *Polyhedron* **2007**, *26*, 1965.

List of Publications Related to The Thesis

Contents of this thesis have been published in:

Chapter 3

- (1) Atsushi Okazawa, Takashi Nogami, Hiroyuki Nojiri, Takayuki Ishida
“Ferromagnetic Dy–Ni and Antiferromagnetic Dy–Cu Couplings in Single-Molecule Magnets [Dy₂Ni] and [Dy₂Cu]”
Inorganic Chemistry, **Vol. 47**, pp 9763–9765 (2008).

Chapter 4

- (2) Atsushi Okazawa, Takashi Nogami, Hiroyuki Nojiri, Takayuki Ishida
“Exchange Coupling and Energy-Level Crossing in a Magnetic Chain [Dy₂Cu₂]_n Evaluated by High-Frequency Electron Paramagnetic Resonance”
Chemistry of Materials, **Vol. 20**, pp 3110–3119 (2008).

Chapter 5

- (3) Atsushi Okazawa, Ryo Watanabe, Hiroyuki Nojiri, Takashi Nogami, Takayuki Ishida
“Magnetic Properties and Exchange Couplings of One-Dimensionally Arrayed 4f–3d Heterometallic [Ln₂Cu₂]_n Compounds”
Polyhedron, (doi: 10.1016/j.poly.2008.12.035).

Chapter 6

- (4) Atsushi Okazawa, Takashi Nogami, Takayuki Ishida
“*tert*-Butyl 2-Pyridyl Nitroxide Available as a Paramagnetic Chelate Ligand for Strongly Exchange-Couples Metal–Radical Compounds”
Chemistry of Materials, **Vol. 19**, pp 2733–2735 (2007).

Chapter 7

- (5) Atsushi Okazawa, Yasunori Nagaichi, Takashi Nogami, Takayuki Ishida
“Magneto-Structure Relationship in Copper(II) and Nickel(II) Complexes Chelated with Stable *tert*-Butyl 5-phenyl-2-pyridyl Nitroxide and Related Radicals”
Inorganic Chemistry, **Vol. 47**, pp 8859–8868 (2008).

Chapter 8

- (6) Atsushi Okazawa, Takashi Nogami, Takayuki Ishida
“Strong Intramolecular Ferromagnetic Couplings in Nickel(II) and Copper(II) Complexes Chelated with *tert*-Butyl 5-Methoxy-2-pyridyl Nitroxide”
Polyhedron, (doi:10.1016/j.poly.2008.10.049).

Chapter 9

- (7) Atsushi Okazawa, Takayuki Ishida, Takashi Nogami
“Ferromagnetic Exchange Coupling in a Spiro-Fused Dinuclear Nickel(II) Complex with an Approximate D_{2d} Symmetry”
Chemical Physics Letters, **Vol. 427**, pp 333–337 (2006).
- (8) Atsushi Okazawa, Takayuki, Ishida, Takashi Nogami
“Dinuclear Manganese(II) Complex Containing Tetrakis(2-pyridyl)methane”
Chemistry Letters, **Vol. 33**, pp 1478–1479 (2004).

Other publication of the author:

- (9) Sohei Ueki, Atsushi Okazawa, Takayuki Ishida, Takashi Nogami, Hiroyuki Nojiri
“Tetranuclear Heterometallic Cycle Dy_2Cu_2 and the Corresponding Polymer Showing Slow Relaxation of Magnetization Reorientation”
Polyhedron, **Vol. 26**, pp 1970–1976 (2007).
- (10) Atsushi Okazawa, Takayuki Ishida, Takashi Nogami
“Preparation, Structures, and Magnetic Properties of Precursors for Chelating Compounds of 2-Pyridyl Nitroxide Derivatives”
Polyhedron, **Vol. 26**, pp 1965–1969 (2007).
- (11) Keita Osanai, Atsushi Okazawa, Takashi Nogami, Takayuki Ishida
“Strong Ferromagnetic Exchange Couplings in Copper(II) and Nickel(II) Complexes with a Paramagnetic Tridentate Chelate Ligand, 2,2'-Bipyridyl-6-yl *tert*-Butyl Nitroxide”
Journal of the American Chemical Society, **Vol. 128**, pp 14008–14009 (2006).
- (12) Atsushi Okazawa, Takayuki Ishida, Takashi Nogami
“Structures and Magnetic Properties of Copper(II) Complexes Containing Tetrakis(2-pyridyl)methane”
Polyhedron, **Vol. 24**, pp 2584–2587 (2005).